

# 博士研究生学位论文

# 大型强子对撞机底夸克实验上 粲重子的研究

培养单位: 物理学院

学 科: 粒子物理与原子核物理

研究生:许傲

指导教师: 高原宁 教 授

二〇二三年一月

# Study of charmed baryons at the LHCb experiment

Dissertation Submitted to

**Peking University** 

in partial fulfillment of the requirement for the degree of

**Doctor of Philosophy** 

in

**Particle Physics and Nuclear Physics** 

by

Xu Ao

Dissertation Supervisor: Professor Gao Yuanning

January, 2023

### 摘要

在粒子物理的标准模型中,强相互作用由量子色动力学(QCD)描述。QCD 是色 SU(3) 规范理论,具有渐进自由的特性,即相互作用耦合系数在高能或短程作用下较小,适用于微扰计算,而在低能或长程作用下耦合系数变大,非微扰效应占主导地位。理解 QCD 的低能非微扰特性是当前粒子物理学的重要任务之一。强子是强相互作用的束缚态,研究其谱学结构和性质是理解 QCD 非微扰特性的重要手段。由于粲夸克质量  $m_c$  较大,对应的能量略高于 QCD 能标,所以研究粲强子对于理解 QCD 非微扰特性具有独特的优势。本论文利用欧洲核子研究中心大型强子对撞机上的底夸克实验(LHCb)采集的质子-质子对撞数据,精确测量了粲重子 $\Omega_c^0$  和  $\Xi_c^0$  的寿命,并寻找了双粲重子  $\Xi_{cc}^+$ ,为深入理解 QCD 提供了重要的实验信息。

理论上通常在重味夸克展开的框架下计算弱衰变粲重子的寿命,其中粲重子的 衰变宽度按1/m。展开为一系列局域算符矩阵元的求和,忽略高阶算符的贡献。非微 扰效应主要体现在非微扰矩阵元中,不同的理论计算对矩阵元采用不同的处理方 式,导致寿命计算结果的差异很大,但给出的粲重子寿命排序基本一致: $\Omega_c^0(css)$ <  $\Xi_c^0(csd) < \Lambda_c^+(cud) < \Xi_c^+(csu)$ 。这一排序也与早期的实验结果一致。然而, 2018 至 2019 年 LHCb 实验利用来自底重子衰变产生的次级粲重子, 更精确地测量了 它们的寿命,其中 $\Omega_c^0$ 和 $\Xi_c^0$ 重子的寿命与以前的结果显著不同,从而导致了新的 粲重子寿命排序:  $\Xi_c^0 < \Lambda_c^+ < \Omega_c^0 < \Xi_c^+$ 。这一巨大差异对理论计算提出了新的挑 战,在实验上则有必要通过独立的实验测量作进一步检验。为此,本论文利用瞬 发产生的  $\Omega_c^0$  和  $\Xi_c^0$  重子,即直接从质子-质子对撞顶点产生的粲重子,精确测量了 它们的寿命。相比于来自底重子衰变产生的次级粲重子,瞬发粲重子的产生截面 很大,但难点是如何去除次级粲重子的成分。本研究利用粲重子衰变顶点与对撞 主顶点的信息,通过细致的建模实现了瞬发粲重子和次级粲重子在统计上的区分。 测量得到  $\Omega_c^0$  重子的寿命是  $\tau(\Omega_c^0) = 276.5 \pm 13.4 \pm 4.4 \pm 0.7 \, \text{fs}$ , $\Xi_c^0$  重子的寿命是  $\tau(\Xi_c^0) = 148.0 \pm 2.3 \pm 2.2 \pm 0.2 \,\text{fs}$ , 其中前两项不确定度分别对应统计不确定度和 系统不确定度,最后一项是由作为参考的  $D^0$  介子寿命的不确定度引入的。这些结 果与 LHCb 实验利用来自底重子衰变产生的次级粲重子的测量结果一致, 且  $\Omega_c^0$  寿 命的测量精度比之前改进了一倍。该测量确认了新的粲重子寿命的排序,为理解 QCD 非微扰效应和重味夸克展开中的高阶效应的影响提供了坚实的实验基础。

在引入粲夸克之后, 夸克模型预言存在双粲重子, 即包含两个粲夸克的重子,

其中三个基态为  $\mathcal{Z}_{cc}^{++}(ccu)$ 、  $\mathcal{Z}_{cc}^{+}(ccd)$  和  $\Omega_{cc}^{+}(ccs)$ 。双粲重子与普通重子的内部结 构具有显著差别,集粲夸克偶素和粲介子的动力学性质于一身,是研究 QCD 非 微扰效应的独特平台。实验上寻找双粲重子并精确测量其性质具有重要意义。许 多实验开展了寻找双粲重子的研究,但直到近年才由 LHCb 实验提供了  $\mathcal{E}_{cc}^{++}$  重子 存在的确切证据。本论文的另一项工作是利用 LHCb 实验的质子-质子对撞数据在  $\Lambda_c^+ K^- \pi^+$  衰变末态中寻找双粲重子  $\Xi_{cc}^+$ 。本研究通过优化触发和事例筛选条件显 著地提高了实验灵敏度,并考虑了  $\mathcal{E}_{cc}^{+}$  重子的寿命相比  $\mathcal{E}_{cc}^{++}$  重子可能短很多的特 点。研究发现  $\Lambda_c^+K^-\pi^+$  不变质量谱在 3.62 GeV 附近存在信号增强的迹象。在  $\Xi_{cc}^+$ 与  $\mathcal{E}_{cc}^{++}$  作为同位旋二重态质量近似相同的假设下,且考虑系统不确定度后, $\mathcal{E}_{cc}^{+}$ 的信号显著度为  $2.7\sigma$ ; 而如果不作此假设,在理论预言的 3.4-3.8 GeV 质量范围内,  $\Xi_{cc}^+$  的信号显著度为  $1.7\sigma$ 。本研究在  $\Xi_{cc}^+$  重子不同的寿命假设下,给出了  $\Xi_{cc}^+$  重子 的产生截面与衰变分支比的乘积相对于瞬发  $\Lambda_c^+$  重子或  $\Xi_{cc}^{++}$  重子产生截面的比值  $(R_{\Lambda_c^+}$  或  $R_{\Xi_{cc}^{++}})$  的上限随  $\Xi_{cc}^+$  质量的变化关系。在 80 fs 的寿命假设下,置信水平 为 95% 的  $R_{A_c^+}$  上限在 3.4-3.8 GeV 的质量范围内的最大值为  $2 \times 10^{-4}$ ,相应的  $R_{\Xi_{cc}^{++}}$ 上限的最大值为 1。该结果比 LHCb 早期的测量改进了一个数量级以上,对  $\Xi_{cc}^+$  重 子的寿命和衰变性质给出了更为严格的限制,为进一步的实验研究和理论计算提 供了重要信息。

关键词: 大型强子对撞机底夸克实验; 强子谱; 寿命; 双粲重子; 量子色动力学

#### **ABSTRACT**

Quantum Chromodynamics (QCD) is the theory of strong interaction in the Standard Model of particle physics. It is a color SU(3) gauge theory which exhibits asymptotic freedom and quark confinement. At the high energy scale, the strong coupling constant is small and the perturbation theory is applicable in calculation, while at the low energy scale, the coupling constant becomes large and only nonperturbative methods can be used. Understanding nonperturbative QCD is one of the most important tasks in modern particle physics. Hadrons are bound states of quarks. Hadron spectroscopy provides important information on QCD in the nonperturbative regime. Weak decays of hadrons constitute a novel laboratory for studying strong dynamics through the interplay with the weak interaction. Charmed hadron is a unique probe into nonperturbative QCD due to the fact that the charm quark mass  $m_c$  is marginally larger than the QCD energy scale. This thesis performed a precise measurement of lifetimes of charmed baryon  $\Omega_c^0$  and  $\Xi_c^0$  and a search for the doubly charmed baryon  $\Xi_{cc}^+$ , using pp collision data collected by the LHCb experiment at the Large Hadron Collider. These measurements provide important information for understanding the nature of QCD.

Lifetimes of weakly decaying charmed baryons are calculated in the framework of Heavy Quark Expansion, in which the total decay width is calculated through an expansion in terms of  $1/m_c$ . Nonperturbative effects are encoded into matrix elements of local operators and lead to large theoretical uncertainties on the calculation of lifetimes. Nevertheless, most theoretical predictions give a consistent lifetime hierarchy of charmed baryons as  $\Omega_c^0(css) < \Xi_c^0(csd) < \Lambda_c^+(cud) < \Xi_c^+(csu)$ , which is also consistent with early experimental measurements. However, LHCb reported precise measurements of charmed baryon lifetimes in 2018 and 2019, using secondary signals, *i.e.* signals from semileptonic beauty baryon decays. The measured lifetimes of  $\Omega_c^0$  and  $\Xi_c^0$  baryon are different from early measurements significantly, leading to a new lifetime hierarchy:  $\Xi_c^0 < \Lambda_c^+ < \Omega_c^0 < \Xi_c^+$ . The large discrepancy challenges theoretical calculations and calls for independent measurements to further clarify the situation. The first part of this thesis reports precise measurements of lifetimes of charmed baryon  $\Omega_c^0$  and  $\Xi_c^0$ , using prompt signals, *i.e.* signals produced directly from pp collisions. Prompt signals have larger production cross-section compared with secondary signals, while it is difficult to

subtract contributions from secondary ones. This measurement discriminates statistically prompt and secondary signals through dedicated modelling of decay-vertex information. The resultant  $\Omega_c^0$  lifetime is  $\tau(\Omega_c^0) = 276.5 \pm 13.4 \pm 4.4 \pm 0.7$  fs, and  $\Xi_c^0$  lifetime is  $\tau(\Xi_c^0) = 148.0 \pm 2.3 \pm 2.2 \pm 0.2$  fs, where the uncertainties are statistical, systematic, and due to the limited knowledge of the  $D^0$  lifetime, which serves as a reference in this measurement. The results are consistent with previous LHCb measurements with secondary signals, and the precision of  $\Omega_c^0$  lifetime is improved by a factor of two. This measurement confirms the new lifetime hierarchy of charmed baryons and lays a firm foundation to understand nonperturbative effects and higher order corrections in the calculation within the heavy quark expansion theory.

After the discovery of charm quark flavour, the quark model predicts doubly charmed baryons, i.e. baryons containing two charm quarks. Ground-state doubly charmed baryons include  $\Xi_{cc}^{++}(ccu)$ ,  $\Xi_{cc}^{+}(ccd)$ , and  $\Omega_{cc}^{+}(ccs)$ . Doubly charmed baryons are unique systems for the study of nonperturbative QCD, because they incorporate dynamics of the charmonium and the charmed meson. Many experimental searches have been performed for doubly charmed baryons, while only the  $\Xi_{cc}^{++}$  baryon is well established by the LHCb experiment recently. The second part of this thesis reports a search for the doubly charmed baryon  $\Xi_{cc}^+$  through the  $\Lambda_c^+K^-\pi^+$  final state. This search optimises the trigger and event selection, taking into account the challenge that the predicted lifetime of  $\Xi_{cc}^+$  baryon is much shorter than that of the  $\Xi_{cc}^{++}$  baryon. An enhancement is seen in the invariant-mass distribution of  $\Lambda_c^+ K^- \pi^+$  system around 3.62 GeV. The signal significance is 2.7 $\sigma$  under the assumption that the mass of  $\Xi_{cc}^+$  and  $\Xi_{cc}^{++}$  is roughly the same according to isospin symmetry, while the significance is reduced to  $1.7\sigma$  in the mass region of 3.4-3.8 GeV. Upper limits of the  $\Xi_{cc}^+$  production cross-section times branching fraction relative to that of prompt  $\Lambda_c^+$  baryons and  $\Xi_{cc}^{++}$  baryons,  $R_{\Lambda_c^+}$  and  $R_{\Xi_{cc}^{++}}$ , are set as a function of invariant mass under different lifetime hypotheses. For a  $\Xi_{cc}^+$  lifetime of 80 fs, the largest upper limit of  $R_{\Lambda_c^+}(R_{\Xi_{cc}^{++}})$  in the mass region of 3.4-3.8 GeV at 95% confidence level is  $2 \times 10^{-4}$ (1). This limit is more than one order of magnitude lower than the previous LHCb search for the  $\Xi_{cc}^{+}$  baryon, and imposes a more stringent constraint on the lifetime and decay properties of  $\Xi_{cc}^+$  baryon. This search provides important information for theoretical calculations and guidance for future experimental searches.

**Keywords:** LHCb; Hadron spectroscopy; Lifetime; Doubly charmed baryon; QCD

# **TABLE OF CONTENTS**

摘 要	I
ABSTRACT	III
TABLE OF CONTENTS	V
LIST OF FIGURES.	VIII
LIST OF TABLES	XXI
CHAPTER 1 INTRODUCTION	1
1.1 Standard Model of particle physics	1
1.1.1 Quark model	4
1.1.2 Quantum Chromodynamics	9
1.1.3 Nonperturbative QCD	12
1.1.4 Charm is charming	16
1.2 Lifetime of charmed baryons	17
1.2.1 Charmed baryon lifetimes from a theoretical perspective	18
1.2.2 Experimental status of charmed baryon lifetimes	22
1.3 Doubly charmed baryons	24
1.3.1 Doubly charmed baryons from a theoretical perspective	26
1.3.2 Experimental status of doubly charmed baryons	39
CHAPTER 2 EXPERIMENTAL FACILITIES	45
2.1 Large Hadron Collider	45
2.2 LHCb experiment.	49
2.2.1 LHCb detector	50
2.2.2 LHCb simulation	56
2.2.3 LHCb data flow	57
2.2.4 Performance of the LHCb detector	58
CHAPTER 3 MEASUREMENT OF $\Omega_c^0$ AND $\Xi_c^0$ LIFETIMES	68
3.1 Analysis overview	68
3.2 Event selection	69
3.2.1 Trigger selection	69

#### TABLE OF CONTENTS

71
76
77
78
82
84
86
88
89
90
91
94
96
97
101
102
104
106
107
109
109
110
110
113
113
114
115
115
116
119
119
120

#### TABLE OF CONTENTS

4.2 Event selection	122
4.2.1 Trigger selection.	122
4.2.2 Offline preselection	123
4.2.3 Multivariate analysis	124
4.2.4 Removal of track-clone candidates	132
4.2.5 Duplicate candidates	134
4.2.6 Study of backgrounds	135
4.3 Strategy for measuring the mass.	137
4.3.1 Systematic uncertainties in the mass measurement	140
4.4 Invariant-mass distribution after unblinding	146
4.5 Upper limits	149
4.5.1 Event selection for setting upper limits	150
4.5.2 Yield of control modes	154
4.5.3 Estimation of efficiency	157
4.5.4 Systematic uncertainties	167
4.5.5 Determination of upper limits	172
4.6 Result and discussion	174
CHAPTER 5 SUMMARY AND PROSPECTS	177
5.1 LHCb upgrade and other programs	178
5.2 Prospects for lifetime measurements.	181
5.3 Prospects for doubly heavy baryons	182
APPENDIX A BOOKKEEPING OF DATA AND SIMULATION SAMPLE	ES 187
APPENDIX B STATISTICAL MODELS	191
APPENDIX C FIT RESULTS FOR PROMPT YIELD DETERMINATION	194
APPENDIX D EVENT SELECTION FOR $\Lambda_c^+$ AND $\varXi_{cc}^{++}$ CONTROL MOD	DES 201
APPENDIX E SELECTION EFFICIENCY FOR RUN 2 DATA	207
REFERENCES	210
致谢	222

Figure 1.1	Particle content of the Standard Model [3]
Figure 1.2	$SU(4)_f$ 20-plets of ground-state (left) $J^P = \frac{1}{2}^+$ and (right) $J^P = \frac{3}{2}^+$
	baryons. Right-handed Cartesian coordinates of $(I_z, S, C)$ are adopted. Con-
	stituent quark contents are indicated at each dot. Circle dots indicate loca-
	tions where tow states are located. The naming scheme follows Sec. 7 in
	Review of Particle Physics [2]6
Figure 1.3	Measurements of $\alpha_s$ as a function of energy scale $Q$ [2]
Figure 1.4	Quark mass function with solutions of Dyson-Schwinger equations in in-
	frared and logarithmic running in the ultraviolet from perturbation the-
	ory [19]
Figure 1.5	Hadron spectrum from lattice QCD in Sec. 15 of Review of Particle Physics
	[2]. Horizontal bars (boxes) denote experimental masses (widths). Lattice
	calculations from different groups are denoted by points with error bars $13$
Figure 1.6	Comparison of ground-state charmed baryon spectrum between experimen-
	tal data and calculations from lattice QCD [20] and quark models [12-13].14
Figure 1.7	Tree-level Feynman diagram of (left) muon and (right) charm quark decay.18
Figure 1.8	Feynman diagrams corresponding to local operators in Eq. 1.32. Reproduced
	from Ref. [27]
Figure 1.9	Measurements of lifetimes of (left) charmed mesons and (right) charmed
	baryons
Figure 1.10	Measurements of lifetimes of (left) beauty mesons and (right) beauty
	baryons
Figure 1.11	The citation summary in March 2022 with the key word doubly charmed
	baryons at INSPIRE HEP. The peaking record corresponds to 40 papers
	in 2018. The steep rises correspond to the observation of $\Omega_c^0$ in 1995, the
	claim of $\Xi_{cc}^+(3520)$ baryon by SELEX in 2002, and the observation of $\Xi_{cc}^{++}$
	baryon by LHCb in 2017
Figure 1.12	Representative Feynman diagrams in different production environments.
	Reproduced from Ref. [53:55:57-58]

Figure 1.13	Theoretical predictions of masses of $J^P = \frac{1}{2}$ doubly charmed baryon (left)
	$\Xi_{cc}$ and (right) $\Omega_{cc}^+$ . The x-axis corresponds to the time of the theoreti-
	cal work. The y-axis corresponds to the predicted mass subtracted by the
	known mass of ${\it J/\psi}$ meson. Isospin splitting is ignored in $\Xi_{cc}$ doublets. Re-
	sults are grouped according to the theoretical method used, including quark
	model (denoted by QM), effective file theory or related method of QCD
	sum rules, HQET, NRQCD and CHPT (denoted by EFT), Bethe-Salpeter
	equation (denoted by BSE), and LQCD (denoted by LQCD). Experimental
	results of $\Xi_{cc}^{+}(3520)$ baryon reported by SELEX in 2002, and $\Xi_{cc}^{++}(3620)$
	baryon reported by LHCb in 2017 are indicated by yellow and pink lines,
	respectively
Figure 1.14	Theoretical predictions of hyperfine splitting between $J^P = \frac{1}{2}^+$ and $J^P =$
	$\frac{3}{2}^+$ baryons for (left) $\Xi_{cc}$ and (right) $\Omega_{cc}^+$ . The x-axis corresponds to the
	time of the theoretical work. The <i>y</i> -axis corresponds to the predicted mass
	difference. Results are grouped according to the theoretical method used,
	including quark model (denoted by QM), effective file theory or related
	method of QCD sum rules, HQET, NRQCD and CHPT (denoted by EFT),
	and LQCD (denoted by LQCD)
Figure 1.15	Theoretical predictions of isospin splitting between $\Xi_{cc}^+$ and $\Xi_{cc}^{++}$ baryon.
	The x-axis corresponds to the time of the theoretical work. The y-axis cor-
	responds to the predicted mass difference. Results are grouped according
	to the theoretical method used, including quark model (denoted by QM),
	effective file theory or related method of QCD sum rules, HQET, NRQCD
	and CHPT (denoted by EFT), and LQCD (denoted by LQCD)35
Figure 1.16	Mass spectra of (left) $\Xi_{cc}$ baryons and (right) $\Omega_{cc}^+$ baryons calculated in
	Ref. [13]. The horizontal dashed line indicates the $\Lambda_c D$ and $\Lambda_c D_s$ threshold
	for $\Xi_{cc}$ and $\Omega_{cc}^+$ baryons, respectively. The notation of $(n_D L n_q l) J^P$ is used
	to describe the quantum numbers of baryons, where $n_D$ and $n_q$ are the radial
	quantum number of the diquark and the light quark, $L$ and $l$ are the orbital
	angular momentum of the diquark and the light quark, and $J^P$ is the total
	angular momentum $J$ and parity $P$ of the baryon
Figure 1.17	Mass spectra of (left) $\Xi_{cc}$ and (right) $\Omega_{cc}^+$ baryons with spin up to $\frac{7}{2}$ calcu-
	lated in Ref. [107]. The masses are shown w.r.t. the known mass of $\eta_c$ 36

Figure 1.18	The topological diagrams for nonleptonic charmed baryon decays [123].38
Figure 1.19	Experimental searches for doubly heavy baryons. Null results are labelled
	with squares. Claims of observation are labelled with states40
Figure 2.1	Schematic layout of the LHC
Figure 2.2	Accelerator complex at CERN
Figure 2.3	View of the LHCb detector
Figure 2.4	Production of $b\overline{b}$ quark pairs as a function of (left) angles w.r.t the beam and
	(right) rapidities, simulated with PYTHIA8 and CTEQ6 NLO [162]. In the
	right plot, The coverage of a general-purpose detector (GPD) is shown as
	comparison
Figure 2.5	Trigger diagrams for (left) 2012 and (right) 2015 data taking, representative
	of Run 1 and 2, respectively
Figure 2.6	The general architecture of the LHCb online system
Figure 2.7	The LHCb data flow. 58
Figure 2.8	Illustration of the various track types. For reference the main $B$ -field com-
	ponent $(B_y)$ is plotted above as a function of the z coordinate60
Figure 2.9	Comparison of track reconstruction efficiency in (top) 2011 and 2012, and
	(bottom) 2012 and 2015, as a function of the (left) momentum and (right)
	pseudorapidity61
Figure 2.10	Relative momentum resolution versus momentum for long tracks in data.61
Figure 2.11	The primary vertex resolution as a function of track multiplicity. The $x$ (red)
	and $y$ (blue) resolutions are separately shown. The superimposed histogram
	shows the distribution of track multiplicity per reconstructed primary vertex
	for all events that pass the HLT. 62
Figure 2.12	Resolution of the (left) $x$ and (right) $y$ components of the impact parame-
	ter
Figure 2.13	Decay time resolution for $B_s^0  o J/\psi \phi$ decays as a function of momen-
	tum63
Figure 2.14	The kaon efficiency (kaons identified as kaons) and pion misidentification
	(pions misidentified as kaons) fraction as a function of momentum for (left)
	2012 and (right) 2016 data taking
Figure 2.15	Trigger efficiency for (left) L0Hadron and (right) HLT1 as a function of $p_{\rm T}$
	in Run 1 65

Figure 2.16	Trigger efficiency for (left) LOHadron and (right) HLT1 as a function of
	$p_{\mathrm{T}}$ in Run 2. Three plots on the right corresponding to Hlt1TrackMVA,
	Hlt1TwoTrackMVA, and inclusive HLT165
Figure 3.1	Schematic view of (left) prompt signal and (right) secondary signal69
Figure 3.2	Invariant mass distribution of (left) $\Omega_c^0$ , (middle) $\Xi_c^0$ , and (right) $D^0$ candi-
	dates in 2018 data samples after the trigger selection
Figure 3.3	Distributions of training variables in 2016 $\Omega_c^0$ simulation (Signal) and $\Omega_c^0$
	mass-sideband data (Background)74
Figure 3.4	Correlation matrices of (left) signal and (right) background samples75
Figure 3.5	BDT responses of training and test samples
Figure 3.6	Distribution of BDT response for 2016 (left) $\Omega_c^0$ simulated sample (with in-
	put lifetime of 250 fs) and the background subtracted data sample, and (right)
	$\Xi_c^0$ simulated sample (with input lifetime of 250 fs) and the background sub-
	tracted $\Xi_c^0$ data sample
Figure 3.7	Distributions of log-sized min( $\theta_{i,j}$ ) in 2018 (left) $\Omega_c^0$ and (right) $\Xi_c^0$ data. 76
Figure 3.8	Invariant mass distributions of 2016 (left) $\Omega_c^0$ (middle) $\Xi_c^0$ and (right) $D^0$
	data samples after all event selection criteria
Figure 3.9	Invariant-mass distributions of $\Omega_c^0$ signals in different decay-time bins in
	2016 simulated samples
Figure 3.10	Fit results of the $\log_{10}(\chi_{\rm IP}^2)$ distribution of simulated prompt and secondary
	$\Omega_c^0$ signals in 2016 sample
Figure 3.11	Parameter $\mu$ in different decay-time bins obtained by fitting to 2016 simu-
	lated samples
Figure 3.12	Parameter $\sigma$ in different decay-time bins obtained by fitting to 2016 simu-
	lated samples. 81
Figure 3.13	Parameter $\xi$ in different decay-time bins obtained by fitting to 2016 simu-
	lated samples
Figure 3.14	Parameter (top) $\rho_1$ and (bottom) $\rho_2$ in different decay-time bins obtained by
	fitting to 2016 simulated samples. 82
Figure 3.15	Fit results of the $\log_{10}(\chi_{IP}^2)$ distribution of background component in differ-
	ent decay-time bins in the $\Omega_c^0$ mass sideband83
Figure 3.16	Distribution of $\log_{10}(\chi_{\text{IP}}^2)$ in 2016 $D^0$ sample in different decay-time bins,
	along with the fit results 84

Figure 3.17	Parameter (left) $\mu$ of (top) prompt and (bottom) secondary component in
	different decay-time bins obtained from fits to the $D^0$ simulated sample and
	data sample, and (right) the difference between $\mu$ in data and simulation for
	the (top) prompt and (right) secondary component
Figure 3.18	Yields of (left) prompt signals and (right) normalized prompt signals for
	(top) $\Omega_c^0$ , (middle) $\Xi_c^0$ and (bottom) $D^0$ modes in 2016-2018 samples. The
	decay time (x-axis) is shown in log scale
Figure 3.19	Fit projections to the invariant-mass distribution in 2016 data for the $\Omega_c^0$
	mode
Figure 3.20	Fit projections to the invariant-mass distribution in 2016 data for the $\Xi_c^0$
	mode
Figure 3.21	Fit projections to the invariant-mass distribution in 2016 data for the $D^0$
	mode90
Figure 3.22	Fit projections to the $\log_{10}(\chi_{\rm IP}^2)$ distribution with the mass in $\pm 2\sigma$ range
	around the signal mass peak in 2016 data for the $\Omega_c^0$ mode91
Figure 3.23	Fit projections to the $\log_{10}(\chi_{\rm IP}^2)$ distribution with the mass in $\pm 2\sigma$ range
	around the signal mass peak in 2016 data for the $\Xi_c^0$ mode92
Figure 3.24	Fit projections to the $\log_{10}(\chi_{\rm IP}^2)$ distribution with the mass in $\pm 2\sigma$ range
	around the signal mass peak in 2016 data for the $D^0$ mode93
Figure 3.25	The fraction of secondary signals in (left) $\Omega_c^0$ , (middle) $\Xi_c^0$ and (right) $D^0$
	data samples93
Figure 3.26	PID efficiency as a function of momentum $p$ and rapidity $\eta$ for (left) pro-
	ton, (middle) kaon and (right) pion and in (top) 2016, (middle) 2017 and
	(bottom) 2018 data of the MagDown polarity94
Figure 3.27	L0 hadron TOS efficiency for (left) $p$ , (middle) $K$ and (right) $\pi$ 94
Figure 3.28	Comparison of phasespace variables for prompt and secondary signals in
	2016 $\Omega_c^0$ MC samples
Figure 3.29	Comparison of 2016 data and simulation before and after the phasespace
	weight for $\Omega_c^0$ mode, where the simulation before (after) weighting is shown
	in gray (blue), and the sWeighted data is shown in red95
Figure 3.30	Comparison of 2016 data and simulation before and after the phasespace
	weight for $\Xi_c^0$ mode96

Figure 3.31	Comparison of 2016 data and simulation before and after the phasespace weight for $D^0$ mode
Figure 3.32	Comparison of additional phasespace variables for (left) $\Omega_c^0$ , (middle) $\Xi_c^0$ , and (right) $D^0$ mode
Figure 3.33	Comparison of prompt distributions between data and simulation for $\Omega_c^0$ mode. The prompt data distribution is extracted with two-dimensional fits
	of invariant-mass and $\log_{10}(\chi_{\rm IP}^2)$ described in Sec. 3.3, in bins of variables under study. The "log" indicates a 10-based logarithmic transformation, and final-state particle $p$ , $K^-$ , and $\pi^+$ of $\Omega_c^0$ are labeled as Pp, Km1, Km2 and Pip, respectively.
Figure 3.34	Comparison of various distributions between data and simulation for $\Xi_c^0$ mode. The prompt data distribution is extracted with two-dimensional fits of invariant-mass and $\log_{10}(\chi_{\rm IP}^2)$ described in Sec. 3.3, in bins of variables under study. The "log" indicates a 10-based logarithmic transformation, and final-state particle $p$ , $K^-$ , and $\pi^+$ of $\Xi_c^0$ are labeled as Pp, Km1, Km2 and Pip, respectively.
Figure 3.35	Comparison of various distributions between 2018 data and simulation for $D^0$ mode. The prompt data distribution is extracted with two-dimensional fits of invariant-mass and $\log_{10}(\chi_{\text{IP}}^2)$ described in Sec. 3.3, in bins of variables under study. The "log" indicates a 10-based logarithmic transformation, and final-state particle $K^-$ , $K^+$ , $\pi^-$ , $\pi^+$ of $D^0$ are labeled as Km, Kp, Pim and Pip, respectively.
Figure 3.36	Normalised decay-time distributions after each correction stage for 2016 (left) $\Omega_c^0$ , (middle) $\Xi_c^0$ and (right) $D^0$ simulation. The input lifetime of $\Omega_c^0$ and $\Xi_c^0$ simulation sample is 250 fs. The input lifetime of $D^0$ simulation sample is 410 fs
Figure 3.37	Decay-time acceptance in 2016 sample for all modes in bins of (left) true decay time and (right) reconstructed decay time
Figure 3.38	Decay-time acceptance ratio of signal to control mode versus the reconstructed decay time

Figure 3.39	Decay-time distributions of (left) data and simulation samples, (middle)
	decay-time ratios of data to simulation samples, and (right) the decay-time
	fit results to the $D^0$ data for (top) 2016, (middle) 2017, and (bottom) 2018
	$D^0$ control mode
Figure 3.40	Decay-time distributions for the (left) $\Omega_c^0$ mode and the (right) $\Xi_c^0$ mode
	with the $\chi^2$ fit superimposed. The uncertainty on the data distribution is
	statistical only
Figure 3.41	Results of consistency checks for (left) $\Omega_c^0$ and (right) $\Xi_c^0$ modes 103
Figure 3.42	Default (in blue) and alternative (in red) binning scheme in ps 105
Figure 3.43	Secondary fraction and its uncertainty with shared fractions in 2016-
	2018
Figure 3.44	Prompt yield ratio of signal to control mode in 2016-2018 data for (left) $\Omega_c^0$
	and (right) $\Xi_c^0$ mode, along with the fit result
Figure 3.45	Prompt yield ratio of signal to control mode in data for each data-taking
	period and for (top) $\Omega_c^0$ and (bottom) $\Xi_c^0$ mode, along with the fit result.106
Figure 3.46	Prompt yields of the $D^0$ mode with alternative configurations in 2016
	data
Figure 3.47	Measured lifetimes of (left) $\Omega_c^0$ and (right) $\Xi_c^0$ baryon with different input
	lifetimes of simulated samples. The <i>x</i> -axis is blinded
Figure 3.48	Momentum distributions of $D^0$ in 2018 data and simulation for $D^0$ sam-
	ple111
Figure 3.49	Distributions of (left) the angle between $D^0$ daughters and (middle and
	right) $p_{\rm T}$ of $D^0$ daughters in 2018 data and simulation
Figure 3.50	The fit result of $t_{K^-\pi^+} - t_{K^+\pi^-}$ in (left) data and (right) MC
Figure 3.51	Distributions of the difference of reconstructed and true decay time in 2016
	simulation for (left) $\Omega_c^0$ , (middle) $\Xi_c^0$ , and (right) $D^0$ modes
Figure 3.52	Distributions of difference between measured lifetimes and input lifetimes
	in pseudo-experiments. Cases in which the resolution is either 20 fs larger
	in data (top) or in simulation (bottom) are shown for both (left) $\Omega_c^0$ and
	(right) $\Xi_c^0$ modes
Figure 3.53	The curve of scaling factor vs compatibility for (blue) Kaon and (red) Pion
	tracks from $D^0$ decay.

Figure 3.54	Distribution of the measured lifetime of (left) $\Omega_c^0$ and (right) $\Xi_c^0$ with ran-
	domized $\tau^{\rm con}$ in the decay-time fit
Figure 3.55	Distribution of the measured lifetime of (left) $\Omega_c^0$ and (right) $\Xi_c^0$ 116
Figure 3.56	Comparison of current, previous and combined LHCb results 117
Figure 4.1	The contributing tree-level Feynman diagram with internal $W$ -emission for
	the decay of $\Xi_{cc}^+ \to \Lambda_c^+ K^- \pi^+$ . 120
Figure 4.2	Distributions of input variables for signal and background samples under de-
	fault lifetime hypothesis
Figure 4.3	Distributions of input variables for signal and background samples under
	zero lifetime hypothesis. 128
Figure 4.4	Correlation matrices of the training variables of (left) signal and (right) back-
	ground samples for default lifetime hypothesis
Figure 4.5	Correlation matrices of the training variables of (left) signal and (right) back-
	ground samples for zero-lifetime hypothesis
Figure 4.6	ROC curves for different algorithms under (left) default and (right) zero-
	lifetime hypotheses
Figure 4.7	Response distributions for (top left) BDT, (top right) BDTG, and (bottom)
	MLP algorithms, under default lifetime hypothesis
Figure 4.8	Response curves for (left) BDTG, (middle) MLP, and (right) MLPBNN al-
	gorithms, under zero lifetime hypothesis
Figure 4.9	Punzi figure of merit $F(t)$ as a function of the MVA response $t$ , under (left)
	default and (right) zero lifetime hypotheses
Figure 4.10	The (left) $\Xi_{cc}^+$ invariant-mass distribution and (right) the background reten-
	tion after the MVA cut in each invariant-mass bin of the WS sample, for
	(top) default and (bottom) zero lifetime hypotheses
Figure 4.11	Punzi FoM evaluated with reweighted MC samples for different lifetime
	hypotheses. The blue line refers to the approach in which reoptimisation is
	performed, and the red line refers to the approach where the default working
	point is used. 132
Figure 4.12	Distributions of angles of tracks with the same charge in the WS sample.
	The right plot zooms in on the zero angle
Figure 4.13	Distributions of angles of tracks with the same charge in the MC sample.
	The right plot zooms in on the zero angle

Figure 4.14	Mass distribution of the internal-track-clone candidates of the WS sam-
	ple
Figure 4.15	Mass distribution of the duplicate candidates of the MC sample 134
Figure 4.16	Invariant-mass distribution of intermediate $\Lambda_c^+$ candidates, with the shaded
	area indicating the signal region (gray horizontal) and the sideband region
	(brown crossed). Events are taken from the WS sample with the MVA cuts applied
Figure 4.17	Invariant-mass distributions of $\Xi_{cc}^+$ candidates in the WS sample. The two
	histograms represent the distributions in the WS sample for (filled square)
	background subtracted $\Lambda_c^+$ candidates and (filled triangle) $\Lambda_c^+$ candidates in
	the sideband region
Figure 4.18	Fit to the $\Lambda_c^+ K^- \pi^+$ invariant-mass distribution of the partially-
	reconstructed $\Xi_{cc}^{++} \rightarrow \Lambda_c^+ K^- \pi^+ \pi^+$ candidates with Argus function,
	studied with 2016 $\Xi_{cc}^{++}$ MC sample
Figure 4.19	Invariant mass distributions of $\Lambda_c^+$ candidates, with $p$ mass hypothesis
	changed to that of (left) $K^+$ and (right) $\pi^+$ respectively
Figure 4.20	Invariant mass distributions of $\Xi_{cc}^+$ candidates in the (left) $D_s^+$ and (right)
	$D^+$ signal regions, defined as $\pm 18$ MeV around the mass peaks observed in
	Fig. 4.19
Figure 4.21	Distribution of $m(\Xi_{cc}^+)$ in the MC sample, along with the fit with a double-
	sided crystal ball function plus a Gaussian function
Figure 4.22	Mass resolution of the reconstructed $\Xi_{cc}^+$ candidates at different $\Xi_{cc}^+$ mass
	hypotheses
Figure 4.23	Distribution of $m(\Xi_{cc}^+)$ in the WS sample, along with the fit with a second-
	order Chebychev polynomial
Figure 4.24	Distribution of (left) $m(\Xi_{cc}^+)$ in simulation, along with the fit with Iptia2
	function, and (right) resultant line shapes of the default and alternative sig-
	nal model
Figure 4.25	Gaussian fit to the distribution of per-candidate mass shift, $\Delta m$ , for the vari-
	ation of momentum correction factor by $1\sigma$ . 142

Figure 4.26	Distribution of (left) $\Xi_{cc}^+$ mass bias (measured value subtracted by true
	value) when the mass difference is used as estimator of the $\Xi_{cc}^+$ mass, along
	with the fit with a Double Gaussian function, and (right) $\Xi_{cc}^+$ mass bias
	(measured value subtracted by true value) when the measured $\Lambda_c^+$ mass is
	constrained to its known value, along with the fit with a DSCB function.143
Figure 4.27	Distribution of difference between the reconstructed mass and the input one
	(left) without applying cuts relating to decay time of $\Xi_{cc}^+$ , and (right) after all
	offline selections, including the MVA variable, along with fits with DSCB
	function
Figure 4.28	Distribution of difference between the reconstructed mass and the input one
	in (left) 2016 and (right) 2012 simulated signal samples, after all offline se-
	lections, including the MVA selection, along with the fit with DSCB func-
	tion
Figure 4.29	Bias of fitted mass at different $\Xi_{cc}^+$ lifetime hypotheses for 2016 and 2012
	simulated signal samples with the same 2016 trigger selection 145
Figure 4.30	Distribution of (left) $\Xi_{cc}^+$ mass calculated from final-state track momenta
	smeared with a Gaussian function for resolution, corrected by the recon-
	structed $\varLambda_c^+$ mass calculated in the same way, and (right) mean $\varXi_{cc}^+$ mass as
	a function of the resolution
Figure 4.31	Mass distributions of the (left) intermediate $\Lambda_c^+$ and (right) $\Xi_{cc}^+$ candi-
	dates for the full data sample. All selection is applied, including the $\varLambda_c^+$
	mass requirement, indicated by the cross-hatched region in the left plot,
	of 2270 MeV $< M([pK^-\pi^+]_{\Lambda_c^+}) < 2306$ MeV. The right-sign (RS)
	$m(\Lambda_c^+ K^- \pi^+)$ distribution is shown in the right plot, along with the wrong-
	sign (WS) $m(\Lambda_c^+ K^- \pi^-)$ distribution normalised to have the same area. The
	dotted red line at 3518.7 MeV indicates the mass of the $\Xi_{cc}^+$ baryon reported
	by SELEX [137] and the dashed blue line at 3621.2 MeV indicates the mass
	of the $\Xi_{cc}^{++}$ baryon [135]
Figure 4.32	Distribution of $m(\Xi_{cc}^+)$ in Run 1 data with the MVA selection optimised for
	(left) default and (right) zero lifetime hypothesis
Figure 4.33	Distribution of $m(\Xi_{cc}^+)$ in Run 2 data with the MVA selection optimised for
	(left) default and (right) zero lifetime hypothesis

Figure 4.34	Distribution of $m(\Xi_{cc}^+)$ in Run 1 and 2 data with the MVA selection opti-
	mised for (left) default and (right) zero lifetime hypothesis
Figure 4.35	Likelihood scan of $\mu$ for the combined Run 1 and Run 2 data with the MVA
	selection optimised for the default lifetime hypothesis
Figure 4.36	Local <i>p</i> -value as a function of $m(\Xi_{cc}^+)$ for the combined Run 1 and Run 2
	data sets with the MVA selection optimised for (left) default and (right)
	zero lifetime hypothesis
Figure 4.37	Profile likelihood ratio distribution of one of the toy experiments. The
	$N(c_0)$ corresponding to this plot is 5
Figure 4.38	Correlation matrices of training variables of (left) the signal and (right) the
	background samples for the first MVA classifier with the default lifetime
	hypothesis. 152
Figure 4.39	Correlation matrices of the training variables of (left) the signal and (right)
	the background samples for the second MVA classifier with the default life-
	time hypothesis. 152
Figure 4.40	ROC curves for the (left) first and (right) second MVA classifiers under the
	default lifetime hypothesis
Figure 4.41	Response curves for the (left) first and (right) second MVA classifiers under
	the default lifetime hypothesis. For the second step, the requirement of
	$t_1 > 0.0$ for MVA1 is applied. 153
Figure 4.42	Punzi figure of merit $F(t_1, t_2)$ for the two-step MVA under the default life-
	time hypothesis
Figure 4.43	The (left) invariant-mass distributions of the $\Xi_{cc}^+$ candidates for the sig-
	nal data sample collected in 2012 and 2016-2018 and (right) local p-
	value as a function of $m(\Lambda_c^+ K^- \pi^+)$ . The event selection for upper-limit
	setting is applied, including the $\Lambda_c^+$ mass requirement of 2270 MeV <
	$M([pK^-\pi^+]_{\Lambda_c^+}) < 2306 \text{MeV}$ . The right-sign (RS) $m(\Lambda_c^+K^-\pi^+)$ distribu-
	tion is shown in the right plot, along with the wrong-sign (WS) $m(\Lambda_c^+ K^- \pi^-)$
	distribution normalized to have the same area as the RS sample. The dashed
	red line of 3518.7 MeV indicates the mass of the $\Xi_{cc}^+$ baryon reported by SE-
	LEX and the dashed blue line of 3621.2 MeV refers to the mass of the $\Xi_{cc}^{++}$
	baryon

Figure 4.44	Invariant-mass distribution of (left) $\Lambda_c^+$ mass in (left) 2012 and (right) 2016
	data, along with the fit results
Figure 4.45	Distributions of $\log_{10}(\chi_{\mathrm{IP}}^2)$ for (left) prompt and (right) secondary $\varLambda_c^+$ sig-
	nals in 2016 simulation
Figure 4.46	Distributions of $\log_{10}(\chi_{\rm IP}^2)$ of $\Lambda_c^+$ in (top left) 2012, (top right) 2016, (bottom
	left) 2017, (bottom right) 2018 data samples for the $\Lambda_c^+$ control mode. 156
Figure 4.47	Distributions of $m(\Xi_{cc}^{++})$ for (top left) 2012, (top right) 2016, (bottom left)
	2017, and (bottom right) data for the $\Xi_{cc}^{++}$ control mode, along with the fit
	results
Figure 4.48	Distributions of (left) $\Xi_{cc}^{++}$ $p_{\rm T}$ and (right) nSPDHits of the $\Xi_{cc}^{++}$ $\to$
	$\Lambda_c^+ K^- \pi^+ \pi^+$ decay for (top) 2016 and (bottom) 2012 data, respectively.
	Blue stands for the background-subtracted data, and magenta (black) for
	the simulation (MC) sample after (before) reweighting
Figure 4.49	Distributions of $\Xi_{cc}^{++}$ y of the $\Xi_{cc}^{++}$ $\to$ $\Lambda_c^+ K^- \pi^+ \pi^+$ decay for (right)
	2016 and (left) 2012 data, respectively. Blue stands for the background-
	subtracted data, and magenta (black) for the simulation (MC) sample after
	(before) reweighting
Figure 4.50	Comparison of the Dalitz-plot distributions of (left) 2016 data and (right)
	simulation for the $\Lambda_c^+ \to pK^-\pi^+$ decay
Figure 4.51	Efficiency of the HLT2 selection for the $\Lambda_c^+$ control mode in bins of (left)
	$m(pK^{-})$ and (right) $m(K^{-}\pi^{+})$
Figure 4.52	Weights in bins of Dalitz-plot variables for the (left) $\Lambda_c^+$ and (right) $\Xi_{cc}^{++}$
	control modes
Figure 4.53	Comparison of projections to (left) $m(pK^-)$ and (right) $m(K^-\pi^+)$ for
	background-subtracted inclusive $\Lambda_c^+$ data and the $\Lambda_c^+$ simulation sample be-
	fore and after reweighting
Figure 4.54	Comparison of projections to (left) $m(pK^-)$ and (right) $m(K^-\pi^+)$ for
	background-subtracted inclusive $\Lambda_c^+$ data and the $\Xi_{cc}^{++}$ simulation sample
	before and after reweighting
Figure 4.55	Efficiencies at different lifetime hypotheses for (left) 2016 and (right) 2012
	data
Figure 4.56	Efficiency as a function of mass hypotheses

Figure 4.57	Distribution of $\log \chi_{\rm IP}^2$ in (left) the 2016 data sample and (right) 2012 data
	sample, along with the fit results
Figure 4.58	Distribution of the extracted prompt yields of toy experiments, for the (left)
	2016 data sample and (right) 2012 data sample, along with the fit results.172
Figure 4.59	Normalized likelihood distribution before (red curve) and after (blue curve)
	convolution for (left) $R_{A_c^+}$ and (right) $R_{\Xi_{cc}^+}$ and for (top) 2012 and (bottom)
	2016 data at the best mass point. The arrow shows the 95% upper limit using
	only statistical uncertainty (red) and using both statistical and systematic
	uncertainties (blue)
Figure 4.60	Upper limits on (left) $\mathcal{R}(\Lambda_c^+)$ and (right) $\mathcal{R}(\Xi_{cc}^{++})$ at 95% credibility level
	as a function of $m(\Lambda_c^+ K^- \pi^+)$ at $\sqrt{s} = 8$ TeV for four $\Xi_{cc}^+$ lifetime hypothe-
	ses
Figure 4.61	Upper limits on (left) $\mathcal{R}(\Lambda_c^+)$ (right) $\mathcal{R}(\Xi_{cc}^{++})$ at 95% credibility level as a
	function of $m(\Lambda_c^+ K^- \pi^+)$ at $\sqrt{s} = 13$ TeV, for four $\Xi_{cc}^+$ lifetime hypothe-
	ses
Figure 4.62	The (left) comparison of the simulated and "background-subtracted"
	decay-time distribution and (right) efficiency-corrected and background-
	subtracted decay-time distribution, along with the fit result with an expo-
	nential function. The selection for setting upper limits is applied. The sim-
	ulated signals have an input lifetime of 80 fs
Figure 5.1	LHCb upgrade trigger diagram. 179
Figure 5.2	Impact parameter resolution (left) in the x projection for Upgrade I, (middle)
	3D resolution for Upgrade I, and (right) 3D resolution for Upgrade II. In the
	left and middle plots, the VELO in Run 2 is shown with black circles and
	the Upgrade I VELO with red squares. In the right plot, different circles
	correspond to different design scenarios

Table 1.1	Quark quantum numbers. The quantum number from top to bottom corre-
	sponds to baryon number, electric charge (in unit of $e$ ), isospin, isospin $z$ -
	component, strangeness, charm, bottomness, and topness. The convention is
	that the quark flavour has the same sign as its charge
Table 1.2	Theoretical calculations of lifetimes of singly charmed baryons up to order
	$1/m_c^3$ in HQE. As a comparison, the lifetime ratio in each prediction is also
	shown. The reference lifetime, $\tau_0$ , is different between predictions22
Table 1.3	Theoretical calculations of lifetimes of doubly charmed baryons up to order
	$1/m_c^3$ in HQE. As a comparison, the lifetime ratio in each prediction is also
	shown. The reference lifetime, $\tau_0$ , is different between predictions23
Table 1.4	Measurements of lifetimes of singly charmed baryons24
Table 1.5	Partial decay widths of semileptonic decays in unit of $10^{-14}$ GeV37
Table 1.6	CF nonleptonic two-body decays of doubly charmed baryons, along with the
	topological diagrams that contribute to these decays [123]39
Table 1.7	Partial decay widths of nonleptonic decays of $\Xi_{cc}^{++}$ baryon in unit of
	$10^{-14} \text{GeV}.$ 40
Table 1.8	Partial decay widths of nonleptonic decays of $\Xi_{cc}^+$ baryon in unit of $10^{-14}$ GeV.
	41
Table 1.9	Partial decay widths of nonleptonic decays of $\Omega_{cc}^+$ baryon in unit of
	$10^{-14} \text{GeV}.$ 42
Table 1.10	Experiments involved in searches for doubly charmed baryons
Table 2.1	LHC beam parameters at collision
Table 2.2	LHC baseline plan for the next decade and beyond
Table 2.3	Operation conditions of the LHCb detector
Table 2.4	Requirements of Hlt1TrackAllL0 trigger line in Run 166
Table 2.5	Requirements of Hlt1(Two)TrackMVA trigger line in Run 267
Table 3.1	HLT2 selections for the $\Omega_c^0$ and $\Xi_c^0$ signal mode. Requirements shown in red
	are also applied to the control mode offline71
Table 3.2	HLT2 selections for the $D^0$ control mode. The index $i$ refers to any of the
	first three daughters in the $D^0$ decay 72

Table 3.3	Offline preselection requirements, where $H_c$ denotes either $\Omega_c^0$ , $\Xi_c^0$ or $D^0$
	hadron
Table 3.4	Total signal yields (prompt and secondary components combined) in the de-
	cay time range of [0.45, 2.00] ps after all event selection for signal and control
	modes
Table 3.5	Efficiency and figure of merit $\frac{S}{\sqrt{S+B}}$ for 2016 $\Omega_c^0$ data after different selection
	stages
Table 3.6	Results of the invariant-mass fit to simulated signal and control samples79
Table 3.7	Results of the $\log_{10}(\chi_{\rm IP}^2)$ fit to simulated prompt signal and control samples.
Table 3.8	Results of the $\log_{10}(\chi_{\rm IP}^2)$ fit to simulated secondary signal and control samples. 85
Table 3.9	Yields of prompt signals for $\Omega_c^0$ , $\Xi_c^0$ , and $D^0$ modes in 2016-2018 samples.87
Table 3.10	Results of key parameters obtained from fits to data samples. Parameter $\Delta \mu_p$
	and $\Delta \mu_s$ are shared across 2016-2018 in the fit
Table 3.11	Decay-time fit results for $D^0$ control mode
Table 3.12	Fit results of the normalisation vectors
Table 3.13	Decay-time fit in each data-taking period. The last column shows the
	weighted average of the resulting lifetime and $\chi^2$ /ndf of the combination with least squares method
Table 3.14	Decay-time fit in each data-taking period and magnetic polarity 104
Table 3.15	Relative difference (in %) of the $D^0$ prompt yield with different fit configu-
1 aoic 3.13	ration
Table 3.16	Summary of systematic uncertainties
Table 4.1	HLT2 selection requirements for $\Xi_{cc}^+$ candidate
Table 4.2	HLT2 trigger requirements of Hlt2CharmHadLambdaC2KPPi line 125
Table 4.3	Preselection requirements
Table 4.4	MVA training variables for default and zero lifetime hypotheses
Table 4.5	Optimal working point and the performance for different algorithms under
1 4010 7.3	
Talala 4.6	default lifetime hypothesis, where $\varepsilon_{\text{MVA}}$ is the efficiency of the MVA cut.131
Table 4.6	Optimal working point and the performance for different algorithms under
	zero lifetime hypotheses, where $\varepsilon_{MVA}$ is the efficiency of MVA cut 131

Table 4.7	Resultant parameters from the fit to the $\Xi_{cc}^+$ invariant-mass distribution in
	simulation, with a Gaussian function plus a DSCB function
Table 4.8	Systematic uncertainties on the $\Xi_{cc}^+$ mass. Values with XXX needs to be de-
	termined with the observed signal peak
Table 4.9	Prompt yields of the $\Lambda_c^+$ control mode
Table 4.10	Yield of the $\Xi_{cc}^{++} \to \Lambda_c^+ K^- \pi^+ \pi^+$ control mode
Table 4.11	Acceptance efficiencies and the ratios of the control to the signal mode.161
Table 4.12	HLT2 (or stripping for 2012 data set) and preselection efficiency and effi-
	ciency ratios of the control modes and the signal mode
Table 4.13	Binning scheme used for $K$ , $\pi$ and $p$ for PID calibration
Table 4.14	PID efficiencies and the ratios of the control modes to the signal mode. 162
Table 4.15	MVA1 efficiencies at the working point MVA1 > 0.00 and their ratios of
	the control modes to the signal mode
Table 4.16	MVA2 efficiencies at the working points MVA1 $> 0.00$ and MVA2 $> 0.70$
	and their ratios of the control modes to the signal mode
Table 4.17	L0 and HLT1 trigger efficiencies and their ratios of the control modes to the
	signal mode
Table 4.18	MC-Match efficiencies and the ratios of the control to the signal modes.164
Table 4.19	Total efficiencies and their ratios of the control modes to the signal mode.
	165
Table 4.20	Efficiencies at different lifetime hypotheses for 2016 data
Table 4.21	Efficiencies at different lifetime hypotheses for 2012 data
Table 4.22	Efficiencies at different mass hypotheses
Table 4.23	Summary of the systematic uncertainties in the upper limit setting 168
Table 4.24	Systematic uncertainties on ratios of the tracking efficiency
Table 4.25	Systematic uncertainties on the ratios of the PID efficiencies
Table 4.26	Summary of the L0 efficiencies of the control channels
Table 4.27	Systematic uncertainties on the L0 efficiency
Table 4.28	Systematic uncertainties due to the fit model
Table 4.29	Single event sensitivity $\alpha(\Lambda_c^+)$ (×10 <sup>-5</sup> ) of the $\Lambda_c^+$ control mode for different
	datasets and lifetime hypotheses
Table 4.30	Single event sensitivity $\alpha(\Xi_{cc}^{++})$ (×10 <sup>-2</sup> ) of the $\Xi_{cc}^{++}$ control mode for dif-
	ferent datasets and lifetime hypotheses

Table 4.31	Summary of the largest upper limits on production ratios at 95% credibility				
	level for four lifetime hypotheses and different centre-of-mass energies.176				
Table 5.1	Operation conditions for LHCb Upgrades				
Table 5.2	Current and future experimental programs that are candidate players of doubly				
	charmed baryon studies				
Table 5.3	Precisions of lifetimes of weakly decaying heavy flavour baryons [2]. The				
	combination values in this thesis are used for lifetimes of $\varOmega_c^0$ and $\varXi_c^0$ baryon.				
	182				
Table 5.4	The expected yield of doubly heavy baryons for LHCb Upgrade 183				
Table 5.5	Projection of the number of doubly charmed baryons produced at future col-				
	liders				
Table 5.6	Relevant branching fractions of decay products of doubly charmed baryons.				
	185				

#### CHAPTER 1 INTRODUCTION

#### 1.1 Standard Model of particle physics

The Standard Model (SM)  $^{\textcircled{1}}$  of particle physics is a quantum field theory with a local gauge symmetry

$$SU(3)_C \times SU(2)_L \times U(1)_Y. \tag{1.1}$$

It is successful in the description of three out of the four fundamental interactions in nature. The strong, electromagnetic, and weak interactions between the known elementary particles are predicted by the SM in terms of a number of parameters that can be determined by experiments.

The gauge group  $SU(3)_C$  is the symmetry of Quantum Chromodynamics (QCD), the theory of strong interactions.  $SU(2)_L$  is the gauge group of weak interactions, and the  $U(1)_Y$  affects all particles carrying hypercharge quantum number Y.  $SU(3)_C$  symmetry is exact, while  $SU(2)_L \times U(1)_Y$  is spontaneously broken down to  $U(1)_{EM}$ , the symmetry group of Quantum Electrodynamics (QED). Quantum numbers corresponding to  $SU(3)_C$ ,  $SU(2)_L$ , and  $U(1)_Y$  groups are called color, weak isospin, and hypercharge, respectively. There are three colors (red, green, and blue) and two weak isospin states.

The particle content of the SM includes twelve fundamental fermions, with spin- $\frac{1}{2}$ , and five fundamental gauge bosons, with spin-1 for gauge bosons and spin-0 for Higgs boson, as shown in Fig. 1.1. The fermions of the SM are grouped in several ways. On the one hand, we distinguish between quarks and leptons. There are six species, referred to as *flavours*, of quarks: down (*d*), up (*u*), strange (*s*), charm (*c*), beauty (*b*), and top (*t*)  $^{(2)}$ . There are also six flavours of leptons: electron (*e*), electron neutrino ( $v_e$ ), muon ( $\mu$ ), muon neutrino ( $v_\mu$ ), tauon ( $\tau$ ), and tauon neutrino ( $v_\tau$ ). Only quarks carry color charge and transform nontrivially under SU(3)<sub>C</sub>. On the other hand, there exist SU(2)<sub>L</sub> doublets (left-handed fields) and SU(2)<sub>L</sub> singlets, with only the former participating in the charged weak interactions. In addition, the fermions exist in three generations: the first generation consists of *u* quark, *d* quark, *e* lepton and  $v_e$  lepton; the second generation consists of *t* quark, *b* quark,

① The term "Standard Model" appeared for the first time in Ref [1] with reference to the electroweak theory of four quarks.

② The beauty quark is also referred to as bottom quark.

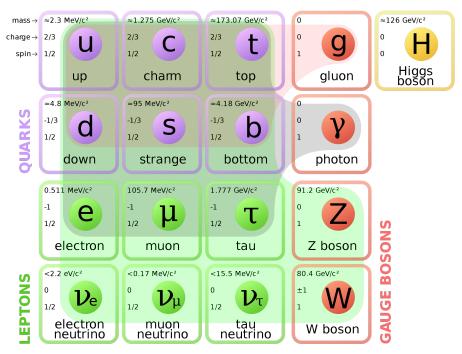


Figure 1.1 Particle content of the Standard Model [3].

 $\tau$  lepton, and  $v_{\tau}$  lepton. The corresponding particles of different generations have exactly the same quantum numbers but quite different masses. The quark masses shown in the plot are "current-quark" masses in the modified minimal subtraction renormalisation scheme at an energy scale around 2 GeV [2], as will be discussed later in Sec. 1.1.2. According to their masses, d quark, u quark, and s quark are called light-flavoured quarks, while c quark, d quark, and d quark are called heavy-flavoured quarks.

Massless gauge bosons are required by the local gauge invariance of the SM. Therefore we have eight gluons  $G_{\mu}^{a}$  for  $SU(3)_{C}$ , three  $W_{\mu}^{a}$  for  $SU(2)_{L}$ , and one  $B_{\mu}$  for  $U(1)_{Y}$ . Gauge bosons  $W_{\mu}^{a}$  and  $B_{\mu}$  mix into  $W_{\mu}^{\pm}$  boson,  $Z_{\mu}$  boson, and  $A_{\mu}$  boson due to electroweak symmetry breaking, where only  $A_{\mu}$  of QED stays massless. The Higgs boson H is introduced to explain the generation mechanism of masses through the Higgs mechanism.

The Standard Model Lagrangian density, which encodes compactly the particle content of the present theory and the basic dynamics of particle interactions, can be split into several parts as

$$\mathcal{L} = \mathcal{L}_{QCD} + \mathcal{L}_{EW} + \mathcal{L}_{Higgs} + \mathcal{L}_{Yukawa}.$$
 (1.2)

The QCD sector  $\mathcal{L}_{\text{QCD}}$  describes the strong interaction and will be discussed in more details in Sec. 1.1.2. The electroweak sector  $\mathcal{L}_{\text{EW}}$  provides a unified description of the electromagnetic and weak interactions, sometimes referred to as Quantum Flavourdynam-

ics (QFD). The Higgs sector  $\mathcal{L}_{\text{Higgs}}$  contains the kinetic term and the potential for Higgs fields. The Yukawa sector  $\mathcal{L}_{\text{Yukawa}}$  includes the couplings of the Higgs to the fermions and determines the flavour structure of the SM. Free parameters in the SM, whose numerical values are established by experiment, include six quark masses, three charged leptons masses, three quark flavour mixing angles, one *CP* violation phase, three coupling constants, and the Higgs mass and vacuum expectation value.

In principle, it is only a matter of will and time to derive testable predictions from this Lagrangian. In practice, it is far from an easy task to confront this theory with experimental data. On the one hand, the derivation of physical predictions requires sophisticated field theoretical methods. On the other hand, experimental results are difficult and expensive to be obtained, especially for phenomena that are rare to take place. Fortunately, there are many quantities whose accurate calculations have been performed and already compared with experimental results. Impressive agreements are achieved in almost all of these tests. At the same time, in many cases available tools that we have at our disposal are not powerful enough to allow for accurate predictions. One of the most outstanding cases is the description of the properties of hadrons, the bound states of quarks and antiquarks such as proton and neutron. This description calls for further understanding of QCD in the long-distance (or equivalently low-energy, or nonperturbative) regime, in contrast to the well-established short-distance (or equivalently high-energy, or perturbative) regime.

Despite its huge success, the SM is believed not to be the Theory of Everything (TOE) for several reasons. From the experimental side, it does not fully explain the baryon asymmetry of our universe as indicated by astrophysics observations. Hints of deviations between experimental data and SM predictions are recently reported in muon anomalous magnetic moment [4] and lepton flavour universality violation [5]. From the theoretical side, it does not incorporate the full theory of gravitation as described by general relativity, and does not incorporate neutrino oscillations. Besides, it does not include candidates of dark matter and dark energy, which are required from observational cosmology. In addition, it has too many free parameters that can only be determined by experiment, which is regarded as not "natural". Therefore, active efforts are made to extend the SM from both theoretical and experimental side. The experimental expedition to physics beyond the SM follows two approaches. The direct approach searches for new particles in its on-shell production, such as ATLAS and CMS experiments at the Large Hadron Collider (LHC). The indirect approach searches for manifestation of new phenomena through quantum effects,

*e.g.* those appeared in weak decays of hadrons. This calls for precision measurements as well as precise predictions of the SM, such that we can distinguish new physics from the SM ones. To make those predictions, the predictive power of QCD at low-energy scale needs to be further improved through the interplay between experiment and theory.

To summarise, it is exciting to confront QCD predictions at the low-energy scale with experimental data, both for testing the SM itself and searching for physics beyond the SM. Hadrons are the main playground of strong interactions at this energy scale. Mass spectra and other intrinsic properties of hadrons provide abundant information for nonperturbative QCD studies. Weak decays of hadrons constitute a novel laboratory for studying strong dynamics through its interplay with the weak interaction. In this thesis, measurements of hadron properties, which aim to provide experimental data in this context, are reported.

In the remainder of this chapter, we first introduce Quark Model, the famous phenomenological model for the classification of hadrons. Then the main aspects of QCD, the underlying theory of the quark model, are discussed. Thereafter, the theoretical frameworks and predictions related to lifetimes of charmed baryons and properties of doubly charmed baryons are reviewed. Finally, the up-to-date experimental status is presented.

#### 1.1.1 Quark model

Historically, a phenomenological model, named *quark model*, was constructed to categorize a number of known hadrons without knowledge of the underlying dynamics of the strong interaction [6-8]. It enjoyed great success in the classification of hadrons and the description of deep inelastic scattering. At present, the quark model is still important as a standard by which one defines the "expected" and "unexpected". It is helpful when other more advanced tools, such as lattice QCD, are not available for a property yet. It can also educate our intuition and help to interpret results obtained from other methods. In addition, it can be used to evaluate certain matrix elements arising in nonperturbative calculations.

In the quark model, hadrons are classified according to their Fermi statistics into mesons (with integer spin) and baryons (with half-integer spin). The quark model assumes that mesons are bound states of a quark and an antiquark, while baryons are bound states of three quarks or three antiquarks. We will focus on the properties of baryons in the following discussion.

Table 1.1 Quark quantum numbers. The quantum number from top to bottom corresponds to baryon number, electric charge (in unit of e), isospin, isospin z-component, strangeness, charm, bottomness, and topness. The convention is that the quark flavour has the same sign as its charge.

	d	и	S	c	b	t
В	$\frac{1}{3}$	$\frac{1}{3}$	$\frac{1}{3}$	$\frac{1}{3}$	$\frac{1}{3}$	$\frac{1}{3}$
Q	$-\frac{1}{3}$	$+\frac{2}{3}$ $\frac{1}{2}$	$-\frac{1}{3}$	$+\frac{2}{3}$	$-\frac{1}{3}$	$+\frac{\frac{1}{3}}{\frac{2}{3}}$
I	$\frac{1}{2}$	$\frac{1}{2}$	0	0	0	0
$I_z$	$-\frac{1}{2}$	$\frac{1}{2}$	0	0	0	0
S	0	0	-1	0	0	0
$\boldsymbol{C}$	0	0	0	+1	0	0
В	0	0	0	0	-1	0
T	0	0	0	0	0	+1

**Quark quantum numbers.** Baryons containing only light quarks are called light baryons, while heavy baryons contain one or more heavy quarks <sup>①</sup>. Hadron physics studying properties of heavy hadrons is referred to as *heavy flavour physics*, or simply flavour physics. The addictive quantum numbers of quarks are shown in Table 1.1. As bound states of quarks, the quantum numbers of baryons are given by those of their constituent quarks or antiquarks.

**Classification scheme.** In the nonrelativistic quark model, the baryon wave function is a product of four components

$$\Psi = \Psi_{\text{colour}} \times \Psi_{\text{flavour}} \times \Psi_{\text{spin}} \times \Psi_{\text{space}}.$$
 (1.3)

According to Fermi statistic and treating all quarks (regardless of colour and flavour) as different states of a single particle, the baryon wave function  $\Psi$  is supposed to be antisymmetric under the permutation of any pair of the three constituent quarks. As all observed baryons are color singlets, the colour component  $\Psi_{\text{colour}}$  is antisymmetric. For ground-state baryons <sup>2</sup>, the spacial component  $\Psi_{\text{space}}$  is symmetric. Therefore, the  $\Psi_{\text{flavour}} \times \Psi_{\text{spin}}$  part needs to be symmetric. First we consider baryons containing only light quarks. In the language of group theory, the direct product of (approximate) flavour symmetry SU(3)<sub>f</sub> can be decomposed into the direct sum of multiplets with different symmetric properties

① Top quarks can not constitute hadrons as constituent quarks, because they are so heavy that they decay weakly before hadronise.

<sup>2)</sup> Throughout this thesis, we refer to the states of a baryon without orbital excitation (i.e. S-wave) as the ground states.

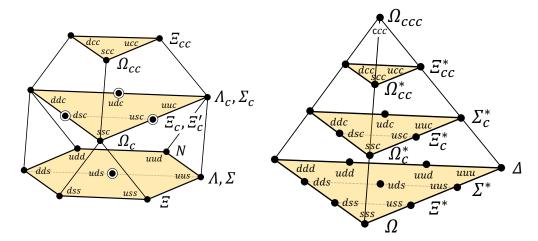


Figure 1.2  $SU(4)_f$  20-plets of ground-state (left)  $J^P = \frac{1}{2}^+$  and (right)  $J^P = \frac{3}{2}^+$  baryons. Right-handed Cartesian coordinates of  $(I_z, S, C)$  are adopted. Constituent quark contents are indicated at each dot. Circle dots indicate locations where tow states are located. The naming scheme follows Sec. 7 in *Review of Particle Physics* [2].

according to

$$\mathbf{3} \otimes \mathbf{3} \otimes \mathbf{3} = \mathbf{10}_S \oplus \mathbf{8}_{MS} \oplus \mathbf{8}_{MA} \oplus \mathbf{1}_A, \tag{1.4}$$

and the direct product of spin symmetry SU(2) can be decomposed into the direct sum of multiplets with different symmetric properties according to

$$\mathbf{2} \otimes \mathbf{2} \otimes \mathbf{2} = \mathbf{4}_S \oplus \mathbf{2}_{MS} \oplus \mathbf{2}_{MA} \oplus \mathbf{1}_A, \tag{1.5}$$

where the subscripts S, A, MS and MA denote symmetry, antisymmetry, mixed symmetry and mixed antisymmetry, respectively. The ground-state multiplets can then be obtained with the combined  $SU(3)_f$  and SU(2) symmetry, including the  $J^P = \frac{1}{2}^+$  octet and the  $J^P = \frac{3}{2}^+$  decuplet. For exinlinecited states, we need to include quark orbital angular momentum with the orthogonal rotation group O(3).

The existence of charm quark was confirmed in 1974 by the discovery of  $Jh\psi$  particle [9-10], now interpreted as an S-wave  $c\bar{c}$  bound state. Baryons containing one or more charm quarks, referred to as singly and doubly charmed baryons respectively, were predicted as a natural extension of the light sector [11]. The decomposition of (approximate) flavour symmetry  $SU(4)_f$ , with the addition of charm flavour, reads

$$\mathbf{4} \otimes \mathbf{4} \otimes \mathbf{4} = \mathbf{20}_S \oplus \mathbf{20}_{MS} \oplus \mathbf{20}_{MA} \oplus \bar{\mathbf{4}}_A. \tag{1.6}$$

The ground-state multiplets are extended to 20-plets when combined with spin symmetry. The diagram of  $SU(4)_f$  20-plets are shown in Fig. 1.2.

**Dynamical models.** The most fundamental assumption of the quark model is that the effective degrees of freedom are the constituent quarks, whose masses enter as parameters of the theory. The Hamiltonian consists of a kinetic part describing these constituent quarks together with a potential for the inter-quark forces. In nonrelativistic quark model it has the form

$$H = \sum_{i} \left( m_i + \frac{p_i^2}{2m_i} \right) + \sum_{i < j} V(\mathbf{r}_{ij}), \tag{1.7}$$

where i labels different constituent quarks,  $V(r_{ij})$  denotes the two-body potential between constituent quarks. Some striking regularities in the mass and mass differences of hadrons can be understood from general properties of the interactions of quarks without an explicit form of the Hamiltonian [11-12], including the Gell-Mann-Okubo formula for the baryon octet

$$2N + 2\Xi = 3\Lambda + \Sigma, \tag{1.8}$$

the equal-spacing rule for the decuplet

$$\Delta - \Sigma^* = \Sigma^* - \Xi^* = \Xi^* - \Omega, \tag{1.9}$$

and the SU(6) relation

$$\Sigma^* - \Sigma = \Xi^* - \Xi. \tag{1.10}$$

The symmetry breaking in multiplets can also be explained. The gluon-exchange interaction violates the spin SU(2) symmetry, while differences in quark masses violates the flavour SU(3) symmetry.

Many specific models exist with different degrees of sophistication, but most contain a similar set of dynamical ingredients. Two models are representative of various models commonly used in literature. The first one is the "Coulomb-plus-linear" potential

$$V_{ij}^{c} = \frac{1}{2} \left[ -\frac{a}{r_{ij}} + br_{ij} + d \right], \tag{1.11}$$

which is supported by lattice calculations. The second one is the "power-law" potential

$$V_{ij}^{c} = \frac{1}{2} \left( A + B r_{ij}^{\beta} \right). \tag{1.12}$$

The above potentials need to be supplemented by the hyperfine interaction of Fermi-Breit type

$$V_{ij}^{ss} = \frac{C}{2} \frac{\mathbf{s}_i \cdot \mathbf{s}_j}{m_i m_j} \delta\left(\mathbf{r}_{ij}\right), \tag{1.13}$$

which is responsible for hyperfine splitting between  $J^P = \frac{1}{2}^+$  and  $J^P = \frac{3}{2}^+$  baryons. The total potential model is given by  $V_{ij} = V_{ij}^c + V_{ij}^{ss}$ .

Various approximation methods are adopted to solve the three-body Schrödinger equation  $H\psi = E\psi$  to obtain the bound-state energy E (i.e., the baryon mass) and the baryon wave function  $\psi$ . Variational methods include harmonic oscillator expansion, in which the wave function is expanded in terms of the eigenstates of a symmetric oscillator, and hyperspherical formalism, in which the wave function is expanded into partial-waves in spherical coordinates [13]. The adiabatic approximation, also known as Born-Oppenheimer approximation, exploits the fact that two heavy quarks have much lower velocity than the light quark [14]. The binding energy of the light quark is calculated for each relative coordinate of two heavy quarks, which is in turn used as the effective potential governing the relative motion of the two heavy quarks. The quark-diquark approximation decomposes the exact three-body problem into two successive two-body problems [15]. First, a diquark D is built out of two quarks  $q_2$  and  $q_3$  and its mass  $m_D$  is computed from two-body Hamiltonian

$$H_{23} = m_2 + m_3 + \frac{p_2^2}{2m_2} + \frac{p_3^2}{2m_3} + V(\mathbf{r}_{23}). \tag{1.14}$$

The diquark is then considered as a point-like object to form the baryon with quark  $q_1$ . The approximate baryon mass is obtained from the two-body Hamiltonian

$$H_{qD} = m_1 + m_D + \frac{p_1^2}{2m_1} + \frac{p_D^2}{2m_D} + 2V\left(\mathbf{r}_{1D}\right). \tag{1.15}$$

Thanks to efforts in nuclear and atomic physics, powerful tools are also available to solve the three-body problem exactly. The *Modified Green Function Monte Carlo method* enables one to obtain exact ground-state masses and wave functions of multiquark states using numerical algorithm [16]. The *Faddeev formalism* can perform exact numerical solutions for both ground and exinlinecited states [17].

The nonrelativistic approximation is not adequate for the light quark, since the estimates of the light quark velocity in e.g. doubly charmed baryons,  $v/c \sim 0.7$ , are highly relativistic. The light quark can be treated fully relativistically with the quasipotential approach without employing the expansion in  $1/m_q$  [18]. In the light-quark-heavy-diquark picture, the quasipotential Schrödinger equation for both the diquark bound state and the quark-diquark bound state reads

$$\left(\frac{b^2(M)}{2\mu_R} - \frac{\mathbf{p}^2}{2\mu_R}\right)\psi(\mathbf{p}) = \int \frac{\mathrm{d}^3 q}{(2\pi)^3} V(\mathbf{p}, \mathbf{q}; M)\psi(\mathbf{q}),\tag{1.16}$$

where  $\mu_R$  is the relativistic reduced mass, b(M) is the relative momentum on mass shell, **p** is the relative momentum, and the kernel  $V(\mathbf{p}, \mathbf{q}; M)$  is the quasipotential operator of the quark-quark or quark-diquark interaction.

To appreciate the predictive power of the quark model, calculations of ground-state charmed baryons are compared with lattice and experimental and data in Fig. 1.6. An agreement within 10 MeV is achieved. In principle, a nonrelativistic treatment is fully justified only for baryons containing three heavy quarks. While in practice, the nonrelativistic potential model has been applied with great success to systems in which its validity may be questioned. The answer is far from definite and one possibility is that the relativistic effect can be effectively simulated in the nonrelativistic scheme with renormalised model parameters.

Despite the huge success beyond expectation, the quark model has its limitations. The number of exinlinecited states predicted by the quark model is far more than the number of observed states, which is the so-called problem of missing resonances. Besides, the ordering of resonances contradicts with data in many cases. Moreover, ever-emerging new states with "exotic" quantum numbers, referred to as exotic hadrons, can not be understood in a systematic way. From the theoretical side, its connection to full QCD and the exact Bethe-Salpeter equation needs to be further elucidated. In addition, no systematic improvement on the theoretical uncertainty of quark model prediction is possible.

### 1.1.2 Quantum Chromodynamics

Quantum Chromodynamics (QCD) is the theory of strong interaction in the SM. Naively speaking, the physical content of the theory is that quarks interact with gluons which also interact among themselves. The QCD Lagrangian in Eq. 1.1 is given by

$$\mathcal{L}_{\text{QCD}} = \sum_{f} \bar{\psi}_{f,a} \left( i \gamma^{\mu} \partial_{\mu} \delta_{ab} - g_{s} \gamma^{\mu} t_{ab}^{C} \mathcal{A}_{\mu}^{C} - m_{f} \delta_{ab} \right) \psi_{f,b} - \frac{1}{4} F_{\mu\nu}^{A} F^{A,\mu\nu}, \tag{1.17}$$

where repeated indices are summed over. Fermion field  $\bar{\psi}_{f,a}$  is the Dirac spinor of the quark field for a quark of flavour f and mass  $m_f$ , with a color index a which runs from 1 to  $N_c = 3$ . Quarks are in the fundamental representation of  $\mathrm{SU}(3)_C$  group, denoted by 3. The  $\bar{\psi}$  is a shorthand notation for  $\psi^\dagger \gamma^0$ .

Boson field  $\mathcal{A}_{\mu}^{C}$  is the gluon field, where C runs from 1 to  $N_{c}^{2}-1=8$ . Matrix  $t_{ab}^{C}$  is one of the eight generators of  $SU(3)_{C}$  group. It can thus be seen that a gluon's interaction with a quark rotates the quark's color in  $SU(3)_{C}$  space. Dimensionless quantity  $g_{s}$ , or  $\alpha_{s} \equiv \frac{g_{s}^{2}}{4\pi}$ , is the strong coupling constant and the only fundamental parameter of QCD.

Quark masses also enter the QCD Lagrangian as free parameters. However, they have an electroweak origin and are flavour-dependent, and therefore are not counted as parameters of QCD.

Field tensor  $F_{\mu\nu}^{A}$  is defined as

$$F_{\mu\nu}^{A} = \partial_{\mu} \mathcal{A}_{\nu}^{A} - \partial_{\nu} \mathcal{A}_{\mu}^{A} - g_{s} f_{ABC} \mathcal{A}_{\mu}^{B} \mathcal{A}_{\nu}^{C}, \tag{1.18}$$

where  $f_{ABC}$  is the structure constant of the SU(3)<sub>C</sub> group. From the QCD Lagrangian, one can immediately see that there exist quark-gluon vertex, three-gluon vertex, and four-gluon vertex in QCD interactions.

QCD is believed to be the underlying theory governing the properties of hadrons. It displays several features that are important for the understanding of hadron structures. We illustrate these features below.

**Running coupling constant.** QCD is a renormalisable theory, in the sense that only a finite number of Feynman diagrams, such as quark self-energy and vacuum polarization, are divergent. The process of renormalization, under certain renormalisation scheme, removes these divergences and obtains finite amplitudes and consequently finite predictions for the observables. The renormalisation process introduces scale-dependence  $\mu$  to the renormalized coupling constant and quark masses, which is governed by the renormalisation group equations. In the modified Minimal Subtraction scheme  $\overline{\text{MS}}$ , the solution to the renormalisation group equation of coupling constant up to leading order is [2]

$$\alpha_s^{(f)}(\mu) = \frac{4\pi}{\beta_0^{(f)} \ln\left(\mu^2/\Lambda_{\text{QCD}}^{(f)2}\right)},$$
(1.19)

where  $\beta_0^{(f)} = \frac{11N_c - 2f}{3}$  and f is the number of effective flavours defined by

$$f = \begin{cases} 3 & \mu \le m_c, \\ 4 & m_c \le \mu \le m_b, \\ 5 & m_b \le \mu \le m_t, \\ 6 & m_t \le \mu. \end{cases}$$
 (1.20)

The continuity of  $\alpha_s$  gives the boundary conditions of the piecewise function. It should be noticed that the renormalisation group equation is only valid in the perturbative QCD regime and breaks down at low-energy scale around  $\Lambda_{\rm QCD}$ . The numerical values of  $\alpha_s$ , measured at various values of  $\mu$  through different processes are shown in Fig. 1.3 [2].

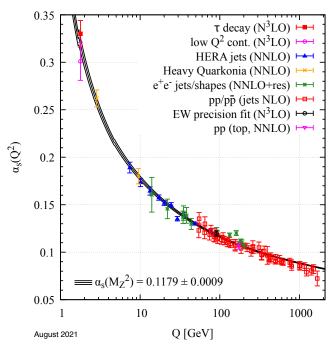


Figure 1.3 Measurements of  $\alpha_s$  as a function of energy scale Q [2].

Asymptotic freedom and confinement. The dependence of  $\alpha_s$  on the energy scale exhibits the feature of asymptotic freedom. At high energy scale, the coupling constant is small and decrease with energy. It also displays confinement, the converse notion that the coupling becomes strong at low-energy scales. This property explains qualitatively why quarks are confined in hadrons and colored states are not observed. At this regime, nonpertaburtive methods or phenomenological models are needed to make quantitative predictions.

**Running quark mass.** The solution to the renormalisation group equation of quark mass up to leading order is

$$m(\mu) = m(\mu_0) \left[ \frac{\alpha_s(\mu)}{\alpha_s(\mu_0)} \right]^{\frac{\gamma_m^0}{2\beta_0}}, \tag{1.21}$$

where  $\gamma_m^0=6C_F$  and  $C_F=\frac{N_c^2-1}{2N_c}$ . The dependence of quark mass on the momentum is illustrated in Fig. 1.4 [19] ①. Quark masses generated at low momentum transfers are obtained from nonpertaburtive methods which will be discussed in next section. The continuous transition of quark masses from perturbative to nonperturbative regime provides insight into the relationship between "current quark" in the QCD Lagrangian and the "constituent quark" in the quark model.

① Natural units with  $\hbar = c = 1$  are used throughout this thesis.

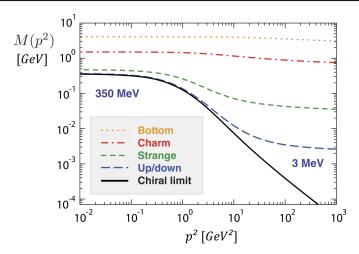


Figure 1.4 Quark mass function with solutions of Dyson-Schwinger equations in infrared and logarithmic running in the ultraviolet from perturbation theory [19].

### 1.1.3 Nonperturbative QCD

Ab initio calculations for observables are possible for perturbative QCD, where the involved interactions are at high-energy scale and perturbative expansions in the small coupling constant are possible. These include, *e.g.*, cross-sections in various high-energy scattering processes. However, this is not the case for description of properties of hadrons, including their masses and matrix elements. Various nonperturbative methods have been developed with different degrees of success. In this section, relevant so-called second-generation theoretical technologies are reviewed. The common features of these methods include a factorisation of short- and long-distance contributions, or/and an expansion in a small quantity other than the coupling constant, which is specific for the given system. Their applications to the prediction of charmed baryon lifetimes and properties of doubly charmed baryon are discussed in Sec. 1.2 and Sec. 1.3, respectively.

Lattice QCD. Lattice QCD (LQCD) is a tool to determine the low energy properties of QCD and to carry out ab initio calculations of hadron properties. LQCD calculations use a discretised version of the QCD Lagrangian as input. In LQCD Euclidean space-time is discretised on a hypercubic lattice with lattice spacing a. Quark fields are placed on lattice sites and gauge fields on the links between sites. The definition of LQCD does not rely on perturbative expansion and allows for nonperturbative calculations of the path integral numerically. The number of input parameters in LQCD is the same as for continuum QCD, including the strong gouge coupling  $\alpha_s$  and the quark masses for each flavour. The gauge coupling is a function of energy scale, which is the inverse lattice spacing 1/a

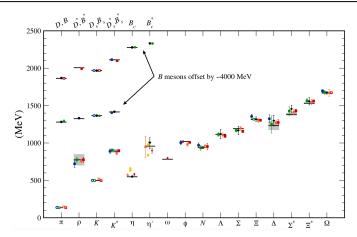


Figure 1.5 Hadron spectrum from lattice QCD in Sec. 15 of *Review of Particle Physics* [2]. Horizontal bars (boxes) denote experimental masses (widths). Lattice calculations from different groups are denoted by points with error bars.

in lattice QCD. Early LQCD calculations were performed in quenched approximations, neglecting the effect of sea quarks. This was due to the lack of computing resources necessary to add virtual quark-antiquark pairs. Recent calculations, with advances in algorithms and computing hardware, include loop effects of light quarks, denoted as  $N_f = 2+1$  simulations, or even loops of charm quarks, referred to as  $N_f = 2+1+1$  simulations. Lattice results usually come with both statistical and systematic uncertainties, arising from limited computing resources and inefficiency of algorithms, respectively. The systematic uncertainties stem from nonzero lattice spacing, unphysical values used for quark masses, finite lattice volume, and how dynamic quarks are added.

LQCD has been applied successfully to calculate spectra, electroweak decay constants and form factors of hadrons, and to determine fundamental parameters of the standard model such as strong gauge coupling and quark masses. The major part of lattice spectroscopy deals with light hadrons up to now. Results are illustrated in Fig. 1.5. LQCD predictions of low-lying light hadrons and heavy mesons agree very well with spectroscopic data within uncertainties. Calculations of ground-state singly charmed baryons from Ref. [20] are shown in Fig. 1.6.

Calculations of exinlinecited states are much more challenging due to the fact that:
a) exinlinecited states are unstable resonances; b) there are many states with the same quantum numbers. So far only a few two-body resonances are well studies.

The present frontier considers electromagnetic effects in lattice simulations, with the inclusion of isospin breaking (use different up and down quark masses) and QED. This introduces a host of technical challenges, one of which is that electromagnetic interactions are long range while lattice volume is finite.

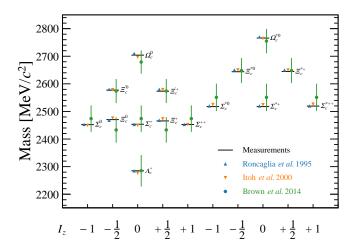


Figure 1.6 Comparison of ground-state charmed baryon spectrum between experimental data and calculations from lattice QCD [20] and quark models [12-13].

Bethe-Salpeter Equations. Hadron properties are encoded in QCD's Green functions. Bound states can appear as poles in n-point correlation functions through their spectral representation. In full QCD the Bethe-Salpeter equation (BSE) is an exact equation for the fully covariant bound state wave function. It can be formulated in terms of the Bethe-Salpeter amplitude  $\Gamma$  as [19]

$$\Gamma = \mathbf{K}\mathbf{G}_0\Gamma,\tag{1.22}$$

where  $G_0$  is the disconnected product of a dressed quark and antiquark propagator and K is the four-quark scattering kernel. Approximation at different levels of sophistication has to be made in actual calculations.

**Operator Product Expansion.** Operator Product Expansion (OPE) is a formal framework that expands the product of quark currents in a series of local operators  $\mathcal{O}_d$  with effective coupling constant  $C_d$ , known as the Wilson coefficient. The operators are ordered according to their energy dimension d. Wilson coefficients receive dominant contributions from short-distance regions, while long-distance dynamics is represented by universal operator matrix elements which are independent of the properties of the quark currents. The most import feature of the OPE is the factorisation of short-distance and long-distance contributions. Low dimension operators include dimension-three operator  $\mathcal{O}_3 = \bar{\psi}\psi$ , dimension-four operator  $\mathcal{O}_4 = F_{\mu\nu}^A F^{A,\mu\nu}$ , dimension-five operator  $\mathcal{O}_5 = \bar{\psi}\sigma_{\mu\nu}t^A F^{A,\mu\nu}\psi$ , dimension-six operator  $\mathcal{O}_6^{\psi} = (\bar{\psi}\Gamma_r\psi)(\bar{\psi}\Gamma_s\psi)$  and  $\mathcal{O}_6^{g} = f_{ABC}F_{\mu\nu}^A F_{\sigma}^{B,\nu}F^{C,\sigma\mu}$ . A generalization of OPE in inverse heavy quark mass  $1/m_Q$ , named Heavy Quark Expansion (HQE), is widely used to investigate inclusive weak decays of heavy hadrons systematically [21].

QCD sum Rules. QCD sum rules is a widely used tool in hadron phenomenology [22]. Hadrons are represented in a model independent way by their interpolating quark currents taken at large virtualities. The correlation function of these currents is expanded in the framework of OPE. The short-distance interactions are calculated using QCD perturbative theory. The long-distance interactions are parameterised in terms of universal vacuum condensates, the vacuum expectation value of the operator. The QCD calculation is matched to a *sum* over hadronic states via dispersion relation. In this way, the sum rule allows for the calculation of observable properties of hadronic states. The accuracy of this method is limited by the truncation of the OPE and the complicated structure of the hadronic dispersion integrals, and can not be improved beyond certain limits.

**Heavy Quark Effective Theory.** Heavy Quark Effective Theory (HQET) provides a systematic expansion of QCD Lagrangian in terms of inverse powers of the heavy quark mass. By definition, the notion of HQET can be applied to charm ( $m_c \approx 1.5 \, \text{GeV}$ ) and beauty ( $m_b \approx 4.8 \, \text{GeV}$ ) quarks in nature. The leading term in this expansion gives rise to new spin- and flavor-symmetry, known as Heavy Quark Symmetry (HQS). For infinitely heavy quarks, HQS states that beauty hadron is identical to a charmed hadron at equal velocity regardless of the spin orientation of the heavy quarks. The picture is similar to hydrogen, deuterium, and tritium atoms in the context of QED. The heavy quark sector in the QCD Lagrangian is reformulated in the HQET at order  $1/m_Q$  as [23]

$$\mathcal{L}_{\text{HQET}} = \bar{h}_v i v \cdot D h_v + \frac{1}{2m_O} \bar{h}_v \left( (iD)^2 - (iv \cdot D)^2 - \frac{g}{2} \sigma_{\mu\nu} F^{\mu\nu} \right) h_v + \cdots, \qquad (1.23)$$

where  $h_v$  is the projection of the Dirac spinor with velocity v to the upper two components,  $D_{\mu} = \partial_{\mu} + i g_s \mathcal{A}_{\mu}$  is the gauge-covariant derivative, and  $F^{\mu\nu}$  is the gluon field tensor in Eq. 1.18. All three terms at order  $1/m_Q$  beak the flavor symmetry, while the last term also breaks the spin symmetry.

**Nonrelativistic QCD.** Nonrelativistic QCD (NRQCD) is an effective field theory designed for separating relativistic from nonrelativistic energy scales. It consists of a nonrelativistic Schrödinger field theory for the heavy quark and antiquark that is coupled to the usual relativistic field theory for light quark and gluons. A finite ultraviolet cut-off of order  $m_Q$  is introduced to excludes relativistic states, whose effect is incorporated through renormalisation of coupling constants, know as low-energy constants (LECs).

The NRQCD Lagrangian is [24-25]

$$\mathcal{L}_{\text{NROCD}} = \mathcal{L}_{\text{light}} + \mathcal{L}_{\text{heavy}} + \delta \mathcal{L}. \tag{1.24}$$

The light degrees of freedom is the same as the full QCD. The heavy quark part coincides with the leading term of HQET Lagrangian in Eq. 1.23. The relativistic effects of full QCD are reproduced through the correction term  $\delta \mathcal{L}$ . Various operators are organised into a hierarchy using velocity scaling rules.

Chiral Perturbation Theory. Chiral Perturbation Theory (CHPT) is the effective theory of the SM below the scale of spontaneous chiral symmetry breaking. It is the common language of nuclear and low-energy particle physics. The QCD Lagrangian exhibits chiral symmetry in the chiral limit of massless light quarks. CHPT assumes that the chiral limit constitutes a realistic starting point for a systematic expansion in chiral symmetry breaking interactions. The CHPT Lagrangian is obtained by extending the full QCD Lagrangian in the chiral limit by coupling the light quarks to external hermitian matrix field  $v_{\mu}$ ,  $a_{\mu}$ , s, p [26]:

$$\mathcal{L}_{\text{CHPT}} = \mathcal{L}_{\text{OCD}}^0 + \bar{q}\gamma^{\mu} \left( v_{\mu} + a_{\mu}\gamma_5 \right) q - \bar{q} \left( s - ip\gamma_5 \right) q, \tag{1.25}$$

where  $\mathcal{L}_{\text{OCD}}^0$  is the full QCD Lagrangian in the chiral limit and q is the light quark field.

# 1.1.4 Charm is charming

Why are charmed baryons of our particular interest in the large particle zoo of hadrons? The simple answer is that there are still unknowns in charmed baryon systems that can be the key to refine our understanding of the SM and the harbinger of new physics.

To be more precise, the challenge of quantitative studies of charmed baryons leads to the test and refinement of theoretical tools, especially QCD in the nonperturbative regime. The uniqueness of charm quark lies partially in its value of mass. On the one hand, the mass of charm quark is large with regard to the hadronic enerngy scale, which makes it possible to benefit from effective theories for heavy flavour physics, such as HQET and NRQCD. On the other hand, the mass of charm quark is not large enough, unlike that of beauty quark, to neglect completely the pre-asymptotic effect in the heavy quark limit. Therefore, higher order corrections manifest themselves nd convergence of theoretical tools can be investigated. In this sense, charmed hadrons act as nature's microscope onto the beauty hadrons.

Studies of hadrons containing charm quarks undergo a revival both experimentally and theoretically in the era of B factories and LHC. The main reasons are threefold: experimental, electroweak, and strong. First, unprecedented number of charmed hadrons have been produced and recorded. Second, the mixing of neutral charmed meson is observed in 2007, followed by the observation of CP violation in charm decays in 2019. Third, the discovery of X(3872) particle in 2003 provides strong evidence that QCD allows for exotic bound states of quarks beyond mesons and baryons.

Given the fact that the light degree of freedom in hadrons is more difficult to cope with than heavy ones we can rank the complexity of meson systems as

$$Q\bar{Q} < Q\bar{q} < q\bar{q} < \cdots, \tag{1.26}$$

and the complexity of baryon sytems as

$$QQQ < QQq < Qqq < qqq < \cdots, \tag{1.27}$$

where Q denotes a heavy quark and q denotes a light quark. From this hierarchy, the context of the measurements of properties of ccq and cqq baryons in this thesis may be more clear.

# 1.2 Lifetime of charmed baryons

Lifetimes of hadrons provide valuable information of the underlying dynamics which can not be accessed by their mass or internal quantum numbers. Experimental determinations of lifetimes thus play an important role in testing various theoretical approaches. More practically, precise measurements of lifetimes serve as an input to translate the measured branching ratios into partial decay widths. Experimental techniques developed and tested in lifetime measurement are further utilised in searching for time-dependent signals and *CP* violations manifested in them.

The lifetimes of charm hadrons are unique probes in that the mass of the charm quark is not large enough, unlike that of the beauty quark, to completely neglect the preasymptotic effect in the heavy quark limit. Therefore, higher order corrections manifest themselves and convergence of theoretical tools can be investigated. While lifetimes of charmed mesons are known with a precision of about 1%, substantial improvements are necessary for lifetimes of charmed baryons. In the sector of doubly charmed baryons, only the  $\Xi_{cc}^{++}$  baryon, one of the three weakly decaying doubly charmed baryons, is observed and its lifetime is measured with a precision of around 10%. The remaining two doubly

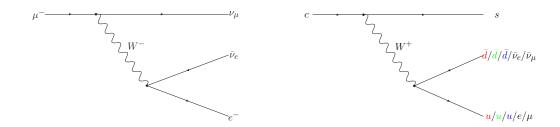


Figure 1.7 Tree-level Feynman diagram of (left) muon and (right) charm quark decay. charmed baryons,  $\Xi_{cc}^+$  and  $\Omega_{cc}^+$ , still need to be observed.

In this section, we first review theoretical calculations of charmed baryons in Sec. 1.2.1. Then we summarise the experimental measurements and motivate new measurement of charm baryon lifetimes in Sec. 1.2.2.

### 1.2.1 Charmed baryon lifetimes from a theoretical perspective

There are four singly charmed baryons and three doubly charmed baryons that decay weakly, *i.e.* the  $J^P = \frac{1}{2}^+$  baryon  $\Lambda_c^+(cud)$ ,  $\Xi_c^+(cus)$ ,  $\Xi_c^0(cds)$ ,  $\Omega_c^0(css)$ ,  $\Xi_{cc}^{++}(ccu)$ ,  $\Xi_{cc}^+(ccd)$ , and  $\Omega_{cc}^+(ccs)$  in the SU(4)<sub>f</sub> 20-multiplets shown in Fig. 1.2.

**Order-of-magnitude estimation.** At the quark level, there is only a single lifetime for a given flavour. In the spectator picture, the order-of-magnitude of the weakly decaying charmed hadrons can be estimated by relating the lifetime of the charm quark to that of a muon. Feynman diagrams of a muon and a charm quark decay are shown in Fig. 1.7. The decay width of a muon up to the leading order reads

$$\Gamma_{\mu}^{(0)} = \frac{G_F^2 m_{\mu}^5}{192\pi^3},\tag{1.28}$$

where  $G_F$  is the Fermi constant and  $m_\mu$  is the muon mass. The lifetime of a charm quark is therefore

$$\tau_c \approx \tau_\mu \times \frac{\Gamma_\mu}{\Gamma_c} \approx \tau_\mu \times \left(\frac{m_\mu}{m_c}\right)^5 \times \frac{1}{N_{\text{channel}}} \times \frac{1}{|V_{cs}|^2} \approx 800 \,\text{fs},$$
(1.29)

where  $m_c \approx 1.5\,\text{GeV}$  is the charm quark mass,  $N_{\text{channel}} = 2 + 3 = 5$  takes into account the effect that there are 2 lepton channels (electron and muon) and 3 quark channels (red, blue, and green) for a charm quark decay while only 1 lepton channel (muon) for a muon decay, and  $|V_{cs}| \approx 1$  is one of the CKM matrix elements. Similarly, the lifetime of a

double-charm system can be estimated as

$$\tau_{cc} \approx \frac{1}{2\Gamma_c} \approx 400 \text{ fs.}$$
(1.30)

In the real world, lifetimes of charmed hadrons span an order of magnitude, from the shortest-lived  $\Xi_c^0$  baryon of about 150 fs, to the longest-lived  $D^+$  meson of about 1050 fs. This indicates that spectator quarks play an important role in the weak decay of charmed hadrons. The weak decay of charmed hadrons constitutes an intriguing and novel laboratory for studying the strong dynamics through the interplay with weak interactions.

**Phenomenological model.** Two mechanisms have been identified to explain differences in the lifetimes of charmed hadrons [27]:

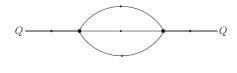
- The W-scattering (WS) of heavy quark Q with the valence diquark system of baryons. For example, the process of  $cd \rightarrow su$  contributes to the  $\Lambda_c^+$ ,  $\Xi_c^0$  and  $\Xi_{cc}^+$  decays.
- The interference between different quark diagrams due to the presence of identical quarks in the final state, known as Pauli interference (PI). For example, the u(s) quark produced in the charm quark decay  $c \to su\bar{d}$  is identical to the spectator quark u(s) in  $\Lambda_c^+$ ,  $\Xi_c^+$  and  $\Xi_{cc}^{++}$  ( $\Xi_c^+$ ,  $\Xi_c^0$ , and  $\Omega_{cc}^+$ ) baryons.

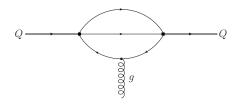
Notice that these mechanisms make implicit assumptions that constituent quarks are the only effective degrees of freedom in charmed hadrons.

Despite a clean picture, these treatments are not systematic and is easy to overlook certain contributions.

**Heavy quark expansion.** Heavy Quark Expansion (HQE) is a systematic approach widely used to express nonperturbative corrections to heavy-flavour decays [21]. In this approach, the decay width is calculated through an expansion in inverse powers of the heavy quark mass  $m_Q$ . The notion of quark-hadron duality is employed implicitly: inclusive transition rates between hadronic systems can be calculated in terms of quarks and gluons [27].

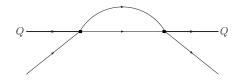
The weak decay of the heavy quark Q in the heavy-flavour hadron  $H_Q$  proceeds in a cloud of light degrees of freedom with which heavy quark Q and its decay products interacting strongly. The imaginary part of a forward scattering operator  $\hat{T}$  can be used

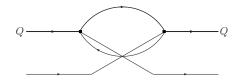




(a)  $\bar{Q}Q$  operator.







(c) Dimension-six operator that generates WS effect.

(d) Dimension-six operator that generates PI effect.

Figure 1.8 Feynman diagrams corresponding to local operators in Eq. 1.32. Reproduced from Ref. [27].

to describe the transition rate to an inclusive final state f [27]

$$\hat{T}(Q \to f \to Q) = i\Im \int d^4x T \left[ \mathcal{L}_W(x) \mathcal{L}_W^{\dagger}(0) \right] \xrightarrow{\text{OPE}} G_F^2 |V_{CKM}|^2 \sum_d C_d^f \times O_d, \quad (1.31)$$

where  $T[\cdots]$  denotes the time-ordered product,  $\mathcal{L}_W$  is the relevant effective weak Lagrangian. The forward scattering operator is expanded as an infinite sum of local operators  $\mathcal{O}_d$  with Wilson coefficients  $C_d$  as shown in the second equation of Eq. 1.31. The master equation of the decay width corresponding to the final state f can then be obtained by taking the expectation value of  $\hat{T}$  for the hadron state  $|H_Q\rangle$ , up to order  $1/m_Q^3$ , as

$$\begin{split} \Gamma(H_Q \to f) &= \langle H_Q | \hat{T}(Q \to f \to Q) | H_Q \rangle \\ &= \frac{G_F^2 m_c^5}{192 \pi^3} \times \left[ C_3^f \left\langle H_Q | \bar{Q}Q | H_Q \right\rangle + C_5^f \frac{\left\langle H_Q | \bar{Q}i\sigma \cdot GQ | H_Q \right\rangle}{m_Q^2} \right. \\ &+ \sum_d C_{6,d}^f \frac{\left\langle H_Q \left| \left( \bar{Q}\Gamma_d q \right) \left( \bar{q}\Gamma_d Q \right) \right| H_Q \right\rangle}{m_Q^3} + O\left( 1/m_Q^4 \right) \right], \end{split} \tag{1.32}$$

where Q and q are the heavy and light quark fields, respectively, G is the gluon field,  $\sigma$  is the Pauli matrix, and  $\Gamma$  is a combination of Dirac and Gell-Mann matrices. Feynman diagrams corresponding to operators in Eq. 1.32 are shown in Fig. 1.8. For baryons

containing two charm quarks, a global factor of two is multiplied, indicating that decays of two heavy quarks are treated independently. To be more specific, the decay width of charmed baryons receive contributions in the following manner up to  $O(1/m_c^3)$ 

$$\Gamma^{(3)}(\Lambda_{c}^{+}) = \Gamma^{(2)}(\Lambda_{c}^{+}) + \Gamma_{WS}(\Lambda_{c}^{+}) - \Gamma_{PI-}(\Lambda_{c}^{+}),$$

$$\Gamma^{(3)}(\Xi_{c}^{0}) = \Gamma^{(2)}(\Xi_{c}^{0}) + \Gamma_{WS}(\Xi_{c}^{0}) + \Gamma_{PI+}(\Xi_{c}^{0}),$$

$$\Gamma^{(3)}(\Xi_{c}^{+}) = \Gamma^{(2)}(\Xi_{c}^{+}) - \Gamma_{PI-}(\Xi_{c}^{+}) + \Gamma_{PI+}(\Xi_{c}^{+}),$$

$$\Gamma^{(3)}(\Omega_{c}^{0}) = \Gamma^{(2)}(\Omega_{c}^{0}) + \Gamma_{PI+}(\Omega_{c}^{0}),$$

$$\Gamma^{(3)}(\Xi_{cc}^{+}) = \Gamma^{(2)}(\Xi_{cc}^{+}) + \Gamma_{WS}(\Xi_{cc}^{+}),$$

$$\Gamma^{(3)}(\Xi_{cc}^{++}) = \Gamma^{(2)}(\Xi_{cc}^{++}) - \Gamma_{PI-}(\Xi_{cc}^{++}),$$

$$\Gamma^{(3)}(\Omega_{cc}^{+}) = \Gamma^{(2)}(\Omega_{cc}^{+}) + \Gamma_{PI+}(\Omega_{cc}^{+}),$$

$$\Gamma^{(3)}(\Omega_{cc}^{+}) = \Gamma^{(2)}(\Omega_{cc}^{+}) + \Gamma_{PI+}(\Omega_{cc}^{+}),$$

where PI- denotes the destructive Pauli interference, PI+ denotes the constructive Pauli interference, and the decay width  $\Gamma$  is a positive quantity. Here only Cabbibo-favoured contributions are listed.

Coefficients  $C_d$  encode short-distance interactions and phase-space factors and can be calculated perturbatively. Therefore, they are known with good precision [28-31]. The hadronic matrix elements can be determined by a) relating the matrix element to other observables, or b) using other nonperturbative methods, such as LQCD, QCD sum rules, HQET, and phenomenological models such as nonrelativistic quark model. The matrix elements for dimension-six operators are still poorly known in the charmed baryon sector. While predictions for absolute lifetimes have relatively large uncertainties, ratios of lifetimes have smaller theoretical uncertainties [32].

Within the HQE framework, the ratio of charmed baryon lifetimes are calculated numerically up to  $O(1/m_Q^3)$  and, as summarised in Table 1.2. In some references the absolute values are also available. It can be seen in Table 1.2 that the expected lifetime hierarchy of singly charmed baryons agrees with experimental measurements up to 2018. It is also clear that although the qualitative feature is reproduced, the quantitative estimates are still far from being satisfactory. The lifetimes of doubly charmed baryons are calculated and summarised in Table 1.3. While predictions of absolute values of lifetimes vary significantly, the lifetime hierarchy seems to be in a good agreement.

In summary, large theoretical uncertainties persist in the prediction of charmed baryon lifetimes, due to both the poorly known matrix elements of dimension-six operators and the slow convergence of HQE in the charm baryon sector. Accurate mea-

Table 1.2 Theoretical calculations of lifetimes of singly charmed baryons up to order  $1/m_c^3$  in HQE. As a comparison, the lifetime ratio in each prediction is also shown. The reference lifetime,  $\tau_0$ , is different between predictions.

	$\Omega_c^0$	$\varXi_c^0$	$\Lambda_c^+$	$\Xi_c^+$
Ref. [27,31,33] Ref. [34]	$ au_0$ $ au_0$	$1.5\tau_0$ $1.2\tau_0$	$3.2\tau_0$ $1.8\tau_0$	$4.0\tau_0$ $2.0\tau_0$
PDG18 [35]  Ref. [34]  PDG18 [35] [fs]	$   \begin{array}{r}     \tau_0 \\     \hline     103 \\     69 \pm 12   \end{array} $	$(1.6 \pm 0.3)\tau_0$ $161$ $112 \pm 11$	$(2.9 \pm 0.5)\tau_0$ $296$ $200 \pm 6$	$\frac{(6.4 \pm 1.2)\tau_0}{306}$ $442 \pm 26$

surements of lifetimes of singly charmed baryons and experimental input to lifetimes of doubly charmed baryons are crucial to further improve our understanding of their decay dynamics.

### 1.2.2 Experimental status of charmed baryon lifetimes

Many measurements of lifetimes of heavy flavour hadrons have been performed in the last thirty years. Precisions of experimental measurements have been continuously improved due to the increase of statistics and development of detector techniques. Measurements of charmed hadron lifetimes are summarised in Fig. 1.9. Lifetimes of charmed mesons are measured with a precision of about 1% and the central values of various measurements agree well with each other. Lifetimes of charmed baryons are measured less precisely, with precision in the range of 3–17% before the recent LHCb measurements. As a comparison, measurements of beauty hadron lifetimes are shown in Fig. 1.10. Lifetimes of beauty hadrons are known with good precision, except for that of the  $\Omega_h^-$  baryon. Fig. 1.10 illustrates that all beauty hadrons have similar lifetimes, indicating that the spectator effects are significantly suppressed with increasing heavy quark mass. It is interesting to notice that there was a change in the central values of  $B^0$  meson over the years. Although successive measurements agree with each other within uncertainty, the central values have been varied by a factor of about two over a span of twenty years. Historically, this lead to a discrepancy between HQE predictions and the measured ratio of  $au_{A_b^0}/ au_{B^0}$  for some time [44].

In the sector of charmed baryons, a surprise occurred when the LHCb experiments recently reported a systematic update of charmed baryon lifetimes [45-46]. These measurements violated the qualitative agreement between theoretical predictions and experi-

Table 1.3 Theoretical calculations of lifetimes of doubly charmed baryons up to order  $1/m_c^3$  in HQE. As a comparison, the lifetime ratio in each prediction is also shown. The reference lifetime,  $\tau_0$ , is different between predictions.

	$\Xi_{cc}^{+}$	$\Omega_{cc}^{+}$	$\Xi_{cc}^{++}$
Ref. [36]	$ au_0$		$3.9\tau_0$
Ref. [37]	$ au_0$	$1.7\tau_0$	$2.9\tau_0$
Ref. [38]	$ au_0$	$1.1\tau_0$	$7.0\tau_0$
Ref. [39]	$ au_0$	$1.4\tau_0$	$2.3\tau_0$
Ref. [40]	$ au_0$	$0.8\tau_0$	$2.7\tau_0$
Ref. [41]	$ au_0$		$3.5\tau_0$
Ref. [42]	$ au_0$	$1.4\tau_0$	$9.0\tau_0$
Ref. [43]	$ au_0$	$1.4\tau_0$	$2.2\tau_0$
Ref. [36] [fs]	110		430
Ref. [37] [fs]	160	270	460
Ref. [38] [fs]	220	250	1550
Ref. [39] [fs]	200	270	450
Ref. [40] [fs]	250	210	670
Ref. [41] [fs]	530		1850
Ref. [42] [fs]	57	78	520
Ref. [43] [fs]	200	270	440

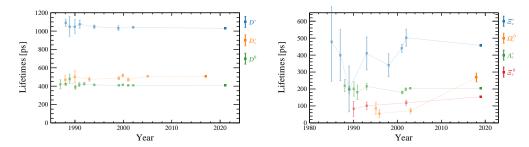


Figure 1.9 Measurements of lifetimes of (left) charmed mesons and (right) charmed baryons.

mental measurements by changing the lifetime hierarchy from

$$\tau_{\Omega_c^0} < \tau_{\Xi_c^0} < \tau_{\Lambda_c^+} < \tau_{\Xi_c^+}$$
(1.34)

into

$$\tau_{\Xi_c^0} < \tau_{\Lambda_c^+} < \tau_{\Omega_c^0} < \tau_{\Xi_c^+}.$$
(1.35)

To be more specific, the measured  $\Omega_c^0$  lifetime,  $\tau_{\Omega_c^0}$ , is nearly four times longer than the previous world average [35], which is inconsistent at a level of seven standard deviations.

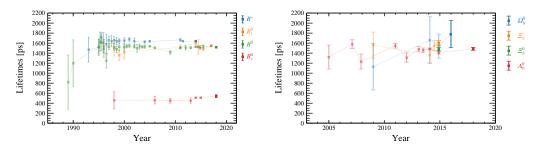


Figure 1.10 Measurements of lifetimes of (left) beauty mesons and (right) beauty baryons.

Table 1.4 Measurements of lifetimes of singly charmed baryons.

	$arOmega_c^0$	$\Xi_c^0$	$arLambda_c^+$	$\Xi_c^+$
PDG18 [fs]	$69 \pm 12$	$112^{+13}_{-10}$	$200 \pm 6$	$442 \pm 26$
LHCb SL [fs]	$268 \pm 26$	$154.5 \pm 2.6$	$203.5 \pm 2.2$	$456.8 \pm 5.5$

The measured  $\Xi_c^0$  lifetime,  $\tau_{\Xi_c^0}$ , is larger than the previous world average by three standard deviations, as can be seen from Table 1.4. These measurements use the charmed baryons produced in semileptonic beauty baryon decays, collected in pp collisions at center-of-mass energies of 7, 8 TeV by the LHCb experiment during 2011-2012, corresponding to an integrated luminosity of 3 fb<sup>-1</sup>. The  $\Omega_c^0$  lifetime is measured using around 1 000  $\Omega_b^- \to \Omega_c^0 \mu^- \overline{\nu}_\mu X$  decays, while the  $\Xi_c^0$  lifetime is measured using around  $2 \times 10^4 \Xi_b^- \to \Xi_c^0 \mu^- \overline{\nu}_\mu X$  decays. Both  $\Omega_c^0$  and  $\Xi_c^0$  baryon are reconstructed in the  $pK^-K^-\pi^+$  final state. The  $D^+ \to K^-\pi^+\pi^+$  decay is used as the normalisation channel to reduce the uncertainties associated with systematic effects. The lifetime of  $\Omega_c^0$  baryon is still limited by the signal sample size.

Resolving the emergent discrepancy is essential for our understanding of weak decays of heavy flavour hadrons. Independent measurements are crucial to establish a sound reference for further theoretical development.

# 1.3 Doubly charmed baryons

The motivation for the study of doubly charmed baryons has been introduced in a broad context in Sec. 1.1. The existence of doubly charmed baryons was predicted [11] in  $SU(4)_f$  20-plets soon after the discovery of  $Jh\psi$  particle in 1974. Since then, theoretical investigations of properties of doubly charmed baryons have been extensively performed with experimental stimulations from time to time, and eventually reached a climax in 2017, when the observation of the doubly charmed baryon  $\Xi_{cc}^{++}$  was reported by the



Figure 1.11 The citation summary in March 2022 with the key word *doubly charmed baryons* at INSPIRE HEP. The peaking record corresponds to 40 papers in 2018. The steep rises correspond to the observation of  $\Omega_c^0$  in 1995, the claim of  $\Xi_{cc}^+$ (3520) baryon by SELEX in 2002, and the observation of  $\Xi_{cc}^{++}$  baryon by LHCb in 2017.

LHCb experiment. The citation summary with the key word *doubly charmed baryons* at INSPIRE HEP is shown in Fig. 1.11. The interplay between theory and experiment was driven by the former in the study of doubly charmed baryons. It is because that despite the observation in 2017, the experimental measurements are still very limited compared to the huge amount of theoretical predictions.

The doubly charmed baryons refer to baryons containing two charm quarks and a light quark. Ground-state doubly charmed baryons constitute a  $J^P = \frac{1}{2}^+$  triplet and a  $J^P = \frac{3}{2}^+$  triplet, as shown in Fig. 1.2. Doubly charmed baryons are expected to combine the dynamics found in the D meson, a relativistic motion of a light quark orbitting around a heavy static color  $\bar{\bf 3}$  source at a distance ( $\sim 1/m_q$ ) much larger than the source size ( $\sim 1/m_c$ ), and the dynamics of Charmonium. A light-quark-heavy-diquark picture is often used as an approximation in calculations of doubly charmed baryons, and is supported by nonrelativistic quark model calculations [15] at least for ground states.

There are several important energy scales in doubly charmed baryons that play import roles in dynamics, including the mass of the charm quark  $m_c$ , its typical three-momentum  $m_c v_c$ , its typical kinetic energy  $m_c v_c^2$ , and the scale associated with nonperturbative effects  $\Lambda_{\rm QCD}$  involving gluons and light quarks. The typical velocity v of the heavy quark decreases as the mass increases. If the mass is sufficiently large, the heavy quark is non-relativistic, with typical velocity  $v \ll 1$ . The average value of  $v_c^2$  is about 0.3 for charmonium according to quark potential model calculations [25]. The nonperturbative scale can be estimated with the coefficient of the linear potential between quarks and is about  $\Lambda_{\rm QCD} \approx 450\,{\rm MeV}$  [25]. Thus, we have well separated energies scales in doubly charmed

baryons:

$$\Lambda_{\text{OCD}}^2 \sim \left( m_c v_c^2 \right)^2 \ll \left( m_c v_c \right)^2 \ll m_c^2, \tag{1.36}$$

which can be employed as expansion parameters in the evaluation of their properties.

Theoretical calculations and interpretations of the properties of the doubly charmed baryons are discussed in Sec. 1.3.1, followed by a review of the experimental status in Sec. 1.3.2.

### 1.3.1 Doubly charmed baryons from a theoretical perspective

In this section, we review in some detail theoretical calculations of the production, mass spectra, and decay properties of the doubly charmed baryons. Other properties, such as magnetic dipole moments and electromagnetic form factors, are also important to identify the dynamic degree of freedom of doubly charmed baryons. However, they are beyond the capacity of experimental facilities at present and in the near future. We refer interested readers to Refs. [47-52] for relevant discussions.

#### **Production**

The theoretical calculation of the production cross-section of doubly charmed baryons in various production environments provides guidance for experimental searches for these particles. The observation and production measurement of doubly charmed baryons in turn test theoretical approaches and constrain values of input parameters. The interplay between theory and experiment already happens in the study of  $\Xi_{cc}^{++}$  baryon, and is promising in the hunting of remaining doubly charmed baryons.

The fundamental mechanism of the inclusive production of doubly charmed baryons can be factorised into three effects:

- 1. The production of two charm quarks, which is a hard process and can be calculated perturbatively in QCD.
- 2. The coalescence of two charm quarks into a diquark  $c + c \rightarrow (cc)$ , which is of non-perturbative nature and can be described by matrix elements within the nonrelativistic QCD framework. These matrix elements are universal in different production environments for each state of diquark. Both color  $\bar{3}$  state  $[^3S_1]_{\bar{3}}$  and color 6 state  $[^1S_0]_6$  are considered [53]. The production of exinlinecited diquarks is discussed at the end of this section.
- 3. The hadronisation of a diquark into a doubly charmed baryon, which is also a non-

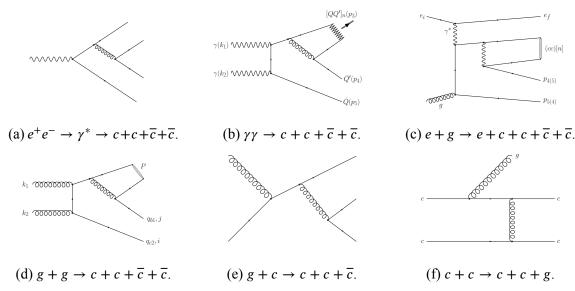


Figure 1.12 Representative Feynman diagrams in different production environments. Reproduced from Ref. [53,55,57-58].

perturbative process. The  $(cc)[^3S_1]_{\bar{3}}$  diquark hadronises into a baryon by absorbing a light quark, while the  $(cc)[^1S_0]_6$  diquark hadronises by capturing a light quark and a soft gluon in order to form a colorless bound state. The probability of this process is usually assumed to be unity [54-56] in the literature, which implies that the momentum of the baryon is roughly the same as the initial diquark. This simple assumption proves to be of good accuracy when compared with the fragmentation function obtained from phenomenological models (2014).

Each production environment provides unique opportunities for the study of doubly charmed baryons. In this section, the production mechanism in different initial states is reviewed and the theoretical prediction of the production cross-section is given for each environment. The representative Feynman diagrams in different production environments are shown in Fig. 1.12 and are explained in detail below.

 $e^+e^-$  **production.** The study of the production of doubly charmed baryon in  $e^+e^-$  collisions can probe the nonperturbative effect in a cleaner environment than hadroproduction without the complication of parton distribution functions (PDFs). Besides, a measurement of the production asymmetry between forward and backward direction at *Z*-factories can probe the effective eletro-weak mixing angle with reduced theoretical and experimental uncertainties compared with traditional measurements with  $e^+e^- \to Z \to f\bar{f}$  production [59].

The production of two charm quarks in  $e^+e^-$  collisions includes the

 $e^+ + e^- \rightarrow \gamma^* \rightarrow c + c + \overline{c} + \overline{c}$  process. In addition, the contribution from  $e^+ + e^- \rightarrow Z^0 \rightarrow c + c + \overline{c} + \overline{c}$  needs to be considered for collisions around  $\sqrt{s} = m_Z$ . The total production cross-section can be factorised into perturbative and nonperturbative contributions and expanded in orders of  $v_c$ , the velocity of the charm quark in the baryon, within the NRQCD framework as

$$\sigma_{ab} = H_{ab \to (cc)[^3S_1]_{\bar{3}}} \times h_3 + H_{ab \to (cc)[^1S_0]_6} \times h_1 + \cdots$$
 (1.37)

The perturbative coefficient H describes the production of two charm quarks and is determined by calculating all contributing Feynman diagrams. The nonperturbative coefficient h corresponds to the binding of two charm quarks into a diquark and can be determined using nonperturbative methods such as potential model or from experimental data. Contributions in higher orders of  $v_c$  are neglected.

Adopting the parameters of  $h_1 = h_3 = 0.039 \, \text{GeV}^3$ ,  $m_c = 1.6 \, \text{GeV}$ , and  $\alpha_s(2m_c) = 0.24$ , the production cross-section of  $\Xi_{cc}^+$  at *B*-factories with  $\sqrt{s} = 10.6 \, \text{GeV}$  is estimated to be  $\sigma_{\Xi_{cc}^+} \approx 230 \, \text{fb}$  [53]. The results will be doubled if we take charge conjugate states into account.

Adopting the parameters of  $h_1 = h_3 = 0.039 \, \text{GeV}^3$ ,  $m_c = 1.5 \, \text{GeV}$ ,  $m_u = m_d = 0.3 \, \text{GeV}$ ,  $m_s = 0.5 \, \text{GeV}$ ,  $\alpha_s(2m_c) = 0.24$ ,  $\alpha = 1/129$ ,  $m_Z = 91.1876 \, \text{GeV}$ ,  $\Gamma_Z = 2.4952 \, \text{GeV}$ , and  $\sin^2 \theta_W^{eff} = 0.232$ , the production cross-section of  $\Xi_{cc}^+$  at super Z-factories with  $\sqrt{s} = m_Z$  is estimated to be  $\sigma_{\Xi_{cc}^+} \approx 395 \, \text{fb}$  [59]. The results will be doubled if we take charge conjugate states into account. If one further assumes the instantaneous luminosity of  $10^{36} \, \text{cm}^{-2} \, \text{s}^{-1}$  and the collider year of  $10^7 \, \text{s}$ , the number of events produced per year is  $\mathcal{O}(10^6)$ .

**Photoproduction.** The production cross-section of doubly charmed baryons through  $e^+ + e^- \rightarrow \gamma^*/Z^0 \rightarrow c + c + \overline{c} + \overline{c}$  in  $e^+e^-$  collisions is highly suppressed when the collision energy is much higher than the  $Z^0$  boson mass. The dominant production mechanism in this case is through the  $\gamma\gamma \rightarrow c + c + \overline{c} + \overline{c}$  process. The high energy  $\gamma$  beam can be obtained by backward Compton scattering of laser light which is focused on the electron beams [60]. The theoretical calculation of the production cross-section is similar to that of  $e^+e^-$  collisions, with the Feynman diagrams replaced by relevant  $\gamma\gamma$  scattering processes. One additional complication is that one needs to take into account the energy distribution of the nonmonochromatic  $\gamma$  beam.

The production cross-section of doubly charmed baryon  $\Xi_{cc}^+$  through photoproduction

is calculated in Ref. [57] at  $\sqrt{s} = 250$  GeV,  $\sqrt{s} = 500$  GeV, and  $\sqrt{s} = 1$  TeV to be 400 fb, 200 fb, and 67 fb, respectively. The collision energies correspond to the condition of ILC. The results indicate that  $\mathcal{O}(10^6)$  number of events can be produced per year at ILC.

**Deep inelastic scattering.** The production of doubly charmed baryons in deep inelastic ep scattering is of special interest due to its reduced uncertainty in theoretical calculations and more experimental observables available. The dominant mechanism in the  $Q^2$  region of [2, 100] GeV<sup>2</sup> is the gluon partonic process  $e + g \rightarrow e + c + c + \overline{c} + \overline{c}$ . According to the factorisation theorem, the inclusive production cross-section can be formulated as

$$\sigma = g(x) \otimes \hat{\sigma}_{eg}(x), \tag{1.38}$$

where g(x) is the gluon distribution function in proton and  $\hat{\sigma_{eg}}(x)$  is the partonic cross-section. The numerical calculation of the partonic cross-section is similar to that in  $e^+e^-$  collisions. In Ref. [58], the production cross-section of  $\Xi_{cc}^+$  in deep inelastic ep scattering at  $E_e = 60$  GeV and  $E_p = 7$  TeV and in the LHeC fiducial region is calculated to be 10 pb with 30% uncertainty. The result implies  $\mathcal{O}(10^6)$  number of event produced per year at LHeC.

**Hadroproduction.** The inclusive production of doubly charmed baryons at hadron colliders is of the most importance thanks to the large data sets accumulated at LHC. The dominant mechanisms for the production of two charm quarks include "gluongluon fusion"  $g+g \to c+c+\overline{c}+\overline{c}$ , "gluon-charm creation"  $g+c \to c+c+\overline{c}$ , and "charm fusion"  $c+c \to c+c+g$ . It should be noted that NLO charm fusion process  $c+c \to c+c+g$  is considered instead of LO process  $c+c \to c+c$ , because the LO process only contributes to production with zero transverse momentum which is usually beyond the reach of experimental facilities. The contribution due to light quark annihilation  $q+\overline{q} \to c+c+\overline{c}+\overline{c}$  is neglected because it is much smaller than gluon-gluon fusion according to the study of  $B_c^+$  production.

As shown in Ref. [55-56], based on which a dedicated event generator GENXICC [61-63] is developed and used in the LHCb experiment, the cross-section of the inclusive production of doubly charmed baryons in hadron collisions  $H_1 + H_2 \rightarrow \Xi_{cc} + X$  is a sum of different contributions

$$\sigma = \sigma_{gg} + \sigma_{gc} + \sigma_{cc} + \cdots, \tag{1.39}$$

with each contribution can be formulated according to the factorisation theorem as

$$\sigma_{gg} = g_{1}(x_{1})g_{2}(x_{2}) \otimes \hat{\sigma}_{gg}(x_{1}, x_{2}),$$

$$\sigma_{gc} = \sum_{i=1}^{2} \sum_{j=1}^{2} \delta_{ij}g_{i}(x_{i})c_{j}(x_{j}) \otimes \hat{\sigma}_{gc}(x_{1}, x_{2}),$$

$$\sigma_{cc} = \sum_{i=1}^{2} \sum_{j=1}^{2} \delta_{ij}c_{i}(x_{i})c_{j}(x_{j}) \otimes \hat{\sigma}_{cc}(x_{1}, x_{2}),$$
(1.40)

where gg, gc, and cc refer to different mechanisms discussed in the first item above,  $g_i(x_i)$  and  $c_i(x_i)$  are parton distribution functions (PDFs) of gluon and c quark inside the collision hadron  $H_i$ ,  $x_i$  is the fraction of  $H_i$ 's momentum carried by the parton i,  $\delta_{ij}$  is the Kronecker delta function, and  $\hat{\sigma}$  is the partonic cross-section. The renormalisation scale and constituent charm quark mass is omitted in the above expression for simplicity.

According to Eq. 1.39, in order to calculate the cross-section numerically, one needs to determine the PDFs as well as the hard-scattering cross-sections corresponding to each subprocess. The PDFs can be determined by global fitting to various partonic cross-sections. It should be noticed that the PDF for charm quark needs to be modified properly to avoid double-counting between the gluon-gluon fusion and gluon-charm creation mechanism. The partonic cross-sections of different production mechanisms can be further factorised into perturbative and nonperturbative contributions and evaluated in the same approach as for  $e^+e^-$  collisions.

Adopting the parameters of  $h_1 = h_3 = 0.039\,\mathrm{GeV}^3$ ,  $m_{\Xi_{cc}} = 3.50\,\mathrm{GeV}$ ,  $m_c = 1.75\,\mathrm{GeV}$ ,  $\Lambda_{QCD}^{n_f=4} = 0.215\,\mathrm{GeV}$ , and the renormalisation scale  $\sqrt{m_{\Xi_{cc}}^2 + p_T^2}$ , the cc diquark production cross-section in pp collisions at  $\sqrt{s} = 14\,\mathrm{TeV}$  is 62 nb in the fiducial region of  $p_T > 4\,\mathrm{GeV}$  and |y| < 1.5, corresponding roughly to the geometric acceptance of ATLAS and CMS detectors at LHC, and is 30 nb in the fiducial region of  $p_T > 4\,\mathrm{GeV}$  and  $1.8 < \eta < 5.0$ , corresponding to the geometric acceptance of the LHCb detector at LHC. If one takes the fragmentation fraction to be  $f((cc) \to \Xi_{cc}^{++}) : f((cc) \to \Xi_{cc}^{+}) : f((cc) \to \Omega_{cc}^{+}) = 10 : 10 : 3$  as shown in Pythia [64], the production cross-section at LHCb is estimated to be  $\sigma_{\Xi_{cc}^{++}} \approx 13\,\mathrm{nb}$ ,  $\sigma_{\Xi_{cc}^{+}} \approx 13\,\mathrm{nb}$ , and  $\sigma_{\Omega_{cc}^{+}} \approx 4\,\mathrm{nb}$ . The results will be doubled if we take charge conjugate states into account. The dominant uncertainties of the calculated production cross-section stem from the choice of renormalisation energy scale and the value of constituent charm quark mass, which are about 30% relative to the central values.

**Heavy ion production.** The study of the doubly charmed baryons in heavy ion collisions provides unique probe of properties of the quark-gluon plasma (QGP) as the production mechanism differs significantly from pp collisions due to nuclear effects [65-66]. The difference occurs in all aspects compared with the hadroproduction. First, the rapidity density of charm quarks produced in a single collision is higher. The nuclear parton distribution function (nPDF) contains a modification of proton PDF due to nuclear multibody effects. Second, the charm quarks can diffuse in the deconfined QGP medium, resulting in a smaller relative momentum of a charm quark pair and an enhancement of the coalescence probability of a cc diquark. Third, the formed cc diquark can diffuse and dissociate in the dynamical evolvement in the QGP medium. Fourth, in the hadronisation of the cc diquark, additional light quark to be captured follows the Fermi-Dirac distribution at certain temperature  $T_c$ .

In Ref. [65], a set of coupled Boltzmann transport equations are used to describe the dynamical evolvement of charm quarks and diquarks in QGP medium and are solved with Monte Carlo simulations. The predicted yield of  $\Xi_{cc}^+$  in the fiducial region of  $0 < p_T < 5 \,\text{GeV}$  and |y| < 1 in PbPb collisions at  $\sqrt{s_{NN}} = 2.76 \,\text{TeV}$ , corresponding to the condition of the ALICE experiment at LHC, is 0.01 per collision assuming a melting temperature of  $T_m = 250 \,\text{MeV}$ .

In Ref. [66], nPDFs are used in the calculation and the obtained production cross-section is  $\sigma_{pPb} = 1.62 \times 10^2 \,\mu b$  in pPb collisions at  $\sqrt{s_{NN}} = 8.16 \,\mathrm{TeV}$ , and  $\sigma_{PbPb} = 1.85 \times 10^4 \,\mu b$  in PbPb collisions at  $\sqrt{s_{NN}} = 5.02 \,\mathrm{TeV}$ , corresponding to the condition of the ALICE experiment at LHC. The production is enhanced by 2–4 orders of magnitude compared with pp collisions.

**Production with exinlinecited diquark.** In previous discussions, only the production of cc diquark in S-wave is considered. Ref. [67] studies the production with exinlinecited cc diquark at LHC using the factorisation approach. It is estimated that the production with radially exinlinecited 2S or 3S cc diquark is about 50% of the total production cross-section, while the contribution of P-wave excitations is about 5%. This observation implies a sizable contribution of  $\Xi_{cc}^{++}$  events from the  $\Xi_{cc}^{+}(nS) \to \Xi_{cc}^{++}\pi^{-}$  decay.

#### Spectroscopy

A vast amount of theoretical predictions and postdictions of masses and mass relations of doubly charmed baryons are available. Theoretical approaches, from phenomenologi-

cal quark models to ab initio calculations of LQCD, are utilized.

**Ground states.** Nonrelativistic quark models are extensively used to calculate the masses of doubly charmed baryons. Mass formulas are used to predict baryons containing two heavy quarks in Refs. [41,68-70]. While these mass formulas are useful to predict the masses of *S*-wave baryons, they are unable to describe exinlinecited states and to give further insights into other properties such as magnetic moments and decays. Predictions using various quark potential models are made in Refs. [11,13-14,16-17,37,71-76].

Bag model is also widely used. The picture of the bag model resembles a bubble (the hadron) in the medium (vacuum) [77]. A hadron is taken to be a finite region of space containing quark and gluon fields. The pressure of the field is balanced by a universal pressure *B*. The dynamics are specified by equations of motion and boundary equations for reach filed. The first application devoted to the ground-state light hadrons by MIT group with the approximation of a rigid cavity with spherical shape [78]. Later the bag model was adopted to describe heavy quark systems [79] and open-flavour systems [80]. One advantage of the bag model is that the mixing of states with the same total angular momentum but different diquark angular momentum can be calculated as the creation and annihilation operators for relevant interaction can be introduced.

The bag model for doubly charmed baryons combine the methods used for quarkonia and for open-flavour hadrons [14]. The spherical bag centred at the middle of the two heavy quarks is considered. The zeroth-order mass is computed as the minimum with respect to the bag radius R of

$$M(R) = \sum_{i} \omega_{i} - \frac{Z_{0}}{R} + \frac{4\pi}{3} B R^{3}, \qquad (1.41)$$

where  $\omega_i = m_c$  for heavy quarks and  $\omega_i = \sqrt{\chi_i^2 + (m_i R)^2}/R$  for light quarks with a hyper parameter  $\chi_i$ . The finite energy  $Z_0/R$  is associated with zero-point fluctuation of the fields. The energy  $\frac{4\pi}{3}BR^3$  is due to the bag pressure. It is noticed that there are dramatic differences between different set of model parameters extracted from different systems. This implies that different approximations result in different renormalisation of the parameters. Unlike the potential model, the bag model involves many parameters with ambiguous phenomenological determination and thus is difficult to extrapolate to other hadrons. The predictions using the bag model are available in Refs [14,81-83].

Quark model predictions with relativistic corrections are calculated in Ref. [84-85].

Relativistic quark model based on quasipotential is used in Ref. [13,86]. the effective interaction is the sum of the one-gluon exchange term with the mixture of the long-distance vector and scalar linear confining potentials. A form factor in the one-gluon exchange interaction is included to consider the structure of the heavy diquark. The expansion in inverse powers of the heavy diquark mass is employed in solving the quark-diquark equation. BSE equation is also used to calculate the mass spectra of doubly charmed baryons [87].

QCD sum rules are also adopted to study doubly charmed baryons in Ref. [88-95]. Calculations based on effective filed theory are conducted in Ref. [96-100]. LQCD calculations of ground-state doubly charmed baryons are performed in Ref. [20,101-111].

Theoretical predictions of masses of  $J^P = \frac{1}{2}^+$  doubly charmed baryons are summarised in Fig. 1.13. Some comments are appropriate here:

- Various quark model predictions are in general consistent with each other, and in extremely good agreement with the  $\Xi_{cc}^{++}$  mass measured by LHCb. However, quark model predictions can not provide reasonable estimation of model uncertainties.
- Predictions based on QCD sum rules, HQET, NRQCD and CHPT agree with experiment within theoretical uncertainties. They provide insight into the structure of doubly charmed baryons based on QCD, although with large but understood uncertainties.
- Calculations with BES equation are relatively new thanks to the technical development in this field.
- LQCD results are in excellent agreement with experiment, with theoretical uncertainties carefully estimated and under control.
- The mass of  $\Omega_{cc}^+$  is about 100 MeV above that of  $\Xi_{cc}$ .
- It should be noted that some postdictions are also included, which agree well with experiment.

Theoretical predictions of hyperfine splitting between  $J^P = \frac{1}{2}^+$  and  $J^P = \frac{3}{2}^+$  baryons are summarised in Fig. 1.14. The hyperfine mass splittings of doubly charmed baryons are related to that of charmed mesons through the mass relations

$$m_{\Xi_{cc}^*} - m_{\Xi_{cc}} = \frac{3}{4}(m_{D^*} - m_D), m_{\Omega_{cc}^*} - m_{\Omega_{cc}} = \frac{3}{4}(m_{D_s^*} - m_{D_s}),$$
 (1.42)

according to HQET [112], NRQCD [96], or the quark model [18]. Most calculations obtain a value below the  $\Xi_{cc}\pi$  or  $\Omega_{cc}\pi$  threshold, which indicates that the transition from  $J^P = \frac{3}{2}^+$  to  $J^P = \frac{1}{2}^+$  state can only proceed radiatively through  $\gamma$  emission.

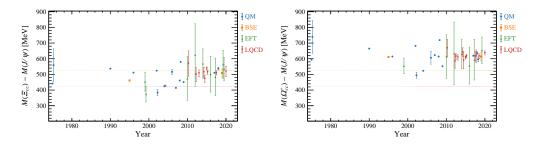


Figure 1.13 Theoretical predictions of masses of  $J^P = \frac{1}{2}^+$  doubly charmed baryon (left)  $\Xi_{cc}$  and (right)  $\Omega_{cc}^+$ . The x-axis corresponds to the time of the theoretical work. The y-axis corresponds to the predicted mass subtracted by the known mass of Jhy meson. Isospin splitting is ignored in  $\Xi_{cc}$  doublets. Results are grouped according to the theoretical method used, including quark model (denoted by QM), effective file theory or related method of QCD sum rules, HQET, NRQCD and CHPT (denoted by EFT), Bethe-Salpeter equation (denoted by BSE), and LQCD (denoted by LQCD). Experimental results of  $\Xi_{cc}^+$ (3520) baryon reported by SELEX in 2002, and  $\Xi_{cc}^{++}$ (3620) baryon reported by LHCb in 2017 are indicated by yellow and pink lines, respectively.

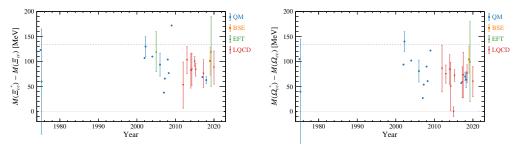


Figure 1.14 Theoretical predictions of hyperfine splitting between  $J^P = \frac{1}{2}^+$  and  $J^P = \frac{3}{2}^+$  baryons for (left)  $\Xi_{cc}$  and (right)  $\Omega_{cc}^+$ . The x-axis corresponds to the time of the theoretical work. The y-axis corresponds to the predicted mass difference. Results are grouped according to the theoretical method used, including quark model (denoted by QM), effective file theory or related method of QCD sum rules, HQET, NRQCD and CHPT (denoted by EFT), and LQCD (denoted by LQCD).

**Isospin splitting.** The isospin splitting of doublet  $\Xi_{cc}^+$  and  $\Xi_{cc}^{++}$  baryon stems from the different mass (QCD) and charge (QED) of up and down quarks. Quark model [13,113-115], effective field theory [97-98], and LQCD [116] are used to calculate the isospin splitting. The results are summarised in Fig. 1.15. All methods predict that  $\Xi_{cc}^{++}$  baryon is heavier than  $\Xi_{cc}^+$  baryon by a few MeV. This is in sharp contradiction with the fact that the  $\Xi_{cc}^+$ (3520) baryon reported by SELEX is isospin partner of the  $\Xi_{cc}^{++}$ (3620) baryon reported by LHCb.

**Exinlinecited states.** Similar approaches are also utilized to calculate the spectra of exinlinecited doubly charmed baryons. The mass spectra of  $\Xi_{cc}$  and  $\Omega_{cc}^+$  baryons obtained with relativistic quark model [13] are shown in Fig. 1.16. States are organized according to the quantum number of diquarks. The spectra are first shown in the infinite diquark

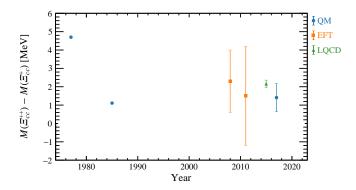


Figure 1.15 Theoretical predictions of isospin splitting between  $\Xi_{cc}^+$  and  $\Xi_{cc}^{++}$  baryon. The x-axis corresponds to the time of the theoretical work. The y-axis corresponds to the predicted mass difference. Results are grouped according to the theoretical method used, including quark model (denoted by QM), effective file theory or related method of QCD sum rules, HQET, NRQCD and CHPT (denoted by EFT), and LQCD (denoted by LQCD).

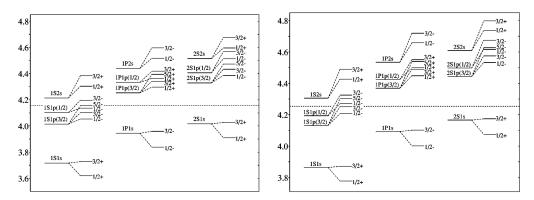


Figure 1.16 Mass spectra of (left)  $\Xi_{cc}$  baryons and (right)  $\Omega_{cc}^+$  baryons calculated in Ref. [13]. The horizontal dashed line indicates the  $\Lambda_c D$  and  $\Lambda_c D_s$  threshold for  $\Xi_{cc}$  and  $\Omega_{cc}^+$  baryons, respectively. The notation of  $(n_D L n_q l) J^P$  is used to describe the quantum numbers of baryons, where  $n_D$  and  $n_q$  are the radial quantum number of the diquark and the light quark, L and l are the orbital angular momentum of the diquark and the light quark, and  $J^P$  is the total angular momentum J and parity P of the baryon.

mass limit. Then the first order corrections in the inverse of diquark mass are considered. LQCD predictions of mass spectra of doubly charmed baryons in Ref. [107] are shown in Fig. 1.17. State are grouped according to their total angular momentum. Some comments are appropriate here:

- The flavour-dependent interaction results in the splitting of degenerate states and the mixing of states with different total light quark angular momentum but the same total angular momentum and parity.
- The spectra for the ground-state diquark are very similar to the ones for heavy-light mesons, as expected in the light-quark-heavy-diquark picture. However, the full spectra are richer thanks to the additional degree of freedom of diquark excitation.

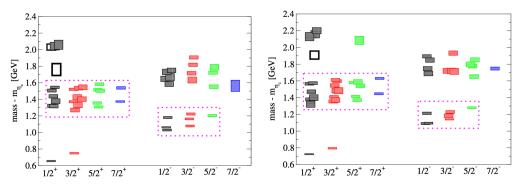


Figure 1.17 Mass spectra of (left)  $\Xi_{cc}$  and (right)  $\Omega_{cc}^+$  baryons with spin up to  $\frac{7}{2}$  calculated in Ref. [107]. The masses are shown w.r.t. the known mass of  $\eta_c$ .

- The first exinlinecited state above the low-lying states is due to the diquark excitation, which can decay strongly to the ground state via pion emission for  $\Xi_{cc}$  excitations.
- The  $\Omega_{cc}^{*+} \to \Omega_{cc}^+ \pi$  decay is isospin violating and suppressed.  $\Omega_{cc}^{*+} \to \Xi_{cc} K$  is allowed for radial excitation of  $\Omega_{cc}^+$ .

#### Weak decay

Inclusive weak decays, or equivalently lifetimes, of doubly charmed baryons are discussed within the framework of Heavy Quark Expansion in Sec. 1.2.1. In summary, the lifetime hierarchy of weakly decaying doubly charmed baryons is predicted in many theoretical calculations to be

$$\tau_{\Xi_{cc}^{+}} < \tau_{\Omega_{cc}^{+}} < \tau_{\Xi_{cc}^{++}},$$
(1.43)

while predictions of absolute values carry large uncertainties.

In this section, we discuss exclusive decays of doubly charmed baryons and focus on Cabbibo-favoured (CF) decay modes, which can provide practical guidance for experimental searches at present and in the near future. Cabbibo-suppressed and flavour-changing-neutral-current processes are studied in the literature [117], although far beyond the reach of experiments currently. Quantitative results are presented in terms of partial widths, due to limited knowledge of lifetimes of doubly charmed baryons. It is straightforward to translate these partial widths into branching fractions once solid information on lifetimes is available.

Back in 80s Bjorken has anticipated the decay modes and branching fractions of doubly charmed baryons via an "unsophisticated, common-sense" approach [118]. The general patterns and order of magnitudes are still valid when compared with predictions made

Table 1.5	Partial decay widths	of semileptonic d	decays in unit of 10 <sup>-14</sup>	GeV.
-----------	----------------------	-------------------	-------------------------------------	------

Channels	Ref. [122]	Ref. [123]	Ref. [124]
$\Xi_{cc}^{++} \to \Xi_c^+ l^+ v_l$	11.5	7.0	8.7
$\Xi_{cc}^{++}\to\Xi_c^{\prime+}l^+v_l$	12.8	9.7	14.3
$\Xi_{cc}^{++}\to\Xi_c^{*+}l^+\nu_l$	1.6	2.2	1.7
$\Xi_{cc}^+ \to \Xi_c^0 l^+ v_l$	11.4	6.9	8.6
$\Xi_{cc}^{+}\to\Xi_{c}^{\prime0}l^{+}v_{l}$	12.7	9.7	14.1
$\Xi_{cc}^+\to\Xi_c^*l^+\nu_l$	1.6	2.2	1.7
$\Omega_{cc}^+ \to \Omega_c^0 l^+ \nu_l$	25.5	18.2	28.0
$\varOmega_{cc}^{+}\to \varOmega_{c}^{*0} l^{+} \nu_{l}$	3.1	4.0	3.5

with more involved methods in recent years. It is still challenging to perform a solid analysis based on QCD since one has to address a three-body problem with two charm quarks involved. Therefore, variants of quark models are utilized in quantitative calculations. Efforts are also made to calculate form factors with QCD sum rules [39,119-120] and to build up the HQET for weak decays of doubly charmed baryons [121] very recently. For a solid analysis based on QCD, one has to take into account all three quarks and nonperturbative contributions, which is very complicated and far beyond our capability now.

**Semileptonic decays.** The semileptonic decays of doubly charmed baryons are induced by the quark-level transition  $c \to sl^+v_l$ . The lepton pair can be  $e^+v_e$  and  $\mu^+v_\mu$ . The hadronic decay product can be either  $J^P = \frac{1}{2}^+$  and  $J^P = \frac{3}{2}^+$  singly charmed baryons. Theoretical predictions of semileptonic partial decay widths are shown in Table 1.5. Several comments are appropriate here:

- Predictions made with different models are in general consistent.
- The partial decay widths of semileptonic decays for  $\frac{1}{2}^+ \to \frac{1}{2}^+$  transition are of order  $10^{-13}$  GeV.
- The partial decay widths of semileptonic decays for  $\frac{1}{2}^+ \to \frac{3}{2}^+$  transition is an order of magnitude smaller than that of the  $\frac{1}{2}^+ \to \frac{3}{2}^+$  transition.
- The partial decay width  $\Gamma(\Xi_{cc}^{++} \to \Xi_c^{(\prime)+} l^+ v_l) \approx \Gamma(\Xi_{cc}^{+} \to \Xi_c^{(\prime)0} l^+ v_l)$  due to SU(3) flavour symmetry.
- The above equation dose not imply equal branching fractions, since the total widths of  $\Xi_{cc}^+$  and  $\Xi_{cc}^{++}$  are quite different.

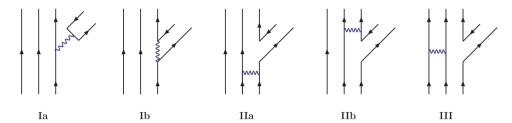


Figure 1.18 The topological diagrams for nonleptonic charmed baryon decays [123].

**Nonleptonic decays.** We concentrate on the discussion of two-body transitions of doubly charmed baryons. Genuine multibody decays are studied with SU(3) flavour symmetry in Refs. [125-126]. According to the spin-parity of the decay products, two-body nonleptonic decays can be classified into four classes:

$$\frac{1}{2}^{+} \rightarrow \frac{1}{2}^{+} + 0^{-},$$

$$\frac{1}{2}^{+} \rightarrow \frac{1}{2}^{+} + 1^{-},$$

$$\frac{1}{2}^{+} \rightarrow \frac{3}{2}^{+} + 0^{-},$$

$$\frac{1}{2}^{+} \rightarrow \frac{3}{2}^{+} + 1^{-},$$
(1.44)

where 0<sup>-</sup> refers to a pseudoscalar meson, and 1<sup>-</sup> denotes a vector meson.

Nonleptonic two-body transitions are also categorised according to their color-flavour topologies, as shown in Fig. 1.18 [123]. Types Ia and Ib refer to diagrams due to the external and internal *W*-emission, respectively. Types II and III refer to different *W*-exchange diagrams. Contributions from the external and internal *W*-emission diagrams are factorizable and have been studied intensively in the literature, with consistent theoretical predictions. Nonfactorizable contributions from internal *W*-emission and *W*-exchange diagrams play an essential role and cannot be neglected. There exist three different approaches for tackling the nonfactorizable contributions in doubly charmed baryon decays: the covariant confined quark model [123,127], final-state interactions [128-130], and the pole model in conjunction with current algebra [131]. Table 1.6 summarises all CF nonleptonic two-body decays of doubly charmed baryons, along with the topological diagrams contributing to these decays.

Numerical predictions of nonleptonic partial decay widths are shown in Table 1.7, Table 1.8, and Table 1.9 for  $\Xi_{cc}^{++}$ ,  $\Xi_{cc}^{+}$ , and  $\Omega_{cc}^{+}$  baryon, respectively. Differential widths and angular distributions are also discussed in Ref. [123]. Several comments are in order:

- Decay modes dominated by external W-emission diagrams have large partial widths. Predictions of these modes agree well between different methods.
- Decay modes that receive contributions from types II and III diagrams can have

Table 1.6 CF nonleptonic two-body decays of doubly charmed baryons, along with the topological diagrams that contribute to these decays [123].

Channels	Ia	Ib	IIa	IIb	III
$\Xi_{cc}^{++} \to \Xi_{c}^{(\prime,*)+} + \pi^{+}(\rho^{+})$	✓			✓	
$\Xi_{cc}^{++} \to \Sigma_c^{(*)++} + \bar{K}^{(*)0}$		✓			
$\Xi_{cc}^{++} \to \Sigma^{(*)+} + D^{(*)+}$				✓	
$\Xi_{cc}^{+} \to \Xi_{c}^{(\prime,*)0} + \pi^{+}(\rho^{+})$	✓		/		
$\Xi_{cc}^+ \to \varLambda_c^+(\Sigma_c^{(*)+}) + \bar{K}^{(*)0}$		✓	✓		
$\Xi_{cc}^+ \to \Sigma_c^{(*)++} + K^{(*)-}$			✓		
$\Xi_{cc}^{+} \to \Xi_{c}^{(\prime,*)+} + \pi^{0}(\rho^{0})$			1	✓	
$\Xi_{cc}^+\to\Xi_c^{(\prime,*)+}+\eta(\eta^\prime)$			✓	✓	
$\Xi_{cc}^+ \to \varOmega_c^{(*)0} + K^{(*)+}$			1		
$\Xi_{cc}^+ \to \varLambda(\Sigma^{(*)0}) + D^{(*)+}$				✓	✓
$\Xi_{cc}^+ \to \varSigma^{(*)+} + D^{(*)0}$					1
$\Xi_{cc}^{+} \to \Xi^{(*)0} + D_s^{(*)+}$					✓
$\Omega_{cc}^+ \to \Omega_c^{(*)+} + \pi^+(\rho^+)$	✓				
$\Omega_{cc}^+\to \Xi_c^{(\prime,*)+} + \bar K^{(*)0}$		1		✓	
$\Omega_{cc}^{+} \to \Xi^{(*)0} + D^{(*)+}$				✓	

sizable partial widths in many cases.

- Unstable two-body decay products can decay strongly or radiatively, which leads to multiple final states for experimental detection.
- The observed  $\Xi_{cc}^{++} \to \Lambda_c^+ K^- \pi^+ \pi^+$  decay by LHCb experiment [132] is predicted and interpreted as two-body  $\Xi_{cc}^{++} \to \Sigma_c^{++} \bar{K}^{*0}$ , followed by  $\Sigma^{++} \to \Lambda_c^+ \pi^+$  and  $\bar{K}^{*0} \to K^- \pi^+$  decay [133-134]. The observed  $\Xi_{cc}^{++} \to \Xi_c^+ \pi^+$  and partially reconstructed  $\Xi_{cc}^{++} \to \Xi_c^{\prime+} \pi^+$  and  $\Xi_{cc}^{++} \to \Xi_c^+ \rho^+$  decay [135-136] are consistent with theoretical predictions.

# 1.3.2 Experimental status of doubly charmed baryons

Many experimental programs have been launched to search for the doubly charmed baryons, since the observation of  $B_c^+$  meson has demonstrated the accessibility of hadrons with open double heavy flavours in modern facilities. These experimental expeditions are summarised in Fig. 1.19 and will be discussed in details below. For completeness, searches for doubly heavy baryons such as  $\Xi_{bc}$  are also included in the plot. The config-

Table 1.7	Partial decay widths	of nonleptonic	decays of $\Xi_{aa}^{++}$	barvon in unit of	of $10^{-14}$ GeV.
			cc c	- · · · J · · · · · · ·	

Channels	Ref. [122]	Ref. [128]	Ref. [123]	Ref. [127]	Ref. [131]	Ref. [129]	Ref. [130]
$\Xi_{cc}^{++}  o \Xi_c^+ \pi^+$	15.7			1.8	1.8	18.3	
$\Xi_{cc}^{++}\to\Xi_c^+\rho^+$	30.3	41.1		6.3			
$\Xi_{cc}^{++}\to\Xi_c^{\prime+}\pi^+$	11.0		7.8	8.2	12.0	12.1	
$\Xi_{cc}^{++}\to\Xi_c^{\prime+}\rho^+$	41.2	42.5	41.4	42.7			
$\Xi_{cc}^{++}\to \varSigma_c^{++}\bar K^0$			3.2		3.5	0.5	
$\Xi_{cc}^{++}\to \varSigma_c^{++}\bar K^{*0}$		13.9	14.4				
$\Xi_{cc}^{++}\to\Xi_c^{*+}\pi^+$	2.2		1.6				
$\Xi_{cc}^{++}\to\Xi_c^{*+}\rho^+$	4.7		11.5				
$\Xi_{cc}^{++}\to \varSigma_c^{*++}\bar K^0$			0.6				
$\Xi_{cc}^{++}\to \varSigma_c^{*++} \bar K^{*0}$			4.2				
$\Xi_{cc}^{++}\to \varSigma^+ D^+$							0.8
$\Xi_{cc}^{++} \to \Sigma^+ D^{*+}$							4.1

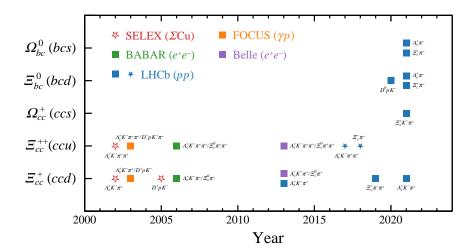


Figure 1.19 Experimental searches for doubly heavy baryons. Null results are labelled with squares. Claims of observation are labelled with states.

uration of experiments involved is shown in Table 1.10.

**SELEX experiment.** SELEX experiment, a charm hadroproduction experiment at Fermilab with configuration shown in Table 1.10, claimed an observation of doubly charmed baryon  $\Xi_{cc}^+$  in the  $\Lambda_c^+ K^- \pi^+$  decay mode [137]. An excess of 15.9 events were observed with a local statistical significance of 6.3 $\sigma$ . The observed mass of the state is 3519±1 MeV with a mass resolution of 3 MeV. The lifetime of the state is less than 33 fs at 90% confidence level. About 20% of the  $\Lambda_c^+$  baryon in the sample are produced by  $\Xi_{cc}^+$  decay.

Table 1.8 Partial decay widths of nonleptonic decays of  $\Xi_{cc}^+$  baryon in unit of  $10^{-14}$  GeV.

Channels	Ref. [122]	Ref. [128]	Ref. [131]	Ref. [129]	Ref. [130]
$\Xi_{cc}^+  o \Xi_c^0 \pi^+$	15.6		56.2	20.4	
$\Xi_{cc}^+ \to \Xi_c^0 \rho^+$	29.9	38.3			
$\Xi_{cc}^+\to\Xi_c^{\prime0}\pi^+$	10.9		22.7	13.4	
$\Xi_{cc}^+\to\Xi_c^{\prime0}\rho^+$	41.0	47.7			
$\Xi_{cc}^+\to\Xi_c^+\pi^0$			34.8	4.8	
$\Xi_{cc}^+ \to \Xi_c^+ \rho^0$		18.2			
$\varXi_{cc}^{+} \to \varXi_{c}^{+} \eta$			61.1		
$\Xi_{cc}^+\to\Xi_c^{\prime+}\pi^0$			2.5	0.5	
$\Xi_{cc}^+ \to \Xi_c^{\prime+} \rho^0$		6.1			
$\Xi_{cc}^+ \to \Xi_c^{\prime+} \eta$			0.7	0.8	
$\Xi_{cc}^+ \to \Lambda_c^+ \bar K^0$			4.5	0.5	
$\Xi_{cc}^+ \to \Lambda_c^+ \bar{K}^{*0}$		7.1			
$\Xi_{cc}^+\to \varSigma_c^+\bar K^0$			5.6	2.2	
$\Xi_{cc}^+\to \varSigma_c^+\bar K^{*0}$		8.4			
$\Xi_{cc}^+\to\Xi_c^{*0}\pi^+$	2.2				
$\Xi_{cc}^+ \to \Xi_c^{*0} \rho^+$	4.7				
$\varXi_{cc}^+ \to \Lambda D^+$					0.6
$\varXi_{cc}^+ \to \varLambda D^{*+}$					18.2
$\Xi_{cc}^+ \to \Sigma^0 D^+$					0.6
$\Xi_{cc}^+\to \varSigma^0 D^{*+}$					21.7

SELEX reported confirmation of this state in the  $pD^+K^-$  decay mode [138], with 5.6 events of a local statistical significance of 4.8 $\sigma$ . In conference proceedings [139-140], SELEX also reported a family of doubly charmed baryon  $\Xi_{cc}^{++}$  in the  $\Lambda_c^+K^-\pi^+\pi^+$  decay mode,  $\Xi_{cc}^{++}$ (3460),  $\Xi_{cc}^{++}$ (3452),  $\Xi_{cc}^{++}$ (3541), and  $\Xi_{cc}^{++}$ (3780).

These claims receive critical comments from the theory community [141]. The arguments are summarised below:

- The state  $\Xi_{cc}^+(3520)$  has extremely exotic characteristics if interpreted as the doubly charmed baryon  $\Xi_{cc}^+$ . The measured lifetime is too short and comparable with detector time resolution. The estimated production cross-section is too large in a fixed target experiment.
- The interpretation of associate charm production can not be ruled out with sufficient evidence.

#### **CHAPTER 1 INTRODUCTION**

Table 1.9	Partial decay	widths of nonle	ptonic decays of	of $\Omega^+$ baryon	in unit of $10^{-14}$	GeV.
			F	- (:(: : ) -		

Channels	Ref. [122]	Ref. [128]	Ref. [123]	Ref. [127]	Ref. [131]	Ref. [129]	Ref. [130]
$\Omega_{cc}^+ \to \Omega_c^0 \pi^+$	21.8		15.8		20.4	22.3	
$\Omega_{cc}^+ \to \Omega_c^0 \rho^+$	82.7	87.5	82.9				
$\varOmega_{cc}^+\to \varXi_c^+ \bar K^0$				9.5	5.9	0.8	
$\varOmega_{cc}^+\to \varXi_c^+ \bar K^{*0}$		13.8		6.2			
$\varOmega_{cc}^+\to \varXi_c^{\prime+} \bar K^0$			1.7	1.5	1.5	1.2	
$\Omega_{cc}^+ \to \Xi_c^{\prime+} \bar{K}^{*0}$		26.4	7.5	7.4			
$\Omega_{cc}^+ \to \Omega_c^{*0} \pi^+$	4.3		3.1				
$\Omega_{cc}^+ \to \Omega_c^{*0} \rho^+$	9.5		22.3				
$\Omega_{cc}^+\to \Xi_c^{*+} \bar K^0$			0.3				
$\varOmega_{cc}^+ \to \varXi_c^{*+} \bar{K}^{*0}$			2.1				
$\varOmega_{cc}^+\to \Xi^0 D^+$							1.9
$\Omega_{cc}^+ \to \Xi^0 D^{*+}$							5.0

Table 1.10 Experiments involved in searches for doubly charmed baryons.

Experiments	Collision	Energy	Statistics
SELEX	$\Sigma$ , $\pi$ , or $p$ beam Cu or diamond target	600 GeV beam	$15 \times 10^9$ inelastic interactions
FOCUS	$\gamma p$ collision	$\sqrt{s} = 200 \text{GeV}$	10 <sup>6</sup> charmed baryons
BaBar	$e^+e^-$ collision	$\sqrt{s} = 10.58 \text{GeV}$	$232 \text{ fb}^{-1}$
Belle	$e^+e^-$ collision	$\sqrt{s} = 10.59 \text{GeV}$	$980  {\rm fb}^{-1}$
LHCb	pp collision	$\sqrt{s} = 7, 8, 13 \text{TeV}$	$9  {\rm fb}^{-1}$

• The reported  $\Xi_{cc}^{++}$  and  $\Xi_{cc}^{+}$  states can not be treated as isospin partners.

It is also noticed that the evaluation of signal significance by SELEX dose not take into account the Look Elsewhere Effect [142], which states that the statistical significance of an observation increases due to the large parameter space searched. After LEE correction, the signal significance is reduced below  $5\sigma$ .

**FOCUS experiment.** FOCUS experiment, a photoproduction experiment with configuration shown in Table 1.10, searched for low lying doubly charmed baryon states in 21 possible decay modes [143]. No evidence was observed in the range of 3.4 to 4.0 GeV, including the region explored by the SELEX experiment.

**B factories. B** factory experiments BaBar and Belle also searched for doubly charmed baryons  $\Xi_{cc}^+$  in the  $\Lambda_c^+ K^- \pi^+$  and  $\Xi_c^0 \pi^+$  decay modes, and doubly charmed baryons  $\Xi_{cc}^{++}$  in the  $\Lambda_c^+ K^- \pi^+ \pi^+$  and  $\Xi_c^0 \pi^+ \pi^+$  decay modes [144-145]. No significant signals were observed in all decay modes.

**LHCb experiment.** In 2013, LHCb experiment reported a search for the  $\Xi_{cc}^+ \to \Lambda_c^+ K^- \pi^+$  decay with pp collision data at center-of-mass energy of 7 TeV, corresponding to an integrated luminosity of 0.65 fb<sup>-1</sup> [146]. No significant signal was found in the mass range 3300–3800 MeV. the ratio of the  $\Xi_{cc}^+$  production cross-section times branching fraction to that of the  $\Lambda_c^+$  was found to be less than  $1.5 \times 10^{-2}$  for a lifetime of 100 fs at 95% confidence level.

Later in 2017, LHCb experiment reported the observation of a highly significant structure, identified as doubly charmed baryon  $\Xi_{cc}^{++}$ , in the  $\Lambda_c^+ K^- \pi^+ \pi^+$  decay mode, with pp collision data center-of-mass energy of 13 TeV, corresponding to an integrated luminosity of 1.7 fb<sup>-1</sup> [132]. The  $\Xi_{cc}^{++}$  mass is determined to be 3621.40  $\pm$  0.72  $\pm$  0.27  $\pm$  0.14 MeV, where the uncertainty is due to statistical, systematic, and the limited knowledge of the  $\Lambda_c^+$  mass. The structure is confirmed in the data collected at center-of-mass energy of 8 TeV. This observation is soon confirmed in the  $\Xi_c^+ \pi^+$  decay mode [135], while no signifiant signal was observed in the  $D^+ p K^- \pi^+$  decay mode [147]. The  $\Xi_{cc}^{++}$  state reported by LHCb experiment can not be the isospin partner of the SELEX  $\Xi_{cc}^+$ (3520) state due the large mass difference.

The properties of  $\Xi_{cc}^{++}$  baryons were measured soon after its discovery. The  $\Xi_{cc}^{++}$  lifetime has been measured to be  $0.256_{-0.022}^{+0.024}(stat) \pm 0.014(syst)$  ps [148], which establishes the weakly decaying nature of the  $\Xi_{cc}^{++}$  baryon. The production cross-section times the branching fraction of  $\Xi_{cc}^{++} \to \Lambda_c^+ K^- \pi^+ \pi^+$  decay is measured with regard to prompt  $\Lambda_c^+$  production cross-section to be  $(2.22 \pm 0.27 \pm 0.29) \times 10^{-4}$  in the fiducial region of  $4 < p_T < 15$  GeV and 2.0 < y < 4.5 in pp collisions at center-of-mass energy of 13 TeV, where the uncertainty is due to statistical and systematic.

In summary, the  $\Xi_{cc}^{++}$  baryon is still the only well-established one of the three doubly charmed baryons. Its properties have been measured extensively with good precision. Based on the known properties of  $\Xi_{cc}^{++}$  baryon and the large data sets collected by the LHCb experiment during Run 1 and Run 2 of the LHC, it is desirable to launch search programs for other doubly charmed baryons, especially the  $\Xi_{cc}^{+}$  baryon.

This thesis reports the measurement of lifetimes of  $\Omega_c^0$  and  $\Xi_c^0$  baryons [149] and

#### CHAPTER 1 INTRODUCTION

the search for doubly charmed baryon  $\Xi_{cc}^+$  [150]. The theoretical motivations and experimental status are reviewed in this Chapter. The experimental facilities and techniques are introduced in Chapter 2. Data analysis of these measurements are discussed in detail in Chapter 3 and 4, with dedicated discussions of the implications of the results. The summary and prospects are presented in Chapter 5.

## **CHAPTER 2 EXPERIMENTAL FACILITIES**

Measurements reporeted in this thesis are performed with data collected by the LHCb detector at the Large Hadron Collider (LHC). We first introduce the LHC, the particle accelatrator that produce charmed baryuons abundantly, in Sec. 2.1. Then the LHCb experiment, which detect and analyze the produced charmed abryons, is desribed in Sec. 2.2. We will focus on most relevant aspects of these broad topics, instead of aiming at a comprehnesive introcustion.

## 2.1 Large Hadron Collider

The Large Hadron Collider beauty (LHCb) experiment detects collisions of particle bunches provided by the Large Hadron Collider (LHC), the most powerful tool for Particle Physics research in the world. The LHC also hosts large-scale experiments A Toroidal LHC Apparatus (ATLAS), the Compact Muon Solenoid (CMS), and A Large Ion Collider Experiment (ALICE). The ATLAS and CMS are general-purposed detectors focusing on measurements of the Higgs boson and searches for new physics beyond the Standard Model in a direct approach [151-152]. The ALICE detector studies quark-gluon plasma by measuring lead-ion collision [153]. The description in this section is based on the LHC Design Report [154-156] and its abridged version in Ref. [157] unless otherwise stated.

The Large Hadron Collider (LHC) is a two-ring-superconducting-hadron accelerator and collider installed in the 26.7 km tunnel at CERN near Geneva. It is designed to collide proton beams with a centre-of-mass energy of 14 TeV and an unprecedented luminosity of  $10^{34}$  cm<sup>-2</sup> s<sup>-1</sup>. It can also collide heavy (Pb) ions with an energy of 2.8 TeV per nucleon and a peak luminosity of  $10^{27}$  cm<sup>-2</sup> s<sup>-1</sup>. The LHC has two rings with counter-rotating beams because it is a particle-particle collider, unlike particle-antiparticle colliders that can have both beams sharing the same phase space in a single ring. The peak beam energy depends on the integrated dipole field around the storage ring, which implies the use of superconducting magnet technology. The LHC beam parameters at collision are shown in Table 2.1.

**Machine layout.** The basic layout of the LHC is illustrated in Figure 2.1. The LHC has eight arcs and eight straight sections. The arcs contain the dipole bending magnets, while

Table 2.1 LHC beam parameters at collision.

Parameters	pp collision	PbPb collision
Energy per nucleon [TeV]	7	2.76
Luminosity [ cm <sup>-2</sup> s <sup>-1</sup> ]	$10^{34}$	$10^{27}$
Number of bunches	2808	592
Bunch spacing [ns]	24.95	
Intensity per bunch	$1.15 \times 10^{11}$	$7.0\times10^7$

each straight section can serve as an experimental or utility insertion. There four straight sections that have collision points. The two high luminosity experimental insertions are located at diametrically opposite straight sections: the ATLAS experiment is located at Point 1 and the CMS experiment at Point 5. Two more experimental insertions are located at Point 2 and Point 8: the ALICE experiment is located at Point 2 and the LHCb experiment at Point 8. Points 2 and 8 also include the injection systems for Beam 1 and Beam 2, respectively. The remaining four straight sections do not have beam crossings. Insertions at Points 3 and 7 each contain two collimation systems. The insertion at Point 4 contains two RF systems. The straight section at Point 6 contains the beam dump insertion.

**Magnets.** There is a large variety of magnets in the LHC, including dipoles, which bending particles in the arcs, quadrupoles, which focus the beam size at the collision points, and other correction magnets such as sextupoles, octupoles, decapoles *etc.*. LHC magnet system makes use of the well-proven technology based on NbTi Rutherford cables, cools the magnets to a temperature below 2 *K* using superfluid helium, and operates at fields above 8 T.

**Vacuum systems.** The LHC has three vacuum systems: the insulation vacuum for cryomagnets, the insulation vacuum for the helium distribution line, and the beam vacuum (ultrahigh vacuum) to avoid beam collisions with gas molecules.

**Cavities.** The LHC cavities keep particle bunches tightly bunched to ensure high luminosity at collision points and deliver radiofrequency (RF) power to the beam.

**Injection chain.** The accelerator complex at CERN is a succession of machines with increasing higher energies, as illustrated in Fig. 2.2. The LHC is the last element of this

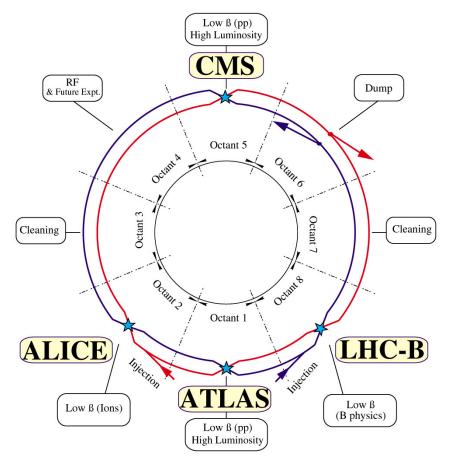


Figure 2.1 Schematic layout of the LHC.

chain. The injection chain of proton is

proton 
$$\xrightarrow{\text{LINAC 2}}$$
 50 MeV  $\xrightarrow{\text{BOOSTER}}$  1.4 GeV  $\xrightarrow{\text{PS}}$  25 GeV  $\xrightarrow{\text{SPS}}$  450 GeV  $\xrightarrow{\text{LHC}}$  6.5 TeV. (2.1)

The injection chain of lead ion is

lead ion 
$$\xrightarrow{\text{LEIR}}$$
 72 MeV/ $u \xrightarrow{\text{PS}}$  5.9 GeV/ $u \xrightarrow{\text{SPS}}$  177 GeV/ $u \xrightarrow{\text{LHC}}$  2.56 TeV/ $u$ . (2.2)

Here the energy achieved in Run 2 is quoted, which is slightly lower than the nominal value in design.

**Luminosity.** The number of events generated in the LHC collisions per second is given by

$$N_{\text{event}} = \mathcal{L} \times \sigma_{\text{event}},$$
 (2.3)

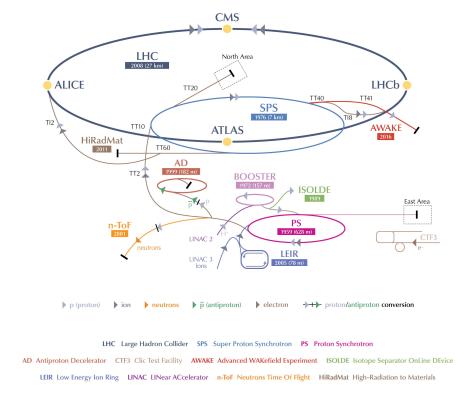


Figure 2.2 Accelerator complex at CERN.

where  $\sigma_{\text{event}}$  is the cross-section for the event under consideration and  $\mathcal{L}$  is the instantaneous luminosity. The machine luminosity depends on beam parameters via

$$\mathcal{L} = \frac{N_p^2 N_b f_{\text{rev}} \gamma_r}{4\pi \varepsilon_n \beta^*} \times F,$$
(2.4)

where  $N_p$  is the number of particles per bunch,  $N_b$  is the number of bunches per beam,  $f_{\rm rev}$  is the revolution frequency,  $\gamma_r$  is the relativistic gamma factor,  $\varepsilon_n$  is the normalised transverse beam emittance,  $\beta^*$  is the beta function at the collision point, and F is the geometric luminosity reduction factor due to nonzero crossing angle and bunch length. The luminosity in the LHC is not constant over a physics run, but decays due to the degradation of intensities and emittances of the circulating beams. The luminosity half-life is estimated to be  $\tau_L \approx 15 \ h$ . The turnaround time, the time between the end of a luminosity run and a new beam at top energy, is approximately 7 hours. The integrated luminosity over one run yields

$$\mathcal{L}_{\text{int}} = \mathcal{L}_0 \times \tau_L \times \left[ 1 - \exp(-T_{\text{run}}/\tau_L) \right], \tag{2.5}$$

where  $T_{\text{run}}$  is the total length of the luminosity run. The overall collider efficiency depends on the ratio of the length of the run to the average turnaround time, and is optimised to be  $80 \text{ fb}^{-1}$  with a run time of 12 hours and a turnaround time of 7 hours.

Run	Periods	Energy [TeV]	Luminosity (ATLAS, CMS) [fb <sup>-1</sup> ]
Run 1	2011-2012	7, 8	30
LS1	2013-2014		
Run 2	2015-2018	13	190
LS2	2019-2021		
Run 3	2022-2024	13-14	350
LS3	2025-2026		

3000

14

2027-2040

Run 4-5

Table 2.2 LHC baseline plan for the next decade and beyond.

**Operation and plan.** The present LHC baseline programme is shown schematically in Table 2.2. During Run 1 the LHC was operated with 50 ns bunch spacing. After the consolidation measures in Long Shutdown 1 (LS1), the LHC was operated in Run 2 at 13 TeV centre-of-mass energy. The bunch spacing was reduced to 25 ns, the design value, and the luminosity was progressively increased, attaining the nominal design luminosity of  $10^{34}$  cm<sup>-2</sup> s<sup>-1</sup> on 26 June 2016. A peak luminosity of  $2 \times 10^{34}$  cm<sup>-2</sup> s<sup>-1</sup> was achieved in 2018 thanks to the small emittances of the beam delivered by the injectors and to a smaller than design  $\beta^*$  value. At present (2022), the LHC is in Long Shutdown 2 (LS2) during which further consolidation measures are being pursued and should enable the LHC to reach its nominal design beam energy of 7 TeV [158]. In the Run 3 period from 2022 to 2024, the LHC aims to further increase the integrated luminosity total: the present goal is to reach 350 fb<sup>-1</sup> by the end of Run 3, well above the initial LHC goal of about 300 fb<sup>-1</sup>. The LHC will need a major upgrade in the 2020s to a) extend its operability by another decade or more; b) increase its collision rate and thus the delivered integrated luminosity [158]. The machine configuration of the upgrade is referred to as the highluminosity LHC (HL-LHC), with the following targets:

- A peak luminosity of  $5 \times 10^{34}$  cm<sup>-2</sup> s<sup>-1</sup> with levelling operation;
- An integrated luminosity of 250 fb<sup>-1</sup> per year, with the goal of 3000 fb<sup>-1</sup> in the 12 years or so after the upgrade.

## 2.2 LHCb experiment

The LHCb experiment is a dedicated heavy-flavour physics experiment at the LHC. Its main goal is to search for indirect evidence of new physics in *CP* violation and rare

decays of beauty and charm hadrons [159]. During Run 1 and 2, the LHCb physics programme was extended to electroweak, QCD and even heavy-ion physics [160]. Thanks to efficient charged particle tracking and dedicated triggers for lepton, hadron and photon signatures, LHCb has accumulated the world's largest sample of exclusive charm and beauty decays with high data quality. This has enabled the LHCb collaboration to publish a wide range of physics results [161], establishing the unique and essential role of LHCb, both as a heavy flavour experiment and as a general-purpose detector in the forward region.

As a heavy flavour experiment, LHCb has various advantages over the  $e^+e^-$  B factories, including a larger cross-section (roughly five order of magnitude higher  $b\bar{b}$  production cross-section), a larger boost of the produced heavy-flavour hadrons, and that all species of beauty hadrons are produced. On the other hand, the less attractive features of the LHC environment include the increased background levels, inherent to hadronic collisions, and the lack of kinematic constraint of the initial state.

Several key features of the detector are important to perform heavy flavour programs:

- Excellent vertex resolution, which is required to measure impact parameters and to achieve a good decay-time resolution. It is essential, for example, to resolve neutral meson oscillations and to reject various sources of background.
- Good momentum and invariant mass resolution, which is important to minimise combinatorial background and to resolve heavy-flavour decays with similar topologies.
- *Charged particle identification*, which is essential, for instance, to isolate suppressed decays and for *b*-quark flavour tagging.
- Detection of photons, which allows the reconstruction of rare radiative decays and more common decays with a  $\pi^0$  or an  $\eta$  meson in the final state.
- *High-bandwidth data acquisition system* and *robust and selective trigger system*, which allows to benefit from the high event rate at the LHC.

In this section, we introduce the LHCb detector and its performance in Run 1 and 2 to demonstrate how the above features are achieved, with an emphasis on aspects that are closely related to nonleptonic decays of charmed baryons into charged final states.

#### 2.2.1 LHCb detector

The description in this section is mainly based on the LHCb detector at LHC [159] unless otherwise stated.

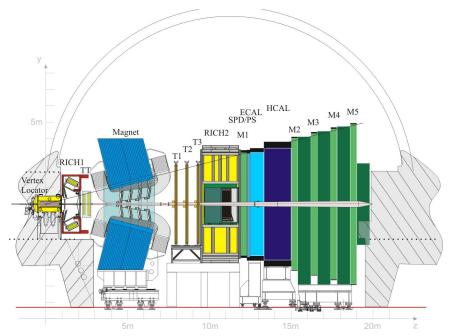


Figure 2.3 View of the LHCb detector.

**Layout.** LHCb detector is a single-arm spectrometer with a forward angular coverage from approximately 15 mrad to 300 (250) mrad in the bending, or horizontal (nonbending, or vertical) plane, corresponding to a rapidity range of  $2 < \eta < 5$ . A schematic view of the detector is shown in Fig. 2.3. The design of the detector geometry is motivated by the fact that production of the b- and  $\bar{b}$ -hadrons is highly correlated, such that they are predominantly produced in the same forward or backward cone. This is illustrated by a simulation of  $b\bar{b}$  production is shown in Fig. 2.4, performed using PYTHIA8 and CTEQ6 NLO [162]. About 25%  $b\bar{b}$  quark pairs are covered with only 2.4% of the  $4\pi$  solid angle, which is an optimal solution within a given budget. A right-handed coordinate system is defined with z along the beam axis into the detector, y vertical and x horizontal. Cylindrical polar coordinates  $(r, \Phi, z)$  are also used when appropriate.

**Magnet.** The spectrometer magnet is a warm dipole magnet providing an integrated field of about 4 Tm. It deflects charged particles in the horizontal plane to allow for the momentum measurement of charged particles.

**Tracking system.** The tracking system consists of the VErtex LOcator (VELO), the Tracker Turicensis (TT) and tracking stations T1-T3, which are situated at the interaction region inside a vacuum tank, upstream of the dipole magnet, and downstream of the magnet, respectively. A minimum momentum of 1.5 GeV is required for charged particles to

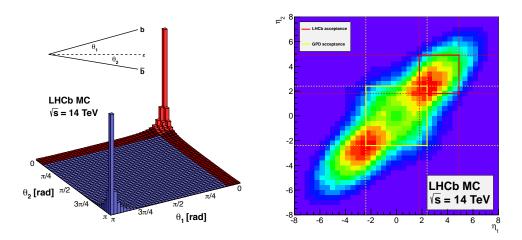


Figure 2.4 Production of  $b\bar{b}$  quark pairs as a function of (left) angles w.r.t the beam and (right) rapidities, simulated with PYTHIA8 and CTEQ6 NLO [162]. In the right plot, The coverage of a general-purpose detector (GPD) is shown as comparison.

reach the tracking stations T1-T3.

The VELO contains 42 silicon modules arranged along the beam. Each module provides a measurement of the r and  $\Phi$  coordinates. The pitch within a module is 38  $\mu$ m at the inner radius of 8.2 mm, and increases linearly to 102  $\mu$ m at the outer radius of 42 mm.

The TT and the region close to the beam-pipe (Inner Tracker, IT) of stations T1-T3 use silicon microstrip sensors with a strip pitch of  $183 \, \mu m$  and  $198 \, \mu m$ , respectively. The TT is about  $150 \, cm$  wide and  $130 \, cm$  high. The IT covers a  $120 \, cm$  wide and  $40 \, cm$  high cross-shaped region in the centre of the three tracking stations T1-T3.

The Outer Tracker, the outer parts of stations T1-T3, is a drift-tube gas detector consisting of approximately 200 gas-tight straw-tube modules with drift-time read-out.

Charged hadron identification. Charged hadron identification is achieved by two Ring Imaging Cherenkov detectors (RICH1 and RICH2) read out by Hybrid Photon Detectors (HPDs). The upstream detector, RICH1, uses Aerogel and  $C_4F_{10}$  as radiators. It covers the low momentum charged particle range from about 2 to 60 GeV and the LHCb acceptance from  $\pm 25$  mrad to  $\pm 300$  mrad (horizontal) and  $\pm 250$  mrad (vertical). The downstream detector, RICH2, uses  $CF_4$  as radiator, covering the high momentum range from about 15 GeV to 100 GeV and a limited angular acceptance of  $\pm 15$  mrad to  $\pm 120$  mrad (horizontal) and  $\pm 100$  mrad (vertical).

Calorimeter system. The calorimeter system consists of a Scintillating Pad Detector (SPD), a Preshower (PS), a shashlik type electromagnetic calorimeter (ECAL) and a

hadronic calorimeter (HCAL). It provides the identification of electrons, photons and hadrons, measures their energies and positions, and selects candidates with high transverse energy at the hardware trigger level (L0).

The SPD improves the separation of electrons and photons. The ECAL is made of a sampling scintillator/lead structure with a total thickness of 25 radiation lengths  $(X_0)$ . A segmentation into three different sections has been chosen. The calorimeter system has a variable lateral segmentation in order to take into account the variation in hit density of two orders of magnitude over the calorimeter surface.

The hadron calorimeter (HCAL) is a sampling device made from iron and scintillating tiles, as absorber and active material, respectively. Given the dimensions of the hadronic showers, the HCAL is segmented into two zones with different lateral dimensions. The thickness of the HCAL is limited to 5.6 nuclear interaction lengths ( $\lambda_i$ ) due to space constraints.

**Muon detection system.** The muon detection system provides muon identification and contributes to the L0 trigger. It is composed of five stations (M1-M5) of rectangular shape equipped predominantly with Multi Wire Proportional Chambers (MWPC). In the highest rate region of M1, triple Gas Electron Multiplier (GEM) detectors are used. Station M1 is placed in front of the calorimeters and is used to improve the  $p_T$  measurement in the trigger. Stations M2-M5 are placed downstream of the calorimeters and are interleaved with 80 cm thick iron absorbers to select penetrating muons. The minimum momentum that a muon traverses the five stations is approximately 6 GeV.

**Trigger system.** The trigger system consists of two levels. The schematic trigger diagrams for Run 1 and 2 are shown in Fig. 2.5.

The first level, L0, is implemented in hardware and is designed to reduce the event rate from the nominal LHC bunch crossing rate of 40 MHz to a maximum of 1 MHz. Trigger selections are made based on the deposit of several GeV of transverse energy in the Calorimeters or the Muon System by charged hadrons (L0Hadron), muons (L0DiMuon), electrons (L0Electron) or photons (L0Photon). While this provides high efficiencies on dimuon events, it typically removes half of the fully hadronic signal decays.

The complete detector is then read out and the data is sent to the second level, the High Level Trigger (HLT), which is a software trigger implemented on the Event Filter Farm (EFF). The EFF consists of approximately 1700 nodes, 800 of which were added

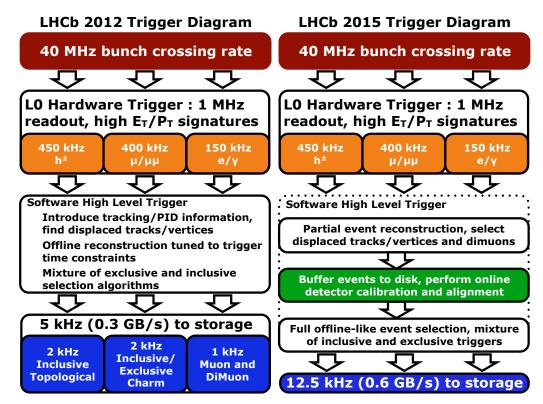


Figure 2.5 Trigger diagrams for (left) 2012 and (right) 2015 data taking, representative of Run 1 and 2, respectively.

for Run 2, with 27000 physical cores. The HLT is subdivided in two stages, HLT1 and HLT2.

In Run 1, HLT1 reconstructs particles in the VELO and determines the position of the PV in the event. HLT1 selects events with at least one track which satisfies minimum requirements in IP, p,  $p_T$ , and track quality. It reduces the rate to a sufficiently low level to allow forward tracking of all VELO tracks. HLT2 searches for secondary vertices, and applies decay length and mass requirements to reduce the rate to the level at which the events can be written to storage. Reconstructions performed at HLT are called online reconstruction. After the HLT, events are stored and later reconstructed with a more accurate alignment and calibration of the sub-detectors, referred to as offline reconstruction. The trigger reduced the rate of events to be saved for physics analysis to 5 kHz.

During Run 2, the increased EFF capacity and improvements in the software allowed the offline reconstruction to be performed in the HLT. HLT1 reconstructs the trajectories of charged particles traversing the full LHCb tracking system with a  $p_{\rm T}$  larger than 500 MeV. In addition, a precise reconstruction of the PV is performed. Unlike in Run 1, the full event reconstruction with offline quality is performed at HLT2, using the real-time calibration and alignment performed between HLT1 and HLT2. This reduces the sys-

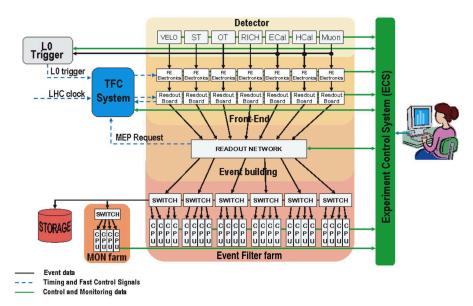


Figure 2.6 The general architecture of the LHCb online system.

tematic uncertainties due to the difference between online and offline reconstructed and makes it possible to use trigger output directly for physics analyses. Selections in HLT2 include both inclusive selections, which require the presence of heavy flavour decay signatures such as a displaced multibody vertex or a high transverse momentum lepton, and exclusive selections, which fully reconstruct signal decays. Most events selected by the charm trigger were persisted in a reduced format, referred to as Turbo, which contains information related only to the reconstructed physics objects, such as four momenta and decay vertex positions, as well as some event summary information [163]. This reduces the average event size and enables a broader physics programme, such as the studies of doubly charmed baryons, within the limitation of available computational resources of the bandwidth. Events are written to offline storage from HLT2 at a rate of around 12.5 kHz.

**Online system.** The online system consists of three components: the Data Acquisition (DAQ) system, the Timing and Fast Control (TFC) system, and the Experiment Control System (ECS). Its task is to ensure the transfer of data from the front-end electronics to permanent storage. This includes the movement of the data, the configuration and monitoring of all operational parameters as well as environmental parameters, and that all detector channels are properly synchronized with the LHC clock. The general architecture of the LHCb online system is shown in Fig. 2.6.

Table 2.3 Operation	n conditions	of the LHCb	detector.
---------------------	--------------	-------------	-----------

Periods	Instantaneous lumi. [cm <sup>-2</sup> s <sup>-1</sup> ]	Integrated lumi. [fb <sup>-1</sup> ]	$\sqrt{s}$ [TeV]	Average pile-up
2010	$1.5 \times 10^{32}$	0.04	7	2.5
2011	$3.5 \times 10^{32}$	1.11	7	1.8
2012	$4.0 \times 10^{32}$	2.08	8	2.0
2015	$4.0 \times 10^{32}$	0.33	13	1.0
2016	$4.0 \times 10^{32}$	1.67	13	1.0
2017	$4.0 \times 10^{32}$	1.71	13	1.0
2018	$4.0 \times 10^{32}$	2.19	13	1.0

Operation. LHCb recorded *pp* collision data for physics analyses during Run 1 and 2 of the LHC. The instantaneous and integrated luminosity, the center-of-mass energy, and the pile-up, defined as the average number of visible interactions per beam-beam crossing, are summarised in Table 2.3. It was demonstrated that the trigger and reconstruction work efficiently under harsh conditions with increased detector occupancy due to 2.5 pile-up. A luminosity levelling procedure was introduced in 2011 at the LHCb interaction point. The instantaneous luminosity could be kept stable to within about 5% during a fill, by adjusting the transverse overlap of the beams at LHCb. This procedure minimises the effect of luminosity decay: the same trigger configuration during a fill can be maintained and systematic uncertainties are reduced due to changes in the detector occupancy. Luminosity calibrations were carried out with the LHCb detector for the various centre-of-mass energy, with both the "van der Meer scan" and "beam-gas imaging" luminosity calibration methods [164]. The precision is about 2%.

The LHCb magnet deflects positive and negative particles in opposite directions in the x-z plane. Consequently, a difference in performance of the left and right sides of the detector leads to charge detection asymmetries. To reduce this effect, the direction of the magnetic field is changed regularly and then combining data sets with different polarity to cancel left-right asymmetries. The samples with different B field directions are referred to as MagDown and MagUp.

#### 2.2.2 LHCb simulation

Simulation of signal decays is required to develop the event selection criteria and to model the effects of the detector acceptance and the imposed selection requirements. In

the simulation, pp collisions are generated using Pythia [64,165] with a specific LHCb configuration [166]. Due to the small production cross-section of the doubly charmed baryons, a dedicated generator, GenXicc2.0 [62], is used to simulate the production  $\Xi_{cc}$  baryon in order to reduce the computing time and provide a more realistic kinematic description of doubly charmed baryons. Decays of unstable particles are described by EvtGen [167], in which final-state radiation is generated using Photos [168]. The interaction of the generated particles with the detector, and its response, are implemented using the Geant4 toolkit [169-170] as described in Ref. [171]. In some cases, to accelerate the simulation the underlying pp interaction is reused multiple times, with an independently generated signal decay for each [172].

#### 2.2.3 LHCb data flow

Collisions recorded by the LHCb detector go through a specific data flow designed to maximise the data-taking efficiency and data quality. To illustrate how real and simulated data are processed to produce physics results, a schematic chart of the data flow is shown in Fig. 2.7. The data flow consists of several steps, each one being controlled by an "application" that processes the data event-by-event, using the data from the previous step as input and creating the results ready for the next. These steps are as follows:

- *Trigger.* Real or simulated data are filtered by the trigger, which is described in Sec. 2.2.1. The application responsible for the software trigger is Moore.
- *Reconstruction*. Triggered, raw data are reconstructed to transform the detector hits into physics objects such as tracks and clusters. This is done by the Brunel application. In Run 2, in addition to the offline reconstruction, part of the data are directly saved for physics analyses thanks to the improved quality of online reconstruction, as discussed in Sec. 2.2.1.
- *Stripping*. The reconstructed data are further filtered centrally through a set of selections called the Stripping, controlled by the DaVinci application.
- Ntuple making. The stripped data now have manageable sample sizes and are further processed for specific physics analyses.

Different applications are based on the same software framework, Gaudi, which is designed to enable flexible and efficient event-data processing [173]. The Gaudi framework separates between data and algorithms and adopts a data-store-centered architectural style. It encapsulates user code in a few specific places, with well defined and generic component interfaces. The standard standard components are re-used wherever possible. The

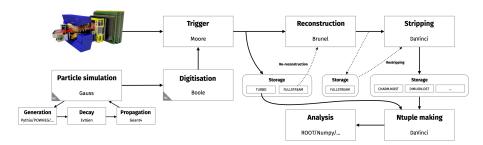


Figure 2.7 The LHCb data flow.

basic ideas of the Gaudi software architecture are following:

- Event Loop. A global EventLoop allows users to process events one by one.
- Transient Event Store. A per-event file system contains different data objects.
- *Algorithms*. An Algorithm is a C++ class that allows users to perform a certain function for each event and is inserted into the EventLoop.
- *Tools*. Tools are common functions that algorithms make use of to achieve certain functionality.
- Options. An option allows users to configure properties of Algorithms and Tools.

Computing resources for the storage, distribution and analysis of the data is provided by the Worldwide LHC Computing Grid (WLCG). WLCG combines the computing resources of about 900 000 computer cores from over 170 sites in 42 countries, producing a massive distributed computing infrastructure. The LHCb Event Filter Farm is also used to complement offline data processing outside the data-taking period.

#### 2.2.4 Performance of the LHCb detector

The description in this section is mainly based on the detector performance in Run 1 [160] and 2 [174] unless otherwise stated.

Charged track reconstruction. The trajectories of charged particles inside the LHCb detector are reconstructed using the tracking system introduced in Sec. 2.2.1. Their momentum can be determined by determining the deflection of the charged particles after traversing the magnetic field. The high spatial resolution of the VELO enables a precise determination of the particle's flight direction close to the primary interaction point, resulting in a good vertex resolution.

The hit efficiencies in general exceeds 99%, which are more than sufficient for an efficient track reconstruction. Hit occupancies are well within acceptable levels and only mildly affecting the track finding efficiency and rate of wrongly reconstructed trajectories.

The trajectories of the charged particles traversing the tracking system, referred to as tracks for short, are reconstructed from hits in the VELO, TT, IT and OT detectors. The following track types are defined as illustrated in Fig. 2.8:

- Long tracks traverse the full tracking system and have the most precise momentum estimate and therefore are the most important set of tracks for physics analyses. All final-state tracks used in measurements of this thesis are long tracks.
- Upstream tracks pass only through the VELO and TT stations.
- Downstream tracks pass only through the TT and T stations. They are used for the reconstruction of long lived particles that decay outside the VELO acceptance, such as  $K_s^0$  and  $\Lambda$ .
- *VELO tracks* pass only through the VELO. They are typically large-angle or backward tracks, which are useful for the primary vertex (PV) reconstruction.
- *T tracks* pass only through the T stations. They are typically produced in secondary interactions.

The long track reconstruction starts with a search in the VELO for straight line trajectories. Then information from the downstream tracking stations are added to these VELO tracks. Hits in the TT consistent with the extrapolated trajectories of each track are added to improve their momentum determination. Finally, the tracks are fitted using a Kalman fitter, taking into account multiple scattering and correcting for energy loss due to ionisation. The  $\chi^2$  per degree of freedom of the fit,  $\chi^2_{trk}$ /ndf, is used to determined the quality of the reconstructed track.

The tracking efficiency is defined as the probability that the trajectory of a charged particle that has passed through the full tracking system is reconstructed. The efficiency is measured using a tag-and-probe technique with  $Jh\psi \to \mu^+\mu^-$  decays [175]. The tracking efficiency is shown Fig. 2.9 as a function of the momentum, p, of the pseudorapidity,  $\eta$ . It can be seen that the average efficiency is above 96%, expect for very low and high momentum tracks in 2015. The performance in the 2012 data is slightly worse, which is partially due to the higher hit multiplicity at the higher centre-of-mass energy. A small reduction in the track reconstruction efficiency is observed in 2015, which is due to the fact that the OT has a readout window which is larger than 25 ns and therefore is prone to spillover effects when reducing the bunch spacing from 50 ns to 25 ns. The track reconstruction efficiency is well reproduced in simulated events. The small residual discrepancy is corrected by assigning per-event weight to simulated events according to the efficiency ratio

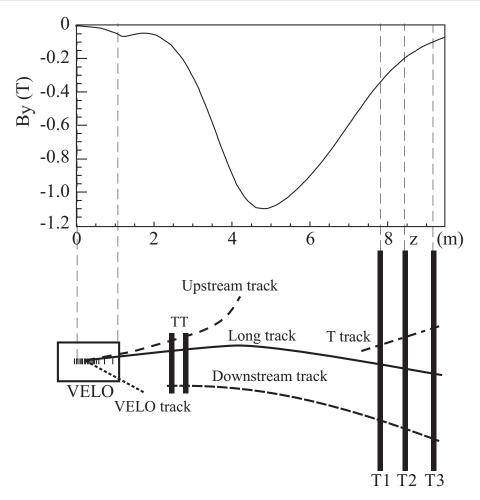


Figure 2.8 Illustration of the various track types. For reference the main B-field component ( $B_y$ ) is plotted above as a function of the z coordinate.

of data to simulation.

The momentum resolution for long tracks in data is extracted using  $J/\psi \rightarrow \mu^+\mu^-$  decays. Figure 2.10 shows the relative momentum resolution,  $\delta p/p$ , as a function of the momentum, p. The momentum resolution is about 5 per mille for particles below 20 GeV, rising to about 8 per mille for particles around 100 GeV.

The momentum scale is calibrated using large samples of  $Jh\psi \rightarrow \mu^{+}\mu^{-}$  and  $B^{+} \rightarrow Jh\psi K^{+}$  decays. A systematic uncertainty of 0.03% on the momentum scale is obtained by comparing the measured masses of known resonances with the world average values.

The alignment of the LHCb tracking detector uses information a) from optical and mechanical surveys and b) from reconstructed charged particle trajectories. The tracking alignment is updated routinely during the data-taking.

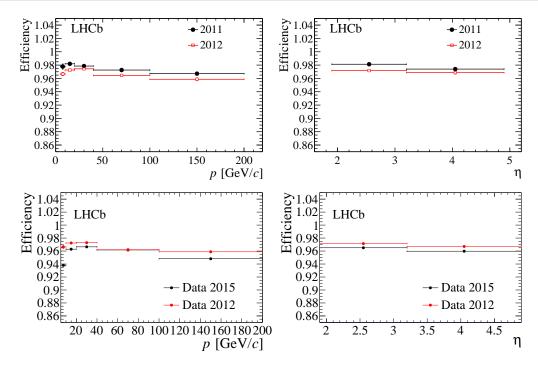


Figure 2.9 Comparison of track reconstruction efficiency in (top) 2011 and 2012, and (bottom) 2012 and 2015, as a function of the (left) momentum and (right) pseudorapidity.

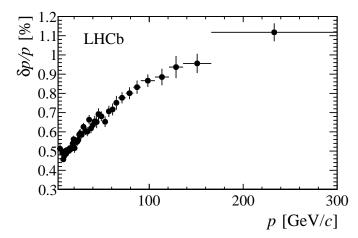


Figure 2.10 Relative momentum resolution versus momentum for long tracks in data.

**Primary vertex reconstruction.** The PV resolution is measured by comparing two independent measurements of the vertex position in the same event. The PV resolution is strongly correlated to the number of tracks, the track multiplicity, in the vertex. The resolution in the x and y direction is shown in Fig. 2.11. A PV with 25 tracks has a resolution of 13  $\mu$ m in the x and y coordinates and 71  $\mu$ m in the z coordinate.

The impact parameter (IP) of a track is defined as its distance from the primary vertex at its point of closest approach to the primary vertex. Particles produced from the decay of long-lived charm or beauty hadrons tend to have larger IP than those of particles produced

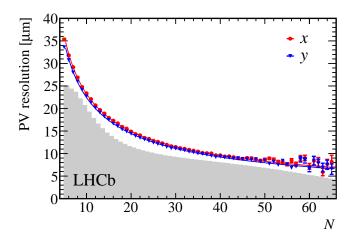


Figure 2.11 The primary vertex resolution as a function of track multiplicity. The x (red) and y (blue) resolutions are separately shown. The superimposed histogram shows the distribution of track multiplicity per reconstructed primary vertex for all events that pass the HLT.

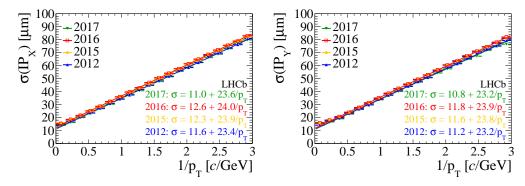


Figure 2.12 Resolution of the (left) x and (right) y components of the impact parameter.

at the primary vertex. The  $\chi_{\rm IP}^2$  is defined as the difference in the vertex-fit  $\chi^2$  of a given PV reconstructed with and without the track under consideration. Selections on IP and  $\chi_{\rm IP}^2$  are extensively used in LHCb analyses, and also measurements in this thesis, to reduce the contamination from prompt backgrounds. The IP resolution is governed by three main effects: a) multiple scattering of particles by the detector material; b) the resolution on the position of hits in the detector associated with tracks; c) and the distance of extrapolation of a track between its first hit in the detector and the interaction point. The VELO is designed to minimise these effects. The minimisation of these factors is achieved in the design of the VELO. The resolution of the projection of the IP vector in the transverse plane is shown in Fig. 2.12. The linear dependence on  $1/p_{\rm T}$  is due to multiple scattering and the geometry of the vertex detector.

**Decay-time resolution.** The distance between the production and secondary decay vertices of long lived hadrons is used to reconstruct the particle's decay time. This is required

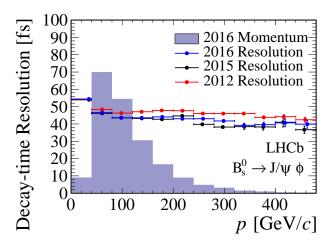


Figure 2.13 Decay time resolution for  $B_s^0 \to Jh\psi \phi$  decays as a function of momentum.

for lifetime measurements and for resolving flavour oscillations in time-dependent CP violation measurements. The reconstructed decay time in the rest frame of the decaying particle can be expressed in terms of the reconstructed decay length l, the momentum p and mass m of the particle in the LHCb frame as

$$t = \frac{m \times l}{p}. (2.6)$$

The decay time uncertainty can be expressed in terms of the decay length uncertainty  $\sigma_l$  and the momentum uncertainty  $\sigma_p$  as

$$\sigma_t^2 = \left(\frac{m}{p}\right)^2 \sigma_l^2 + \left(\frac{t}{p}\right)^2 \sigma_p^2,\tag{2.7}$$

which is dominated by the  $\sigma_l$  within a few times the B meson lifetime. The decay time resolution depends on the topology of the decay. The decay time resolution for  $B_s^0 \to Jh\psi \,\phi$  decays as a function of momentum is shown in Fig. 2.13. It is noticed that the decay time resolution is essentially independent of the B momentum. This is because that the larger the momentum is, the smaller the opening angle, and hence the larger the uncertainty on the position of the vertex in the direction of the boost. The average resolution is about 45 fs for a 4-track vertex.

**Charged particle identification.** The RICH detectors provide the main discrimination between deuterons, kaons, pions, and protons. For each track the likelihood that it is an electron, muon, pion, kaon or proton is computed. The performance of the RICH particle identification is determined using the tag-and-probe technique, where exclusive decays are reconstructed purely from kinematic selections. The following decays,  $K_S^0 \to \pi^+\pi^-$ ,  $\Lambda \to p\pi^-$ , and  $D^{*+} \to D^0 (\to K^-\pi^+)\pi^+$ , are used as control decay modes. The kaon

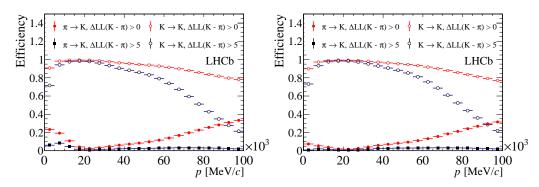


Figure 2.14 The kaon efficiency (kaons identified as kaons) and pion misidentification (pions misidentified as kaons) fraction as a function of momentum for (left) 2012 and (right) 2016 data taking.

efficiency (kaons identified as kaons) and pion misidentification (pions misidentified as kaons) fraction, as a function of momentum, are shown in Fig. 2.14. Averaging over the momentum range 2-100 GeV, it can be found that the kaon efficiency to be  $\sim 95\%$  with a pion misidentification rate of  $\sim 10\%$ .

The simulation of the PID response of the detector is non-trivial, which involves modelling of the kinematics of the particle, the occupancy of the detectors, and the experimental conditions such as alignments, temperature, and gas pressure. These considerations have motivated the use of data-driven techniques, implemented in the *PIDCalib* package, to measure the efficiency of selections involving particle identification, similar to the "tag-and-probe" approach used for the measurement of tracking efficiency [176].

**Trigger.** The trigger performance is evaluated relative to offline reconstruction and selections, and thus contains only the additional inefficiency due to a) simplifications used in the trigger, b) possible alignment inaccuracies, c) worse resolution than the offline reconstruction, and d) tighter requirements imposed by rate and/or processing time limitations. Representative channels that cover a majority of LHCb physics analyses are used. The trigger performance on each channel is measured by determining the number of signals using fits to the invariant mass distributions, hence avoiding any background contamination. The term "signal" refers to a combination of tracks that form the reconstructed and selected beauty or charm hadron candidate. To determine the trigger efficiency, trigger objects are associated to signal tracks by requiring an overlap of clusters or hits in subdetectors between the two.

A triggered event is classified as TOS (Trigger on Signal), if the trigger objects that are associated with the signal are sufficient to trigger the event. A triggered event is

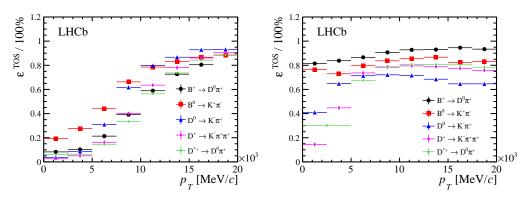


Figure 2.15 Trigger efficiency for (left) L0Hadron and (right) HLT1 as a function of  $p_T$  in Run 1.

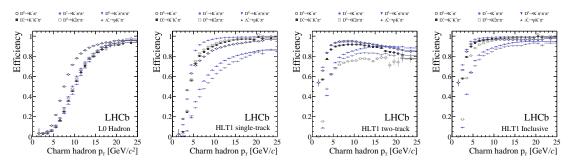


Figure 2.16 Trigger efficiency for (left) L0Hadron and (right) HLT1 as a function of  $p_T$  in Run 2. Three plots on the right corresponding to Hlt1TrackMVA, Hlt1TwoTrackMVA, and inclusive HLT1.

classified as TIS (Trigger Independent of Signal), if it could have been triggered by those trigger objects that are not associated to the signal. A triggered event (TIS||TOS) can be classified as both TIS and TOS (TIS&TOS). The efficiency to trigger an event on the signal or to trigger an event independently of the signal can be evaluated as

$$\varepsilon^{\text{TOS}} \equiv \frac{N^{\text{TOS}}}{N^{\text{Total}}} = \frac{N^{\text{TIS\&TOS}}}{N^{\text{TIS}}},$$

$$\varepsilon^{\text{TIS}} \equiv \frac{N^{\text{TIS}}}{N^{\text{Total}}} = \frac{N^{\text{TIS\&TOS}}}{N^{\text{TOS}}},$$
(2.8)

where  $N^{\text{Total}}$  is the total number of signals. A factorisation of TIS and TOS efficiency,  $\varepsilon^{\text{TIS\&TOS}} = \varepsilon^{\text{TOS}} \times \varepsilon^{\text{TOS}}$ , is assumed in the above calculation. The total trigger efficiency can therefore be evaluated as

$$\varepsilon^{\text{TIS}||\text{TOS}} = \frac{N^{\text{Trigger}}}{N^{\text{TIS}}} \times \varepsilon^{\text{TIS}} = \frac{N^{\text{Trigger}}}{N^{\text{TOS}}} \times \varepsilon^{\text{TOS}}, \tag{2.9}$$

where  $N^{\text{Trigger}}$  is the number of triggered (TIS||TOS) event.

The L0 trigger L0Hadron selects heavy flavour decays with hadrons in the final state. The performance of L0Hadron in Run 1 and Run 2 are shown in the left plot of Fig. 2.15 and Fig. 2.16, respectively. Signals with fewer final state tracks have a higher efficiency.

Table 2.4 Requirements of Hlt1TrackAllL0 trigger line in Run 1.

Variable	Cut
Track IP [mm]	> 0.1
Number VELO hits/track	> 9
Number missed VELO hits/track	< 3
Number OT + IT $\times$ 2 hits/track	> 16
Track $\chi_{\text{IP}}^2$	> 16
Track $p_{\mathrm{T}}$ [ GeV ]	> 1.7
Track p [ GeV ]	> 10
$\chi^2_{\rm trk}$ /ndf	< 2.5

The inclusive HLT1 track triggers are designed to select hadron decays which are significantly displaced from a PV. In Run 1, Hlt1TrackAllL0 line requires one track with sufficient IP and  $p_T$ , as shown in Table 2.4. In Run 2, the single track line was reoptimised to be Hlt1TrackMVA. In addition, a new displaced two-track vertex trigger, Hlt1TwoTrackMVA, was developed. Both lines start by selecting good quality tracks that are inconsistent with originating from the PV. The single-track trigger then selects events based on a hyperbolic requirement in the 2D plane of the track displacement and  $p_T$ . The two-track displaced vertex trigger selects events based on a MatrixNet classifier whose input variables are the vertex-fit quality, the vertex displacement, the scalar sum of the  $p_T$ of the two tracks, and the displacement of the tracks making up the vertex. The selection criteria are shown in Table 2.5. The performance of inclusive HLT1 track triggers in Run 1 and Run 2 are shown in the right plot of Fig. 2.15 and Fig. 2.16, respectively. In general, inclusive HLT1 track lines provide an efficient trigger for all heavy flavour decays with a significant flight distance from their PV. Decays with larger flight distance have larger trigger efficiency. The Run 2 two-track line is more efficient at low  $p_T$ , whereas the single track line performs best at high  $p_T$ . Their combination provides high efficiency over the full  $p_{\rm T}$  range.

 $Table \ 2.5 \quad Requirements \ of \ \mbox{Hlt1(Two)TrackMVA trigger line in } Run \ 2.$ 

Trigger	Selections ( $p_T$ in GeV/ $c$ )
	$p > 5 \mathrm{GeV}$
	$p_{\rm T} > 1  {\rm GeV}$
	$\chi^2_{\rm trk}/{\rm ndf} < 2.5$
Hlt1TrackMVA	Prob(ghost) < 0.2
	$\log \chi_{\text{IP}}^2 > \left(\frac{1}{(p_{\text{T}}-1)^2} + \frac{1.1 \times (25 - p_{\text{T}})}{25} + \log(7.4)\right) \text{ for } p_{\text{T}} \in (1, 25) \text{ GeV}$
	$\chi_{\rm IP}^2 > 7.4 \text{ for } p_{\rm T} > 25 \text{GeV}$
	$p > 5 \mathrm{GeV}$
	$p_{\rm T} > 0.6  {\rm GeV}$
	$\chi^2_{\rm trk}$ /ndf < 2.5
Hlt1TwoTrackMVA	Prob(ghost) < 0.2
	$\chi_{\mathrm{IP}}^2 > 4$
	$\chi_{\rm vtx}^2$ /ndf < 10
	$M(\pi\pi) > 1 \text{ GeV}$

# CHAPTER 3 MEASUREMENT OF $\varOmega_c^0$ AND $\varXi_c^0$ LIFETIMES

This chapter reports a measurement of the lifetimes of  $\Omega_c^0(css)$  and  $\Xi_c^0(csd)$  baryon [149]. This measurement makes use of signals produced directly from pp collisions, different from the previous LHCb measurement using signals from semileptonic beauty baryon decays. An overview of the data analysis strategy and method is presented in Sec. 3.1. Event selection is discussed in Sec. 3.2. Determination of the yield and estimation of the efficiency are described in Sec. 3.3 and Sec. 3.4, respectively. Extraction of lifetimes is shown in Sec. 3.5, followed by a discussion of systematic uncertainties in Sec. 3.6. To conclude, the result and its interpretation are presented in Sec. 3.7.

## 3.1 Analysis overview

In this analysis, the lifetimes of  $\Omega_c^0$  and  $\Xi_c^0$  baryon are measured, using signals produced directly from pp collisions, referred to as the "prompt" signals. This sample is different from signals from semileptonic beauty baryon decays, referred to as the "secondary" signals. A schematic view of the decay topology is shown in Fig. 3.1. Both  $\Omega_c^0$  and  $\Xi_c^0$  baryon are reconstructed through the  $pK^-K^-\pi^+$  final state. The data sample was collected by the LHCb detector during 2016-2018, corresponding to an integrated luminosity of 5.4 fb<sup>-1</sup>, as detailed in Appendix A. The four-body  $D^0$  decay  $D^{*+} \to D^0 (\to K^-K^+\pi^-\pi^+)\pi^+$  is used as the control mode in order to a) reduce systematic uncertainties, b) estimate sources of systematic uncertainties, and c) validate the analysis procedure.

The advantage of using prompt signals include the large production cross-section relative to that of the secondary production, and the better primary vertex (PV) resolution relative to that of the secondary vertex (SV). Each advantage comes with its challenge. The benefit of a large signal yield is reduced by the high combinatorial background level due to random combination of tracks from PV. In addition, we need to discriminate between signals from PV and those from SV.

In general, the analysis procedure includes:

• Selection of signal decays. A multivariate analysis is used to suppress background besides the rectangular requirements.

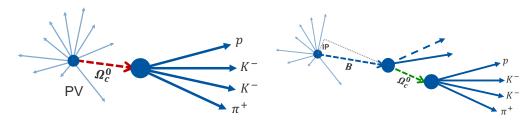


Figure 3.1 Schematic view of (left) prompt signal and (right) secondary signal.

- Determination of the prompt signal yield. A dedicated model is developed to obtain the prompt signal yields in the selected sample out of the contamination of combinatorial background and secondary signals. The invariant mass and the  $\log_{10}(\chi_{\text{IP}}^2)$  distributions are used to differentiate various components statistically.
- Estimation of selection efficiency. The selection requirement applied to suppress the background leads to a distortion of the decay-time distribution from an ideal exponential function. This deviation is modelled with simulation in order to obtain an unbiased estimation of the lifetime.
- Extraction of the lifetime with the least square fit.

Since we are measuring controversial quantities and in order to avoid experimentalists' subjective bias, the measured central values of  $\Omega_c^0$  and  $\Xi_c^0$  lifetimes were blinded with different random numbers uniformly distributed in [-100, 100] fs before the whole analysis procedure was carefully reviewed and finalised. The unblinding of the results was achieved by disabling the random numbers in the least square fit.

### 3.2 Event selection

The event reconstruction and selection are performed in a data flow consisting several steps, as introduced in Sec. 2.2.3. In this section, selection requirements at different steps are shown in detail. The online trigger selection has to make a comprise due to limited readout rate and storage bandwidth, while the offline selection can be implemented with more involved algorithms.

## 3.2.1 Trigger selection

Selection requirements in both the hardware and software level trigger are applied in order to reduce the sample size and improve the signal purity.

**L0 trigger.** To have a good estimation of L0 trigger efficiency, we require L0Hadron TOS (hTOS) on the  $\Omega_c^0$ ,  $\Xi_c^0$  and  $D^0$  candidates for corresponding decay modes. According to simulation, hTOSed prompt signals constitute around half of the total L0-triggered events.

**HLT1 trigger.** The HLT1 TOS requirement of Hlt1Track||Hlt1TwoTrack is applied to the  $\Omega_c^0$ ,  $\Xi_c^0$  and  $D^0$  candidates for corresponding decay modes, which is embedded in the signal HLT2 line. The HLT1 track lines and their performance are discussed in Sec. 2.2.4. According to simulation, for  $D^0$  prompt signals the ratio of Hlt1Track TOS only, Hlt1TwoTrack TOS only, and Hlt1Track&&Hlt1TwoTrack TOS is about 1:2:7. The ratio obtained from the fit to data is about 1:3:6, which is similar to the value from simulation.

**HLT2 trigger.** In HLT2 trigger, exclusive decays of  $\Omega_c^0$  and  $\Xi_c^0$  baryon are reconstructed in the  $pK^-K^-\pi^+$  final state with a set of rectangular requirements. The major selection requirements are summarised in Table 3.1 for signal modes and in Table 3.2 for the control mode. For the  $\Omega_c^0$  and  $\Xi_c^0$  signal mode, the signal candidate is reconstructed in three steps:

- 1. Selection of final-state tracks (DaughtersCuts). Each of the final-state particles is required to have a good track quality, a large transverse (p<sub>T</sub>) and total (p) momentum, and particle-identification information (DLL) consistent with the corresponding p, K<sup>-</sup>, or π<sup>+</sup> hypothesis. All final-state tracks are required to be inconsistent with originating from any PV. The PV associated to a single charged particle is defined to be the PV with the smallest χ<sub>IP</sub><sup>2</sup>. The χ<sub>IP</sub><sup>2</sup> is defined as the difference in the vertex-fit χ<sup>2</sup> (χ<sub>vtx</sub><sup>2</sup>) of a given PV reconstructed with and without the particle under consideration.
- 2. Requirement of the combination of tracks (CombinationCuts). The scalar sum and the maximum of the  $p_T$  of final-state tracks is required to be large. The maximum and second maximum  $\chi_{IP}^2$  of the final-state tracks is required to be large.
- 3. Requirement on the signal candidate (MotherCuts). Charmed hadron candidates are required to have a decay vertex with good quality that is displaced from its associated PV. The decay time is required to be larger than 0.1 ps. The angle between the reconstructed momentum vector of a charmed baryon candidate and the direction from its associated PV to its decay vertex, the direction angle (acos(DIRA)), is

Table 3.1 HLT2 selections for the  $\Omega_c^0$  and  $\Xi_c^0$  signal mode. Requirements shown in red are also applied to the control mode offline.

Items	Variables	Requirements
	$p_{ m T}$	> 0.5 GeV
	p	> 1 GeV
	$\chi^2_{ ext{IP}}$	> 4
DaughtersCuts	Proton $\mathrm{DLL}_{p\pi}$	> 10
	Proton $\mathrm{DLL}_{pK}$	> 5
	Kaon $\mathrm{DLL}_{K\pi}$	> 10
	Pion $\mathrm{DLL}_{K\pi}$	< 0
	$\Sigma p_{ m T}$	> 3 GeV
CombinationCuts	$Max(p_T)$	> 1 GeV
ComomationCuts	$Max(\chi_{IP}^2)$	> 8
	Second max( $\chi_{IP}^2$ )	> 6
	$\chi^2_{\rm vtx}$ /ndf	< 10
MotherCuts	Decay time	> 0.1 ps
Monicicuts	$\chi^2_{ m VD}$	> 10
	DIRA	> cos(0.01)

required to be small to suppress combinatorial background.

For the  $D^0$  control mode, similar requirements are applied in the above three steps. In addition, the distance of the closest approach (DOCA) between final-state tracks is required to be small for a good vertex quality. The  $\Omega_c^0$  and  $\Xi_c^0$  signal decays are filtered with the same selection, except for the window of the reconstructed mass. The requirements shown in red in Table 3.1 are also applied offline to the control mode, such that the effect of potential mismodelling of IP and decay-time resolution can be further reduced in the efficiency ratio of signal to control modes. To get an idea of the signal purity after the trigger selection, the invariant mass distributions of 2018 data samples after the trigger selection are shown in Fig. 3.2.

#### 3.2.2 Offline selection

The offline event selections are applied in several steps in order to further suppress the background.

Table 3.2 HLT2 selections for the  $D^0$  control mode. The index i refers to any of the first three daughters in the  $D^0$  decay.

DaughtersCuts $p > 1 \text{ GeV}$ $p > 1 \text{ GeV}$ $\chi_{\text{IP}}^2 > 3$ $\text{Kaon DLL}_{K\pi} > 5$ $\text{Pion DLL}_{K\pi} < 5$ $\sum p_{\text{T}} > 1.8 \text{ GeV}$ $p > 25 \text{ GeV}$ $DOCA(i, 4) < 100$ $\chi_{\text{DOCA}}^2(i, 4) < 10$ $p_{\text{T}} > 2 \text{ GeV}$ $p > 30 \text{ GeV}$ $\chi_{\text{vtx}}^2/\text{ndf} < 12$ $Decay time > 0.1 \text{ ps}$ $\chi_{\text{VD}}^2 > 25$ $DIRA > \cos(0.02)$ $p^* \text{ Cuts}$ $\chi_{\text{vtx}}^2/\text{ndf} < 15$	Items	Variables	Requirements
DaughtersCuts $\chi_{\mathrm{IP}}^{2} > 3$ $\mathrm{Kaon\ DLL}_{K\pi} > 5$ $\mathrm{Pion\ DLL}_{K\pi} < 5$ $\Sigma p_{\mathrm{T}} > 1.8\ \mathrm{GeV}$ $p > 25\ \mathrm{GeV}$ $\mathrm{DOCA}(\mathrm{i}, 4) < 100$ $\chi_{\mathrm{DOCA}}^{2}(\mathrm{i}, 4) < 10$ $p_{\mathrm{T}} > 2\ \mathrm{GeV}$ $p > 30\ \mathrm{GeV}$ $\chi_{\mathrm{vtx}}^{2}/\mathrm{ndf} < 12$ $\mathrm{Decay\ time} > 0.1\ \mathrm{ps}$ $\chi_{\mathrm{VD}}^{2} > 25$ $\mathrm{DIRA} > \cos(0.02)$ $D^{*}\ \mathrm{Cuts}$ $M(D^{*+}) - M(D^{0}) - M(\pi^{+}) \in [-5.0, 30.43]\ \mathrm{Month}$		$p_{\mathrm{T}}$	> 0.25 GeV
Kaon DLL $_{K\pi}$ > 5 Pion DLL $_{K\pi}$ < 5 $\Sigma p_{\mathrm{T}} > 1.8 \mathrm{GeV}$ $p > 25 \mathrm{GeV}$ DOCA(i, 4) < 100 $\chi^2_{\mathrm{DOCA}}(\mathrm{i}, 4) < 10$ $p_{\mathrm{T}} > 2 \mathrm{GeV}$ $p > 30 \mathrm{GeV}$ $\chi^2_{\mathrm{Vtx}}/\mathrm{ndf} < 12$ Decay time > 0.1 ps $\chi^2_{\mathrm{VD}} > 25$ DIRA > $\cos(0.02)$ $D^* \mathrm{Cuts}$ $\chi^2_{\mathrm{Vtx}}/\mathrm{ndf} < 15$ $\chi^2_{\mathrm{Vtx}}/\mathrm{ndf} < 15$ $\chi^2_{\mathrm{Vtx}}/\mathrm{ndf} < 15$ $\chi^2_{\mathrm{Vtx}}/\mathrm{ndf} < 15$		p	> 1 GeV
Pion DLL $_{K\pi}$ < 5 $\Sigma p_{\mathrm{T}} > 1.8 \mathrm{GeV}$ $p > 25 \mathrm{GeV}$ DOCA(i, 4) < 100 $\chi^2_{\mathrm{DOCA}}(\mathrm{i}, 4) < 10$ $p_{\mathrm{T}} > 2 \mathrm{GeV}$ $p > 30 \mathrm{GeV}$ $\chi^2_{\mathrm{vtx}}/\mathrm{ndf} < 12$ Decay time > 0.1 ps $\chi^2_{\mathrm{VD}} > 25$ DIRA > $\cos(0.02)$ $p^* \mathrm{Cuts}$ $\chi^2_{\mathrm{vtx}}/\mathrm{ndf} < 15$ $\chi^2_{\mathrm{vtx}}/\mathrm{ndf} < 15$	aughtersCuts	$\chi^2_{ ext{IP}}$	> 3
CombinationCuts $\begin{array}{cccccccccccccccccccccccccccccccccccc$		Kaon $\mathrm{DLL}_{K\pi}$	> 5
CombinationCuts $\begin{array}{cccccccccccccccccccccccccccccccccccc$		Pion $\mathrm{DLL}_{K\pi}$	< 5
DOCA(i, 4) < 100 $\chi^2_{\text{DOCA}}(i, 4) < 10$ $p_{\text{T}} > 2 \text{ GeV}$ $p > 30 \text{ GeV}$ $\chi^2_{\text{vtx}}/\text{ndf} < 12$ Decay time > 0.1 ps $\chi^2_{\text{VD}} > 25$ DIRA > $\cos(0.02)$ $D^* \text{ Cuts}$ $M(D^{*+}) - M(D^0) - M(\pi^+) \in [-5.0, 30.43] \text{ Mosc}$		$\Sigma p_{ m T}$	> 1.8 GeV
$\begin{array}{cccccccccccccccccccccccccccccccccccc$	mbinationCuta	p	> 25 GeV
$p_{\mathrm{T}} > 2 \mathrm{GeV}$ $p > 30 \mathrm{GeV}$ $\chi^2_{\mathrm{vtx}}/\mathrm{ndf} < 12$ $\mathrm{Decay \ time} > 0.1 \mathrm{ps}$ $\chi^2_{\mathrm{VD}} > 25$ $\mathrm{DIRA} > \cos(0.02)$ $D^* \mathrm{Cuts}$ $M(D^{*+}) - M(D^0) - M(\pi^+) \in [-5.0, 30.43] \mathrm{MeV}$	inomationcuts	DOCA(i, 4)	< 100
MotherCuts $p > 30 \text{ GeV}$ $\chi^2_{\text{vtx}}/\text{ndf} < 12$ Decay time $> 0.1 \text{ ps}$ $\chi^2_{\text{VD}} > 25$ DIRA $> \cos(0.02)$ $p^* \text{ Cuts}$ $M(D^{*+}) - M(D^0) - M(\pi^+) \in [-5.0, 30.43] \text{ Mostering Model}$		$\chi^2_{\mathrm{DOCA}}(\mathrm{i},4)$	< 10
MotherCuts $ \frac{\chi^2_{\text{vtx}}/\text{ndf}}{2} < 12 $ Decay time $> 0.1 \text{ ps}$ $ \chi^2_{\text{VD}} > 25 $ DIRA $> \cos(0.02)$ $ \frac{\chi^2_{\text{vtx}}/\text{ndf}}{2} < 15 $ $ M(D^{*+}) - M(D^0) - M(\pi^+) \in [-5.0, 30.43] \text{ Mosterior} $		$p_{ m T}$	> 2 GeV
MotherCuts $Decay time > 0.1 \text{ ps}$ $\chi^2_{\text{VD}} > 25$ $DIRA > \cos(0.02)$ $D^* \text{ Cuts}$ $\chi^2_{\text{vtx}}/\text{ndf} < 15$ $M(D^{*+}) - M(D^0) - M(\pi^+) \in [-5.0, 30.43] \text{ MotherCuts}$		p	> 30 GeV
Decay time > 0.1 ps $ \chi_{\text{VD}}^{2} > 25 $ DIRA > cos(0.02) $ \chi_{\text{vtx}}^{2}/\text{ndf} < 15 $ $ M(D^{*+}) - M(D^{0}) - M(\pi^{+}) \in [-5.0, 30.43] \text{ Most} $	Mother Cute	$\chi^2_{\rm vtx}$ /ndf	< 12
DIRA $> \cos(0.02)$ $\chi^{2}_{\text{vtx}}/\text{ndf} < 15$ $M(D^{*+}) - M(D^{0}) - M(\pi^{+}) \in [-5.0, 30.43] \text{ M}$	WioniciCuts	Decay time	> 0.1 ps
$\chi^2_{\text{vtx}}/\text{ndf} < 15$ $M(D^{*+}) - M(D^0) - M(\pi^+) \in [-5.0, 30.43] \text{MeV}$		$\chi^2_{ m VD}$	> 25
$M(D^{*+}) - M(D^0) - M(\pi^+) \in [-5.0, 30.43] \text{Most}$		DIRA	$> \cos(0.02)$
$M(D^{*+}) - M(D^0) - M(\pi^+) \in [-5.0, 30.43] \mathrm{Mg}$	D* C 4	$\chi^2_{\rm vtx}$ /ndf	< 15
25000 LIHCE 2018	D' Cuts	$M(D^{*+}) - M(D^0) - M(\pi^+)$	$\in [-5.0, 30.43] \text{MeV}$
2-5000 F LHCb 2018 A ] 2 con [ 1 HCb 2018 A			
2000	www.mm	35000 LHCb 2018 20000 LHCb 2018	90 600 LHC5 2018
35000 d 400	refresh	35000 - S	ad 400
1 200	ndudu	1	<sup>200</sup> E
2700 2750 2400 2450 2500 1850	2700	<u> </u>	

Figure 3.2 Invariant mass distribution of (left)  $\Omega_c^0$ , (middle)  $\Xi_c^0$ , and (right)  $D^0$  candidates in 2018 data samples after the trigger selection.

**Preselection.** After the trigger selection, loose preselections, with very high signal efficiency, are applied to both signal and control modes to reduce obvious backgrounds, as shown in Table. 3.3. These requirements reject candidates whose final-state tracks are too far away from PV and whose vertex quality is too poor. An additional mass window requirement of  $|M(D^{*+}) - M(D^0) - 146| < 6 \text{ MeV}$  is applied to  $D^0$  control mode to improve the signal purity.

Table 3.3 Offline preselection requirements, where  $H_c$  denotes either  $\Omega_c^0$ ,  $\Xi_c^0$  or  $D^0$  hadron.

Variables	Requirements
$- \ln \chi^2_{\rm FD}(H_c)$	< 9
$\ln \text{Sum}(\text{final state }\chi_{\text{IP}}^2)$	< 8
$\ln \text{Min}(\text{final state } \chi_{\text{IP}}^2)$	< 5
$\chi^2_{ m vtx}(H_c)$	< 20

**Multivariate analysis.** A multivariate classifier based on the Boosted Decision Tree (BDT) algorithm implemented in the TMVA toolkit [177-178] is trained to further suppress the combinatorial background. Simulated prompt  $\Omega_c^0$  decays with an input lifetime of 250 fs are used as the signal sample in the training. The  $\Omega_c^0$  data samples in the invariant mass sideband ([2620, 2670]  $\cup$  [2720, 2770] MeV) are used as the background sample. Eleven variables that show good discriminating power between signal and background candidates are used as training variables, including

- Topological variables:  $\chi^2_{\rm vtx}(\Omega_c^0)$ , DIRA of  $\Omega_c^0$ , natural log of the sum of  $\chi^2_{\rm IP}$  of four final-state tracks, and natural log of the minimum of  $\chi^2_{\rm IP}$  of four final-state tracks.
- Kinematic variables:  $p_T(\Omega_c^0)$ ,  $\eta(\Omega_c^0)$ ,  $p_T$  of the four final-state tracks, and minimum of the  $p_T$  of four final-state tracks.

Distributions of training variables for signal and background samples are shown in Fig. 3.3. Correlation matrices of signal and background samples are shown in Fig. 3.4. BDT responses of training and test samples are shown in Fig. 3.5.

Distributions of the BDT response for simulated  $\Omega_c^0$  sample and the background subtracted  $\Omega_c^0$  data sample are shown in the left plot in Fig. 3.6. Background subtraction is performed with the mass fit to the  $\Omega_c^0$  data sample before the BDT selection. The discrepancy of the responses between data and simulation is due to the discrepancy in some of the training variables. To improve the signal purity while not biasing the decay-time distribution, a loose BDT cut of -0.2 is applied to the  $\Omega_c^0$  signal mode. The same BDT selection is applied to the  $\Xi_c^0$  signal mode. No BDT selection is applied to the  $D^0$  control mode. The comparison of the BDT response for the  $\Xi_c^0$  signal mode is shown in the right plot in Fig. 3.6. The background-like tail in the left of the data distribution is due to the large secondary contributions in the  $\Xi_c^0$  mode. It should be noticed that we do not expect the distribution in simulation is the same as in data, as the input lifetime in simulation is not the same as the true value.

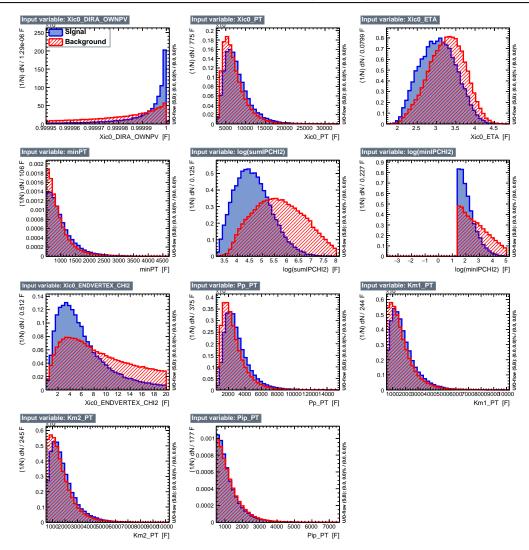


Figure 3.3 Distributions of training variables in 2016  $\Omega_c^0$  simulation (Signal) and  $\Omega_c^0$  mass-sideband data (Background).

**PID requirements.** Besides the PID selections applied in the trigger, further PID requirements are applied to both signal and control modes after the BDT selection, including

- DLL<sub> $p\pi$ </sub> > 15 and DLL<sub>pK</sub> > 5 for protons,
- DLL<sub> $K\pi$ </sub> > 13 for kaons,
- DLL $_{K\pi}$  < 0 for pions.

**Removal of track-clone candidates.** Track-clone candidates refer to those candidates in which at least one pair of final-state tracks are clones of each other. Two reconstructed tracks are clones of each other if they are reconstructed from a set of hits generated by one genuine track. Fig. 3.7 shows the distributions of log-sized min( $\theta_{i,j}$ ) for  $\Omega_c^0$  and  $\Xi_c^0$  2018 data, where min( $\theta_{i,j}$ ) for a given candidate is defined as the minimum of the angles

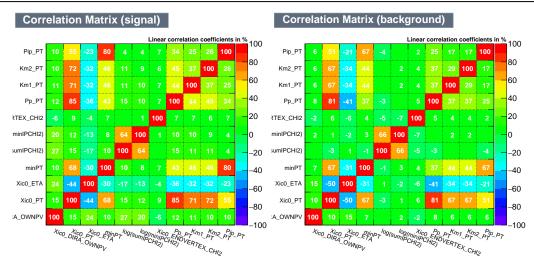


Figure 3.4 Correlation matrices of (left) signal and (right) background samples.

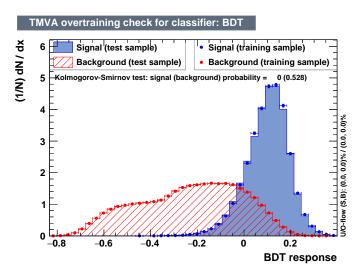


Figure 3.5 BDT responses of training and test samples.

between any pair of the four charged final-state tracks. It is found that the contribution of clones is at 10% level. A requirement of  $\min(\theta_{i,j}) > 0.5$  mrad (indicated in red dashed line in the figure) is applied to remove track-clone candidates with a signal efficiency close to 100%.

As an illustration of the signal purity, the invariant mass distributions of 2016 signal and control samples after all event selection criteria are shown in Fig. 3.8. The total signal yields (prompt and secondary signals combined) in the decay time range of [0.45, 2.00] ps are shown in Table 3.4. The time-integrated selection efficiency and the figure of merit  $(\frac{S}{\sqrt{S+B}})$  where S and B are calculated in 2.5 $\sigma$  region around the  $\Omega_c^0$  mass peak) after different selection stages for 2016  $\Omega_c^0$  data is shown in Table 3.5.

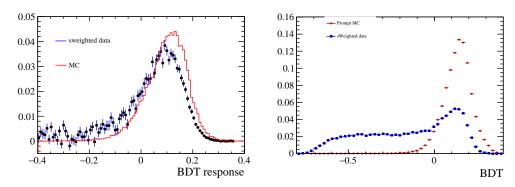


Figure 3.6 Distribution of BDT response for 2016 (left)  $\Omega_c^0$  simulated sample (with input lifetime of 250 fs) and the background subtracted data sample, and (right)  $\Xi_c^0$  simulated sample (with input lifetime of 250 fs) and the background subtracted  $\Xi_c^0$  data sample.

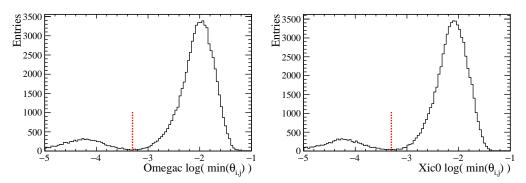


Figure 3.7 Distributions of log-sized  $\min(\theta_{i,j})$  in 2018 (left)  $\Omega_c^0$  and (right)  $\Xi_c^0$  data.

## 3.3 Determination of signal yield

Simultaneous fits of invariant mass and  $\log_{10}(\chi_{\rm IP}^2)$  are performed in decay-time bins to discriminate prompt signal decays from combinatorial backgrounds and from b-hadron decays. To estimate the signal yields as functions of the decay time, samples are separated into decay-time bins according to the binning scheme of

$$[0.45, 0.52, 0.57, 0.63, 0.69, 0.75, 0.81, 0.90, 1.05, 2.00]$$
 ps. (3.1)

The binning scheme is chosen to have a comparable prompt  $\Omega_c^0$  signal yield in each bin of the decay time. The choice of the lower boundary of the decay time region is to have

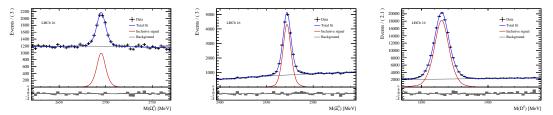


Figure 3.8 Invariant mass distributions of 2016 (left)  $\Omega_c^0$  (middle)  $\Xi_c^0$  and (right)  $D^0$  data samples after all event selection criteria.

Table 3.4 Total signal yields (prompt and secondary components combined) in the decay time range of [0.45, 2.00] ps after all event selection for signal and control modes.

	$\Omega_c^0  [\times 10^3]$	$\Xi_c^0  [\times 10^3]$	$D^0 [\times 10^3]$
2016	$4.3 \pm 0.2$	$16.6 \pm 0.2$	$126.9 \pm 0.5$
2017	$5.6 \pm 0.2$	$20.6 \pm 0.2$	$170.3 \pm 0.5$
2018	$5.9 \pm 0.2$	$23.0 \pm 0.2$	$182.2 \pm 0.6$

Table 3.5 Efficiency and figure of merit  $\frac{S}{\sqrt{S+B}}$  for 2016  $\Omega_c^0$  data after different selection stages.

Stages	Signal efficiency	$\frac{S}{\sqrt{S+B}}$
Pre-selection	94%	48.7
+ BDT> -0.2	93%	60.1
+ offline PID	80%	64.5

a relatively flat ratio of decay-time acceptance between the signal and control mode. The choice of the upper boundary is due to the decay of the yield. In the following subsections, the modelling of the invariant-mass,  $\log_{10}(\chi_{\text{IP}}^2)$  and their two-dimensional distribution is discussed in details.

#### 3.3.1 Invariant-mass model

**Signal model.** The invariant-mass distribution of the signal component is studied with fully simulated samples. The invariant-mass distributions of signal and control modes can be well described by the sum of a Gaussian distribution and a double-sided crystal ball (DSCB) function sharing the mean value  $m_0$  as

$$\mathcal{G}(x; m_0, \sigma_m) = f \times \mathcal{G}_{\text{Gaussian}}(x) + (1 - f) \times \mathcal{G}_{\text{DSCB}}(x), \tag{3.2}$$

where f is the fraction of the Gaussian and  $\sigma_m$  is the effective resolution. The definition of DCSB function can be found in Appendix B. The effective resolution is defined as  $\sigma_m = \sqrt{f \times \sigma_{m1}^2 + (1-f) \times \sigma_{m2}^2}$ , where  $\sigma_{m1}$  ( $\sigma_{m2}$ ) is the width of the Gaussian (DSCB). The width of the DSCB  $\sigma_{m2}$  is scaled from the width of the Gaussian  $\sigma_{m1}$  as  $r \equiv \sigma_{m2}/\sigma_{m1}$ . Due to its strong correlations with other parameters, the parameter f is fixed to 0.3 according to the studies in MC simulations. As an illustration, the fit results of 2016 simulated samples for the  $\Omega_c^0$  mode is shown in Fig. 3.9 The input lifetime of the simulation is 250 fs. It can be seen that the model can describe the data very well. The same degree of agreement is observed in the  $\Xi_c^0$  and  $D^0$  modes. Due to imperfect momentum scale and modelling

of detector resolution in simulation, the parameters  $m_0$  and  $\sigma_m$  are free when fitting to the data samples, while other parameters are fixed to values obtained from simulation as shown in Table 3.6. According to the fit results of the simulated samples, all parameters but  $m_0$  in the signal mass model are shared in decay-time bins.

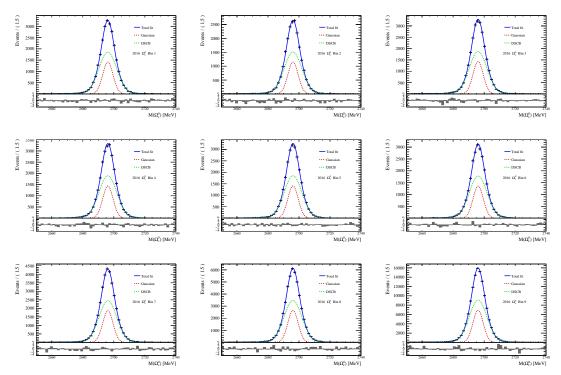


Figure 3.9 Invariant-mass distributions of  $\Omega_c^0$  signals in different decay-time bins in 2016 simulated samples.

**Background model.** Invariant-mass distribution of the background component can be well described by the first order Chebychev polynomial (namely a straight line)

$$C(x; c_{1,i}), \tag{3.3}$$

where i is the index of the decay-time bin under consideration. Parameters  $c_{1,i}$  are different and free to vary when fitting to the data samples.

## 3.3.2 Model of $\chi_{IP}^2$ distribution

**Signal model.** It is found that the  $\log_{10}(\chi_{\text{IP}}^2)$  distribution of simulated prompt and secondary signals can be described by Bukin function very well. As an illustration, the  $\log_{10}(\chi_{\text{IP}}^2)$  fit results of simulated prompt and secondary signals in 2016 samples for the  $\Omega_c^0$  mode are shown in Fig. 3.10. respectively. The input lifetime in the simulation is 250 fs. The same degree of agreement can be observed in the  $\Xi_c^0$  and  $D^0$  mode. The

Table 3.6 Results of the invariant-mass fit to simulated signal and control samples.

Mode	Parameter	2016	2017	2018
	r	$1.72 \pm 0.01$	$1.73 \pm 0.01$	$1.73 \pm 0.01$
	$a_L$	$2.20 \pm 0.02$	$2.16 \pm 0.02$	$2.19 \pm 0.02$
$\varOmega_c^0$	$a_R$	$2.16\pm0.02$	$2.15\pm0.02$	$2.11 \pm 0.03$
3 2 c	$n_L$	$1.49 \pm 0.05$	$1.62\pm0.05$	$1.56\pm0.06$
	$n_R$	$3.16 \pm 0.15$	$3.14 \pm 0.11$	$3.26 \pm 0.18$
	r	$1.68 \pm 0.03$	$1.73 \pm 0.02$	$1.75 \pm 0.02$
	$a_L$	$2.24 \pm 0.05$	$2.32 \pm 0.04$	$2.35 \pm 0.02$
$\Xi_c^0$	$a_R$	$1.80 \pm 0.04$	$2.05 \pm 0.03$	$2.06 \pm 0.03$
<i>□</i> <sub>c</sub>	$n_L$	$1.65 \pm 0.13$	$1.45\pm0.10$	$1.31 \pm 0.06$
	$n_R$	$5.37 \pm 0.46$	$3.29 \pm 0.20$	$3.11 \pm 0.20$
	r	1.71 ± 0.02	$1.75 \pm 0.04$	$1.72 \pm 0.01$
$D^0$	$a_L$	$2.13 \pm 0.02$	$2.14 \pm 0.03$	$2.11 \pm 0.02$
	$a_R$	$2.06 \pm 0.03$	$2.03 \pm 0.14$	$2.02 \pm 0.02$
	$n_L$	$1.56\pm0.07$	$1.56 \pm 0.09$	$1.60 \pm 0.05$
	$n_R$	$4.79 \pm 0.34$	$5.30 \pm 1.57$	$5.50 \pm 0.34$

parameters in different decay-time bins obtained by fitting simulated samples are shown in Fig. 3.11, 3.12, 3.13, and 3.14, for parameter  $\mu$ ,  $\sigma$ ,  $\xi$ ,  $\rho_1$ , and  $\rho_2$ , respectively. It can be seen that parameter  $\sigma$ ,  $\xi$ ,  $\rho_1$  and  $\rho_2$  are consistent in decay-time bins for both prompt and secondary signal decays.

**Background model.** The  $\log_{10}(\chi_{\mathrm{IP}}^2)$  distribution of the background component is also described by the Bukin function, whose parameters are obtained by fitting to the invariant mass sideband data in each decay-time bin and are fixed when fitting to data in the signal window. As an illustration, the fit results are shown for  $\Omega_c^0$  mode in 2016 data in Fig. 3.15. The same degree of agreement can be observed in the  $\Xi_c^0$  and  $D^0$  mode. For  $\Omega_c^0$  mode, a mixture of lower sideband [2695 – 75, 2695 – 50] MeV and upper sideband [2695 + 50, 2695 + 75] MeV/ $c^2$  is used. For  $\Xi_c^0$  mode, a mixture of lower sideband [2471 – 75, 2471 – 50] MeV and upper sideband [2471 + 50, 2471 + 75] MeV is used. For  $D^0$  mode, only upper sideband [1835 + 50, 1835 + 75] MeV is used to avoid partial reconstruction contributions in the lower sideband. A comparison of the background  $\log_{10}(\chi_{\mathrm{IP}}^2)$  distribution obtained from lower sideband, upper sideband and sWeighted background from invariant mass fit for  $D^0$  control mode has been performed. Good agreement between different samples is observed and the residual effect due to the mismodelling of the background shape is considered in the systematic uncertainty studies.

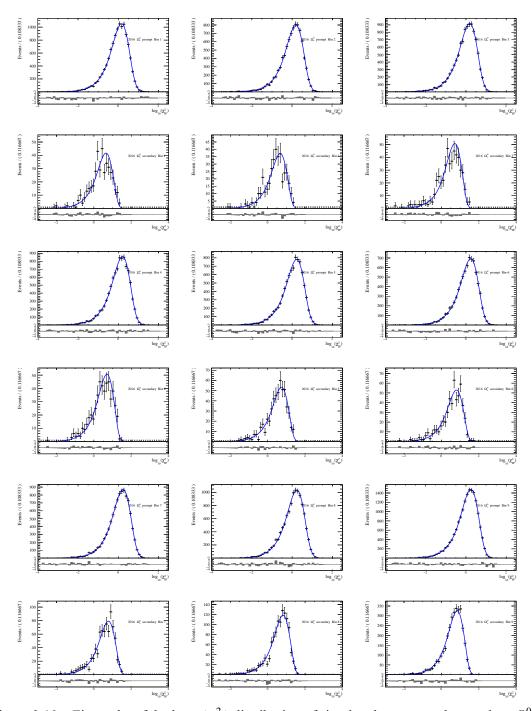


Figure 3.10 Fit results of the  $\log_{10}(\chi_{\text{IP}}^2)$  distribution of simulated prompt and secondary  $\Omega_c^0$  signals in 2016 sample.

**Study with**  $D^0$  **control mode.** Modelling of the signal and background  $\log_{10}(\chi_{\text{IP}}^2)$  distributions is validated with the  $D^0$  control mode. In this validation, parameter  $\mu$  in the prompt and secondary signal models is free to vary and different between decay-time bins, while other parameters are fixed to values obtained from simulation. It is found that good descriptions can be achieved in all decay-time bins, as shown in Fig. 3.16 for

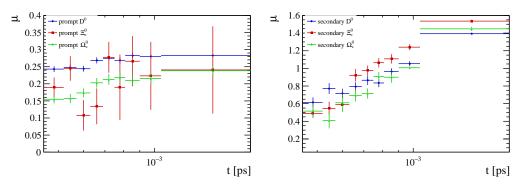


Figure 3.11 Parameter  $\mu$  in different decay-time bins obtained by fitting to 2016 simulated samples.

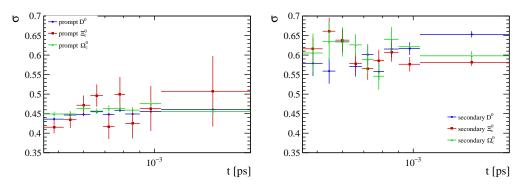


Figure 3.12 Parameter  $\sigma$  in different decay-time bins obtained by fitting to 2016 simulated samples.

the fit results of 2016  $D^0$  samples in 20 even decay-time bins in the decay-time range of [0.4, 2.4] fs. Parameter  $\mu$  of prompt and secondary components in different decay-time bins obtained from fits to the simulated sample and to the data sample are shown in Fig. 3.17. It can be seen that the values from fits to data is consistently larger than those from fits to simulation. This results mainly from the mismodelling of multiple scattering effects in simulation due to imprecise knowledge of the material budget in the detector. It is also noticed that the difference is similar between decay-time bins.

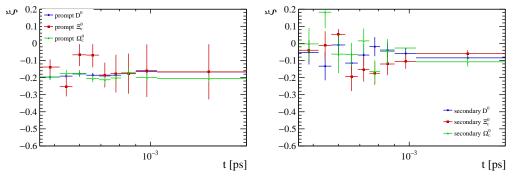


Figure 3.13 Parameter  $\xi$  in different decay-time bins obtained by fitting to 2016 simulated samples.

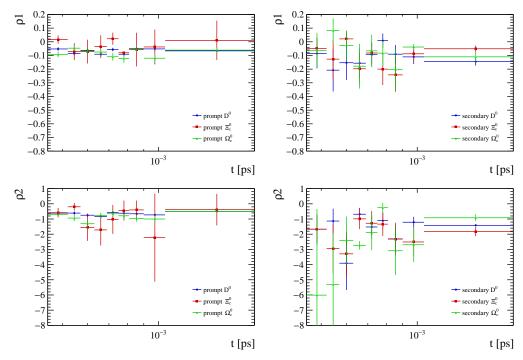


Figure 3.14 Parameter (top)  $\rho_1$  and (bottom)  $\rho_2$  in different decay-time bins obtained by fitting to 2016 simulated samples.

**Parameter constraints.** Studies above and the requirement of fit stability motivate the configuration of the  $\log_{10}(\chi_{\mathrm{IP}}^2)$  model when fitting to data. Parameters  $\sigma$ ,  $\xi$ ,  $\rho_1$ , and  $\rho_2$  in the prompt and secondary signal models are shared across decay-time bins and are fixed to values obtained from simulation as shown in Table 3.7 and 3.8. Parameter  $\mu$  is constructed as  $\mu_i = \mu_{\mathrm{MC},i} + \Delta \mu$ , where  $\mu_{\mathrm{MC},i}$  is fixed to the value obtained from the fit to simulation sample in *i*-th decay-time bin,  $\Delta \mu$  is a free parameter that describes the difference of  $\mu$  between data and simulation sample. Parameter  $\Delta \mu$  is shared across decay-time bins and data-taking years for both prompt and secondary models.

#### 3.3.3 Total fit model

The total model of the two-dimensional fit is constructed as the product of the invariant mass model and the  $\log_{10}(\chi_{\rm IP}^2)$  model for different components

$$\begin{split} \mathcal{P}_{i}(m,\log_{10}(\chi_{\mathrm{IP}}^{2})) &= N_{p,i} \times \mathcal{G}(m;m_{0,i},\sigma_{m}) \times \mathcal{B}(\log_{10}(\chi_{\mathrm{IP}}^{2});\Delta\mu_{p}) \\ &+ N_{s,i} \times \mathcal{G}(m;m_{0,i},\sigma_{m}) \times \mathcal{B}(\log_{10}(\chi_{\mathrm{IP}}^{2});\Delta\mu_{s}) \\ &+ N_{\mathrm{bkg},i} \times \mathcal{C}(m;c_{1,i}) \times \mathcal{B}_{i}(\log_{10}(\chi_{\mathrm{IP}}^{2})) \end{split} \tag{3.4}$$

where  $N_{p,i}$ ,  $N_{s,i}$ ,  $N_{\text{bkg},i}$  are the prompt signal, secondary signal, and background yield in i-th decay-time bin, respectively. The m and  $\log_{10}(\chi_{\text{IP}}^2)$  is assumed to be independent in this construction. The correlation between m and  $\log_{10}(\chi_{\text{IP}}^2)$  is checked with simulation and

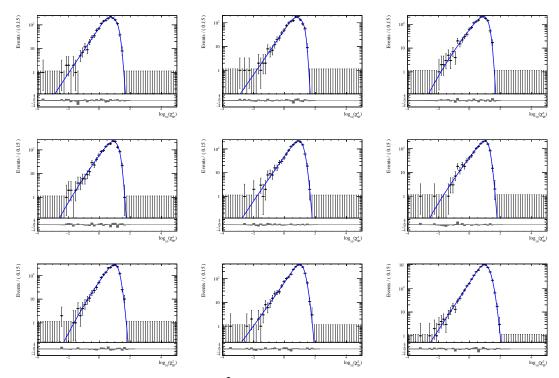


Figure 3.15 Fit results of the  $\log_{10}(\chi_{\text{IP}}^2)$  distribution of background component in different decaytime bins in the  $\Omega_c^0$  mass sideband.

Table 3.7 Results of the  $\log_{10}(\chi_{\text{IP}}^2)$  fit to simulated prompt signal and control samples.

Mode	Parameter	2016	2017	2018
	σ	$0.453 \pm 0.002$	$0.450 \pm 0.002$	$0.450 \pm 0.001$
$\Omega_c^0$	ξ	$-0.172 \pm 0.006$	$-0.169 \pm 0.005$	$-0.166 \pm 0.002$
3 2 <sub>c</sub>	$ ho_1$	$-0.061 \pm 0.006$	$-0.058 \pm 0.005$	$-0.052 \pm 0.003$
	$ ho_2$	$-1.366 \pm 0.080$	$-1.380 \pm 0.059$	$-1.372 \pm 0.050$
	σ	$0.454 \pm 0.003$	$0.454 \pm 0.002$	$0.452 \pm 0.002$
$\varXi_c^0$	ξ	$-0.163 \pm 0.007$	$-0.162 \pm 0.006$	$-0.168 \pm 0.005$
<i>□</i> <sub>c</sub>	$ ho_1$	$-0.053 \pm 0.007$	$-0.048 \pm 0.005$	$-0.052 \pm 0.005$
	$ ho_2$	$-0.975 \pm 0.066$	$-1.115 \pm 0.061$	$-1.091 \pm 0.055$
	σ	$0.451 \pm 0.001$	$0.453 \pm 0.001$	$0.453 \pm 0.001$
$D^0$	ξ	$-0.181 \pm 0.004$	$-0.180 \pm 0.003$	$-0.176 \pm 0.003$
	$ ho_1$	$-0.065 \pm 0.004$	$-0.064 \pm 0.003$	$-0.062 \pm 0.003$
	$ ho_2$	$-0.779 \pm 0.032$	$-0.802 \pm 0.024$	$-0.853 \pm 0.025$

is found to be negligible. Free parameters in the fit include  $m_{0,i}$ ,  $\sigma_m$ ,  $c_{1,i}$ ,  $\Delta \mu_p$ ,  $\Delta \mu_s$ , where the index i indicates the time dependence, i.e. the parameters are different between decaytime bins. The effects due to fixing some parameters to values obtained from simulation or sharing across decay-time bins are taken into account in the systematic uncertainty studies discussed in Sec. 3.6.1.

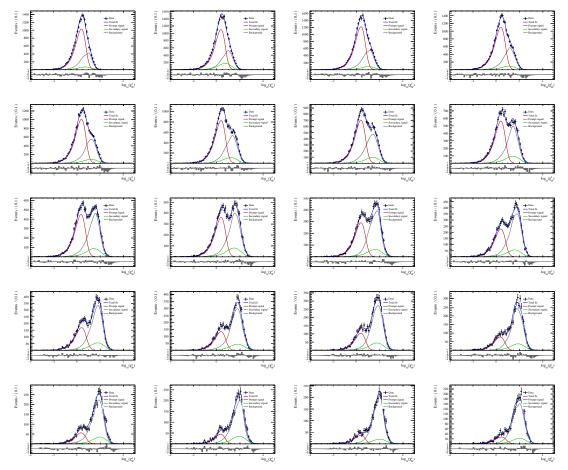


Figure 3.16 Distribution of  $\log_{10}(\chi_{\text{IP}}^2)$  in 2016  $D^0$  sample in different decay-time bins, along with the fit results.

### 3.3.4 Raw prompt yield

Extended unbinned maximum likelihood fits to the invariant-mass and  $\log_{10}(\chi_{\rm IP}^2)$  distributions are performed to estimate the prompt yields simultaneously in decay-time bins and data-taking periods. The resulting raw prompt yields of signal and control modes in 2016-2018 samples are shown in Fig. 3.18 and tabulated in Table 3.9. Results of key fit parameters are shown in Table 3.10. Distributions of raw prompt yields are similar for different data-taking years. As an illustration, the fit projections to the invariant-mass in 2016 data for signal and control modes are shown in Fig. 3.19, 3.20, and 3.21, respectively. the fit projections to  $\log_{10}(\chi_{\rm IP}^2)$  distributions with the invariant mass in  $\pm 2\sigma$  range around the signal mass peak in 2016 data for signal and control modes are shown in Fig. 3.22, 3.23, and 3.24, respectively. Projections of fits for other data-taking years are shown in Appendix C.

We can see from Table 3.10 that  $\Delta \mu_p$  is consistent between different modes within uncertainty, while  $\Delta \mu_s$  is different in different modes. This is expected as the contribution

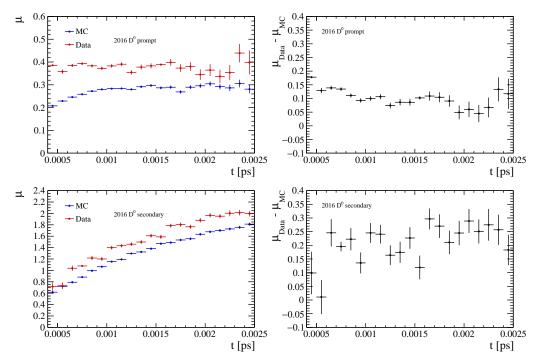


Figure 3.17 Parameter (left)  $\mu$  of (top) prompt and (bottom) secondary component in different decay-time bins obtained from fits to the  $D^0$  simulated sample and data sample, and (right) the difference between  $\mu$  in data and simulation for the (top) prompt and (right) secondary component.

Table 3.8 Results of the  $log_{10}(\chi_{IP}^2)$  fit to simulated secondary signal and control samples.

Mode	Parameter	2016	2017	2018
	σ	$0.442 \pm 0.007$	$0.445 \pm 0.005$	$0.438 \pm 0.005$
$arOmega_c^0$	ξ	$-0.186 \pm 0.022$	$-0.211 \pm 0.017$	$-0.224 \pm 0.016$
3 Z <sub>C</sub>	$ ho_1$	$-0.048 \pm 0.019$	$-0.051 \pm 0.014$	$-0.073 \pm 0.015$
	$ ho_2$	$-2.665 \pm 0.521$	$-1.706 \pm 0.260$	$-1.603 \pm 0.242$
	σ	$0.460 \pm 0.009$	$0.458 \pm 0.013$	$0.441 \pm 0.007$
$\varXi_c^0$	ξ	$-0.274 \pm 0.020$	$-0.257 \pm 0.001$	$-0.294 \pm 0.022$
<u></u> -с	$ ho_1$	$-0.129 \pm 0.028$	$-0.113 \pm 0.021$	$-0.119 \pm 0.021$
	$ ho_2$	$-2.375 \pm 0.522$	$-2.509 \pm 0.887$	$-1.654 \pm 0.337$
	σ	$0.621 \pm 0.003$	$0.621 \pm 0.004$	$0.632 \pm 0.002$
$D^0$	ξ	$-0.057 \pm 0.001$	$-0.093 \pm 0.010$	$-0.066 \pm 0.000$
D	$ ho_1$	$-0.085 \pm 0.010$	$-0.149 \pm 0.017$	$-0.134 \pm 0.008$
	$ ho_2$	$-1.803 \pm 0.114$	$-1.441 \pm 0.114$	$-1.782 \pm 0.032$

for prompt signals is clear and the source of data-simulation discrepancy is expected to be similar in different modes, while the contribution of secondary signals is a mixture of many different decay modes and the agreement between data and simulation may be at different levels for different modes, depending on how well the simulation describes the inclusive secondary *b*-decays.

The fraction of secondary signals for each decay modes are obtained by using

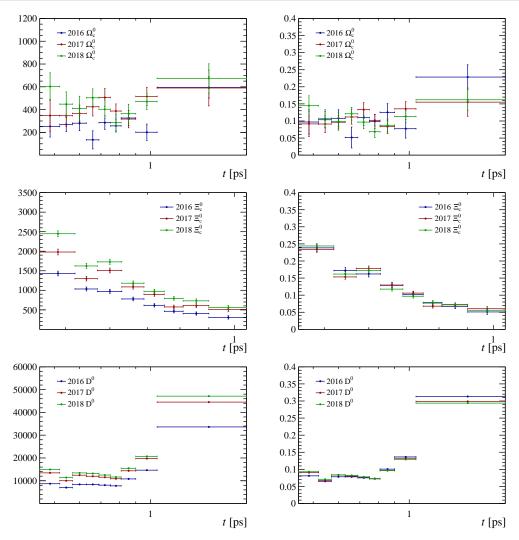


Figure 3.18 Yields of (left) prompt signals and (right) normalized prompt signals for (top)  $\Omega_c^0$ , (middle)  $\Xi_c^0$  and (bottom)  $D^0$  modes in 2016-2018 samples. The decay time (x-axis) is shown in log scale.

 $N_s/(N_p + N_s)$  as free parameters in the fit and are shown in Fig. 3.25. The fraction of secondary signals in a given decay-time region can already provide information of the lifetime hierarchy. It is noticed that the secondary fraction in 2016  $D^0$  data is different from those in 2017–2018 data. The effect on the measured lifetime is investigated in Sec. 3.5.2.

# 3.4 Estimation of efficiency

The efficiency of event selection is defined as the ratio of the number of events after event selection to that before event selection. The selection efficiency is decay-time dependent due to requirements of displaced tracks in the event selection. Consequently, the exponential decay-time distribution is distorted and the variation of efficiency with

Table 3.9 Yields of prompt signals for  $\Omega_c^0$ ,  $\Xi_c^0$ , and  $D^0$  modes in 2016-2018 samples.

Mode	Bin	2016	2017	2018
	1	$253 \pm 93$	$348 \pm 142$	602 ± 121
	2	$270 \pm 62$	$346 \pm 96$	$448 \pm 108$
	3	$281 \pm 65$	$366 \pm 74$	$410\pm108$
	4	$135 \pm 79$	$425\pm80$	$504 \pm 78$
$arOmega_c^0$	5	$285 \pm 59$	$506 \pm 78$	$403 \pm 80$
	6	$257 \pm 54$	$387 \pm 62$	$286 \pm 71$
	7	$326 \pm 66$	$317 \pm 76$	$364 \pm 82$
	8	$201 \pm 72$	$515 \pm 80$	$470 \pm 71$
	9	$595 \pm 93$	$590 \pm 157$	$675 \pm 128$
	1	$1432 \pm 60$	$1980 \pm 74$	$2448 \pm 76$
	2	$1033 \pm 51$	$1297 \pm 57$	$1623 \pm 64$
	3	$973 \pm 52$	$1507 \pm 61$	$1727 \pm 64$
	4	$778 \pm 47$	$1087 \pm 56$	$1181 \pm 57$
$\varXi_c^0$	5	$615 \pm 42$	$897 \pm 49$	$973 \pm 54$
	6	$463 \pm 40$	$574 \pm 46$	$792 \pm 47$
	7	$404 \pm 41$	$606 \pm 49$	$730 \pm 51$
	8	$306 \pm 43$	$511 \pm 50$	$561 \pm 52$
	1	8697 ± 120	$13457 \pm 140$	14928 ± 146
	2	$6991 \pm 101$	$10008 \pm 121$	$11373 \pm 126$
	3	$8404 \pm 112$	$12442 \pm 130$	$13441 \pm 134$
	4	$8388 \pm 110$	$11972 \pm 127$	$13186 \pm 132$
$D^0$	5	$8071 \pm 106$	$11554\pm122$	$12509 \pm 127$
	6	$7761 \pm 102$	$10885 \pm 117$	$11642 \pm 123$
	7	$10807 \pm 118$	$14370\pm134$	$15465 \pm 140$
	8	$14641 \pm 137$	$19731 \pm 158$	$20697 \pm 161$
	9	$33618 \pm 208$	$44517 \pm 237$	$47125 \pm 243$

decay-time, referred to as the decay-time acceptance, has to be considered in the decay-time fit.

Simulated samples are used to estimate the reconstruction and selection efficiency. There exist known mismodellings of simulation. Therefore, several corrections are applied to simulated samples, including those to correct for tracking efficiency, PID efficiency, and hTOS efficiency 3.4.3. The phase-space distributions and the kinematic distributions are weighted to match those in data as they are correlated to efficiency mentioned above. These corrections are implemented as per-event weight

$$w = \prod_{i} w_{i}, \tag{3.5}$$

where w is the total per-event weight and  $w_i$  is the weight from each individual contribution.

Table 3.10 Results of key parameters obtained from fits to data samples. Parameter  $\Delta \mu_p$  and  $\Delta \mu_s$  are shared across 2016-2018 in the fit.

Mode	Parameter	2016	2017	2018
$arOmega_c^0$	$\sigma_m \ \Delta \mu_p \ \Delta \mu_s$	$5.863 \pm 0.191$	$5.768 \pm 0.147$ $0.058 \pm 0.025$ $-0.117 \pm 0.050$	$5.569 \pm 0.145$
$\varXi_{c}^{0}$	$\sigma_m$ $\Delta \mu_p$ $\Delta \mu_s$	$4.827 \pm 0.051$	$4.653 \pm 0.042$ $0.114 \pm 0.007$ $0.078 \pm 0.003$	$4.598 \pm 0.036$
$D^0$	$\sigma_m \ \Delta \mu_p \ \Delta \mu_s$	$6.172 \pm 0.020$	$5.926 \pm 0.016$ $0.091 \pm 0.001$ $0.281 \pm 0.007$	5.915 ± 0.016

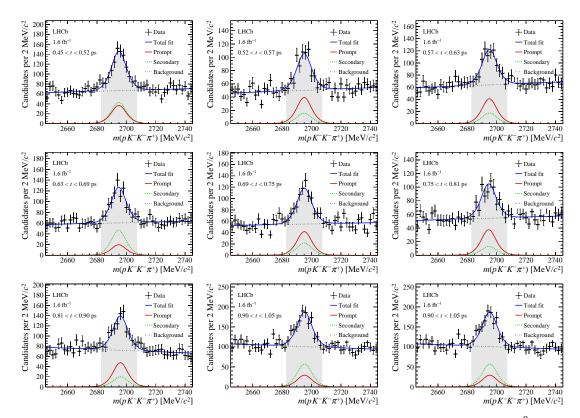


Figure 3.19 Fit projections to the invariant-mass distribution in 2016 data for the  $\Omega_c^0$  mode.

### 3.4.1 Tracking efficiency correction

There is known small discrepancy between data and simulation in the tracking reconstruction efficiency. This is taken into account using the efficiency ratio of simulation to data in kinematic bins, which is obtained with the tag-and-probe method. The per-event correction factor is calculated as

$$w_{\text{trk}} = \prod_{i=1}^{4} r_{h_i}(p_i, \eta_i)$$
 (3.6)

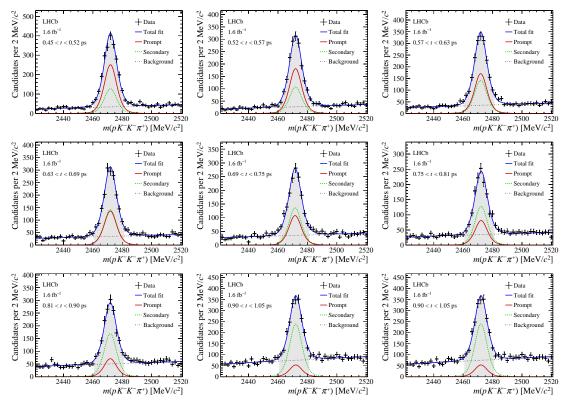


Figure 3.20 Fit projections to the invariant-mass distribution in 2016 data for the  $\Xi_c^0$  mode.

for each candidate, where  $r_{h_i}(p_i, \eta_i)$  is the correction factor for each final-state track. This correction is at the order of 1% or smaller.

### 3.4.2 PID efficiency correction

The PIDCalib package is used to determine the efficiency of PID requirements, as discussed in Sec. 2.2.4. The per-event efficiency is calculated as

$$w_{\text{PID}} = \prod_{i}^{4} \varepsilon_{h_i}(p_i, \eta_i), \tag{3.7}$$

where  $\varepsilon_{h_i}(p_i,\eta_i)$  is the PID efficiency for each final-state track, as a function of the momentum and rapidity. The calibration sample used for kaons and pions is the  $D^{*+} \to D^0(\to K^-\pi^+)\pi^+$  sample, and that used for protons is the  $\Lambda \to p\pi$  sample. Efficiency of PID requirements on each final-state track is determined in p and q bins. the binning scheme as well as the efficiency in each bin for MagDown polarity is shown in Fig. 3.26 as an illustration. The total PID efficiency of a candidate is the product of efficiencies of each final-state track.

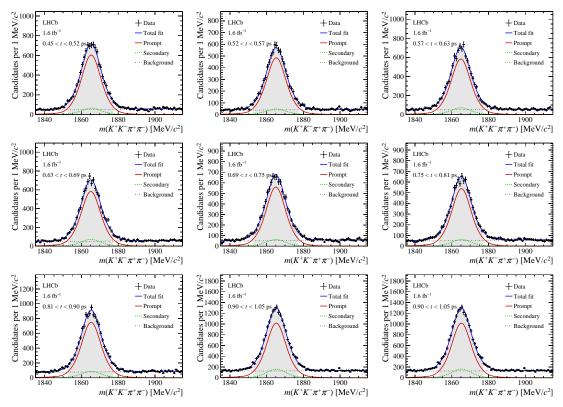


Figure 3.21 Fit projections to the invariant-mass distribution in 2016 data for the  $D^0$  mode.

### 3.4.3 L0 efficiency correction

It is known from other LHCb analyses that simulated samples dose not to model the L0 efficiency precisely due to the imprecise description of processes in the ECAL subdetector. Instead of calculating the hTOS efficiency directly from simulation, we parametrise hTOS efficiency as a function of the transverse energy deposited in the HCAL HCAL\_realET of the final-state tracks. The efficiency of each fina-state track at different transverse energy  $E_T$  is then determined from calibration data with the TISTOS method, as described in [179]. Efficiency tables for 2016-2018 data are obtained with  $\Lambda_b^0 \to \Lambda_c^+ \mu \nu X$  decays for different particles, HCAL regions, and charges, and are visualized in Fig 3.27. The per-event correction factor is calculated as

$$w_{h\text{TOS}} = 1 - \prod_{i}^{4} (1 - \varepsilon_{h_i}(\text{HCAL\_realET})), \tag{3.8}$$

where  $\varepsilon_{h_i}$ (HCAL\_realET) is the hTOS efficiency for each final-state track, determined as a function of HCAL\_realET according to the particle ID and the region in the HCAL.

The higher order effect on the calculation of transverse energy due to the overlapping of clusters of final-state tracks is also estimated. The transverse energy deposited in the HCAL HCAL\_realET is corrected as follows before it is used to get the hTOS efficiency

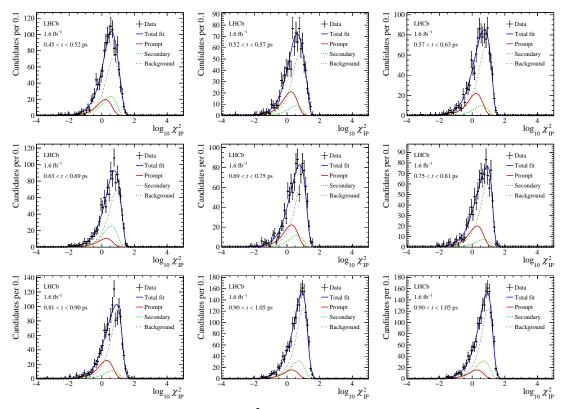


Figure 3.22 Fit projections to the  $\log_{10}(\chi_{\rm IP}^2)$  distribution with the mass in  $\pm 2\sigma$  range around the signal mass peak in 2016 data for the  $\Omega_c^0$  mode.

per track. For the closest cluster pair  $(E_{T1}, E_{T2})$  of each decay, the corrected transverse energy  $(E_{T1}^{\rm corr}, E_{T2}^{\rm corr})$  is calculated as

$$\begin{cases} (E_{T1} + E_{T2}, E_{T1} + E_{T2}), & \text{for } |\Delta x| < 0.5d, |\Delta y| < 0.5d \\ (E_{T1} + 0.5E_{T2}, 0.5E_{T1} + E_{T2}), & \text{for } |\Delta x| < 0.5d, 0.5d < |\Delta y| < 1.0d \\ (E_{T1} + 0.5E_{T2}, 0.5E_{T1} + E_{T2}), & \text{for } 0.5d < |\Delta x| < 1.0d, |\Delta y| < 0.5d \\ (E_{T1} + 0.25E_{T2}, 0.25E_{T1} + E_{T2}), & \text{for } 0.5d < |\Delta x| < 1.0d, 0.5d < |\Delta y| < 1.0d \end{cases}$$

$$(3.9)$$

where  $\Delta x$  ( $\Delta y$ ) is the distance in the x (y) direction of the closest cluster pair in the HCAL plane, d is the tile size of the HCAL. The fitted lifetime with or without considering the effect due to the overlapping of final-state tracks is found to be at sub-fs level and negligible. Therefore, we do not include this correction in the default procedure.

### 3.4.4 Phasespace correction

Simulation samples are generated with the phasespace decay model and resonant structures in the four-body decay are not considered. This may lead to a mismodelling of the distributions of kinematic variables of final-state tracks, and hence the efficiency

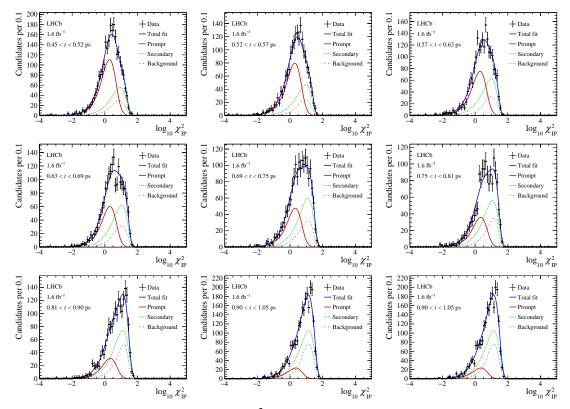


Figure 3.23 Fit projections to the  $\log_{10}(\chi_{\rm IP}^2)$  distribution with the mass in  $\pm 2\sigma$  range around the signal mass peak in 2016 data for the  $\Xi_c^0$  mode.

as a function of decay time. To correct the phasespace distributions, five Cabibbo-Maksymowicz (CM) variables are used. For  $D^0$  control mode, they are calculated as

- $M(K^+K^-)$ , the invariant mass of the  $K^+K^-$  system;
- $M(\pi^+\pi^-)$ , the invariant mass of the  $\pi^+\pi^-$  system;
- $\cos(\theta_{K^+}^{K^+K^-})$ , the cosine of the angle between the direction of the  $D^0$  and that of one of the kaons in the rest frame of the two kaons;
- $\cos(\theta_{\pi^+}^{\pi^+\pi^-})$ , the cosine of the angle between the direction of the  $D^0$  and that of one of the pions in the rest frame of the two pions;
- $\phi_{\pi^+\pi^-}^{K^+K^-}$ , the angle in the  $D^0$  rest frame between the plane defined by the directions of the two kaons and the plane defined by the directions of the two pions

which are sufficient to describe the whole decay structure. CM variables for signal modes are defined in a similar way. Background subtracted data distributions of CM variables are obtained from the invariant-mass fit and are used to reweight the simulation. This indicates that the signal distributions in data include contributions from both prompt and secondary signals. This approximation is checked by comparing the phasespace distributions of prompt and secondary signals in simulation, as shown in Fig. 3.28 for the  $\Omega_c^0$ 

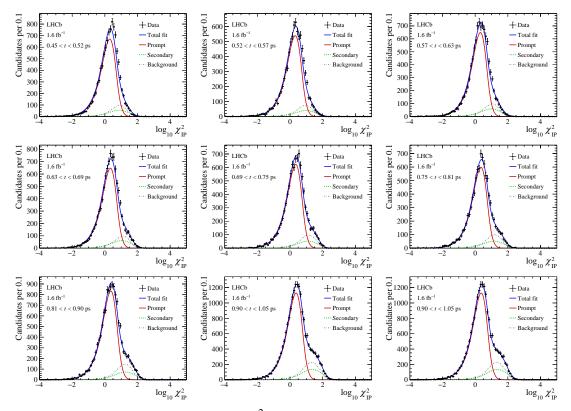


Figure 3.24 Fit projections to the  $\log_{10}(\chi_{\rm IP}^2)$  distribution with the mass in  $\pm 2\sigma$  range around the signal mass peak in 2016 data for the  $D^0$  mode.

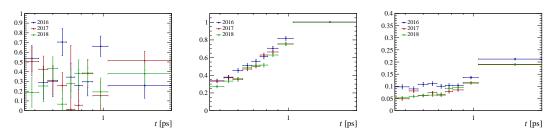


Figure 3.25 The fraction of secondary signals in (left)  $\Omega_c^0$ , (middle)  $\Xi_c^0$  and (right)  $D^0$  data samples.

mode. The same degree of agreement is observed for  $\Xi_c^0$  and  $D^0$  modes. The comparison indicates that it is a good approximation not to distinguish prompt and secondary signals in data distributions in the reweighting procedure.

Five-dimensional weight is calculated using GBReweighter from the hep\_ml package [180]. The comparison of 2016 data and simulation before and after the phasespace weight is shown in Fig. 3.29, 3.30, and 3.31 for  $\Omega_c^0$ ,  $\Xi_c^0$ , and  $D^0$  mode, respectively. To check that the correlations of different phasespace variables are handled properly, comparisons of additional phasespace variables are shown in Fig. 3.32, in which good agreement is observed after the five-dimensional weighting.

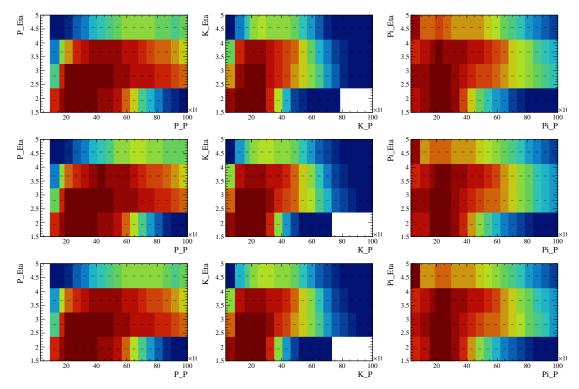


Figure 3.26 PID efficiency as a function of momentum p and rapidity  $\eta$  for (left) proton, (middle) kaon and (right) pion and in (top) 2016, (middle) 2017 and (bottom) 2018 data of the MagDown polarity.

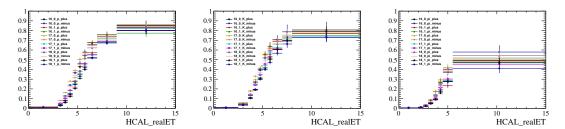


Figure 3.27 L0 hadron TOS efficiency for (left) p, (middle) K and (right)  $\pi$ .

### 3.4.5 Kinematic corrections

Kinematic distributions, including the  $p_{\rm T}$  and y of the charmed hadron and the  $p_{\rm T}$  of the final-state tracks, between prompt signals in data and simulation are found to be different after the corrections described above. Further kinematic weights are applied to correct for this discrepancy.

The kinematic weights are obtained as follows. First, binned one-dimensional distributions in data of  $p_T$  and y of the charmed hadron and  $p_T$  of its final-state tracks for prompt signals are extracted with the two-dimensional invariant-mass and  $\log_{10}(\chi_{IP}^2)$  fit described in Sec. 3.3 (in this case the sample is split in bins of kinematic variables under consideration instead of the decay time). Second, the weight is calculated according

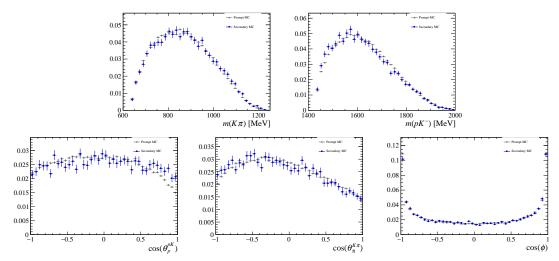


Figure 3.28 Comparison of phasespace variables for prompt and secondary signals in 2016  $\Omega_c^0$  MC samples.

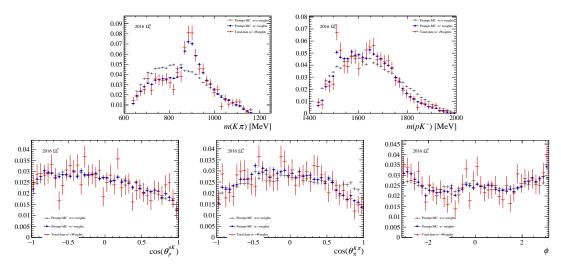


Figure 3.29 Comparison of 2016 data and simulation before and after the phasespace weight for  $\Omega_c^0$  mode, where the simulation before (after) weighting is shown in gray (blue), and the sWeighted data is shown in red.

to the observed data-simulation discrepancy for each kinematic variable (six in total) sequentially. Third, the second step is repeated until (it turns out that two iterations are sufficient) the kinematic distributions between prompt signals in data and simulation are in good agreement. The procedure is performed for both signal and control modes and for each data-taking period. The fact that only one-dimensional distributions are used in the reweighting is because the sample size of the signal mode is limited.

The comparison of the kinematic distributions between prompt signals in data and simulation after the kinematic correction is shown Fig. 3.33, Fig. 3.34 and Fig. 3.35 for 2018 data. The same degree of agreement is observed in other data-taking years.

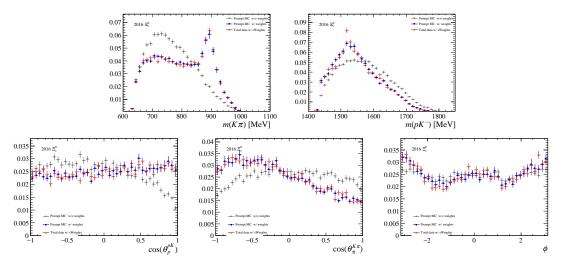


Figure 3.30 Comparison of 2016 data and simulation before and after the phasespace weight for  $\Xi_c^0$  mode.

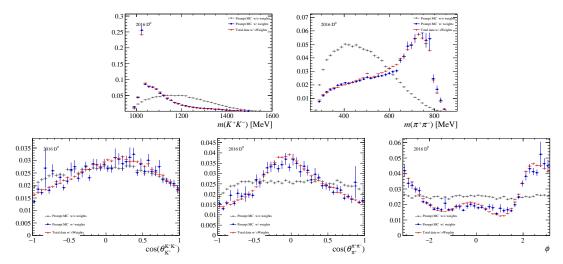


Figure 3.31 Comparison of 2016 data and simulation before and after the phasespace weight for  $D^0$  mode.

## 3.4.6 Decay-time acceptance

To understand how various corrections affect the decay-time distributions in simulation, the normalised decay-time distributions after each correction stage are shown in Fig. 3.36, where the most significant correction is due to the L0 efficiency correction.

The decay-time acceptance is defined as the selection efficiency as a function of decay time. It is estimated by taking the ratio of the selected and generated number of events in each decay-time bin, where the selected number of events are obtained from the corrected simulation samples. The decay-time acceptances of 2016 sample in bins of decay time are shown in Fig. 3.37 for all modes overlaid. The ratio of the decay-time acceptance between signal and control mode is shown in Fig. 3.38, with 2016 simulation samples

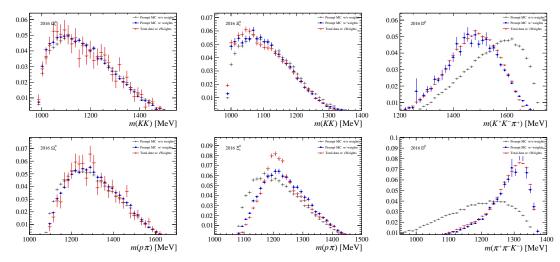


Figure 3.32 Comparison of additional phasespace variables for (left)  $\Omega_c^0$ , (middle)  $\Xi_c^0$ , and (right)  $D^0$  mode.

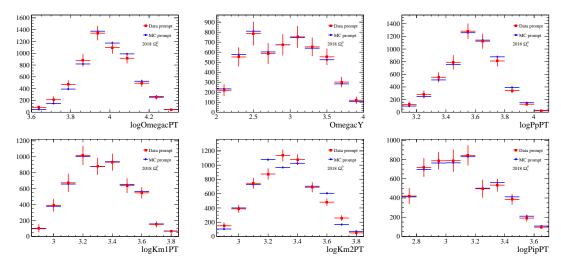


Figure 3.33 Comparison of prompt distributions between data and simulation for  $\Omega_c^0$  mode. The prompt data distribution is extracted with two-dimensional fits of invariant-mass and  $\log_{10}(\chi_{\rm IP}^2)$  described in Sec. 3.3, in bins of variables under study. The "log" indicates a 10-based logarithmic transformation, and final-state particle p,  $K^-$ , and  $\pi^+$  of  $\Omega_c^0$  are labeled as Pp, Km1, Km2 and Pip, respectively.

(input lifetimes of  $\tau(\Omega_c^0) = 250 \, \text{fs}$ ,  $\tau(\Xi_c^0) = 250 \, \text{fs}$ , and  $\tau(D^0) = 410 \, \text{fs}$ ). In the decaytime region of [0.45,2.0] ps, which is chosen to perform the lifetime measurement, the deviation from a flat acceptance ratio is about 10–20% (mainly at low decay-time region). The fluctuation at 1.3 ps for  $D^0$  mode is due to some weights in the phasespace correction and is checked to have negligible effect on the decay-time fit.

## 3.4.7 Validation with $D^0$ control mode

As a stringent validation, the normalised decay-time distributions of data and simulation samples for  $D^0$  control mode are compared, as shown in Fig. 3.39. Figure 3.39 also

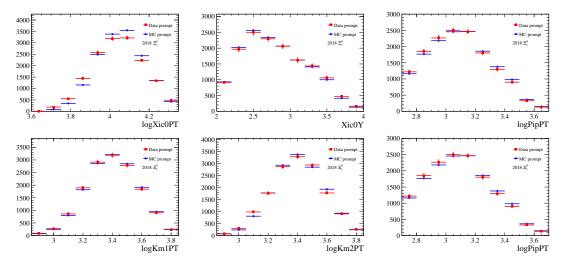


Figure 3.34 Comparison of various distributions between data and simulation for  $\Xi_c^0$  mode. The prompt data distribution is extracted with two-dimensional fits of invariant-mass and  $\log_{10}(\chi_{\rm IP}^2)$  described in Sec. 3.3, in bins of variables under study. The "log" indicates a 10-based logarithmic transformation, and final-state particle p,  $K^-$ , and  $\pi^+$  of  $\Xi_c^0$  are labeled as Pp, Km1, Km2 and Pip, respectively.

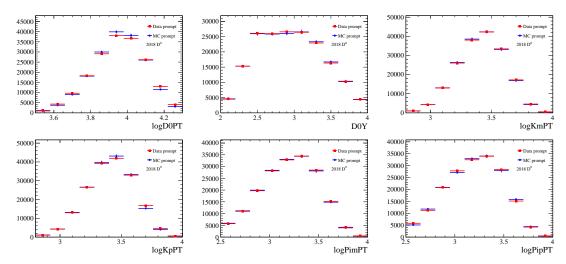


Figure 3.35 Comparison of various distributions between 2018 data and simulation for  $D^0$  mode. The prompt data distribution is extracted with two-dimensional fits of invariant-mass and  $\log_{10}(\chi_{\rm IP}^2)$  described in Sec. 3.3, in bins of variables under study. The "log" indicates a 10-based logarithmic transformation, and final-state particle  $K^-$ ,  $K^+$ ,  $\pi^-$ ,  $\pi^+$  of  $D^0$  are labeled as Km, Kp, Pim and Pip, respectively.

shows the decay-time ratio of data to simulation. The data distribution is obtained with the two-dimensional invariant-mass and  $\log_{10}(\chi_{\rm IP}^2)$  fit described in Sec. 3.3. The simulated distribution has been corrected as discussed above in this section. The input lifetime for  $D^0$  simulation is its PDG value of 410 fs. Good agreement between data and simulation is observed in the decay-time region of [0.45,2.50] ps. Defining  $\chi^2 \equiv \frac{(N_{data} - N_{mc})^2}{\sigma_{N_{data}}^2 + \sigma_{N_{mc}}^2}$ , the  $\chi^2$ /ndof for 2016-2018 distributions are 26/21, 27/21, and 15/21, respectively. The

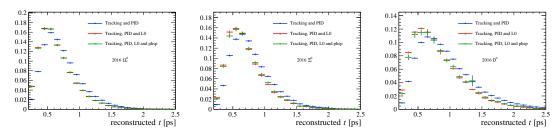


Figure 3.36 Normalised decay-time distributions after each correction stage for 2016 (left)  $\Omega_c^0$ , (middle)  $\Xi_c^0$  and (right)  $D^0$  simulation. The input lifetime of  $\Omega_c^0$  and  $\Xi_c^0$  simulation sample is 250 fs. The input lifetime of  $D^0$  simulation sample is 410 fs.

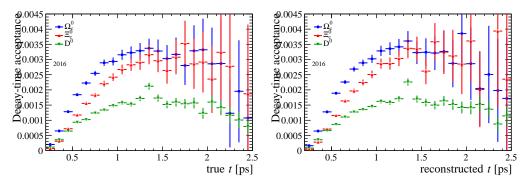


Figure 3.37 Decay-time acceptance in 2016 sample for all modes in bins of (left) true decay time and (right) reconstructed decay time.

ratio of decay time is described with a linear function and the fit results are shown in Figure 3.39. The results indicate that the slope is consistent with zero within  $3\sigma$  for 2016-2018 data. Since this is a comparison of data and simulation for only one decay mode, the residual discrepancy is expected to be further reduced when the ratio is taken between the signal and control mode.

Quantitatively, a test is performed by measuring the  $D^0$  lifetime in an absolute manner with a chi-squared fit to the data decay-time distribution with the simulated sample as template. The method used here is very similar to what is to be used in the default decay-time fit discussed in Sec. 3.5, except for that there is no control mode to be used to

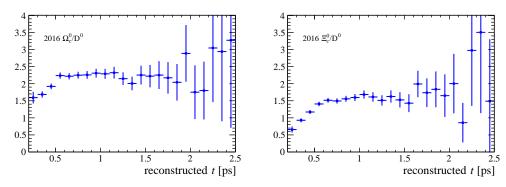


Figure 3.38 Decay-time acceptance ratio of signal to control mode versus the reconstructed decay time.

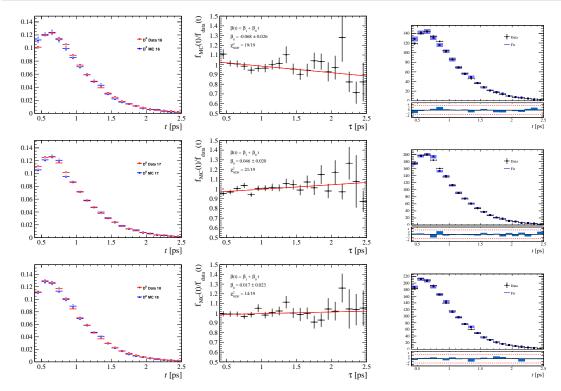


Figure 3.39 Decay-time distributions of (left) data and simulation samples, (middle) decay-time ratios of data to simulation samples, and (right) the decay-time fit results to the  $D^0$  data for (top) 2016, (middle) 2017, and (bottom) 2018  $D^0$  control mode.

construct a "double ratio" in this case. For each data-taking year, we define the ratio of the measured prompt yield in data,  $N_i$ , and the effective yield in simulation, which includes all the corrections applied to simulation,  $M_i$ , in the *i*-th decay-time bin as

$$r_i^{\text{con}} = \frac{N_i^{\text{con}}}{M_i^{\text{con}}} \tag{3.10}$$

for the  $D^0$  control (denoted as "con") mode. We also define the expected prompt yield ratio of data to simulation as

$$f_i^{\text{con}} = \frac{\int_i \exp(-t/\tau^{\text{con}})dt}{\int_i \exp(-t/\tau_{\text{sim}}^{\text{con}})dt}$$
(3.11)

for the control mode, where  $\tau_{\rm con}$  is the  $D^0$  lifetime to be measured and  $\tau_{\rm sim}^{\rm con}=410$  fs is the input lifetime in simulation. The integral runs from the lower bin edge to the upper bin edge of the *i*-th decay-time bin. Then the  $\chi^2$  for each year is defined (to avoid confusion

Table 3.11 Decay-time fit results for  $D^0$  control mode.

	2016	2017	2018	Simultaneous
τ[ fs]	$420.9 \pm 4.6$	$401.5 \pm 3.1$	$406.8 \pm 3.6$	$407.9 \pm 2.1$
$\chi^2/\text{NDF}$	19/19	19/19	13/19	63/59

with the default fit in next section, a bar is added in the notation) and evaluated as

$$\bar{\chi}_{\text{year}}^{2}(\tau^{\text{con}}, C_{\text{year}}) \equiv \sum_{i} \frac{(N_{i}^{\text{con}} - C_{\text{year}} \times f_{i}^{\text{con}} \times M_{i}^{\text{con}})^{2}}{\sigma_{N_{i}^{\text{con}}}^{2} + C_{\text{year}}^{2} \times f_{i}^{\text{con2}} \times \sigma_{M_{i}^{\text{con}}}^{2}}$$

$$= \sum_{i} \frac{(r_{i}^{\text{con}} - C_{\text{year}} \times f_{i}^{\text{con}})^{2}}{r_{i}^{\text{con2}} \times \left(\frac{\sigma_{N_{i}^{\text{con}}}}{N_{i}^{\text{con}}}\right)^{2} + C_{\text{year}}^{2} \times f_{i}^{\text{con2}} \times \left(\frac{\sigma_{M_{i}^{\text{con}}}}{M_{i}^{\text{con}}}\right)^{2}},$$
(3.12)

where  $\sigma_Q$  denotes the variance of the relevant quantity Q,  $C_{\rm year}$  is the normalisation factor introduced to account for the different sample size of data and simulation, and the sum runs through all decay-time bins. The modelling of decay-time acceptance with simulation is included implicitly in  $M_i^{\rm con}$ . The fit results are shown in Fig. 3.39, where the bin content of the "Data" curve is proportional to  $N_i^{\rm con}$ , the bin content of the "Fit" curve is proportional to  $C_{\rm year} \times f_i^{\rm con} \times M_i^{\rm con}$ , and the pull is evaluated as  $(N_i^{\rm con} - C_{\rm year} \times f_i^{\rm con} \times M_i^{\rm con})/\sqrt{\sigma_{N_i^{\rm con}}^2 + C_{\rm year}^2 \times f_i^{\rm con2} \times \sigma_{M_i^{\rm con}}^2}$ . The  $D^0$  lifetime can also be extracted with a simultaneous fit to 2016-2018 data. In this case the total chisquare is constructed as

$$\bar{\chi}^2(\tau^{\text{con}}, \vec{C}) = \sum_{\text{vear}} \bar{\chi}_{\text{year}}^2(\tau^{\text{con}}, C_{\text{year}}), \tag{3.13}$$

where  $\tau^{\rm con}$  is the  $D^0$  lifetime to be measured,  $\vec{C} = (C_{16}, C_{17}, C_{18})$  is the normalisation vector,  $\bar{\chi}^2_{\rm year}$  is defined as in Eq. 3.12 and the sum runs from 2016-2018 data.

The fit results for each data-taking year and for 2016-2018 data simultaneously are shown in Table 3.11, which look good given that an absolute measurement is performed. The largest discrepancy with the PDG value of  $D^0$  lifetime (410.1  $\pm$  1.5 fs) is 2.4 $\sigma$  in 2017 data. The largest discrepancy between years is 3.4 $\sigma$  between 2016 and 2017 data. No systematic uncertainties are considered at this stage.

#### 3.5 Extraction of lifetimes

The lifetime of  $\Omega_c^0$  and  $\Xi_c^0$  baryons are determined from a binned  $\chi^2$  fit comparing the signal yields in data with those from the simulation, where the input lifetime is known.

Table 3.12 Fit results of the normalisation vectors.

	$C_{16}$	$C_{17}$	$C_{18}$
$\Omega_c^0$	$(2.078 \pm 0.274) \times 10^{-2}$	$(2.390 \pm 0.308) \times 10^{-2}$	$(1.743 \pm 0.229) \times 10^{-2}$
$\varXi_c^0$	$0.769 \pm 0.059$	$0.654 \pm 0.047$	$0.696 \pm 0.051$

The total  $\chi^2$  is constructed as

$$\chi^{2}(\tau, \vec{C}) = \sum_{j} \sum_{i} \frac{\left(N_{i,j}^{\text{sig}} - C_{j} \times F_{i}(\tau) \times R_{i,j}\right)^{2}}{\sigma_{N_{i,j}^{\text{sig}}}^{2} + C_{j}^{2} \times F_{i}^{2}(\tau) \times \sigma_{R_{i,j}}^{2}}, \qquad R_{i,j} = \frac{N_{i,j}^{\text{con}}}{M_{i,j}^{\text{con}}} \times M_{i,j}^{\text{sig}}, \quad (3.14)$$

where  $N_{i,j}^{\text{sig}}$  ( $N_{i,j}^{\text{con}}$ ) is the signal yield in data for the signal (control) mode in decay-time interval i and for the data-taking period j;  $M_{i,j}$  is the effective yield predicted from simulation;  $C_j$  is a normalisation factor to account for the difference in size between the data and the simulated samples; and  $\sigma$  is the uncertainty of the relevant quantity. The difference in lifetime between data and simulated samples is accounted for by

$$F_i(\tau) = \frac{\int_i \exp(-t/\tau) dt}{\int_i \exp(-t/\tau_{\text{sim}}) dt} \times \frac{\int_i \exp(-t/\tau_{\text{sim}}^{\text{con}}) dt}{\int_i \exp(-t/\tau_{\text{con}}) dt},$$
(3.15)

where  $\tau_{\text{sim}} = 250 \text{ fs}$  is the signal mode lifetime in simulation and  $\tau^{\text{con}} = \tau_{\text{sim}}^{\text{con}}$  is the known  $D^0$  lifetime [2], but is allowed to vary for estimating the systematic uncertainty.

The resulting lifetimes are

$$\tau(\Omega_c^0) = 276.5 \pm 13.4 \text{ fs},$$

$$\tau(\Xi_c^0) = 148.0 \pm 2.3 \text{ fs},$$
(3.16)

with  $\chi^2/\text{ndf} = 22/23$  (p-value = 0.52) and  $\chi^2/\text{ndf} = 30/20$  (p-value = 0.06), where the uncertainties are statistical only. The blinded central values are 177 fs for  $\Omega_c^0$  and 78.9 fs for  $\Xi_c^0$ , which serve as the reference to the cross-checks. The resulting values of the normalisation vectors are shown in Table 3.12. The fit results of  $\Omega_c^0$  and  $\Xi_c^0$  modes are shown in Fig. 3.40. The "Data" distribution is the raw data yield in 2016-2018 samples combined, divided by the bin width  $\Delta t_i$  of each decay-time bin. The "Fit" distribution is  $C \times F_i \times M_i^{\text{sig}} \times r_i^{\text{con}}$  with free parameters taking fitted values, divided by the bin width  $\Delta t_i$  of each decay-time bin.

## 3.5.1 Consistency checks

To check that the measured lifetimes are robust against variation of data-taking conditions and the choice of binning scheme, several consistency checks are performed, in

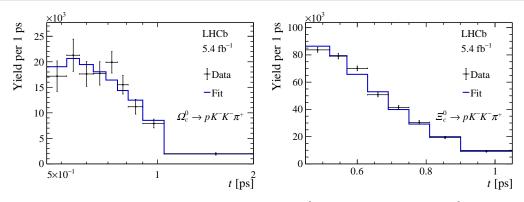


Figure 3.40 Decay-time distributions for the (left)  $\Omega_c^0$  mode and the (right)  $\Xi_c^0$  mode with the  $\chi^2$  fit superimposed. The uncertainty on the data distribution is statistical only.

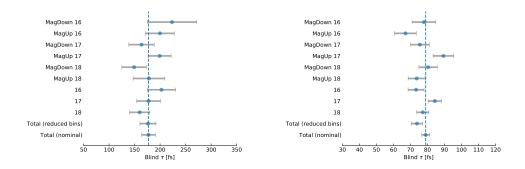


Figure 3.41 Results of consistency checks for (left)  $\Omega_c^0$  and (right)  $\Xi_c^0$  modes.

which the total data sample is split into different subsamples and the lifetimes are measured and compared. A summary of results of these checks are shown in Fig. 3.41.

**Data-taking period.** To check that results of each data-taking period are consistent with each other, the decay-time fit is performed in each year with independent  $\tau^{\rm sig}$  parameters. The results are summarised in Table 3.13 and illustrated in Fig. 3.41. The last column shows the weighted average of the resulting lifetime and  $\chi^2$ /ndf of the combination with least squares method. It can be seen that results of different data-taking period are compatible with each other within  $2\sigma$  statistical uncertainty.

**Magnetic polarity.** To check that results of each magnetic polarity are consistent with each other, the data and simulation samples are split by year and magnetic polarity. The prompt yield and decay-time fits are performed for each sub-sample, respectively. The results are summarised in Table 3.14 and illustrated in Fig. 3.41. It can be seen that results of different polarities are compatible with each other within  $1.5\sigma$  statistical uncertainty for  $\Omega_c^0$  mode and within  $2.5\sigma$  statistical uncertainty for  $\Xi_c^0$  mode.

Table 3.13 Decay-time fit in each data-taking period. The last column shows the weighted average of the resulting lifetime and  $\chi^2$ /ndf of the combination with least squares method.

		16	17	18	Average
$\Omega_c^0$	$\tau$ [ fs] $\gamma^2$ /ndf	$203 \pm 28$ 9/7	$177 \pm 23$ $11/7$	$160 \pm 20$ $2/7$	$176 \pm 13$
$\Xi_c^0$	τ[ fs]	$73.3 \pm 4.7$		$77.3 \pm 3.6$	$78.7 \pm 2.3$
	$\chi^2$ /ndf	6/6	12/6	9/6	

Table 3.14 Decay-time fit in each data-taking period and magnetic polarity.

		16	17	18
$\Omega_c^0$ MagDown	τ[ fs]	$223 \pm 48$	$164 \pm 25$	$149 \pm 24$
$\Omega_c^0$ MagUp	τ[ fs]	$200 \pm 29$	199 ± 22	$178 \pm 31$
$\Xi_c^0$ MagDown	τ[ fs]	$77.9 \pm 7.0$	$75.5 \pm 5.5$	$80.4 \pm 5.4$
$\varXi_c^0$ MagUp	τ[ fs]	$67.0 \pm 6.5$	$89.4 \pm 6.1$	$73.7 \pm 5.0$

**Reduced decay-time bins.** To check that the measured lifetime dose not vary significantly with the choice of the lower edge of the decay-time region, the decay-time fit is performed with reduced decay-time bins, in which the first two bins in the default binning scheme are removed. The measured lifetime is  $176 \pm 16$  fs for  $\Omega_c^0$  and  $73.8 \pm 3.4$  fs for  $\Xi_c^0$ , both in good agreement with default results within statistical uncertainties.

**Alternative binning scheme.** To check that the measured lifetime is stable w.r.t the choice of binning scheme, an alternative binning scheme,

$$[0.45, 0.49, 0.54, 0.59, 0.65, 0.71, 0.77, 0.84, 0.94, 1.15, 2.00]$$
 ps, (3.17)

is used to perform the lifetime measurement. Fig. 3.42 shows a comparison of the default (in blue) and alternative (in red) binning scheme. The data and simulated samples are split according to the alternative decay-time bins and the procedure to measure lifetimes are repeated. The resulting difference in the measured lifetime is 0.4 fs for  $\Omega_c^0$  and 2.5 fs for  $\Xi_c^0$ , both in good agreement with the nominal results.

#### 3.5.2 Additional checks

Several additional checks are performed to further validate the results.



Figure 3.42 Default (in blue) and alternative (in red) binning scheme in ps.

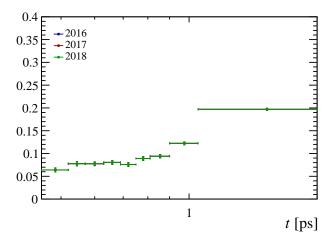


Figure 3.43 Secondary fraction and its uncertainty with shared fractions in 2016-2018.

Fit with shared secondary fractions. The secondary fraction between data-taking periods is found to be different for  $D^0$  control mode. To check that there is no mismodelling effect, we perform the fit to the invariant-mass and  $\log_{10}(\chi_{\text{IP}}^2)$  distribution with secondary fraction  $f_{s,i}$  in each decay time bin shared in 2016-2018 data-taking year. The resultant secondary fractions are shown in Fig. 3.43. The relative difference of the  $D^0$  prompt yield in each decay-time bin is shown in Table 3.15.

This effect is propagated to the measured signal lifetimes with pseudoexperiments. In each pseudoexperiment, the prompt data yield  $N_i^{\rm sig}$  and  $N_i^{\rm con}$  in each decay-time bin are sampled from Gaussian distributions whose means are the default prompt yields and widths are the default prompt yield times the relative difference in Table 3.15. Then the  $\chi^2$  fit to the decay time is repeated with the sampled prompt data yields. The resulting lifetime distribution from pseudo-experiments is fitted with a Gaussian function whose width is taken as the uncertainty on the measured lifetime. The resultant value is 0.9 fs for  $\Omega_c^0$  lifetime and 0.4 fs for  $\Xi_c^0$  lifetime, which indicates that the effect is under control with the constraint of secondary fraction.

Year	1	2	3	4	5	6	7	8	9
16	3.3	1.1	2.8	2.2	1.9	0.8	0.7	0.9	1.0
17	0.7	0.8	0.3	0.2	0.8	0.5	0.6	0.2	0.3
18	0.7	1.1	0.9	0.8	0.0	0.2	0.4	0.2	0.2

Table 3.15 Relative difference (in %) of the  $D^0$  prompt yield with different fit configuration.

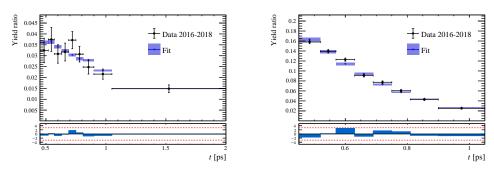


Figure 3.44 Prompt yield ratio of signal to control mode in 2016-2018 data for (left)  $\Omega_c^0$  and (right)  $\Xi_c^0$  mode, along with the fit result.

**Ratios of raw prompt yields.** As a post-unblinding check, the prompt yield ratio of signal to control mode in data,  $N^{\text{sig}}/N^{\text{con}}$ , and the fit result,  $C_{\text{year}} \times F \times M^{\text{sig}}/M^{\text{con}}$ , is show in Fig. 3.44 for 2016-2018 data, and shown in Fig. 3.45 for each data-taking period. Good agreement between the data and the fit can be observed.

# 3.6 Systematic uncertainties

Sources of systematic uncertainties on the measured lifetimes of the  $\Omega_c^0$  and  $\Xi_c^0$  baryon are considered, including:

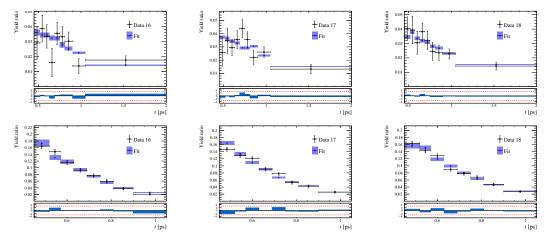


Figure 3.45 Prompt yield ratio of signal to control mode in data for each data-taking period and for (top)  $\Omega_c^0$  and (bottom)  $\Xi_c^0$  mode, along with the fit result.

- Mismodelling of the prompt signal yield;
- Limited statistics of calibration sample;
- Precision of kinematic correction;
- Input lifetime of the simulation samples;
- Decay time resolution;
- VELO hit error;
- Decay length scale;
- Uncertainty of  $D^0$  lifetime;
- $D^0$  mixing.

In general, systematic uncertainties are considered by repeating the decay-time fit (and the two-dimensional  $(m, \log_{10}(\chi_{\rm IP}^2))$  fit) with alternative configurations. The numerical results are summarised in Table 3.16 and are discussed in the following subsections in detail.

### 3.6.1 Modelling of prompt yield

As mentioned in Sec. 3.3, several parameters in the signal model are fixed to values obtained from simulation. The effect on the fitted yield is studied with the  $D^0$  control mode by removing these constraints of parameters in the alternative fits by turns, including  $\sigma_p$ ,  $\sigma_s$ ,  $\xi_p$ ,  $\xi_s$ ,  $\rho_{1p}$ ,  $\rho_{1s}$ ,  $\rho_{2p}$ , and  $\rho_{2s}$ .

In the default fit model of prompt yield, parameter  $\Delta \mu_p$  and  $\Delta \mu_s$  in the signal models

Table 3.16 Summary of systematic uncertainties.

Sources	$\varOmega_c^0$ [ fs ]	$\mathcal{\Xi}_{c}^{0}$ [ fs ]
Fit model	2.2	1.0
Limited calibration sample	0.1	0.1
Kinematic correction	3.4	0.4
Decay time resolution	1.3	1.8
VELO hit error	1.1	0.5
Decay length scale	0.1	0.1
$D^0$ mixing	0.8	0.6
Total syst.	4.4	2.2
$D^0$ lifetime	0.7	0.2
Total stat.	13.4	2.3

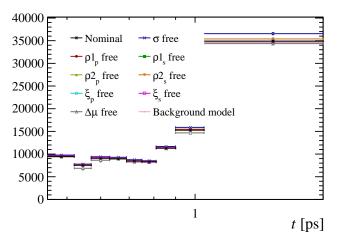


Figure 3.46 Prompt yields of the  $D^0$  mode with alternative configurations in 2016 data.

are shared across decay-time bins. This effect on the fitted yield is studied with the  $D^0$  control mode by allowing them to be different in each decay-time bins in the alternative fits.

The background  $\log_{10}(\chi_{\text{IP}}^2)$  distribution is modelled with data in the invariant-mass sideband. An alternative background distribution obtained with the background sWeights from the invariant-mass fit is used in the alternative fits to estimate the bias due to the background modelling.

Prompt yields obtained in these alternative fits are shown in Fig. 3.46 for the 2016  $D^0$  sample. Taking half of the difference between the maximum and minimum yield in each bin as systematic uncertainty, the relative uncertainty of the prompt yield in each bin is

$$[2.2, 6.1, 4.2, 2.3, 2.9, 2.1, 2.1, 4.0, 3.1]\%.$$
 (3.18)

The uncertainty due to the fit model is propagated to the measured decay time with pseudoexperiments. In each pseudoexperiment, the prompt data yields  $N_i^{\text{sig}}$  and  $N_i^{\text{con}}$  in each bin are sampled from Gaussian distributions whose means are the nominal prompt yields and widths are the nominal prompt yield times the relative systematic uncertainty. Then the chi-squared fit to the decay time is repeated with the sampled prompt data yields. The resulting lifetime distribution from pseudoexperiments is fitted with a Gaussian function whose width is taken as the systematic uncertainty. The numerical result is shown in Table 3.16.

### 3.6.2 Limited statistics of calibration samples

As discussed in Sec. 3.4, calibration data samples are used to correct for some datasimulation discrepancy. We consider the systematic uncertainties due to limited statistics of calibration data samples with pseudo-experiments. For this purpose, the calibration efficiency tables obtained from calibration data are varied by changing the value in each bin according to its value and uncertainty assuming Gaussian distribution in each pseudoexperiment. Then the per-event weights are re-evaluated and the chi-squared fit is performed with fluctuated weights to obtain the lifetime. The width of the distribution of the measured lifetime is assigned as systematic uncertainty.

The procedure is performed for PID and L0 efficiency tables. For PID efficiency, the width is found to be negligible for both  $\Omega_c^0$  and  $\Xi_c^0$  mode. This is expected as the PID efficiency is only weakly time-dependent. For L0 efficiency, the width is found to be 0.13 fs for  $\Omega_c^0$  mode and 0.06 fs for  $\Xi_c^0$  mode.

#### 3.6.3 Kinematic corrections

As discussed in Sec. 3.4.5, per-event weights are applied to simulation samples to correct for the data-simulation discrepancy in kinematic distributions ( $p_T$  and y of the charmed hadron and  $p_T$  of the final-state particles). The binned prompt background subtracted data distribution is obtained by performing two-dimensional mass and  $\log_{10}(\chi_{IP}^2)$  fits in bins of the variable under consideration. The precision of the kinematic correction is largely limited by the statistical uncertainty of the data distribution obtained from the fit, especially for the  $\Omega_c^0$  mode.

The effect of the uncertainty of the correction factors on the measured lifetime is quantified with pseudo-experiments. In each pseudoexperiment, the binned prompt background subtracted kinematic distributions in data are fluctuated, following Gaussian distribution, according to its value and uncertainty in each bin, and the per-event weight of kinematic correction is re-calculated. The decay time is then measured with re-calculated per-event weight. A fit to the resulting distribution of measured decay time is performed with a Gaussian function, whose width is taken as the systematic uncertainty due to the limited precision of the kinematic correction. The numerical results for  $\Omega_c^0$  and  $\Xi_c^0$  mode are shown in Table 3.16.

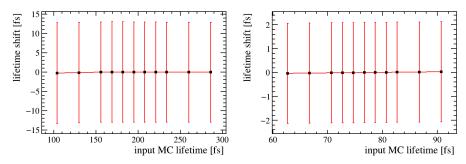


Figure 3.47 Measured lifetimes of (left)  $\Omega_c^0$  and (right)  $\Xi_c^0$  baryon with different input lifetimes of simulated samples. The *x*-axis is blinded.

## 3.6.4 Input lifetime of simulated samples

Simulated signal samples used in the nominal fit is generated with an input lifetime of  $\tau_0=250\,\mathrm{fs}$  for both  $\Xi_c^0$  and  $\Omega_c^0$  signal modes. To study the effect of different input lifetimes, the simulated samples are re-weighted w.r.t. the true decay time  $t_{\mathrm{true}}$  by

$$w(t_{\text{true}}) = \frac{\frac{1}{\tau} \exp(-\frac{t_{\text{true}}}{\tau})}{\frac{1}{\tau_0} \exp(-\frac{t_{\text{true}}}{\tau_0})}$$
(3.19)

to several alternative lifetimes  $\tau$ . The alternative lifetimes are chosen to be values within about seven times statistical uncertainty region of the measured central value. The chi-squared fit to the decay time is repeated with the alternative prompt simulation yield  $M_i$ . The resulting difference in lifetime with different input lifetimes is negligible, as shown in Fig. 3.47. Note that the x-axis is blinded in Fig. 3.47.

## 3.6.5 Decay-time resolution

In the default fit, the decay-time resolution is taken as modeled by simulation. The distributions of the difference of reconstructed and true decay time in simulation are shown in Fig. 3.51 for all modes. The decay-time resolutions are estimated by fitting with a Gaussian function and are found to be 57 fs, 65 fs, and 56 fs for  $\Omega_c^0$ ,  $\Xi_c^0$ , and  $D^0$  modes, respectively.

The control mode  $D^{*+} \to \pi^+ D^0 (\to K^- K^+ \pi^- \pi^+)$  is used to quantify the level of difference of decay-time resolution between data and simulation. The decay time is defined in Eq. 2.6 and the most important contribution to the decay-time resolution is the resolution of the decay vertex of the charmed hadron. To be able to compare the resolution observed in data and in simulation, we calculate the  $D^0$  decay-time with the  $D^0$  decay vertices reconstructed with both  $K^-\pi^+$  and  $K^+\pi^-$  final-state tracks denoted as  $t_{K^-\pi^+}$  and  $t_{K^+\pi^-}$ , respectively. The difference of  $t_{K^-\pi^+}$  and  $t_{K^+\pi^-}$  is taken as a measure of the decay-

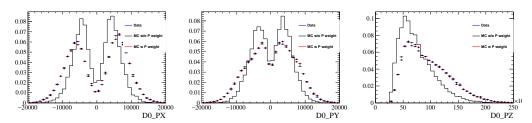


Figure 3.48 Momentum distributions of  $D^0$  in 2018 data and simulation for  $D^0$  sample.

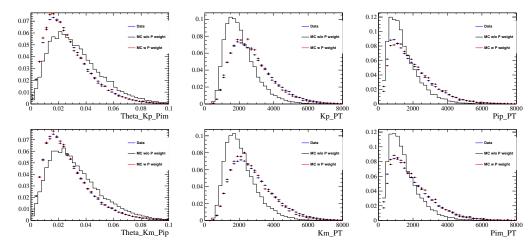


Figure 3.49 Distributions of (left) the angle between  $D^0$  daughters and (middle and right)  $p_T$  of  $D^0$  daughters in 2018 data and simulation.

time resolution.

To minimize the difference introduced due to kinematic effects, several corrections are applied to MC, including the tracking efficiency, the PID efficiency, the efficiency due to the hTOS requirement, and phasespace distributions. The momentum of  $D^0$  between data and simulation are also re-weighted to be the same, as shown in Fig. 3.48. We also check some other variables related to the decay time resolution, including the angle between  $K^-\pi^+$  ( $K^+\pi^-$ ) from  $D^0$ ,  $p_T$  of  $D^0$  daughters, as shown in Fig. 3.49.

The distribution of  $t_{K^-\pi^+} - t_{K^+\pi^-}$  in data and MC are shown in Fig. 3.50. A maximum likelihood fit is performed to extract the resolution. The distribution of  $t_{K^-\pi^+} - t_{K^+\pi^-}$  can be well described by a double Gaussian function defined as

$$G(x; m_0, \sigma_t) = f \times G_{\text{Gaussian1}}(x) + (1 - f) \times G_{\text{Gaussian2}}(x), \tag{3.20}$$

and the effective resolution is  $\sigma_t = \sqrt{f \times \sigma_{t1}^2 + (1-f) \times \sigma_{t2}^2}$ . The fit results show that the difference between data and MC is about 10%. In the pseudo-experiment below, a conservative value of 20 fs is used as the difference of resolution between data and simulation.

The effect of different decay-time resolution in data and simulation is estimated with

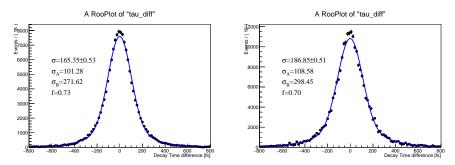


Figure 3.50 The fit result of  $t_{K^-\pi^+} - t_{K^+\pi^-}$  in (left) data and (right) MC.

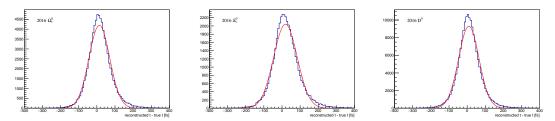


Figure 3.51 Distributions of the difference of reconstructed and true decay time in 2016 simulation for (left)  $\Omega_c^0$ , (middle)  $\Xi_c^0$ , and (right)  $D^0$  modes.

pseudo-experiments for both  $\Omega_c^0$  and  $\Xi_c^0$  mode. The pseudo-experiment is performed as follows:

1. Generate pseudo-data and pseudo-mc samples according to

$$(\exp(-t/\tau) \times Acc(t)) * Gaussian(\sigma_t), \tag{3.21}$$

where  $\tau$  is the input lifetime in simulation, Acc(t) is the decay-time acceptance obtained from simulation, and  $\sigma_t$  is the decay-time resolution. The decay-time resolution  $\sigma_t$  is different by 20 fs in pseudo-data and pseudo-mc samples. Cases in which the resolution is either larger in data or in simulation are both considered. The total yield of the pseudo-data sample is normalised to that of the real data sample.

- 2. The chi-squared fit to the decay time is performed with pseudo-data and pseudo-mc samples, following the same procedure as the nominal fit.
- 3. Repeat the above two steps to get the distribution of difference between measured and input lifetimes.
- 4. Fit the distribution of difference with a Gaussian distribution. The mean value of the Gaussian distribution is taken as the bias due to decay-time resolution.

The distribution of difference between measured and input lifetimes is shown in Fig. 3.52. Taking the maximum bias in both cases, the systematic uncertainty due to decay-time resolution is 1.31 fs and 1.81 fs for  $\Omega_c^0$  and  $\Xi_c^0$  modes, respectively.

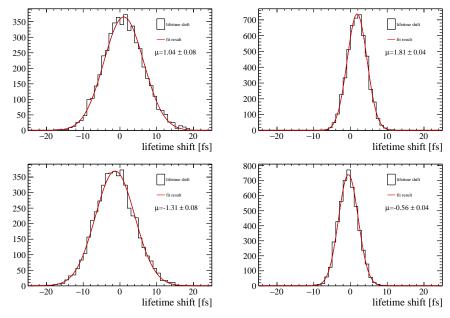


Figure 3.52 Distributions of difference between measured lifetimes and input lifetimes in pseudo-experiments. Cases in which the resolution is either 20 fs larger in data (top) or in simulation (bottom) are shown for both (left)  $\Omega_c^0$  and (right)  $\Xi_c^0$  modes.

## 3.6.6 Change of VELO hit error parametrization

As discussed in Sec. A.1, the change of VELO hit error parametrization in 2017–2018 data can lead to a worse time-dependent agreement between data and simulation, and this effect is corrected in the nominal fit by applying a scaling factor to  $\chi_{\rm IP}^2$  variables of the final-state particles for 2017–2018 simulation samples.

The uncertainty on the scaling factor is obtained by making the  $\chi^2$  test of the binned  $\chi^2_{\rm IP}$  distributions in 2016 and 2018 data with different scaling factors. A curve of scaling factor vs compatibility (in this case the  $\chi^2$  from the  $\chi^2$  test with the degrees of freedom of 50) is shown in Fig. 3.53. The range corresponding to one sigma internal is taken as the uncertainty of the scaling factor, which is about 0.03. The difference between the nominal lifetime and the alternative lifetime obtained with a scaling factor of unit is 1.8 fs for  $\Omega^0_c$  and 0.8 fs for  $\Xi^0_c$ . The systematic uncertainty due to the uncertainty of the scaling factor is estimated by scaling the above difference with 0.03/0.05, which leads to 1.1 fs for  $\Omega^0_c$  and 0.5 fs for  $\Xi^0_c$ .

## 3.6.7 Decay length scale

The calculation of decay time requires information of the flight distance between the original vertex (in this case PV) and the decay vertex. The precision of this distance is dependent on the precision with which the relative position along the beam line (*z*-axis)

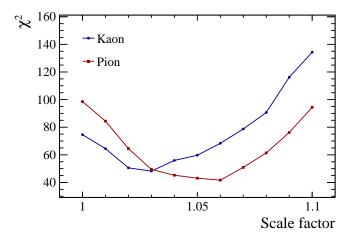


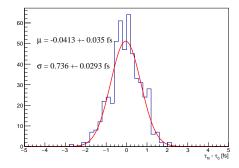
Figure 3.53 The curve of scaling factor vs compatibility for (blue) Kaon and (red) Pion tracks from  $D^0$  decay.

of the LHCb modules. There are two contributions: the precision with which the VELO modules were assembled and the track-based alignment. The overall relative uncertainty is assigned to be  $\sigma_{z-scale} = 0.022\%$ , which corresponds to 0.06 fs for  $\Omega_c^0$  and 0.03 fs for  $\Xi_c^0$ .

#### 3.6.8 Hadronic interaction of final-state tracks

In tracking efficiency estimation, the material effects for hadrons mainly come from the hadronic interactions with the material. In most cases the interaction will be inelastic, thereby creating many secondary particles while the original particle cannot be reconstructed anymore. It is known from other LHCb analyses that about 14% of the pions, 11% of the kaons, and 22% of the protons cannot be reconstructed due to hadronic interactions that occur before the last tracking station. The MC simulation describes all the material effects discussed above. However, due to the uncertainty on the material budget and on the cross sections, the reconstruction efficiency obtained from simulation has an intrinsic uncertainty. When assuming that the total material budget in the simulation has an uncertainty of 10% following LHCb-PUB-2011-025, the systematic uncertainty due to material interactions is 1.4%, 1.1%, and 2.2% for pion, kaon, and proton, respectively.

Given the origin of this uncertainty, the systematic uncertainty on hadronic interaction of tracks is assumed to be correlated for different types, decay time bins and data-taking years and propagated to the measured lifetime with pseudo-experiments. In each pseudo-experiment, the efficiency in each decay time bin is varied according to the systematic uncertainty due to material interactions and the width of the distribution of measured lifetime is assigned as systematic uncertainty. The value is found to be  $6.5 \times 10^{-3}$  fs for



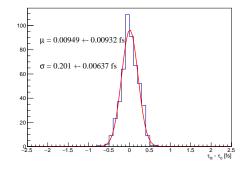


Figure 3.54 Distribution of the measured lifetime of (left)  $\Omega_c^0$  and (right)  $\Xi_c^0$  with randomized  $\tau^{\rm con}$  in the decay-time fit.

 $\Omega_c^0$  and  $1.1 \times 10^{-2}$  for  $\Xi_c^0$ , which is negligible compared to other systematic uncertainties.

# 3.6.9 Uncertainty of the $D^0$ lifetime

The four-body  $D^0$  decay is taken as the control channel of this measurement, and the lifetime of  $D^0$  used in the decay-time fit is the PDG value of 410.1 fs. The limited precision of  $D^0$  lifetime, 1.5 fs, is propagated to the measured lifetime of  $\Omega_c^0$  and  $\Xi_c^0$  with pseudo-experiments. In each pseudo-experiment, the lifetime of  $D^0$ ,  $\tau^{\rm con}$ , in Eq. 3.15 is randomized according to the Gaussian with the mean of 410.1 fs and the standard deviation of 1.5 fs, and the decay-time fit is repeated. Then the spread in the distribution of the measured lifetime is taken as the systematic uncertainty, as shown in Fig. 3.54. The resultant uncertainty is 0.7 fs for  $\Omega_c^0$  and 0.2 fs for  $\Xi_c^0$ .

# **3.6.10** $D^0$ mixing

The charm mixing of the  $D^0$  meson is neglected in the nominal measurement. As we do not distinguish  $D^0$  and  $\bar{D}^0$  in the analysis, the total time dependent decay rate is

$$\frac{d\Gamma(D^0)}{dt} + \frac{d\Gamma(\bar{D}^0)}{dt} = N_f e^{-t/\tau} \{ (|A_f|^2 + |\bar{A}_f|^2) \cosh(yt/\tau) - 2Re(A_f^* \bar{A}_f) \sinh(yt/\tau) \}$$
(3.22)

assuming |q/p| = 1 and arg(q/p) = 0. When y (0.00645 in PDG20) is small, we have (up to the first order in Taylor expansion of y)

$$\frac{d\Gamma(D^0)}{dt} + \frac{d\Gamma(\bar{D}^0)}{dt} = N_f e^{-t/\tau} (|A_f|^2 + |\bar{A}_f|^2) \{1 - \frac{2Re(A_f^* \bar{A}_f)}{(|A_f|^2 + |\bar{A}_f|^2)} yt/\tau \}. \tag{3.23}$$

 $F_{+}^{KK\pi\pi}$  is defined as

$$F_{+} \equiv \frac{\int |A_{+}|^{2}}{\int |A_{+}|^{2} + |A_{-}|^{2}}, A_{+} = A + \bar{A}, A_{-} = A - \bar{A}, \tag{3.24}$$

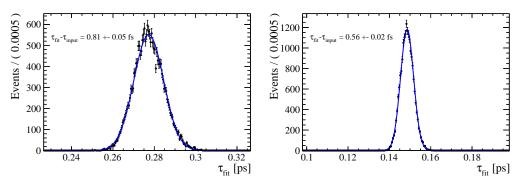


Figure 3.55 Distribution of the measured lifetime of (left)  $\Omega_c^0$  and (right)  $\Xi_c^0$ .

so we have

$$F_{+} = \frac{\int \{|A|^{2} + |\bar{A}|^{2} + 2Re(A\bar{A}^{*})\}}{\int 2(|A|^{2} + |A|^{2})}.$$
 (3.25)

Thus,

$$2F_{+} - 1 = \frac{\int 2Re(A\bar{A}^{*})}{\int (|A|^{2} + |A|^{2})}.$$
 (3.26)

 $F_{+}$  is measured to be  $(75.3 \pm 1.8 \pm 3.3 \pm 3.5)\%$  [181].

The impact of  $D^0$  mixing is taken into account with pseudo-experiments. In each pseudo-experiment, the data distribution of  $D^0$  mode is generated assuming a decay time distribution of 3.22, with parameters of y and  $F_+$  taken its measured value. Other components are generated according to the exponential distribution. Then the nominal  $\chi^2$  fit is performed to obtained the lifetime, i.e., no mixing is considered in the construction of  $\chi^2$ . An unbinned maximum likelihood fit with a Gaussian function is performed to the distribution of the obtained lifetime. The difference of the mean of the Gaussian function w.r.t to the input lifetime in toy generation is taken as the systematic uncertainty. The resultant uncertainty is 0.81 fs for  $\Omega_c^0$  and 0.56 fs for  $\Xi_c^0$ .

### 3.7 Result and discussion

In summary, a measurement of the lifetimes of the  $\Omega_c^0$  and  $\Xi_c^0$  baryons is reported with  $\Omega_c^0$  and  $\Xi_c^0$  baryons produced directly in proton–proton collisions at a centre-of-mass energy of 13 TeV, corresponding to an integrated luminosity of 5.4 fb<sup>-1</sup> collected by the LHCb experiment. The  $\Omega_c^0$  lifetime is measured to be

$$\tau_{\Omega_c^0} = 276.5 \pm 13.4 \pm 4.4 \pm 0.7 \text{ fs},$$

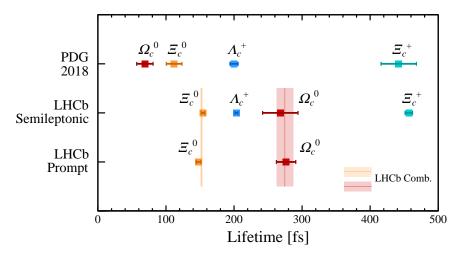


Figure 3.56 Comparison of current, previous and combined LHCb results.

and the  $\Xi_c^0$  lifetime is measured to be

$$\tau_{\Xi_c^0} = 148.0 \pm 2.3 \pm 2.2 \pm 0.2 \text{ fs},$$

where the first uncertainty is statistical, the second systematic, and the third due to the uncertainty of the  $D^0$  lifetime. This result is consistent with the previous LHCb measurements of the  $\Omega_c^0$  and  $\Xi_c^0$  lifetimes, using signals from semileptonic beauty baryon decays [45-46], and confirms the new charmed-baryon lifetime hierarchy of  $\tau_{\Xi_c^+} > \tau_{\Omega_c^0} > \tau_{\Lambda_c^+} > \tau_{\Xi_c^0}$ . The precision of the  $\Omega_c^0$  lifetime is improved by a factor of two compared with that of the previous result [45].

This result is independent of previous LHCb measurements [45-46] due to the use of independent data sample and analysis technique. Combining this measurement with previous LHCb measurements [45-46], given that both the statistical uncertainties and the dominant systematic uncertainties are uncorrelated, results in the weighted average lifetimes of

$$\tau_{\Omega_c^0} = 274.5 \pm 12.4 \text{ fs},$$

$$\tau_{\Xi_c^0} = 152.0 \pm 2.0 \text{ fs}.$$

The uncertainty includes both the statistical and systematic uncertainties. A visual comparison is given in Fig. 3.56.

Recent theoretical efforts have been made to consider dimension-seven operators (up to order  $1/m_Q^4$ ) in heavy quark expansion [34,182-183], including four-quark operators times the spectator quark mass and four-quark operators with an additional derivative. The  $1/m_Q^4$  correction brings the lifetime ratio of  $\Xi_c^+$  to  $\Lambda_c^+$  more close to the measured value, indicating that higher order corrections are in the right direction. However, the

# CHAPTER 3 MEASUREMENT OF $\Omega_c^0$ AND $\Xi_c^0$ LIFETIMES

 $1/m_Q^4$  correction will lead to a negative semileptonic decay width of  $\Omega_c^0$  baryon, indicating unknown suppressions due to baryon matrix elements or other high order operators. Nevertheless, the new lifetime hierarchy of charmed baryon lifetime confirmed in this measurement can be conjectured by requiring that the semileptonic width of  $\Omega_c^0$  baryon to be positive and comparable to that of  $\Lambda_c^+$  and  $\Xi_c$ . In general, theoretical activity concerning the intriguing lifetime of  $\Omega_c^0$  is largely absent and desirable.

# CHAPTER 4 SEARCH FOR THE DOUBLY CHARMED BARYON $\varXi_{cc}^+$

This chapter reports a search for the doubly charmed baryon  $\Xi_{cc}^+$  through the  $\Lambda_c^+K^-\pi^+$  decay channel [150]. This search is an update of the previous LHCb search, with a more than ten times larger data set and the improved analysis method. An overview of the data analysis strategy and method is presented in Sec. 4.1. Event selection, which is the key to observation of rare signals, is discussed extensively in Sec. 4.2. The strategy for measuring the mass of  $\Xi_{cc}^+$  baryon is presented in Sec. 4.3. Distributions of the invariant mass of  $\Xi_{cc}^+$  baryon is shown in Sec. 4.4. With the lack of significant signals, upper limits are set relative to two control modes in Sec. 4.5. To conclude, result and its interpretation are presented in Sec. 4.6.

### 4.1 Analysis overview

In this analysis, a search for the  $\Xi_{cc}^+$  baryon through  $\Lambda_c^+K^-\pi^+$  final state was reported. The contributing tree-level Feynman diagram with internal W-emission is shown in Fig. 4.1. This final state is chosen given a) a large predicted branching fraction of the doubly charmed baryon decay; b) a large decay branching fraction of subsequent  $\Lambda_c^+$  decay; c) decay products are all charged particles that are easy to detect. The data samples collected by the LHCb detector during Run 1 and Run 2 of the LHC are used corresponding to an integrated luminosity of 9 fb<sup>-1</sup>, as detailed in Appendix A. The  $\Lambda_c^+$  baryon is reconstructed through the  $pK^-\pi^+$  final state. The searching mass window is chosen to be 3.4-3.8 GeV, which centered at the  $\Xi_{cc}^{++}$  mass measured by the LHCb experiment [132], and covers most theoretical predictions of the mass of ground-state  $\Xi_{cc}^+$  baryon, as well as the  $\Xi_{cc}^+$  (3520) state reported by the SELEX experiment [137]. It is interesting to notice that this window also covers the mass of  $\Omega_{cc}^+$  baryon decaying to the same final state.

Since this analysis is a search for nonestablished particles and in order to avoid experimentalists' subjective bias, the signal window was not examined nor used in the development of the analysis until the whole analysis procedure was reviewed and finalised. When the green light to unblind is given, we may find ourselves in two different situations, well-defined by the significance of the signal structure in Sec. 4.1.1. If any significant peak structure consistent with the  $\Xi_{cc}^+$  baryon is observed, as we hope, the  $\Xi_{cc}^+$  mass will be

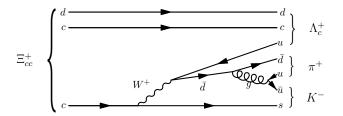


Figure 4.1 The contributing tree-level Feynman diagram with internal W-emission for the decay of  $\Xi_{cc}^+ \to \Lambda_c^+ K^- \pi^+$ .

measured. If not, upper limits on the ratio of production cross-section times branching fraction between the signal and the control mode will be set. Two control modes are chosen as the reference: the prompt  $\Lambda_c^+$  baryon reconstructed through  $pK^-\pi^+$  final state and the  $\Xi_{cc}^{++}$  baryon reconstructed through  $\Lambda_c^+K^-\pi^+\pi^+$  final state, with  $\Lambda_c^+\to pK^-\pi^+$ . The ratios of the production cross-section times branching fraction are defined as

$$R(\Lambda_c^+) \equiv \frac{\sigma(\Xi_{cc}^+) \times \mathcal{B}(\Xi_{cc}^+ \to \Lambda_c^+ K^- \pi^+)}{\sigma(\Lambda_c^+)},$$

$$R(\Xi_{cc}^{++}) \equiv \frac{\sigma(\Xi_{cc}^+) \times \mathcal{B}(\Xi_{cc}^+ \to \Lambda_c^+ K^- \pi^+)}{\sigma(\Xi_{cc}^{++}) \times \mathcal{B}(\Xi_{cc}^{++} \to \Lambda_c^+ K^- \pi^+ \pi^+)}.$$
(4.1)

The  $R(\Lambda_c^+)$  gives us an idea on the ratio between the production cross-sections of the doubly charm and the singly charm. It can be compared with the previous LHCb search, as well as the SELEX search. The  $R(\Xi_{cc}^{++})$  tells us the combined information of relationship of the branching fractions and lifetimes between  $\Xi_{cc}^+ \to \Lambda_c^+ K^- \pi^+$  and  $\Xi_{cc}^{++} \to \Lambda_c^+ K^- \pi^+ \pi^+$  decays, as the production cross-sections of the  $\Xi_{cc}^+$  baryon is expected, with great reason, to be similar to that of the  $\Xi_{cc}^{++}$  baryon.

The displace decay vertices of charmed baryons serve as a signature in both the trigger and offline selection. Consequently, the lifetime of the weakly decaying particle has an significant effect on the selection efficiency. According to the theoretical predictions and the measurement of  $\Xi_{cc}^{++}$  lifetime, the lifetime value of  $\tau_{\Xi_{cc}^{+}} = 80$  fs is used as the default value for the development of event selection, corresponding to around one third of that of the  $\Xi_{cc}^{++}$  baryon. A dedicated multivariate classifier is also trained, assuming the lifetime of  $\Xi_{cc}^{+}$  is negligible.

## 4.1.1 Strategy for evaluating significance and setting limits

To be quantitative, we describe the criteria of choosing different paths. In the discussion below, we will refer to local and global significances. By a local significance, we mean the significance of a signal evaluated for one particular mass hypothesis. By a

global significance, we mean the significance of a signal in the whole mass range taking into account the look-elsewhere effect (LEE). That is, the global significance reflects the probability under the null hypothesis for such a signal to pop up anywhere in the mass range scanned.

In the previous  $\Xi_{cc}^+ \to \Lambda_c^+ K^- \pi^+$  search, carried out on the 2011 data, we evaluated local and global significances for a search range of 500 MeV. It is found that there was a factor of roughly 30 between the local and global *p*-values. (This makes intuitive sense to within a factor of two or so: the resolution was roughly 5 MeV, so if you imagine dividing the data into disjoint  $\pm 2\sigma$  chunks you have 25 such chunks.) To put this into context, here is how the integral of a Gaussian distribution for various intervals (*i.e.* the relation between significance and *p*-value):

Range around peak	Integral outside range
±1σ	$3.2 \times 10^{-1}$
$\pm 2\sigma$	$4.6 \times 10^{-2}$
±3σ	$2.7 \times 10^{-3}$
$\pm 4\sigma$	$6.3 \times 10^{-5}$
±5σ	$5.7 \times 10^{-7}$
±6σ	$2.0 \times 10^{-9}$
±7σ	$2.6 \times 10^{-12}$

The key point is that this relation is highly nonlinear. For significances of  $2-3\sigma$ , the LEE is an important correction. (If the local/global factor is about 30, it will turn a local significance of  $3\sigma$  into a global significance of well under  $2\sigma$ , for example.) But for high significances it is much less important: the difference in *p*-value between  $5\sigma$  and  $6\sigma$  is a factor of around 300, for example. As a consequence, the LEE is only important for results that are marginally significant.

Depending on what we see in data, we will need to choose one of a few different paths:

- If there is a peak whose local significance is above  $6\sigma$ , we will quote that local significance (along with how it was evaluated) but will not fuss with a LEE correction. We will measure its mass and yield in a fit to the invariant mass distribution.
- If there is a peak whose local significance is moderate (3–6 $\sigma$ ), we will compute an LEE correction and quote both local and global significances. If the global significances.

nificance remains above  $3\sigma$ , we will measure the mass and yield as above. If the global significance is below  $3\sigma$ , we will quote upper limits on the production rate (see below) as a function of the reconstructed mass of  $\Xi_{cc}^+$  candidates for different lifetime hypotheses.

• If there is no peak at even  $3\sigma$  local, we will quote upper limits as above.

#### 4.2 Event selection

In this section, the selection criteria are shown for the  $\Xi_{cc}^+ \to \Lambda_c^+ K^- \pi^+$  signal mode. The whole reconstruction and selection sequence is similar to that of the singly charmed baryon, except that there are two intermediate states ( $\Xi_{cc}$  and  $\Lambda_c^+$  baryon), and hence two decay vertices instead of one in the decay chain. The selection is developed with the 2016 data and simulation samples, which is representative of the major data sets, and are applied to the datasets of other data-taking years without reoptimisation.

In this analysis, the  $\Lambda_c^+$  mass window is defined to be [2270,2306] MeV, corresponding roughly to  $\pm 3\sigma_m$  around the known  $\Lambda_c^+$  mass [2], where  $\sigma_m$  refers to the invariant mass resolution of  $\Lambda_c^+$  baryon. The  $\Xi_{cc}^+$  mass window is defined to be [3300,3800] MeV, which covers most of the theoretical predictions of the  $\Xi_{cc}^+$  baryon mass.

#### 4.2.1 Trigger selection

**L0 trigger.** To retain maximal statistic power, no specific L0 trigger lines are required, which means every event that is L0-triggered will be considered in following steps.

**HLT1 trigger.** The software trigger has evolved between Run 1 and Run 2 and between different data-taking years during Run 2, to reflect the improvement of algorithm and increase of computational resources, as discussed in Sec. 2.2.1.

For data samples taken in 2011-2012, the Hlt1TrackAllL0 TOS is required on  $\Lambda_c^+$  candidates. For 2016 data, the HLT1 TOS requirement Hlt1TrackMVA||Hlt1TwoTrackMVA| is embedded in the HLT2 line to  $\Lambda_c^+$  candidates. Details of these two HLT1 lines are discussed in Sec. 2.2.4. For 2017-2018 data, the HLT1 TOS requirement Hlt1TrackMVA||Hlt1TwoTrackMVA|| is removed in the HLT2 line to increase the trigger efficiency.

**HLT2 trigger.** For 2011-2015 data, the offline exclusive Stripping line is the counterpart of the exclusive HLT2 line in 2016-2018. Therefore, they are introduced here instead of as a part of the offline selection. The selection requirements are summarised in Table 4.1 and are introduced below:

- Selection of  $\Lambda_c^+$  decay products. The  $\Lambda_c^+$  candidates are reconstructed in the  $pK^-\pi^+$  final state. Three tracks used to reconstruct the  $\Lambda_c^+$  candidate are required to have a large transverse momentum, a good track quality, and not to originate from any PV. PID requirements are imposed on all three tracks to suppress combinatorial background and misidentified charmed meson decays.
- Selection of the  $\Lambda_c^+$  candidate. The  $\Lambda_c^+$  vertex is required to be displaced from its PV. The  $\Lambda_c^+$  candidate is required to have a mass in the range of 2211-2362 MeV, and to be consistent with originating from its PV.
- Selection of  $\Xi_{cc}^+$  decay products. The  $\Xi_{cc}^+$  candidates are reconstructed by combining a  $\Lambda_c^+$  candidate with two tracks, one identified as a  $K^-$  and one as a  $\pi^+$ . The kaon and pion tracks are required to have a large transverse momentum and a good track quality. These three tracks are required to form a common vertex. To suppress duplicate tracks, the angle between each pair of final-state tracks with the same charge is required to be larger than 0.5 mrad.
- Selection of the  $\Xi_{cc}^+$  candidate. The  $\Xi_{cc}^+$  candidate is required to have  $p_T > 4$  GeV/c and to originate from its PV. Similar requirements are imposed to reconstruct the  $\Xi_{cc}^{++}$  candidates in the  $\Xi_{cc}^{++}$  normalization mode, with an additional  $\pi^+$  in the final state.

For 2017-2018 data, the DIRA cut on  $\Lambda_c^+$  candidates is looser compared to that in 2016 data, which reflects the improved knowledge of the  $\Xi_{cc}^+$  lifetime after the observation of the  $\Xi_{cc}^{++}$  baryon. For 2012 data, an additional HLT2 requirement of Hlt2CharmHadLambdaC2KPPi TOS is applied to  $\Lambda_c^+$  candidates, which is dedicated to charm baryon studies in Run 1 and is shown in Table 4.2.

#### 4.2.2 Offline preselection

After the trigger selection, the  $\Xi_{cc}^+$  candidates are refitted with DecayTreeFitter (DTF) and additional preselection is applied. The DTF is performed to the whole decay chain, and the  $\Xi_{cc}^+$  candidate is constrained to originate from its PV. Details of the preselection is shown in Table 4.3. The purpose is to have high overall signal efficiency while cleaning up most of the obvious combinatorial or misidentification backgrounds.

Table 4.1 HLT2 selection requirements for  $\Xi_{cc}^+$  candidate.

Particle         Variable         Requirements           Particle         2011–2015         2016         2017–2018           Ran and Pion Momentum         > 2 GeV         > 1 GeV         > 1 GeV           Proton momentum         > 2 GeV         > 1 GeV         > 0.2 GeV           Arithmetic sum of daughter $ρ_T$ -         > 3 GeV         > 0.2 GeV           Arithmetic sum of daughter $ρ_T$ -         > 3 GeV         > 0.4 GeV           Maximum of daughter $ρ_T$ -         > 3 GeV         > 0.4 GeV           Maximum of daughter $χ_H^2$ -         > 0.4 GeV         > 0.4 GeV           Λ <sub>c</sub> <sup>*</sup> daughter         Second maximum of daughter $χ_H^2$ -         > 9         > 9           Maximum of daughter $χ_H^2$ -         > 9         > 9           HASRICH         1         1         16         > 16           Proton particle ID DLL <sub>ps</sub> > 5         > 5         > 5         > 5           Proton particle ID DLL <sub>ps</sub> > 0         > 5         > 5         > 5         > 5         > 5         > 5         > 5         > 5         > 5         > 5         > 5         > 5         > 5         > 5         > 5         > 5         > 5         > 5					
Track $χ^2$ /ndf   < 5   < 3   < 3   < 3	Particla Variable		Requirements		
$ \begin{array}{c ccccccccccccccccccccccccccccccccccc$	1 article	variable	2011–2015	2016	2017–2018
$ \begin{array}{c ccccccccccccccccccccccccccccccccccc$		Track χ²/ndf	< 5	< 3	< 3
$ \begin{array}{c ccccccccccccccccccccccccccccccccccc$		Kaon and Pion Momentum	> 2 GeV	> 1 GeV	> 1 GeV
$A_c^+ \text{ daughter } P_T = - \\ Naximum \text{ of daughter } P_T = - \\ Naximum  of daugh$		Proton momentum	> 2 GeV	> 10 GeV	> 10 GeV
$A_c^+ \text{ daughter } P_T                                  $		Transverse momentum	> 0.25 GeV	> 0.2 GeV	> 0.2 GeV
Second maximum of daughter $p_T$ - $>0.4  \mathrm{GeV}$ $>0.4  \mathrm{GeV}$ $\chi_{\mathrm{p}}^{+}$ to $\mathrm{PV}$ $>4$ $>6$ $>6$ $>6$ Maximum of daughter $\chi_{\mathrm{p}}^{-}$ $>4$ $>16$ $>16$ Second maximum of daughter $\chi_{\mathrm{p}}^{-}$ $>9$ $>9$ $>9$ HASRICH $= 100000000000000000000000000000000000$		Arithmetic sum of daughter $p_T$	_	> 3 GeV	> 3 GeV
$A_c^+ \   daughters \\ A_c^+ \   daughter$		Maximum of daughter $p_T$	-	> 1 GeV	> 1 GeV
$ \begin{array}{c ccccccccccccccccccccccccccccccccccc$		Second maximum of daughter $p_T$	-	> 0.4 GeV	> 0.4 GeV
	$\Lambda_c^+$ daughters	$\chi_{\rm IP}^2$ to PV	> 4	> 6	> 6
		Maximum of daughter $\chi_{\text{IP}}^2$	> 4	> 16	> 16
		Second maximum of daughter $\chi_{\rm IP}^2$	_	> 9	> 9
		HASRICH	1		
		Proton particle ID $DLL_{p\pi}$	> 5	> 5	> 5
$ \begin{array}{c ccccccccccccccccccccccccccccccccccc$		Proton particle ID $DLL_{pK}$	> 0	> 5	> 5
		Kaon particle ID $\mathrm{DLL}_{K\pi}$	> 5	> 5	> 5
$A_c^+ \begin{tabular}{lllllllllllllllllllllllllllllllllll$		Pion particle ID $\mathrm{DLL}_{K\pi}$	< 0	< 5	< 5
Maximum DOCA < 0.5 mm		Transverse momentum	> 1 GeV		
$ A_c^+ & \text{Cosine of decay angle (DIRA)} & > 0.99 & > 0.99995 & > 0 \\ & \text{Vertex distance } \chi^2 & > 16.0 & & & > 0.15 \text{ ps} \\ & \text{Decay time} & & & > 0.15 \text{ ps} & > 0.15 \text{ ps} \\ & \text{Invariant mass [MeV]} & (2211,2362) & (2211,2362) & (2211,2362) \\ & & & & & & & & & & & & & & & & & & $		Vertex $\chi^2_{\rm vtx}/{\rm ndf}$	< 10	< 10	< 10
Vertex distance $\chi^2$ > 16.0           Decay time         > 0.15 ps         > 0.15 ps           Invariant mass [MeV]         (2211, 2362)         (2211, 2362)         (2211, 2362)           Track $\chi^2$ /ndf         < 5		Maximum DOCA	< 0.5 mm		
Decay time         > 0.15 ps         > 0.15 ps           Invariant mass [MeV]         (2211, 2362)         (2211, 2362)         (2211, 2362)           Track $\chi^2$ /ndf         < 5	$arLambda_c^+$	Cosine of decay angle (DIRA)	> 0.99	> 0.99995	> 0
		Vertex distance $\chi^2$	> 16.0		
		Decay time		> 0.15 ps	> 0.15 ps
		Invariant mass [ MeV ]	(2211, 2362)	(2211, 2362)	(2211, 2362)
		Track $\chi^2$ /ndf	< 5	< 3	< 3
$\begin{array}{cccccccccccccccccccccccccccccccccccc$		Transverse momentum	> 0.25 GeV	> 0.5 GeV	> 0.5 GeV
$ \begin{array}{cccccccccccccccccccccccccccccccccccc$	$\varXi_{cc}^+$ daughters	Momentum	> 2 GeV	> 1 GeV	> 1 GeV
Pion particle ID DLL $_{K\pi}$ < 0 < 0 < 0 < 0 Vector sum of daughter $p_{\rm T}$ > 2 GeV > 2 GeV > 2 GeV Vertex $\chi^2_{\rm vtx}/{\rm ndf}$ < 10 < 30 < 30 Maximum DOCA		HASRICH	1		
$\begin{array}{cccccccccccccccccccccccccccccccccccc$		Kaon particle ID $\mathrm{DLL}_{K\pi}$	> 5	> 10	> 10
$ \begin{array}{cccccccccccccccccccccccccccccccccccc$		Pion particle ID $\mathrm{DLL}_{K\pi}$	< 0	< 0	< 0
$\begin{array}{cccccccccccccccccccccccccccccccccccc$		Vector sum of daughter $p_T$	> 2 GeV	> 2 GeV	> 2 GeV
DOCA between $(\Lambda_c^+, \pi^+)$ , $(K^-, \pi^+)$ < 10 mm < 10 mm $\Xi_{cc}^+$ $\Lambda_c^+$ vertex z displacement w.r.t. $\Xi_{cc}^+$ > 0.01 mm > 0.01 mm > 0.01 mm DIRA > 0 > 0 > 0 > 0		Vertex $\chi^2_{\rm vtx}$ /ndf	< 10	< 30	< 30
$\Xi_{cc}^+$ $\Lambda_c^+$ vertex $z$ displacement w.r.t. $\Xi_{cc}^+$ $> 0.01 \mathrm{mm}$ $> 0.01 \mathrm{mm}$ $> 0.01 \mathrm{mm}$ $> 0.01 \mathrm{mm}$ $> 0$ $> 0$ $> 0$ $> 0$		Maximum DOCA		< 0.5 mm	< 0.5 mm
DIRA $> 0$ $> 0$ $> 0$		DOCA between $(\Lambda_c^+, \pi^+), (K^-, \pi^+)$		< 10 mm	< 10 mm
Vertex distance $\chi^2$ > -1	$\varXi_{cc}^{+}$	$\Lambda_c^+$ vertex z displacement w.r.t. $\Xi_{cc}^+$	> 0.01 mm	> 0.01 mm	> 0.01 mm
		DIRA	> 0	> 0	> 0
Invariant mass [ MeV ] < 4000 (3100, 4000) (3100, 4000)		Vertex distance $\chi^2$	> -1		
		Invariant mass [ MeV ]	< 4000	(3100, 4000)	(3100, 4000)

# 4.2.3 Multivariate analysis

After the preselection, a multivariate analysis (MVA) is performed to further improve the sensitivity. The MVA selectors are trained with the lifetime hypotheses of  $\tau(\Xi_{cc}^+) = 80$  fs (default) and  $\tau(\Xi_{cc}^+) = 0$  fs (zero), respectively.

Table 4.2 HLT2 trigger requirements of Hlt2CharmHadLambdaC2KPPi line.

Particle	Variable	Cut
	Track $\chi^2$ /ndf	< 3
	Transverse momentum	> 0.5 GeV
Daughters of $\Lambda_c^+$	$\chi_{\mathrm{IP}}^2$ to PV	> 9
	Proton transverse momentum	> 1.5 GeV
	Proton Momentum	> 10 GeV
	Proton particle ID $\mathrm{DLL}_{p\pi}$	> 0
	Arithmetic sum of daughter $p_{\rm T}$	> 2.5 GeV
	Transverse momentum	> 2.5 GeV
	Vertex $\chi^2_{\rm vtx}$ /ndf	< 15
$arLambda_c^+$	Cosine of decay angle (DIRA)	> 0.99985
	$\rho$ distance between the end vertex and PV	< 4.0 mm
	Vertex distance $\chi^2$	> 49

Table 4.3 Preselection requirements.

Particle	Variable	Cut
All final tracks	Momentum Pseudorapidity	in (2, 150) GeV in (1.5, 5.0)
Proton	ProbNNghost	< 0.9 > 0.1
Kaon	ProbNNp ProbNNk	> 0.1
Pion	ProbNNpi	> 0.1
	$\log(\chi_{\mathrm{IP}}^2)$	< 4
$\varXi_{cc}^{+}$	$\chi^2_{\rm vtx}$ /ndf $p_{\rm T}$	< 10 > 4 GeV
	$\chi^2_{ m DTF}$	< 50

**Training samples.** The training samples for signal are 2016 MC samples filtered by trigger selection and preselection. The MC sample reweighted to  $\tau(\Xi_{cc}^+) = 80$  fs is used for the  $\tau(\Xi_{cc}^+) = 80$  fs lifetime hypothesis. The MC sample generated with  $\tau(\Xi_{cc}^+) = 0$  fs is used for the  $\tau(\Xi_{cc}^+) = 0$  fs lifetime hypothesis. The training sample for the background is the 2016 WS sample filtered by the same trigger selection and preselection. Due to the large statistics, only 5% of the total filtered WS sample is used in the training. Both

Table 4.4 MVA training variables for default and zero lifetime hypotheses.

Variable	Nominal lifetime	Zero lifetime
$\chi^2_{\rm vtx}$ /ndf of the $\Lambda_c^+$ vertex fit	$\sqrt{}$	
$\chi^2_{\rm vtx}$ /ndf of the $\Xi_{cc}^+$ vertex fit (without DTF)	$\checkmark$	$\sqrt{}$
DTF $\chi^2_{\rm vtx}$ /ndf of the $\Xi^+_{cc}$ candidate with PV constraint	$\checkmark$	$\sqrt{}$
Maximum distance of the closest approach of $\Xi_{cc}^+$	$\checkmark$	$\sqrt{}$
Maximum distance of the closest approach of $\Lambda_c^+$		$\sqrt{}$
Log sized $p_{\rm T}$ of $\Xi_{cc}^+$ , $\Lambda_c^+$ and of their daughters	$\checkmark$	
Minimum $p_{\rm T}$ of daughters of $\Xi_{cc}^+$		$\sqrt{}$
Minimum $p_T$ of daughters of $\Lambda_c^+$		$\sqrt{}$
Scalar sum of $p_{\rm T}$ of daughters of $\Xi_{cc}^+$		$\sqrt{}$
Log sized $\chi_{\rm IP}^2$ of $\Xi_{cc}^+$ to PV	$\checkmark$	
$\cos^{-1}(\text{DIRA}) \text{ of } \Xi_{cc}^+ \text{ to PV}$	$\checkmark$	
Log sized flight distance $\chi^2$ of $\Lambda_c^+$ to PV	$\checkmark$	$\sqrt{}$
Log sized flight distance $\chi^2$ of $\Lambda_c^+$ to its original vertex		$\sqrt{}$
Log sized flight distance $\chi^2$ of $\Xi_{cc}^+$ to PV	$\checkmark$	
Log sized $\chi_{\rm IP}^2$ of daughters of $\Xi_{cc}^+$ to PV	$\checkmark$	
Minimum log sized $\chi^2_{\mathrm{IP}}$ of daughters of $\Xi^+_{cc}$ to PV		$\checkmark$

the signal and background samples are required to lie in the  $\Lambda_c^+$  and  $\Xi_{cc}^+$  mass windows. Following the standard TMVA approach, both the signal and background samples are randomly split into two equally-sized disjoint subsamples for the purpose of training and test, respectively.

**Training variables.** The training variables are selected from a long list of candidate variables. Those that do not significantly contribute to the overall performance and/or are highly correlated with other variables are removed. For zero lifetime hypothesis, variables strongly correlated to the lifetime of the  $\Xi_{cc}^+$  baryon are removed. The final training variables for default lifetime hypothesis are summarised in Table 4.4. Their distributions for signal and background samples are shown in Fig. 4.2. The final training variables for zero lifetime hypothesis are also summarised in Table 4.4. Their distributions for signal and background samples are shown in Fig. 4.3. The correlation matrices of the training variables for default and zero lifetime hypotheses are shown in Fig. 4.4 and Fig. 4.5, respectively.

**MVA algorithms.** Several classification algorithms are considered in the training. Boosted-decision-tree (BDT) and multilayer-perceptron (MLP) based algorithms show best performance and are considered further. Receiver Operation Characteristics (ROC) curves of BDT and MLP based algorithms are shown in Fig. 4.6. The response distribu-

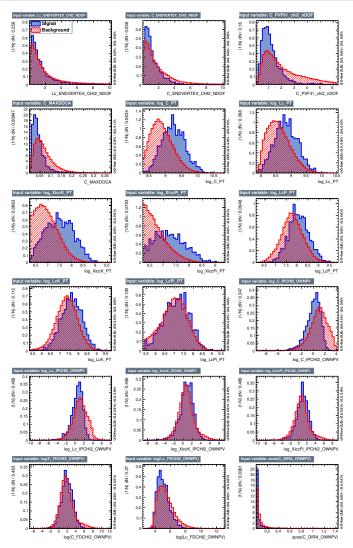


Figure 4.2 Distributions of input variables for signal and background samples under default lifetime hypothesis.

tions are shown in Fig. 4.7 and Fig. 4.8 for default and zero lifetime hypothesis, respectively.

**Determination of working point.** Punzi figure of merit (FoM) is used to quantify the performance of classification algorithms and to determine their optimal working point [184]. The FoM as a function of the MVA response cut *t* is defined as

$$F(t) = \frac{\varepsilon(t)}{\frac{a}{2} + \sqrt{B(t)}},\tag{4.2}$$

where  $\varepsilon(t)$  is the total signal efficiency, B(t) the expected background in the  $\Xi_{cc}^+$  signal window of the RS sample, and a=5 is the desired significance. The signal efficiency

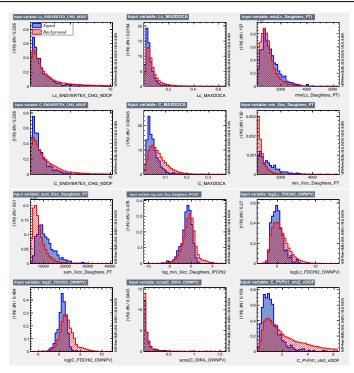


Figure 4.3 Distributions of input variables for signal and background samples under zero lifetime hypothesis.

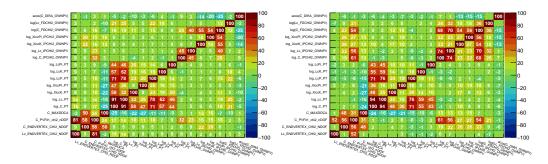


Figure 4.4 Correlation matrices of the training variables of (left) signal and (right) background samples for default lifetime hypothesis.

 $\varepsilon(t)$  is calculated by

$$\varepsilon(t) = \frac{N_{\text{pass}}(t)}{N_{\text{gen}}},$$

where  $N_{\rm gen}$  is the number of signals generated and  $N_{\rm pass}(t)$  the number of signals passing the trigger selection, the preselection and with the MVA response larger than t. The expected background B(t) is evaluated as

$$B(t) = B_{\text{raw}}(t) \times f_{\text{scale}} \times f_{\text{RS}} \times f_{\text{window}},$$

where

•  $B_{\text{raw}}(t)$  is the number of events of the test sample passing the turbo selection, the

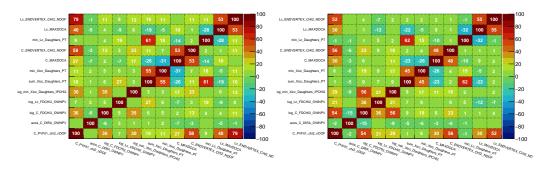


Figure 4.5 Correlation matrices of the training variables of (left) signal and (right) background samples for zero-lifetime hypothesis.

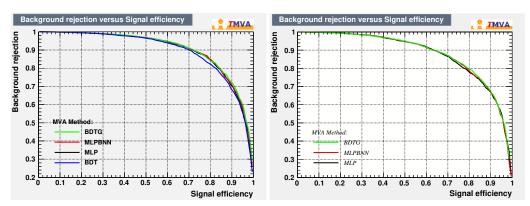


Figure 4.6 ROC curves for different algorithms under (left) default and (right) zero-lifetime hypotheses.

preselection and the MVA cut t;

- $f_{\text{scale}} = 40$  is the factor for the use of partial WS sample (the test background sample, which is  $50\% \times 5\%$  of the total WS sample);
- $f_{RS} = 0.960$  is the factor for the difference of the background level between the RS and the WS samples. It is taken as the ratio of the number of events in the  $\Xi_{cc}^+$  mass sideband of the RS and WS samples;
- $f_{\text{window}} = 0.056$  is the factor to normalize the number of events from the wide  $\Xi_{cc}^+$  mass window to that in the narrow signal window of  $\pm 2.5\sigma$  ( $\sigma = 5 \text{ MeV}/c^2$ , determined from simulated signal) around the nominal  $\Xi_{cc}^+$  mass (chosen to be  $3621.4 \, \text{MeV}/c^2$ ). It is evaluated with the WS sample by first fitting the  $\Xi_{cc}^+$  mass spectrum with the second order polynomials and then calculating the fraction of events in the signal window by integral.

The variation of F(t) for different algorithms are shown in Fig. 4.9. The optimal working point and the performance for each algorithm are summarised in Tables 4.5 and 4.6 for default and zero lifetime hypotheses, respectively. For default lifetime hypothesis, it is found that the performance is similar among algorithms. The BDTG algorithm

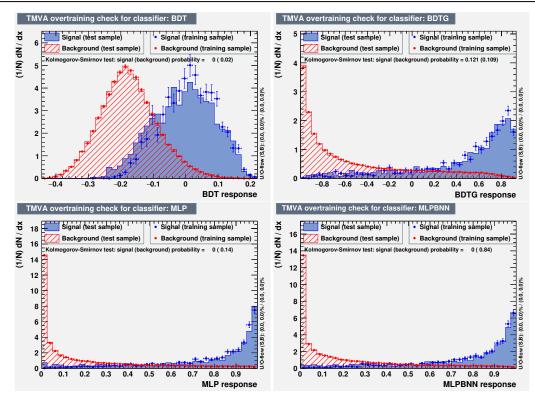


Figure 4.7 Response distributions for (top left) BDT, (top right) BDTG, and (bottom) MLP algorithms, under default lifetime hypothesis.

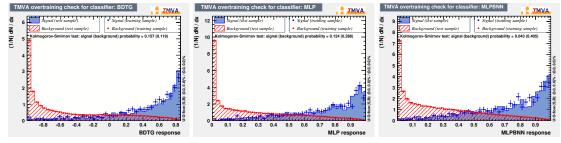


Figure 4.8 Response curves for (left) BDTG, (middle) MLP, and (right) MLPBNN algorithms, under zero lifetime hypothesis.

at working point t = 0.70 is chosen due to the slightly better performance. For zero lifetime hypothesis, the MLPBNN algorithm at working point t = 0.88 shows the best performance.

**Cross-checks.** Some cross-checks are performed of the chosen MVA algorithms and optimal working points. Firstly, the  $\Xi_{cc}^+$  mass distribution and the background retention rate in each mass bin of the WS sample are examined, as illustrated in Fig. 4.10. No peaking structure is observed in this background sample. Secondly, the performance of the MVA selection is studied at different lifetime hypotheses by reweighting the decay time. Two approaches are adopted here: 1) apply the default MVA algorithm with reop-

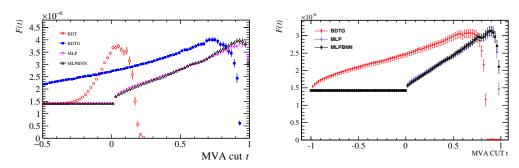


Figure 4.9 Punzi figure of merit F(t) as a function of the MVA response t, under (left) default and (right) zero lifetime hypotheses.

Table 4.5 Optimal working point and the performance for different algorithms under default lifetime hypothesis, where  $\varepsilon_{\text{MVA}}$  is the efficiency of the MVA cut.

Algorithm	Optimal cut	$F(t) (\times 10^{-6})$	$arepsilon_{ ext{MVA}}$
BDT	0.04	3.74±0.10	0.33±0.01
BDTG	0.70	$4.01 \pm 0.10$	$0.43 \pm 0.01$
MLP	0.92	$3.85 \pm 0.09$	$0.41 \pm 0.01$
MLPBNN	0.92	$3.98 \pm 0.10$	$0.38 \pm 0.01$

timised working point for different lifetime hypotheses; 2) apply the default MVA algorithm and the working point directly to reweighted samples. The results are summarised in Fig. 4.11. The vertical axis shows the Punzi FoM, which also reflects the variation of efficiency, since the denominator (desired significance and the number of background) is not affected by reweighting. As expected, the performance is better at longer lifetimes. It can be seen that the performance varies roughly linearly with the lifetime hypothesis in the neighbourhood of default lifetime. By comparing the two approaches, the default MVA algorithm and the corresponding working point gives similar although less optimal performance when the genuine lifetime of the sample is different from that used to train the MVA classifier. Therefore, the MVA selection works well in a wide range of lifetime hypotheses.

Table 4.6 Optimal working point and the performance for different algorithms under zero lifetime hypotheses, where  $\varepsilon_{\text{MVA}}$  is the efficiency of MVA cut.

Algorithm	Optimal cut	$F(t) (\times 10^{-6})$	$arepsilon_{ ext{MVA}}$
BDTG	0.66	3.07±0.12	0.38±0.01
MLP	0.92	$3.12 \pm 0.14$	$0.27 \pm 0.01$
MLPBNN	0.88	$3.13 \pm 0.13$	$0.35 \pm 0.01$

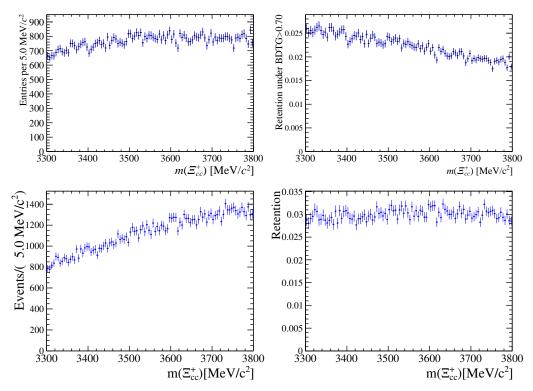


Figure 4.10 The (left)  $\Xi_{cc}^+$  invariant-mass distribution and (right) the background retention after the MVA cut in each invariant-mass bin of the WS sample, for (top) default and (bottom) zero lifetime hypotheses.

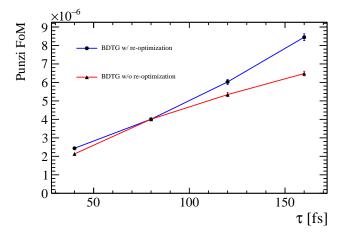


Figure 4.11 Punzi FoM evaluated with reweighted MC samples for different lifetime hypotheses. The blue line refers to the approach in which reoptimisation is performed, and the red line refers to the approach where the default working point is used.

#### 4.2.4 Removal of track-clone candidates

As a multi-body decay with five final tracks, the reconstructed  $\Xi_{cc}^+$  candidates are expected to suffer from the contamination of internal-track-clone candidates. An internal-track-clone candidate refers to the candidate in which at least one track is a clone of another track of the same candidate. The distribution of the angle between such two clone tracks,

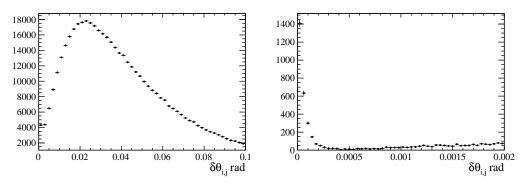


Figure 4.12 Distributions of angles of tracks with the same charge in the WS sample. The right plot zooms in on the zero angle.

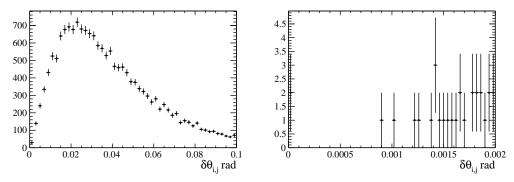


Figure 4.13 Distributions of angles of tracks with the same charge in the MC sample. The right plot zooms in on the zero angle.

 $\delta\theta_{i,i}$ , is supposed to peak at zero.

The distributions of the angles for any pair of tracks with the same charge are shown in Figs 4.12 and 4.13 for WS and MC samples, respectively. A peak around zero is observed in the WS sample, while not in the MC sample. A requirement of  $\delta\theta_{i,j}>0.5$  mrad is added to the selection sequence to remove the internal-track-clone candidates. This will remove around 2.2% candidates in the WS sample, while keeping > 99% of the signals in the MC sample. The mass distribution of the internal-track-clone candidates of the WS sample is shown in Fig. 4.14, in which there is no significant peak.

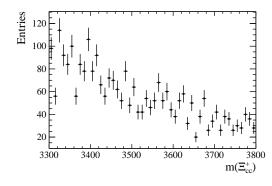


Figure 4.14 Mass distribution of the internal-track-clone candidates of the WS sample.

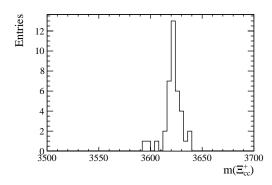


Figure 4.15 Mass distribution of the duplicate candidates of the MC sample.

#### 4.2.5 Duplicate candidates

Multiple candidates in the same event are expected since track multiplicity of the final state is high. In one scenario, two or more candidates in the same event share a  $\Lambda_c^+$  candidate but have different additional tracks to form the  $\Xi_{cc}^+$  candidate. It is known that this kind of candidates do not create fake narrow peaks and confirmed in the mass measurement of  $\Xi_{cc}^{++}$  baryon. We tend to keep them to avoid any possible bias and reduction of the signal significance.

Duplicate candidates are a special kind of multiple candidates, which may increase the signal significance artificially. There are three scenarios: 1) the  $K^-$  from the  $\Lambda_c^+$  decay is swapped with the  $K^-$  directly from the  $\Xi_{cc}^+$  decay; 2) the  $\pi^+$  from the  $\Lambda_c^+$  decay is swapped with the  $\pi^+$  directly from the  $\Xi_{cc}^+$  decay; 3) a combination the above two cases. The selection requirements such as the  $\Lambda_c^+$  mass window and vertex fit quality help to suppress duplicate candidates, but they may still have a chance to survive.

The mass distribution of the duplicate candidates is studied with the MC sample. The truth-matching requirements in the MC sample are loosened to allow in the duplicate candidates. A total of 39 sets of duplicate candidates (involving 79 candidates) are found out of 3 593 entries. The mass distribution is shown in Fig. 4.15, where a peak around the hypothetical  $\Xi_{cc}^+$  mass is observed. In practice, only one of the duplicate candidates of the same set can be a signal due to the small production cross-section of doubly charmed baryons. To avoid artificial increase of the significance, the following procedure is adopted. Events with multiple candidates are examined to see whether or not the final tracks are exactly the same. If yes, a single candidate is randomly selected out of the set of duplicate candidates.

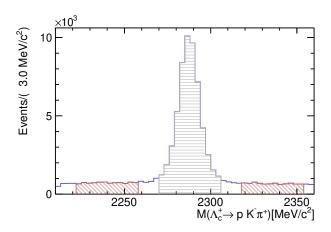


Figure 4.16 Invariant-mass distribution of intermediate  $\Lambda_c^+$  candidates, with the shaded area indicating the signal region (gray horizontal) and the sideband region (brown crossed). Events are taken from the WS sample with the MVA cuts applied.

#### 4.2.6 Study of backgrounds

In this section we summarise studies on background components. We try to show that these background contributions do not create fake peaking structure in the  $\Lambda_c^+ K^- \pi^+$  invariant-mass distribution. Studies performed with the WS sample will be applied to RS sample after unblinding.

 $\Lambda_c^+$  background. As mentioned in the previous section, the  $\Lambda_c^+$  signal window is defined as [2270, 2306] MeV, shown as cross-shaded region in Fig 4.16. The  $\Lambda_c^+$  sideband regions are defined as [2222, 2258]  $\cup$  [2318, 2354] MeV, which are also indicated in Fig 4.16. Figure 4.17 shows the  $\Xi_{cc}^+$  invariant-mass distributions of the WS sample, for intermediate  $\Lambda_c^+$  candidate in the signal region (labelled as "sig") and in the sideband region (labelled as "bkg"). For  $\Lambda_c^+$  candidates in the signal region, the  $\Lambda_c^+$  combinatorial background is subtracted using sWeights. There is no narrow peaking structure in both samples.

**Partially reconstructed background.** One source of the partially reconstructed background is the  $\Xi_{cc}^{++} \to \Lambda_c^+ K^- \pi^+ \pi^+$  decay where one pion is not reconstructed. This is studied by applying the same reconstruction and selection procedure to the  $\Xi_{cc}^{++} \to \Lambda_c^+ K^- \pi^+ \pi^+$  MC sample (with the input  $\Xi_{cc}^{++}$  mass of 3600 MeV). The total efficiency for a  $\Xi_{cc}^{++}$  baryon being partially-reconstructed and selected as a  $\Xi_{cc}^+$  candidate is about twice of the efficiency that it is fully-reconstructed and selected as a  $\Xi_{cc}^{++}$  candidate. This is due to one less track to be considered in the partial reconstruction case. Taking the  $\Xi_{cc}^{++}$  signal yield of 313 in 2016 data as input, we expect about 700 partially-reconstructed

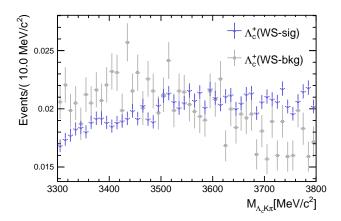


Figure 4.17 Invariant-mass distributions of  $\Xi_{cc}^+$  candidates in the WS sample. The two histograms represent the distributions in the WS sample for (filled square) background subtracted  $\Lambda_c^+$  candidates and (filled triangle)  $\Lambda_c^+$  candidates in the sideband region.

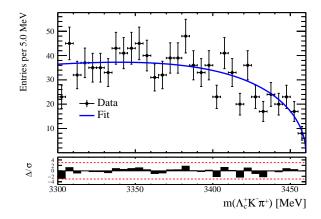


Figure 4.18 Fit to the  $\Lambda_c^+ K^- \pi^+$  invariant-mass distribution of the partially-reconstructed  $\Xi_{cc}^{++} \to \Lambda_c^+ K^- \pi^+ \pi^+$  candidates with Argus function, studied with 2016  $\Xi_{cc}^{++}$  MC sample.

candidates in the  $\Xi_{cc}^+$  invariant-mass distribution, widely distributed below the mass of  $m(\Xi_{cc}^{++}) - m(\pi^+)$ . It is found that the partially reconstructed background can be well described by the Argus function, as shown in Fig. 4.18.

**Misidentification background.** Tight PID requirements are applied in the selection to suppress misidentification backgrounds. However, some misidentification backgrounds may still survive. For  $\Lambda_c^+ \to p K^- \pi^+$  candidates, there could be contamination from the  $D_s^+ \to K^+ K^- \pi^+$  and  $D^+ \to \pi^+ K^- \pi^+$  decays, in which  $K^+$  or  $\pi^+$  is misidentified as a proton. The invariant-mass distributions of the selected  $\Lambda_c^+$  candidates are shown in Fig. 4.19, where the proton mass hypothesis is changed to that of  $K^+$  and  $\pi^+$ , respectively. There are some indication of the  $D_s^+$  and  $D^+$  decays. Fig. 4.20 shows the  $\Xi_{cc}^+$  invariant-mass distributions of candidates in the  $D_s^+$  and  $D^+$  signal regions, defined as  $\pm 18$  MeV

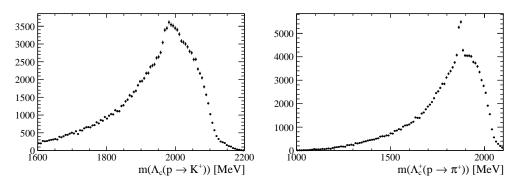


Figure 4.19 Invariant mass distributions of  $\Lambda_c^+$  candidates, with p mass hypothesis changed to that of (left)  $K^+$  and (right)  $\pi^+$  respectively.

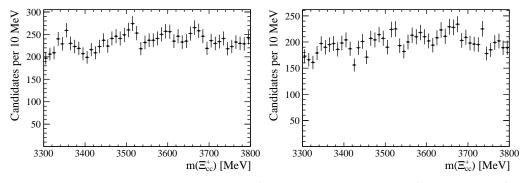


Figure 4.20 Invariant mass distributions of  $\Xi_{cc}^+$  candidates in the (left)  $D_s^+$  and (right)  $D^+$  signal regions, defined as  $\pm 18$  MeV around the mass peaks observed in Fig. 4.19.

around the mass peaks observed in Fig. 4.19. No obvious narrow peaking structures are observed for the background due to misidentified  $\Lambda_c^+$  candidates.

There is no other known decays which can be misidentified as  $\Lambda_c^+ K^- \pi^+$  in the considered mass window.

# 4.3 Strategy for measuring the mass

In this section, the procedure of measuring the invariant mass of  $\Xi_{cc}^+$  with  $\Xi_{cc}^+ \to \Lambda_c^+ K^- \pi^+$  decay is established, following the strategy used in the  $\Xi_{cc}^{++} \to \Lambda_c^+ K^- \pi^+ \pi^+$  analysis [132]. The numbers given below are from the studies performed using 2016 data and simulation if not otherwise specified.

The  $\varXi_{cc}^+$  invariant mass is measured by fitting to the invariant-mass distribution of  $\varLambda_c^+ K^- \pi^+$  final state. The mass difference corrected by the known  $\varLambda_c^+$  mass

$$m(\Lambda_c^+ K^- \pi^+) \equiv M([pK^- \pi^+]_{\Lambda_c^+} K^- \pi^+) - M([pK^- \pi^+]_{\Lambda_c^+}) + M_{\text{PDG}}(\Lambda_c^+)$$
 (4.3)

is used in the study, where  $M([pK^-\pi^+]_{\Lambda_c^+}K^-\pi^+)$  is the reconstructed mass of the  $\Xi_{cc}^+$  candidate,  $M([pK^-\pi^+]_{\Lambda_c^+})$  is the reconstructed mass of the  $\Lambda_c^+$  candidate with kinematic

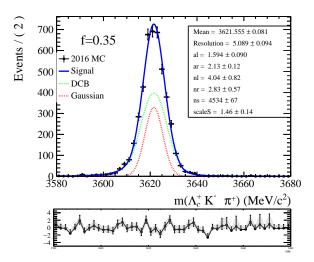


Figure 4.21 Distribution of  $m(\Xi_{cc}^+)$  in the MC sample, along with the fit with a double-sided crystal ball function plus a Gaussian function.

and geometric refit (DecayTreeFitter) to constrain  $\Xi_{cc}^+$  candidate pointing to its associated primary vertex, and  $M_{\rm PDG}(\Lambda_c^+)$  is the known value of the  $\Lambda_c^+$  mass [35]. The kinematic refitting helps to improve the mass resolution and perform the momentum scaling correction.

The shape of the signal component is studied with fully simulated  $\Xi_{cc}^+$  sample. The  $m(\Lambda_c^+ K^- \pi^+)$  distribution can be well described by a Gaussian distribution plus double-sided crystal ball function (DSCB) sharing the mean value  $\mu$ 

$$\mathcal{P}(x) = f \times \mathcal{P}_{\text{Gaussian}}(x) + (1 - f) \times \mathcal{P}_{\text{DSCR}}(x) \tag{4.4}$$

as shown in Fig. 4.21. The width of the DSCB function is scaled according to the width of the Gaussian function. We define the effective resolution as  $\sigma = \sqrt{f \times \sigma_1^2 + (1-f) \times \sigma_2^2}$ , where  $\sigma_1$  ( $\sigma_2$ ) is the width of Gaussian (DSCB) function and f is the fraction of the Gaussian function. Due to the strong correlation of f with other parameters, it is fixed to f = 0.35 according to simulation. Resultant parameters are given in Table 4.7. Due to imperfect modelling of the detector resolution in simulation, the expected mass resolution in data is different from that in simulation. When we fit to the RS sample, parameter  $\mu$  and  $\sigma$  of the signal component are free to vary. Other parameters are fixed to values obtained in the fit to  $\Xi_{cc}^+$  simulation as shown in Table 4.7. The effects of the fraction of the Gaussian will be checked after unblinding, by using the fit models obtained with different fraction of Gaussian.

The mass resolution is a function of the energy release  $Q \equiv M(\Xi_{cc}^+) - M(\Lambda_c^+) - M(K^-) - M(\pi^+)$ , and therefore varies as a function of the  $\Xi_{cc}^+$  invariant-mass. To take

Table 4.7 Resultant parameters from the fit to the  $\Xi_{cc}^+$  invariant-mass distribution in simulation, with a Gaussian function plus a DSCB function.

Parameter	Value
μ	$3621.555 \pm 0.081 \text{MeV}$
$\sigma$	$5.09 \pm 0.09 \text{MeV}$
$R \equiv \frac{\sigma(\text{DSCB})}{\sigma(\text{Gaussian})}$	$1.46 \pm 0.14$
f	0.35 (fixed)
$a_L$	$1.59 \pm 0.09$
$n_L$	$4.04 \pm 0.82$
$a_R$	$2.13 \pm 0.12$
$n_R$	$2.83 \pm 0.57$

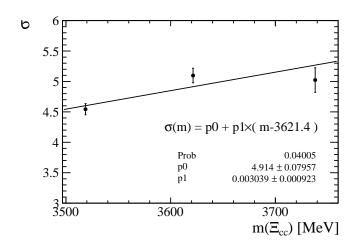


Figure 4.22 Mass resolution of the reconstructed  $\Xi_{cc}^+$  candidates at different  $\Xi_{cc}^+$  mass hypotheses.

into account this effect, the simulated signals generated with  $m(\Xi_{cc}^+) = 3518.7$  MeV and  $m(\Xi_{cc}^+) = 3738.0$  MeV mass hypotheses are used to determine the resolution at other Q values. Assuming that the resolution parameter of the signal lineshape scales linearly with the value of  $m(\Xi_{cc}^+)$ , the resolution can be parametrised as a linear function of  $m(\Xi_{cc}^+)$ , as is shown in Fig. 4.22.

The background component can be well described by the second order Chebychev polynomial, as shown in Fig. 4.23. A mass window of  $\pm 150$  MeV around the signal peak will be used to measure the invariant mass, which is large enough compared with the mass resolution, and sufficient to constrain the background distribution.

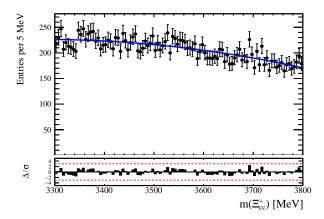


Figure 4.23 Distribution of  $m(\Xi_{cc}^+)$  in the WS sample, along with the fit with a second-order Chebychev polynomial.

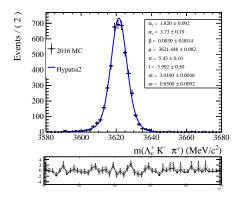
Table 4.8 Systematic uncertainties on the  $\Xi_{cc}^+$  mass. Values with XXX needs to be determined with the observed signal peak.

Source	Systematics [ MeV ]
Fit model	XXX
Momentum scale calibration	0.26
Reconstructed $\Lambda_c^+$ mass	0.05
Event selection	0.08
Unknown $\Xi_{cc}^+$ lifetime	2.06
FSR	XXX
Uncertainty of $\Lambda_c^+$ mass	0.14
Total	XXX

## 4.3.1 Systematic uncertainties in the mass measurement

Sources of systematic effects on the mass measurements, including the fit model, uncertainty on the momentum scaling calibration, the bias of reconstructed  $\Lambda_c^+$  invariant mass, the final state radiation, and the uncertainty on the known  $\Lambda_c^+$  mass. Contributions of the systematic uncertainties from the above sources are summarized in Table 4.8.

**Fit model.** The effects due to choice of the fit model will be checked after unblinding. For the signal line shape, the difference between the default model (Gaussian plus double-sided Crystal ball function) and and an alternative one (the Iptia2 function), will be taken as a systematic uncertainty. The difference of two models are 0.11 MeV according to simulation, as shown in Fig. 4.24. As the simulation is known to describe well the final state radiation and to describe the reconstructed mass resolution to a 10% precision,



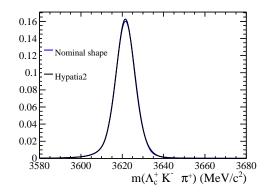


Figure 4.24 Distribution of (left)  $m(\Xi_{cc}^+)$  in simulation, along with the fit with Iptia2 function, and (right) resultant line shapes of the default and alternative signal model.

the correlation between the mean and the resolution in the default fit model, -0.135, is considered to have negligible effects ( $-0.135 \times 10\%$ ) on the mass measurement in this analysis.

**Momentum scale calibration.** Measured track momenta need to be calibrated to correct for possible biases, due to the imperfect alignment of the tracking system, imprecise material map, and the uncertainty on the magnetic field. For Run 2 data, the momentum scale is calibrated with large samples of detached  $Jh\psi$  in  $Jh\psi \rightarrow \mu^+\mu^-$  decay and  $B^+ \rightarrow Jh\psi K^+$  decays [185-187]. The momentum correction factor  $\xi$  is determined by scaling the track momenta by  $1 - \xi$  so that the measured  $Jh\psi$  and  $B^+$  masses are consistent with their world averages. The momentum correction is performed for each data taking period, magnetic field polarity and track charge. The overall correction factor is about  $3 \times 10^{-4}$ . The correction shifts the measured mass of a given particle, reconstructed through a certain decay, by an amount of  $\Delta\mu \approx Q \times \xi$ , where Q is the energy release of the decay channel. The momentum scale calibration is cross-checked with masses of many other resonance decays including b-hadrons and quarkonia. The measured masses after the calibration agree with their known values within  $\pm 3 \times 10^{-4}$ , which is quoted as the systematic uncertainty on the momentum correction factor.

The uncertainty on the momenta of the final-state tracks leads to the uncertainty of the reconstructed invariant mass of  $\Xi_{cc}^+$  candidates. The effect is studied with simulated sample by varying the momentum correction factor  $\xi$  by its uncertainty,  $3 \times 10^{-4}$ , and measuring  $\Delta m$ , the per-candidate mass shift of  $\Xi_{cc}^+$  baryon. A fit to the distribution of the shift with a Gaussian function is performed to extract the mean value, as is shown in Fig. 4.25. The mean mass shift is found to be 0.26 MeV, which needs to be corrected by

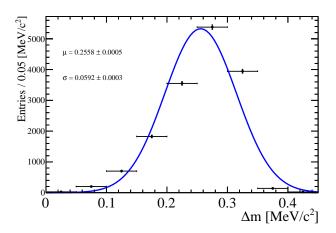


Figure 4.25 Gaussian fit to the distribution of per-candidate mass shift,  $\Delta m$ , for the variation of momentum correction factor by  $1\sigma$ .

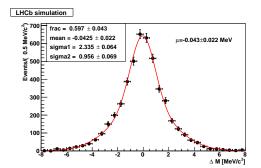
the ratio of the observed Q value in data and the hypothetical Q value in MC,

$$r_Q \equiv Q_{\text{data}}(\Xi_{cc}^+)/Q_{\text{MC}}(\Xi_{cc}^+), \tag{4.5}$$

where the  $Q(\Xi_{cc}^{+}) \equiv M(\Xi_{cc}^{+}) - M_{\rm PDG}(\Lambda_{c}^{+}) - M(K^{-}) - M(\pi^{+})$ .

Bias due to the  $\Lambda_c^+$  reconstructed mass. It is found in simulation that the reconstructed  $\Xi_{cc}^+$  mass is biased by a similar amount to the bias of  $\Lambda_c^+$  mass. Therefore, the corrected mass  $m(\Lambda_c^+K^-\pi^+) \equiv M(\Xi_{cc}^+) - M(\Lambda_c^+) + M_{\rm PDG}(\Lambda_c^+)$  can be used as an approximately unbiased estimator of  $\Xi_{cc}^+$  invariant mass. To check whether the effect of  $\Lambda_c^+$  mass bias is removed or reduced by using the mass difference variable, we calculate the mass of  $\Xi_{cc}^+$  candidate (denoted as  $M_{\rm REC}$ ) using  $\Lambda_c^+$  kinematics in combination with the true kinematics of the accompanying  $K^-$ ,  $\pi^+$  tracks without resolution effect, subtracted by the reconstructed  $\Lambda_c^+$  mass. By using the true kinematics for accompanying  $K^-$ ,  $\pi^+$  tracks, the effect of  $\Lambda_c^+$  mass bias is isolated from other effects (momentum scaling of the accompanying tracks etc.). The difference of  $M_{\rm REC}$  and the input value in simulation is shown in the left plot in Fig 4.26, from which the mean value of bias is determined to be 0.04 MeV.

An alternative way to reduce the bias due to  $\Lambda_c^+$  reconstructed mass is to recalculate  $\Lambda_c^+$  momentum, constraining  $\Lambda_c^+$  mass to its known value using the kinematic refit. In this case, the  $\Xi_{cc}^+$  mass is calculated using the refitted  $\Lambda_c^+$  momentum combined with those of the other two tracks. This is studied in a similar way as discussed above, in which the refitted  $\Lambda_c^+$  momentum is combined the true momenta of accompanying  $K^-$ ,  $\pi^+$  tracks to



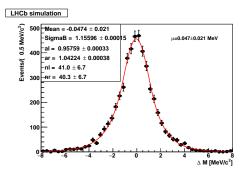


Figure 4.26 Distribution of (left)  $\Xi_{cc}^+$  mass bias (measured value subtracted by true value) when the mass difference is used as estimator of the  $\Xi_{cc}^+$  mass, along with the fit with a Double Gaussian function, and (right)  $\Xi_{cc}^+$  mass bias (measured value subtracted by true value) when the measured  $\Lambda_c^+$  mass is constrained to its known value, along with the fit with a DSCB function.

calculate the  $\Xi_{cc}^+$  mass. The difference between the reconstructed and input  $\Xi_{cc}^+$  mass is shown in the right plot in Fig 4.26, with an average bias of 0.05 MeV.

Bias due to event selection. The measured  $\Xi_{cc}^+$  mass could be biased due to the lifetime-based selections [132]. In trigger selections, no further lifetime related variables are used when reconstructing  $\Xi_{cc}^+$  candidate from  $\Lambda_c^+$ , kaon, and pion candidates, except for DIRA > 0, while further offline selections explores the lifetime information. These selections are expected to bias the  $\Xi_{cc}^+$  mass similar to the effect discussed above for  $\Lambda_c^+$  mass. The effect is studied with the  $\Xi_{cc}^+$  simulation, in which we intentionally remove all the decay time related requirements. The distribution of the difference between the reconstructed mass and the input one for this "unbiased" sample is shown in the left plot of Fig 4.27, The distribution for events surviving offline selections including MVA is shown in the right plot in Fig 4.27. Comparing the fitted results in these two plots, it can be seen that there is an additional bias of  $\delta\mu=0.29\,\mathrm{MeV}$  (with an input lifetime of  $\tau=0.33\,\mathrm{ps}$ ). The same comparison for 2012 data is shown in Figure 4.28. It has very similar behavior to 2016 data.

With a lifetime of 80 fs in simulation, the observed bias is 1.12 MeV with MVA selection applied. The bias depends on the lifetime of the  $\Xi_{cc}^+$  baryon. The effect of unknown lifetime is studied using other lifetime hypotheses by reweighting the  $\Xi_{cc}^+$  simulation sample to match other lifetime value  $\tau'$  according to

$$w = \frac{1/\tau' exp^{-t/\tau'}}{1/\tau_0 exp^{-t/\tau_0}},\tag{4.6}$$

where  $\tau'(\tau_0)$  is the target (input) lifetime and t is the reconstructed decay time. For each target lifetime, the mean mass bias is studied in the same way as in the default case.

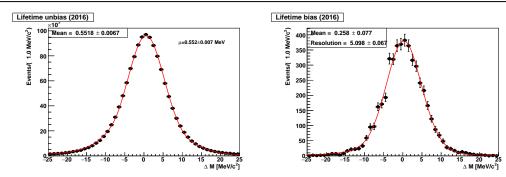


Figure 4.27 Distribution of difference between the reconstructed mass and the input one (left) without applying cuts relating to decay time of  $\Xi_{cc}^+$ , and (right) after all offline selections, including the MVA variable, along with fits with DSCB function.

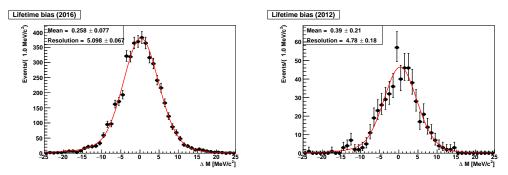


Figure 4.28 Distribution of difference between the reconstructed mass and the input one in (left) 2016 and (right) 2012 simulated signal samples, after all offline selections, including the MVA selection, along with the fit with DSCB function.

Using the default MVA selections, the bias as a function of lifetime is shown in Fig 4.29. As expected, the bias is getting smaller when the lifetime becomes larger. The largest variation of measured mass bias for lifetimes in the range  $40 < \tau < 333$  fs, which covers most theoretical predictions, is 2.06 MeV.

Concerning the selection-related bias and its dependence on  $\Xi_{cc}^+$  lifetime, 1.12 MeV/ $c^2$  is used to correct the measured  $\Xi_{cc}^+$  mass with an uncertainty of 0.11 MeV due to limited statistics in simulation for this study, and an uncertainty of 2.06 MeV due to the lifetime dependence.

**Final state radiation.** In the  $\Xi_{cc}^+ \to \Lambda_c^+ K^- \pi^+$  decay, soft photons are radiated by the final states. Since only charged tracks are used to reconstructed  $\Xi_{cc}^+$  candidates, the observed mass is biased to smaller value due to loss of energy carried out by the photons. The effect is studied using simulated  $\Xi_{cc}^+$  events with a smear procedure. The  $\Xi_{cc}^+$  mass calculated with the true momenta of the final states in the simulated signal sample is smeared by a Gaussian with a mass resolution in the interested range (covering the expected mass resolution in data). The mass constraints of the intermediate states are also considered

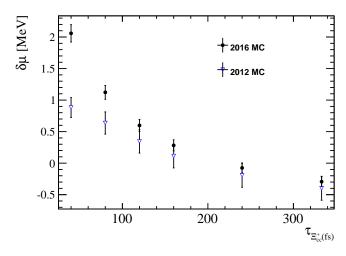


Figure 4.29 Bias of fitted mass at different  $\Xi_{cc}^+$  lifetime hypotheses for 2016 and 2012 simulated signal samples with the same 2016 trigger selection.

when calculating the  $\Xi_{cc}^+$  mass. Then the mass difference defined previously is fitted to obtain the  $\Xi_{cc}^+$  mean mass, with the same fit model used to fit the signal in data.

An example of the fit is shown in the left plot of Fig 4.30. In the right plot of Fig 4.30, the bias as a function of resolution  $\sigma$  is shown, suggesting that the effect is quite small. The distribution is fitted with a linear function, and the bias is XXX for the resolution observed in data.

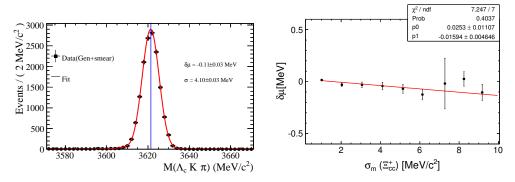


Figure 4.30 Distribution of (left)  $\Xi_{cc}^+$  mass calculated from final-state track momenta smeared with a Gaussian function for resolution, corrected by the reconstructed  $\Lambda_c^+$  mass calculated in the same way, and (right) mean  $\Xi_{cc}^+$  mass as a function of the resolution.

Uncertainty due to  $\Lambda_c^+$  mass. The  $\Lambda_c^+$  mass is known with an uncertainty of 0.14 MeV/ $c^2$  [2], which should be propagated to measurement of  $\Xi_{cc}^+$  mass. The study is performed using kinematic fit, where we modify the known  $\Lambda_c^+$  mass slightly and study the corresponding change of  $\Xi_{cc}^+$  mass candidate by candidate. Since the kinematic for the  $\Xi_{cc}^{++}$  and  $\Xi_{cc}^+$  are quite similar, we quote the results of the  $\Xi_{cc}^{++}$  variation as a function of

 $\Lambda_c^+$  mass from the  $\Xi_{cc}^{++}$  mass measurement. For the uncertainty of 0.14 MeV on  $\Lambda_c^+$  mass, the corresponding  $\Xi_{cc}^+$  mass uncertainty is estimated to be 0.14 MeV, which is quoted as the systematic uncertainty.

#### 4.4 Invariant-mass distribution after unblinding

With the green light to unblind the total Run 1 and Run 2 data in the signal window, we apply the event selection elaborated in Sec. 4.2 to the RS data. Figure 4.31 shows the distributions of  $M([pK^-\pi^+]_{\Lambda_c^+})$  and  $m(\Lambda_c^+K^-\pi^+)$  in the  $\Lambda_c^+$  mass range of 2270-2306 MeV in the full data sample. As a comparison, the  $m(\Lambda_c^+ K^- \pi^+)$  distribution of the WS control sample is also shown in the right plot of Fig. 4.31. The dotted red line indicates the mass of the  $\Xi_{cc}^{+}(3520)$  baryon reported by SELEX [137] and the dashed blue line refers to the mass of the  $\Xi_{cc}^{++}$  baryon [132,135]. A small enhancement is seen near a mass of 3620 MeV. There is no excess near a mass of 3520 MeV. The small enhancement below 3500 MeV in the RS sample, compared with the WS sample, is due to partially reconstructed  $\Xi_{cc}^{++}$  decays. Distributions of  $m(\Lambda_c^+ K^- \pi^+)$  defined in Eq. 4.3 are also shown in 4.32, 4.33, and 4.34 for Run 1, Run 2 and the combined data sets, respectively. Results with MVA optimised for both default and zero lifetime hypotheses are shown in each figure. To determine the statistical significance of this enhancement, an extended unbinned maximum-likelihood fit is performed. The signal component is described with the sum of a Gaussian function and a doubly-sided crystal ball function. The parameters of the signal model are fixed from simulation except for the common peak position  $\mu$ , of the two functions that is allowed to vary freely in the fit. The background component is described by a second-order Chebyshev polynomial with all parameters free to vary in the fit. It is found that the fit result of  $\mu$  is not stable against the choice of initial values, which is guided by the likelihood scan of  $\mu$  discussed below. For example, the fit result in the left plot of Fig. 4.34 can only be obtained with initial values in [3600,3640] MeV, as indicated by the likelihood scan of  $\mu$  in Fig. 4.35.

The  $\sqrt{2\Delta \ln L}$ , corresponding to the local significance according to Wilk's theorem, is reported in each plot. The largest  $\sqrt{2\Delta \ln L}$  is  $3.1\sigma$  for the total data set with MVA selection optimised for the default lifetime hypothesis. The systematic uncertainty is incorporated by convolving the negative log likelihood versus the signal yield curve with a Gaussian distribution with a width equal to the systematic uncertainty. The systematic is about 10%, which is dominated by the difference of resolution in data and in simulation.

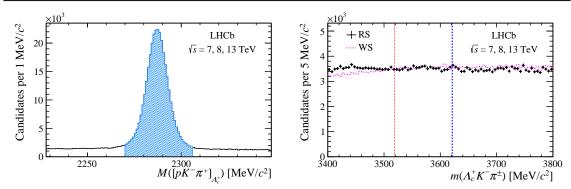


Figure 4.31 Mass distributions of the (left) intermediate  $\Lambda_c^+$  and (right)  $\Xi_{cc}^+$  candidates for the full data sample. All selection is applied, including the  $\Lambda_c^+$  mass requirement, indicated by the cross-hatched region in the left plot, of 2270 MeV  $< M([pK^-\pi^+]_{\Lambda_c^+}) <$  2306 MeV. The right-sign (RS)  $m(\Lambda_c^+K^-\pi^+)$  distribution is shown in the right plot, along with the wrong-sign (WS)  $m(\Lambda_c^+K^-\pi^-)$  distribution normalised to have the same area. The dotted red line at 3518.7 MeV indicates the mass of the  $\Xi_{cc}^+$  baryon reported by SELEX [137] and the dashed blue line at 3621.2 MeV indicates the mass of the  $\Xi_{cc}^{++}$  baryon [135].

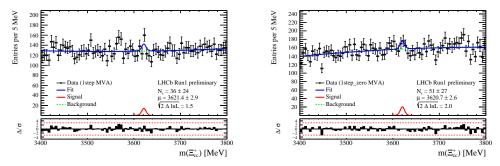


Figure 4.32 Distribution of  $m(\Xi_{cc}^+)$  in Run 1 data with the MVA selection optimised for (left) default and (right) zero lifetime hypothesis.

This uncertainty is studied with the  $\Xi_{cc}^{++}$  control sample [132]. The largest local significance is determined to be  $2.7\sigma$ , taking into account the systematic uncertainty. The local *p*-value is calculated using the one-sided Gaussian tail convention as

$$0.5*TMath::Prob(2\Delta ln L, 1)$$
 (4.7)

as a function of  $m(\Xi_{cc}^+)$  for Run 1, Run 2, and total data sets, as shown in Fig. 4.36.

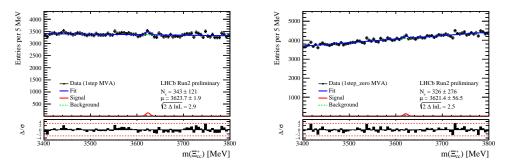
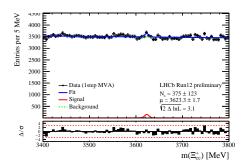


Figure 4.33 Distribution of  $m(\Xi_{cc}^+)$  in Run 2 data with the MVA selection optimised for (left) default and (right) zero lifetime hypothesis.



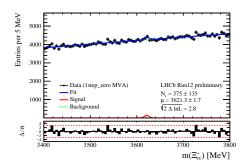


Figure 4.34 Distribution of  $m(\Xi_{cc}^+)$  in Run 1 and 2 data with the MVA selection optimised for (left) default and (right) zero lifetime hypothesis.

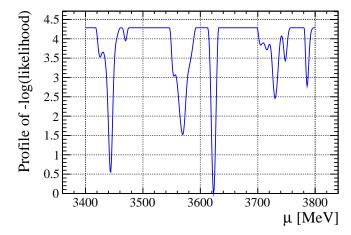


Figure 4.35 Likelihood scan of  $\mu$  for the combined Run 1 and Run 2 data with the MVA selection optimised for the default lifetime hypothesis.

The look elsewhere effect is taken into account according to Ref. [142]. In Ref. [142], an upper limit of the global *p*-value is given by

$$P(\chi_s^2 > c) + \langle N(c_0) \rangle \left(\frac{c}{c_0}\right)^{(s-1)/2} e^{-(c-c_0)/2},$$
 (4.8)

where c is the observed profile likelihood ratio  $2\Delta \ln L$ , s=1 the degree of freedom of the  $\chi^2$  distribution, reference level  $c_0$  chosen to be 0.5, and  $\langle N(c_0) \rangle$  the so-called

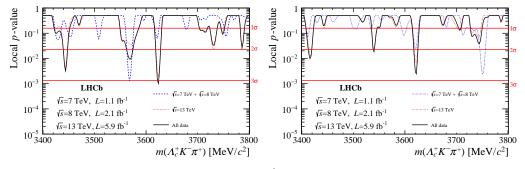


Figure 4.36 Local *p*-value as a function of  $m(\Xi_{cc}^+)$  for the combined Run 1 and Run 2 data sets with the MVA selection optimised for (left) default and (right) zero lifetime hypothesis.

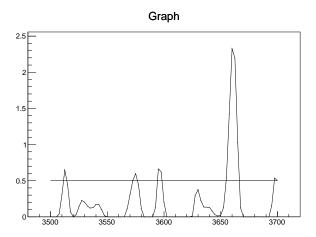


Figure 4.37 Profile likelihood ratio distribution of one of the toy experiments. The  $N(c_0)$  corresponding to this plot is 5.

expected number of "upcrossing" at reference level  $c_0$ . The number of "upcrossing"  $N(c_0)$  is the number of times that the profile likelihood ratio curve goes from below to above a certain threshold  $c_0$ . The  $\langle N(c_0) \rangle$  is evaluated with a small number (one thousand) of background-only toy experiments. The mass region of interest is chosen to be [3500,3700] MeV, which covers most theoretical predictions and the mass of the structure reported by the SELEX experiment. As an illustration, the profile likelihood ratio distribution of one of the toy experiments is shown in Fig. 4.37. The  $N(c_0)$  corresponding to this plot is 5. In the case of the total data set with MVA selection optimised for the default lifetime hypothesis,  $\langle N(c_0) \rangle$  is found to be 3.729, and hence the global p-value is 0.042. Converting the p-value to significance according to

$$\sqrt{2}$$
\*TMath::ErfcInverse(2\*p-value), (4.9)

we can get the global significance of 1.7 for the largest local significance. No excess above  $3.0\sigma$  is observed after taking into account the correction of the look elsewhere effect.

# 4.5 Upper limits

Since no excess above three standard deviations is observed, upper limits on the production ratios are set using the data recorded at  $\sqrt{s} = 8$  TeV in 2012 and at  $\sqrt{s} = 13$  TeV in 2016-2018, which is discussed in detail below.

The ratio of the production cross-sections, defined in Eq. 4.1, can be evaluated as

$$R = \frac{\mathcal{L}_{\text{con}}}{\mathcal{L}_{\text{sig}}} \frac{\varepsilon_{\text{con}}}{\varepsilon_{\text{sig}}} \frac{N_{\text{sig}}}{N_{\text{con}}} \equiv \alpha N_{\text{sig}}, \tag{4.10}$$

where  $\mathcal{L}_{con}$  and  $\mathcal{L}_{sig}$  are the luminosity of the control mode and signal mode,  $\varepsilon_{con}$  and

 $\varepsilon_{\rm sig}$  are the corresponding efficiency. It can be seen from Eq. 4.10 that the single event sensitivity,  $\alpha$ , needs to be measured to evaluate the ratio of the production cross-sections  $R_{A_c^+}$  and  $R_{\Xi_{cc}^{++}}$ . This implies that yields of control modes, as well as the luminosity and selection efficiency of signal and control modes need to be evaluated.

For 2012 and 2016-2018 data, the  $\Lambda_c^+$  control mode,  $\Xi_{cc}^{++}$  control mode, and the signal mode are collected at the same time, which leads to the ratio of luminosities in Eq. 4.10 to be 1.

#### 4.5.1 Event selection for setting upper limits

Two control modes are chosen as the control mode: the prompt  $\Lambda_c^+$  baryon reconstructed through  $pK^-\pi^+$  final state, and the  $\Xi_{cc}^{++}$  baryon reconstructed through  $\Lambda_c^+K^-\pi^+\pi^+$  final state, with  $\Lambda_c^+\to pK^-\pi^+$ . To calculate upper limits, exclusive decays of  $\Lambda_c^+$  and  $\Xi_{cc}^{++}$  baryons are reconstructed and selected, as detailed in Appendix D. To reduce systematic uncertainties in the estimation of efficiency, fiducial cuts are applied to the signal mode. Tighter trigger requirements are applied. In addition, the MVA classifier to select the signal decay is factorised into two: one for the selection of intermediate  $\Lambda_c^+$  candidates, the other for the selection of  $\Xi_{cc}^+$  candidates. The former is applied to both the signal mode and the  $\Lambda_c^+$  control mode.

**Fiducial region.** The fiducial region is defined to better estimate the selection efficiency. For the signal mode, the  $\Xi_{cc}^+$  candidate is required to lie in the kinematic region of

$$2.0 < y < 4.5, \ 4 < p_{\rm T} < 15 \,\text{GeV}.$$
 (4.11)

**Trigger requirements.** For L0 and HLT1 trigger, a  $\Lambda_c^+$  TOS chain is used. For 2011-2012 data, these are

- L0: L0Hadron TOS on  $\Lambda_c^+$ ,
- HLT1: Hlt1TrackAllL0 TOS on  $\varLambda_c^+,$

For 2015-2018 data, these are

- L0: L0Hadron TOS on  $\Lambda_c^+$ ,
- HLT1: Hlt1TrackMVA||Hlt1TwoTrackMVA on  $\varLambda_c^+$ .

These trigger requirements are applied to both the signal and control modes.

In terms of HLT2 trigger, the selection of the signal mode and the  $\Xi_{cc}^{++}$  control mode is tightened by the requirements marked with a dagger (†) in Table D.1, in order to be

consistent with the  $\Lambda_c^+$  control mode.

**Multivariate analysis of**  $\Xi_{cc}^+ \to \Lambda_c^+ K^- \pi^+ \text{decay.}$  The multivariate classifier previously developed is factorised into two steps, with the first step applies also to the  $\Lambda_c^+$  control mode. The motivation of breaking one MVA down into two steps is to minimise the systematic uncertainties due to the  $\Lambda_c^+$  selections. In the first step, an MVA classifier (MVA1) is trained to remove fake  $\Lambda_c^+$  candidates and will be applied to both the signal and the  $\Lambda_c^+$  control mode. In the second step, another MVA classifier (MVA2) is trained to remove fake  $\Xi_{cc}^+$  candidates and will be applied only to the signal mode. In the remaining discussion, the result for the default lifetime hypothesis is shown. The same approach is used to train the two-step MVA assuming that the lifetime of  $\Xi_{cc}^+$  baryon is negligible.

**Training.** For the first step, the training sample for the signal is the 2016 simulation sample filtered by the trigger selection and preselection. The training sample for the background is the 2016 WS sample filtered by the same event selection. Due to the large sample size, only 5% of the total filtered WS sample is used in the training. Candidates of the signal sample are required to lie in the  $\Xi_{cc}^+$  and the  $\Lambda_c^+$  mass windows, while candidates of the background sample are required to be in the  $\Xi_{cc}^+$  mass window and the  $\Lambda_c^+$  mass sideband, which is defined to be (2223, 2258)  $\cup$  (2318, 2353) MeV. For the second step, candidates of both the signal and background samples are required to lie in the  $\Xi_{cc}^+$  and the  $\Lambda_c^+$  mass window, and to pass the requirement on the response of MVA1 classifier.

Training variables are determined with the same strategy as discussed in Sec. 4.2. In the first step, variables that significantly bias the source of  $\Lambda_c^+$  candidate are avoided such that they are applicable to both  $\Lambda_c^+$  signals from  $\Xi_{cc}^+$  decays and from PV. The final set of training variables under the default lifetime hypothesis includes:

- $\chi^2_{\rm vtx}$ /ndf of the  $\Lambda_c^+$  vertex fit,
- Maximum distance of the closest approach of  $\Lambda_c^+$ ,
- $p_{\rm T}$  of  $\Lambda_c^+$  and its secondaries,
- Log sized flight distance  $\chi^2$  of  $\Lambda_c^+$  to PV,
- Log sized  $\chi_{\rm IP}^2$  of  $\Lambda_c^+$  secondaries to PV

for the first MVA classifier and

- $\chi^2_{\rm vtx}$ /ndf of  $\Xi_{cc}^+$  (without DTF),
- DTF  $\chi^2_{\rm vtx}$ /ndf of  $\Xi_{cc}^+$  with PV constraint,
- Maximum distance of the closest approach of  $\Xi_{cc}^+$ ,

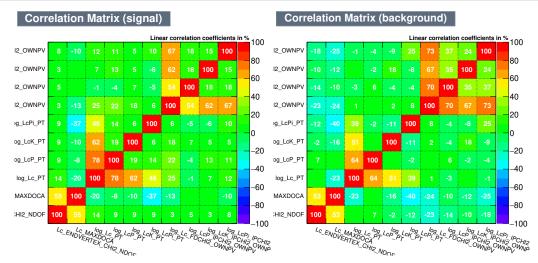


Figure 4.38 Correlation matrices of training variables of (left) the signal and (right) the background samples for the first MVA classifier with the default lifetime hypothesis.

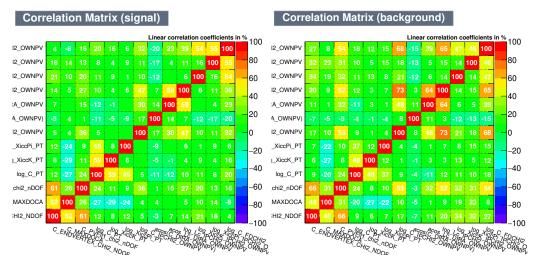


Figure 4.39 Correlation matrices of the training variables of (left) the signal and (right) the background samples for the second MVA classifier with the default lifetime hypothesis.

- $p_{\mathrm{T}}$  of  $\Xi_{cc}^+$ , and  $\pi^+$  and  $K^-$  from  $\Xi_{cc}^+$ ,
- Log sized  $\chi_{IP}^2$  of  $\Xi_{cc}^+$  to PV,
- $\cos^{-1}(\text{DIRA})$  of  $\Xi_{cc}^+$  to PV,
- Log sized flight distance  $\chi^2$  of  $\Xi_{cc}^+$  to PV,
- Log sized  $\chi^2_{\mathrm{IP}}$  of  $\Lambda_c^+$ , and  $\pi^+$  and  $K^-$  from  $\varXi_{cc}^+$ ,
- $\cos^{-1}(\text{DIRA})$  of  $\Lambda_c^+$  to PV

for the second MVA classifier. The correlation matrices of the training variables under the default lifetime hypothesis are shown in Figs 4.38 and 4.39 for input variables in the first and second steps, respectively.

Based on the performance of different MVA algorithms in Sec. 4.2, the BDTG algorithm is used in the two-step MVA. The ROC curves for the first and second MVA

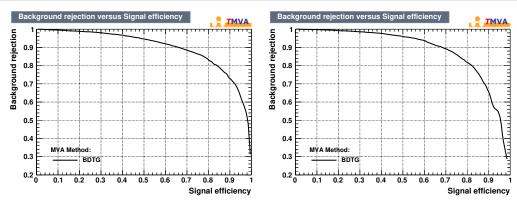


Figure 4.40 ROC curves for the (left) first and (right) second MVA classifiers under the default lifetime hypothesis.

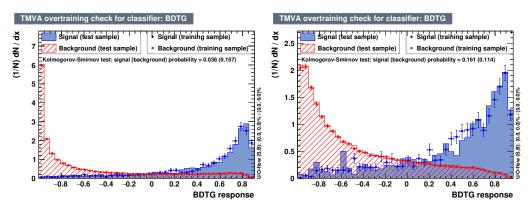


Figure 4.41 Response curves for the (left) first and (right) second MVA classifiers under the default lifetime hypothesis. For the second step, the requirement of  $t_1 > 0.0$  for MVA1 is applied.

classifiers are shown in Fig. 4.40, while the response curves are illustrated in Fig. 4.41.

**Determination of the working point.** To determine the optimal working points of the two MVA classifiers, we maximize the Punzi FoM defined as

$$F(t_1, t_2) = \frac{\varepsilon(t_1, t_2)}{\frac{a}{2} + \sqrt{B(t_1, t_2)}},$$
(4.12)

where  $t_1$  and  $t_2$  are selection criteria on the first and the second MVA responses, respectively;  $\varepsilon$  and B are defined and evaluated in the same manner as in Eq. 4.2. The scan of the MVA responses is shown in Fig. 4.42. The optimal working points are found to be  $t_1 > 0.0$  and  $t_2 > 0.70$ . The trained MVA algorithms and the optimal working points are applied also to 2012 datasets.

**Invariant-mass distribution after event selection.** The invariant-mass distribution of  $m(\Lambda_c^+ K^- \pi^+)$  after additional event selection for upper-limit setting is shown in Fig. 4.43, with candidates in the  $\Lambda_c^+$  mass range from 2270 MeV to 2306 MeV. As a comparison, the  $m(\Lambda_c^+ K^- \pi^+)$  distribution of the WS control sample is also shown in Figure 4.43. The

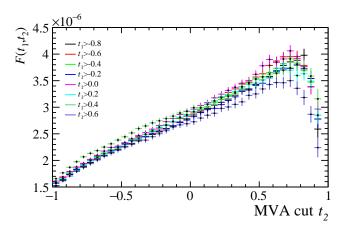


Figure 4.42 Punzi figure of merit  $F(t_1, t_2)$  for the two-step MVA under the default lifetime hypothesis.

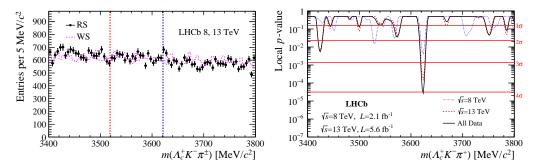


Figure 4.43 The (left) invariant-mass distributions of the  $\Xi_{cc}^+$  candidates for the signal data sample collected in 2012 and 2016-2018 and (right) local p-value as a function of  $m(\Lambda_c^+ K^- \pi^+)$ . The event selection for upper-limit setting is applied, including the  $\Lambda_c^+$  mass requirement of 2270 MeV  $< M([pK^-\pi^+]_{\Lambda_c^+}) <$  2306 MeV. The right-sign (RS)  $m(\Lambda_c^+ K^-\pi^+)$  distribution is shown in the right plot, along with the wrong-sign (WS)  $m(\Lambda_c^+ K^-\pi^-)$  distribution normalized to have the same area as the RS sample. The dashed red line of 3518.7 MeV indicates the mass of the  $\Xi_{cc}^+$  baryon reported by SELEX and the dashed blue line of 3621.2 MeV refers to the mass of the  $\Xi_{cc}^{++}$  baryon.

dashed red line indicates the mass of the  $\Xi_{cc}^+$  baryon reported by SELEX [137], and the dashed blue line refers to the mass of the  $\Xi_{cc}^{++}$  baryon [132,135]. The local *p*-value is also calculated in this case as a function of  $m(\Xi_{cc}^+)$  for 2012, 2016–2018, and total data sets, as shown in the right plot in Fig. 4.43. Taking into account the look elsewhere effect in the mass range of 3500 MeV to 3700 MeV according to Ref. [142], the global *p*-value increases to  $1.3 \times 10^{-3}$ , corresponding to a global significance of  $3.0\sigma$ .

#### 4.5.2 Yield of control modes

To calculate upper limits, signal yields of exclusive decays of  $\Lambda_c^+$  and  $\Xi_{cc}^{++}$  baryons are determined.

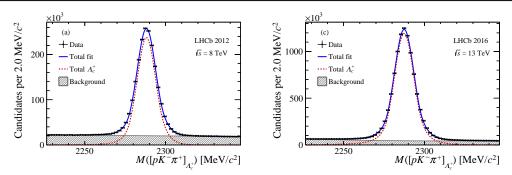


Figure 4.44 Invariant-mass distribution of (left)  $\Lambda_c^+$  mass in (left) 2012 and (right) 2016 data, along with the fit results.

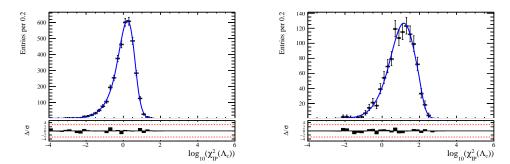


Figure 4.45 Distributions of  $\log_{10}(\chi_{\text{IP}}^2)$  for (left) prompt and (right) secondary  $\Lambda_c^+$  signals in 2016 simulation.

**Yield of the**  $\Lambda_c^+$  **control mode.** An extended unbinned maximum likelihood fit is performed to the invariant mass distribution of the  $\Lambda_c^+$  candidates to extract the  $\Lambda_c^+$  yield in the  $\Lambda_c^+$  control sample. The signal shape is described by the sum of a double-sided crystal ball function and a Gaussian function. The fraction of the Gaussian function is determined from simulation. The second-order Chebychev polynomial is used to describe the background shape. As an illustration, the fit results are shown in Fig. 4.44 for 2012 and 2016 data.

To determine the prompt yield from the inclusive  $\Lambda_c^+$  production, a fit to the  $\log \chi_{\rm IP}^2$  distribution of the  $\Lambda_c^+$  candidates is performed. As in the measurement of lifetime, the Bukin function is used to model both the prompt and secondary signal components. Shape parameters of the prompt and secondary components are determined from the fits to the distributions in simulation, as shown in Figs 4.45. The shape of the background component is obtained from the mass sideband sample. The number of background events is constrained to that in the mass fit. Distributions of  $\log_{10}(\chi_{\rm IP}^2)$ , along with the fit results, are shown in Fig. 4.46. The obtained prompt yields are summarised in Table 4.9. The prompt fraction is found to be around 70%.

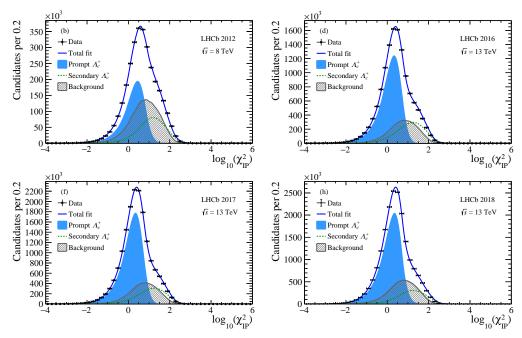


Figure 4.46 Distributions of  $\log_{10}(\chi_{\rm IP}^2)$  of  $\Lambda_c^+$  in (top left) 2012, (top right) 2016, (bottom left) 2017, (bottom right) 2018 data samples for the  $\Lambda_c^+$  control mode.

Table 4.9 Prompt yields of the  $\Lambda_c^+$  control mode.

Year	2012	2016	2017	2018
Yield [×10 <sup>5</sup> ]	$11.75 \pm 0.03$	$73.39 \pm 0.13$	$98.83 \pm 0.09$	$111.84 \pm 0.13$

**Yield of the**  $\Xi_{cc}^{++}$  **control mode.** To extract the yield of the  $\Xi_{cc}^{++}$  control mode, the unbinned maximum likelihood fits are performed to the distributions of  $m(\Xi_{cc}^{++})$ . The signal is described by a Gaussian plus a double-sided Crystal Ball function with the same mean  $\mu$ . Shape parameters are fixed to the values obtained from the fully simulated  $\Xi_{cc}^{++}$  sample. The background mass distribution is well described by the second-order Chebychev polynomial with parameters free to vary in the fit. Simultaneous fit is performed for 2016-2018 data with a shared resolution parameter to reduce the statistical uncertainty. Distributions of  $m(\Xi_{cc}^{++})$ , along with the fit results, are shown in Fig. 4.47. Yields of the  $\Xi_{cc}^{++} \to \Lambda_c^+ K^- \pi^+ \pi^+$  control mode are summarised in Table 4.10.

Table 4.10 Yield of the  $\Xi_{cc}^{++} \to \Lambda_c^+ K^- \pi^+ \pi^+$  control mode.

Year	2012	2016	2017	2018
Yield	$38 \pm 9$	121 ± 19	$153 \pm 24$	188 ± 24

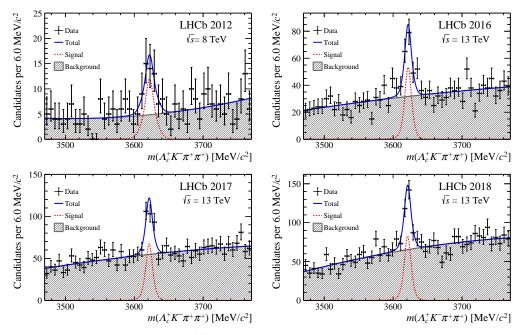


Figure 4.47 Distributions of  $m(\Xi_{cc}^{++})$  for (top left) 2012, (top right) 2016, (bottom left) 2017, and (bottom right) data for the  $\Xi_{cc}^{++}$  control mode, along with the fit results.

## 4.5.3 Estimation of efficiency

To calculate upper limits, the efficiency of the reconstruction and selection of exclusive decays of  $\Lambda_c^+$  and  $\Xi_{cc}^{++}$  baryons is estimated.

The total efficiency can be factorised into several components as

$$\varepsilon = \varepsilon^{\text{Acc}} \times \varepsilon^{\text{Sel}|\text{Acc}} \times \varepsilon^{\text{PID}|\text{Sel}} \times \varepsilon^{\text{MVA1}|\text{PID}} \times \varepsilon^{\text{MVA2}|\text{MVA1}} \times \varepsilon^{\text{Trigger}|\text{MVA2}}, \quad (4.13)$$

where the pieces are acceptance (Acc), HLT2 and cut-based preselection (Sel), PID requirements (PID), the first (MVA1) and second (MVA2) MVA, and the L0 and HLT2 trigger (Trigger). The symbol "|" means conditional (e.g.  $\varepsilon^{\rm Sel|Acc}$  is the efficiency given that the candidate has passed the acceptance requirement) and all selections are cumulative. It should be noted that this factorisation dose not have to be the same as the sequence in which these selections are applied.

Correction of  $\Xi_{cc}^+$  kinematics. Distributions of  $p_T$  of  $\Xi_{cc}^+$  and the number of SPD hits (nSPDHits) in the signal simulation are reweighted according to the data-simulation discrepancy observed in the  $\Xi_{cc}^{++} \to \Lambda_c^+ K^- \pi^+ \pi^+$  mode. It is with a good reason to assume that the production mechanism is the same for  $\Xi_{cc}^+$  and  $\Xi_{cc}^{++}$  baryons, given that these are isospin partners. Distributions of  $p_T$  of  $\Xi_{cc}^{++}$  and nSPDHits with background-subtracted data, and simulation samples before and after the reweighting, are shown in Fig. 4.48. It is found that the discrepancy of the distribution of rapidity y of  $\Xi_{cc}^{++}$  between data and sim-

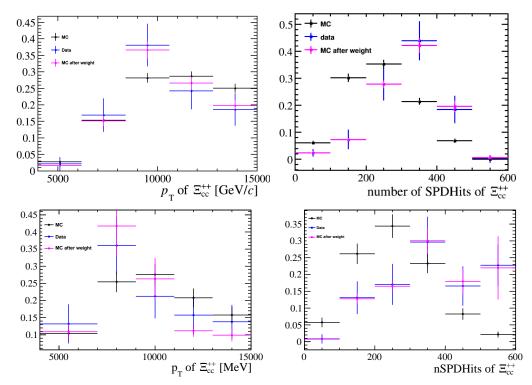


Figure 4.48 Distributions of (left)  $\Xi_{cc}^{++}$   $p_{\rm T}$  and (right) nSPDHits of the  $\Xi_{cc}^{++} \to \Lambda_c^+ K^- \pi^+ \pi^+$  decay for (top) 2016 and (bottom) 2012 data, respectively. Blue stands for the background-subtracted data, and magenta (black) for the simulation (MC) sample after (before) reweighting.

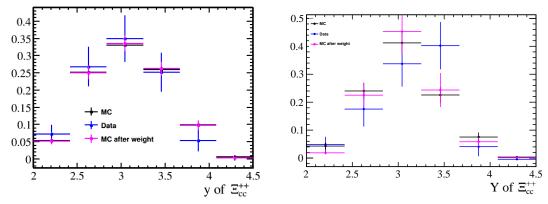


Figure 4.49 Distributions of  $\Xi_{cc}^{++}$  y of the  $\Xi_{cc}^{++} \to \Lambda_c^+ K^- \pi^+ \pi^+$  decay for (right) 2016 and (left) 2012 data, respectively. Blue stands for the background-subtracted data, and magenta (black) for the simulation (MC) sample after (before) reweighting.

ulation samples is small after the  $p_{\rm T}$  and nSPDHits reweighting, as illustrated in Fig. 4.49. Given the small number of signals in data, no further reweighting of rapidity is applied. The  $p_{\rm T}$  of the mother particles and nSPDHits of  $\Lambda_c^+$  and  $\Xi_{cc}^{++}$  control modes are reweighted with the same procedure. This reweighting procedure removes the dependence on the  $\Xi_{cc}^+$  kinematic distribution in the event generator GENXICC.

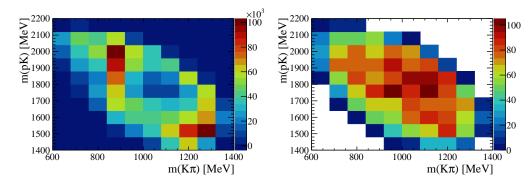


Figure 4.50 Comparison of the Dalitz-plot distributions of (left) 2016 data and (right) simulation for the  $\Lambda_c^+ \to p K^- \pi^+$  decay.

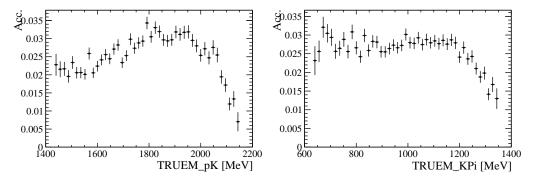


Figure 4.51 Efficiency of the HLT2 selection for the  $\Lambda_c^+$  control mode in bins of (left)  $m(pK^-)$  and (right)  $m(K^-\pi^+)$ .

Correction of intermediate  $\Lambda_c^+$  kinematics. Simulation used in this analysis does not well model the resonance structure of the  $A_c^+$  decays. Simulation samples of the  $\Xi_{cc}^+$ signal and  $\Lambda_c^+$  control modes implement phase-space models in the  $\Lambda_c^+$  decay, while the simulation samples of the  $\Xi_{cc}^{++}$  control mode utilize a pseudo-resonant model, taking into account the  $K^{*0}$ ,  $\Delta^{++}$  and  $\Lambda(1520)^0$  resonances. In order to illustrate the discrepancy, distributions in 2016 data and simulation of the  $\Lambda_c^+ \to pK^-\pi^+$  decay in bins of the  $\Lambda_c^+$ Dalitz-plot variables  $m(pK^-)$  and  $m(K^-\pi^+)$  (the invariant mass of the proton-Kaon and Kaon-Pion system) are shown in Fig. 4.50. The selection efficiency shows strong dependence on the  $\Lambda_c^+$  Dalitz-plot variables. This is illustrated in Fig. 4.51 by the efficiency of the HLT2 selection as a function of  $m(pK^-)$  and  $m(K^-\pi^+)$  for the  $\Lambda_c^+$  control sample. Therefore,  $m(pK^-)$  and  $m(K^-\pi^+)$  distributions are reweighted when estimating the selection efficiencies. Simulation samples of both signal and control modes are reweighted in two-dimensional bins of  $m(pK^-)$  and  $m(K^-\pi^+)$  to the inclusive  $\Lambda_c^+$  data, with background subtracted through sWeights from the mass fit shown in Fig. 4.44. Tables of weights are summarised in Fig. 4.52. Good agreements of Dalitz-plot distributions are achieved after reweighing, as shown in the projections to  $m(pK^-)$  and  $m(K^-\pi^+)$  distributions in Fig. 4.53

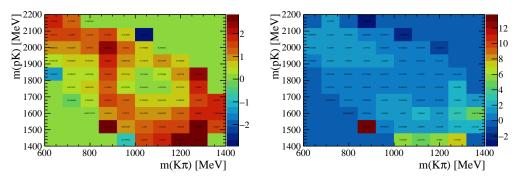


Figure 4.52 Weights in bins of Dalitz-plot variables for the (left)  $\Lambda_c^+$  and (right)  $\Xi_{cc}^{++}$  control modes.

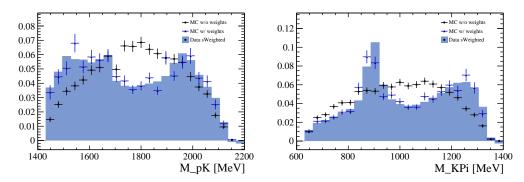


Figure 4.53 Comparison of projections to (left)  $m(pK^-)$  and (right)  $m(K^-\pi^+)$  for background-subtracted inclusive  $\Lambda_c^+$  data and the  $\Lambda_c^+$  simulation sample before and after reweighting.

and Fig. 4.54, for the  $\Lambda_c^+$  and  $\Xi_{cc}^{++}$  control mode, respectively. We compare the efficiency estimated with and without reweighting the Dalitz-plot distributions. It turns out that in spite of the change of efficiency in individual modes, the difference of efficiency ratio of signal to control modes is small. The difference is less than 1% to the  $\Lambda_c^+$  control mode, and 4% to the  $\Xi_{cc}^{++}$  control mode.

In the following sub-sections, we present the results of different efficiency components for 2012 and 2016 data. Results of 2017 and 2018 data are evaluated with the same

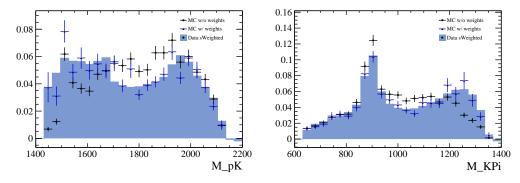


Figure 4.54 Comparison of projections to (left)  $m(pK^-)$  and (right)  $m(K^-\pi^+)$  for background-subtracted inclusive  $\Lambda_c^+$  data and the  $\Xi_{cc}^{++}$  simulation sample before and after reweighting.

Table 4.11 Acceptance efficiencies and the ratios of the control to the signal mode.

	2016	2012
$\varepsilon(\Xi_{cc}^+)$	$(92.922 \pm 0.210) \times 10^{-2}$	$(91.742 \pm 0.250) \times 10^{-2}$
$\varepsilon(\Lambda_c^+)$	$(98.587 \pm 0.076) \times 10^{-2}$	$(98.514 \pm 0.099) \times 10^{-2}$
$\varepsilon(\Xi_{cc}^{++})$	$(96.600 \pm 0.030) \times 10^{-2}$	$(92.832 \pm 0.484) \times 10^{-2}$
$r(\Lambda_c^+) \equiv \varepsilon(\Lambda_c^+)/\varepsilon(\Xi_{cc}^+)$	$1.061 \pm 0.003$	$1.074 \pm 0.003$
$r(\Xi_{cc}^{++}) \equiv \varepsilon(\Xi_{cc}^{++})/\varepsilon(\Xi_{cc}^{+})$	$1.040 \pm 0.002$	$1.012 \pm 0.006$

procedure and summarised in Appendix E.

Ratio of acceptance efficiency. The acceptance efficiency  $\varepsilon^{\rm Acc}$  in this context is defined as the efficiency for the decay products of the signal candidates in the fiducial region (defined as 2.0 < y < 4.5,  $4 < p_{\rm T} < 15\,{\rm GeV}$ ) to be in the LHCb acceptance ( $10 < \theta < 400\,{\rm mrad}$ ). It is determined with generator-level simulation samples, *i.e.* only signal kinematic and decay are simulated, but not the interaction with detector materials. Results are listed in Table 4.11, which includes ratios of the control mode to the signal mode.

Ratio of HLT2 and preselection efficiency. The HLT2 (or stripping for the 2012 dataset) and preselection efficiencies  $\varepsilon^{\text{Sel}|\text{Acc}}$  are determined with simulation samples. PID requirements are excluded and will be calculated separately. Track reconstruction efficiency is included implicitly in the HLT2 efficiency. There is known data-simulation discrepancy to be corrected in the track reconstruction efficiency. This is taken into account using correction tables obtained with the tag-and-probe method. The correction value for each final-state track is multiplied to get the total correction of the candidate. Systematic uncertainties associated with this method are discussed in Sec. 4.5.4. The efficiencies are listed in Table 4.12.

**Ratio of PID efficiency.** The PIDCalib package is used to determine the efficiency of PID requirements  $\varepsilon^{\text{Pid|Sel}}$ . For 2016 data, the calibration sample used for kaons and pions is the  $D^{*+} \to D^0(\to K^-\pi^+)\pi^+$  sample, and that used for protons is the  $\Lambda \to p\pi$  sample. For 2012 data, additional samples of  $\Lambda_c^+ \to pK^-\pi^+$  decay are also included for protons. It is found that the proton PID efficiency given by  $\Lambda \to p\pi$  and  $\Lambda_c^+ \to pK^-\pi^+$  can differ by a few percents. However such difference would mostly cancel in the ratio

Table 4.12 HLT2 (or stripping for 2012 data set) and preselection efficiency and efficiency ratios of the control modes and the signal mode.

	2016	2012
$arepsilon(\Xi_{cc}^+)$	$(0.290 \pm 0.004) \times 10^{-2}$	$(0.064 \pm 0.005) \times 10^{-2}$
$\varepsilon(\Lambda_c^+)$	$(1.545 \pm 0.037) \times 10^{-2}$	$(0.345 \pm 0.017) \times 10^{-2}$
$\varepsilon(\Xi_{cc}^{++})$	$(0.235 \pm 0.005) \times 10^{-2}$	$(0.089 \pm 0.005) \times 10^{-2}$
$r(\Lambda_c^+) \equiv \varepsilon(\Lambda_c^+)/\varepsilon(\Xi_{cc}^+)$	$5.319 \pm 0.147$	$5.386 \pm 0.527$
$r(\Xi_{cc}^{++}) \equiv \varepsilon(\Xi_{cc}^{++})/\varepsilon(\Xi_{cc}^{+})$	$0.809 \pm 0.020$	$1.397 \pm 0.139$

Table 4.13 Binning scheme used for K,  $\pi$  and p for PID calibration.

Variable	Binning
<i>p</i> [ GeV ]	[ 2.0, 5.6, 9.2, 12.8, 16.4, 20.0, 26.0, 32.0, 38.0, 44.0, 50.0, 56.0, 62.0, 68.0, 74.0, 80.0, 90.0, 100.0, 110.0, 120.0, 150.0 ]
η	$[\ 1.5, 2.25, 2.5, 2.75, 3.0, 3.25, 3.5, 3.75, 4.0, 4.33, 5.0\ ]$

between  $\varXi_{cc}^+(\to \Lambda_c^+ K^-\pi^+)/\Lambda_c^+$  or  $\varXi_{cc}^+(\to \Lambda_c^+ K^-\pi^+)/\varXi_{cc}^+(\to \Lambda_c^+ K^-\pi^+\pi^+)$ . The efficiency for PID requirements on each final-state track is determined in each p and q bin. The binning scheme for each type of final-state tracks is listed in Table 4.13. The same binning schemes are used for the signal and control modes. The total PID efficiency of the candidate is the product of efficiencies of each final track. The PID efficiency for the signal and control modes is summarised in Table 4.14.

**Ratio of MVA efficiency.** In the case of setting upper limits, the MVA selection consisting of two steps is developed, as discussed in Sec. 4.5.1. The MVA efficiency and their ratios of the control modes to the signal mode at the optimal working points MVA1 > 0.00 and MVA2 > 0.70 are summarised in Tables 4.15 and 4.16, for MVA1 and MVA2, re-

Table 4.14 PID efficiencies and the ratios of the control modes to the signal mode.

	2016	2012
$\varepsilon(\Xi_{cc}^+)$	$(65.595 \pm 0.746) \times 10^{-2}$	$(58.671 \pm 4.466) \times 10^{-2}$
$\varepsilon(\Lambda_c^+)$	$(79.304 \pm 1.179) \times 10^{-2}$	$(74.055 \pm 2.647) \times 10^{-2}$
$\varepsilon(\Xi_{cc}^{++})$	$(63.635 \pm 1.039) \times 10^{-2}$	$(47.244 \pm 2.601) \times 10^{-2}$
$r(\Lambda_c^+) \equiv \varepsilon(\Lambda_c^+)/\varepsilon(\Xi_{cc}^+)$	$1.209 \pm 0.023$	$1.262 \pm 0.106$
$r(\Xi_{cc}^{++}) \equiv \varepsilon(\Xi_{cc}^{++})/\varepsilon(\Xi_{cc}^{+})$	$0.970 \pm 0.019$	$0.805 \pm 0.076$

Table 4.15 MVA1 efficiencies at the working point MVA1 > 0.00 and their ratios of the control modes to the signal mode.

	2016	2012
$arepsilon(\Xi_{cc}^+)$	$(73.202 \pm 0.638) \times 10^{-2}$	$(67.967 \pm 4.654) \times 10^{-2}$
$\varepsilon(\Lambda_c^+)$	$(82.152 \pm 0.969) \times 10^{-2}$	$(81.957 \pm 2.023) \times 10^{-2}$
$\varepsilon(\Xi_{cc}^{++})$	$(81.421 \pm 0.788) \times 10^{-2}$	$(81.958 \pm 2.140) \times 10^{-2}$
$r(\Lambda_c^+) \equiv \varepsilon(\Lambda_c^+)/\varepsilon(\Xi_{cc}^+)$	$1.122 \pm 0.016$	$1.206 \pm 0.088$
$r(\Xi_{cc}^{++}) \equiv \varepsilon(\Xi_{cc}^{++})/\varepsilon(\Xi_{cc}^{+})$	$1.112 \pm 0.014$	$1.206 \pm 0.088$

Table 4.16 MVA2 efficiencies at the working points MVA1 > 0.00 and MVA2 > 0.70 and their ratios of the control modes to the signal mode.

	2016	2012
$egin{aligned} arepsilon & arepsilon (\Xi_{cc}^+) \ & arepsilon (\Lambda_c^+) \ & arepsilon (\Xi_{cc}^{++}) \end{aligned}$	$(29.742 \pm 0.725) \times 10^{-2}$ $(100.000 \pm 0.000) \times 10^{-2}$ $(50.722 \pm 1.180) \times 10^{-2}$	$(17.644 \pm 2.391) \times 10^{-2}$ $(100.000 \pm 0.000) \times 10^{-2}$ $(25.391 \pm 2.130) \times 10^{-2}$
$r(\Lambda_c^+) \equiv \varepsilon(\Lambda_c^+)/\varepsilon(\Xi_{cc}^+)$ $r(\Xi_{cc}^{++}) \equiv \varepsilon(\Xi_{cc}^{++})/\varepsilon(\Xi_{cc}^+)$	$3.362 \pm 0.082$ $1.705 \pm 0.057$	$5.668 \pm 0.768$ $1.439 \pm 0.229$

spectively.

**Ratio of trigger efficiency.** The efficiencies of L0 and HLT1 trigger requirements are evaluated with simulation samples. The results are summarised in Table 4.17.

**Ratio of MC-Match efficiency.** The MC truth-matching is defined as follows. A reconstructed particle is matched to a simulated particle if there is an overlap of at least 70%

Table 4.17 L0 and HLT1 trigger efficiencies and their ratios of the control modes to the signal mode.

	2016	2012
$\varepsilon(\Xi_{cc}^+)$	$(21.606 \pm 1.184) \times 10^{-2}$	$(18.462 \pm 4.959) \times 10^{-2}$
$arepsilon(arLambda_c^+)$	$(19.968 \pm 1.002) \times 10^{-2}$	$(21.141 \pm 2.035) \times 10^{-2}$
$\varepsilon(\Xi_{cc}^{++})$	$(15.861 \pm 1.064) \times 10^{-2}$	$(18.133 \pm 2.527) \times 10^{-2}$
$r(\Lambda_c^+) \equiv \varepsilon(\Lambda_c^+)/\varepsilon(\Xi_{cc}^+)$	$0.924 \pm 0.069$	$1.145 \pm 0.327$
$r(\Xi_{cc}^{++}) \equiv \varepsilon(\Xi_{cc}^{++})/\varepsilon(\Xi_{cc}^{+})$	$0.734 \pm 0.064$	$0.982 \pm 0.297$

Table 4.18 MC-Match efficiencies and the ratios of the control to the signal modes.

	2016	2012
$\varepsilon(\Xi_{cc}^+)$	$(91.960 \pm 0.729) \times 10^{-2}$	$(94.353 \pm 2.242) \times 10^{-2}$
$\varepsilon(\Lambda_c^+)$	$(99.704 \pm 0.173) \times 10^{-2}$	$(99.832 \pm 0.229) \times 10^{-2}$
$\varepsilon(\Xi_{cc}^{++})$	$(89.581 \pm 1.520) \times 10^{-2}$	$(89.240 \pm 2.474) \times 10^{-2}$

between the hits created by the reconstructed particle and those associated to the simulated particle. The choice of the percentage threshold will lead to an inefficiency in the truth matching. Therefore, the selection efficiency estimated with simulation samples needs to be corrected as  $\varepsilon_{\rm corr}^{\rm Sel} = \varepsilon^{\rm Sel}/\varepsilon^{\rm MC-Match}$ , where the  $\varepsilon^{\rm MC-Match}$  is the MC-Match efficiency.

The MC-Match efficiency is calculated as the ratio of the number of MC-matched signals to the number of signals obtained by fitting to the invariant-mass distribution without MC-matching. Both numbers are obtained with samples after full event selection. The results are summarized at Table 4.18.

**Summary of efficiency.** Each of the efficiency ratios in Eq. 4.13 has been determined. The total efficiencies of the control modes and the signal mode as well as their ratios are summarised in Table 4.19.

The  $\Lambda_c^+$  efficiency is much higher as it decays to only three final-state particles. The  $\Xi_{cc}^+ \to \Lambda_c^+ K^- \pi^+$  efficiency is lower than that of the  $\Xi_{cc}^{++} \to \Lambda_c^+ K^- \pi^+ \pi^+$  because the  $\Xi_{cc}^+$  lifetime is lower by around a factor of three than that of  $\Xi_{cc}^{++}$ . The inefficiency is compensated partially by one less track.

According to the isospin symmetry, the  $\Xi_{cc}^+$  production cross-section is expected to be very similar, if not identical, to that of the  $\Xi_{cc}^{++}$ . Some theoretical calculations predict that the  $\mathcal{B}(\Xi_{cc}^+ \to \Lambda_c^+ K^- \pi^+)$  is a factor of five smaller than  $\mathcal{B}(\Xi_{cc}^{++} \to \Lambda_c^+ K^- \pi^+ \pi^+)$  [133]. Therefore the expected yield can be estimated through the efficiency comparison of  $\Xi_{cc}^+$  with  $\Xi_{cc}^{++}$  ( $r_{\Xi_{cc}^{++}}$ )), which is about 27 for the 2016 case and 4 for the 2012 case.

Variation of the efficiency with lifetime. The efficiency depends strongly on the  $\Xi_{cc}^+$  lifetime, due to variables that explore displaced vertices in the selection. Unfortunately, the prediction of  $\Xi_{cc}^+$  lifetime has a large theoretical uncertainty, as discussed in Sec. 1.2.1. Therefore, upper limits vary under different lifetime hypotheses. To take this effect into account, the efficiency is recalculated under different lifetime hypotheses. A discrete set of 40 fs, 80 fs, 120 fs, and 160 fs is considered.

	2016	2012
$egin{aligned} arepsilon & arepsilon (\Xi_{cc}^+) \ & arepsilon (\Lambda_c^+) \ & arepsilon (\Xi_{cc}^{++}) \end{aligned}$	$(9.053 \pm 0.576) \times 10^{-5}$ $(1.987 \pm 0.109) \times 10^{-3}$ $(10.562 \pm 0.764) \times 10^{-5}$	$(0.809 \pm 0.240) \times 10^{-5}$ $(0.437 \pm 0.045) \times 10^{-3}$ $(1.660 \pm 0.227) \times 10^{-5}$
$r(\Lambda_c^+) \equiv \varepsilon(\Lambda_c^+)/\varepsilon(\Xi_{cc}^+)$ $r(\Xi_{cc}^{++}) \equiv \varepsilon(\Xi_{cc}^{++})/\varepsilon(\Xi_{cc}^+)$	$21.947 \pm 1.850$ $1.167 \pm 0.114$	$53.998 \pm 17.021$ $2.051 \pm 0.675$

Table 4.19 Total efficiencies and their ratios of the control modes to the signal mode.

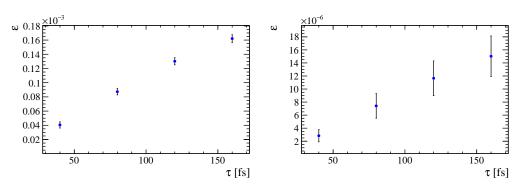


Figure 4.55 Efficiencies at different lifetime hypotheses for (left) 2016 and (right) 2012 data.

For non-zero lifetime hypotheses, the simulation sample generated with an input lifetime of  $\tau_0 = 333$  fs is reweighted according to the TRUE decay time t with the weight w(t) defined as

$$w(t) = \frac{\frac{1}{\tau} \exp(-\frac{t}{\tau})}{\frac{1}{\tau_0} \exp(-\frac{t}{\tau_0})},$$
(4.14)

where  $\tau$  is the target lifetime hypothesis to be considered. Hence, the efficiency for a given selection is

$$\varepsilon = \frac{\sum_{\text{pass}} w_i}{\sum_{\text{before}} w_j},\tag{4.15}$$

where the sum i runs over the events that pass the selection and j runs over all the events before the selection. For zero lifetime hypothesis, a dedicated simulation sample generated with  $\tau = 0$  fs is used to calculate the efficiency. The results are summarised in Tables 4.20 and 4.21, and are visualised in Fig. 4.55. A roughly linear dependence of the efficiency on lifetime hypotheses is observed. The variation of the efficiency with lifetime hypotheses for 2017 and 2018 data is studied with the same approach and summarised in Appendix E.

Table 4.20 Efficiencies at different lifetime hypotheses for 2016 data.

ε [×10 <sup>-2</sup> ]	$\tau = 40 \text{ fs}$	$\tau = 80 \text{ fs}$	$\tau = 120 \text{ fs}$	$\tau = 160 \text{ fs}$
Acc	$92.922 \pm 0.210$	$92.922 \pm 0.210$	$92.922 \pm 0.210$	$92.922 \pm 0.210$
Sel	$0.198 \pm 0.005$	$0.290 \pm 0.004$	$0.391 \pm 0.004$	$0.497 \pm 0.004$
PID	$65.337 \pm 1.278$	$65.595 \pm 0.746$	$65.324 \pm 0.535$	$64.869 \pm 0.431$
MVA1	$73.626 \pm 1.079$	$73.202 \pm 0.638$	$71.872 \pm 0.465$	$69.791 \pm 0.382$
MVA2	$18.503 \pm 0.985$	$29.742 \pm 0.725$	$35.515 \pm 0.597$	$37.411 \pm 0.520$
Trigger	$25.044 \pm 2.705$	$21.606 \pm 1.184$	$20.378 \pm 0.839$	$19.733 \pm 0.711$
Total [×10 <sup>-5</sup> ]	$4.456 \pm 0.584$	$9.053 \pm 0.576$	$13.440 \pm 0.631$	$16.771 \pm 0.683$

Table 4.21 Efficiencies at different lifetime hypotheses for 2012 data.

$\varepsilon \left[ \times 10^{-2} \right]$	$\tau = 40 \text{ fs}$	$\tau = 80 \text{ fs}$	$\tau = 120 \text{ fs}$	$\tau = 160 \text{ fs}$
Acc	$91.742 \pm 0.250$	$91.742 \pm 0.250$	$91.742 \pm 0.250$	$91.742 \pm 0.250$
Sel	$0.040 \pm 0.006$	$0.064 \pm 0.005$	$0.092 \pm 0.005$	$0.123 \pm 0.006$
PID	$59.368 \pm 7.486$	$58.671 \pm 4.466$	$58.678 \pm 3.141$	$58.694 \pm 2.546$
MVA1	$64.253 \pm 8.196$	$67.967 \pm 4.654$	$67.506 \pm 3.075$	$65.072 \pm 2.433$
MVA2	$8.820 \pm 1.745$	$17.644 \pm 2.391$	$21.357 \pm 2.399$	$22.328 \pm 2.355$
Trigger	$19.980 \pm 6.077$	$18.462 \pm 4.959$	$18.462 \pm 4.542$	$19.040 \pm 4.420$
Total [×10 <sup>-5</sup> ]	$0.262 \pm 0.084$	$0.809 \pm 0.240$	$1.404 \pm 0.381$	$1.943 \pm 0.495$

Variation of the efficiency with the  $\Xi_{cc}^+$  mass. Kinematic distributions of final-state tracks depend on the invariant mass of  $\Xi_{cc}^+$  baryons. Therefore, the efficiency may vary as a function of the mass.

To study this effect, a weighting procedure is used. Firstly, generator-level simulation samples is produced with different  $\Xi_{cc}^+$  mass hypotheses of 3518.7 MeV and 3700.0 MeV. Secondly, the full-simulated sample, which is generated with  $m_0=3621.4$  MeV, is weighted according to the generator-level  $p_{\rm T}$  distributions of  $\Xi_{cc}^+$  decay products,  $\Lambda_c^+$ ,  $K^-$  and  $\pi^+$  track. The efficiency is then recalculated for each mass hypothesis with weighted samples. The weights are obtained with the GBReweightor from the hep\_ml python module, a reweighting algorithm based on ensemble of regression trees [188].

The results are shown in Table 4.22 and visualized in Fig. 4.56. The dependence of the total efficiency on the  $\Xi_{cc}^+$  mass hypotheses is weak in a wide range of mass hypothesis. Therefore, we do not include this effect when calculating the upper limits at different mass

ε [×10 <sup>-2</sup> ]	$m(\Xi_{cc}) = 3518 \text{ MeV}$	$m(\Xi_{cc}) = 3621 \text{ MeV}$	$m(\Xi_{cc}) = 3700 \text{ MeV}$
Acc	$94.211 \pm 0.320$	$92.922 \pm 0.210$	$92.416 \pm 0.356$
Sel	$0.296 \pm 0.004$	$0.290 \pm 0.004$	$0.278 \pm 0.004$
PID	$65.852 \pm 0.756$	$65.595 \pm 0.746$	$65.170 \pm 0.753$
MVA1	$74.063 \pm 0.635$	$73.202 \pm 0.638$	$72.153 \pm 0.655$
MVA2	$27.706 \pm 0.698$	$29.742 \pm 0.725$	$30.588 \pm 0.740$
Trigger	$22.010 \pm 1.195$	$21.606 \pm 1.184$	$21.502 \pm 1.206$
$Total [\times 10^{-5}]$	$8.281 \pm 0.524$	$8.325 \pm 0.530$	$7.934 \pm 0.519$

Table 4.22 Efficiencies at different mass hypotheses.

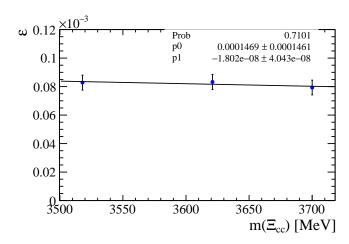


Figure 4.56 Efficiency as a function of mass hypotheses.

hypotheses.

#### 4.5.4 Systematic uncertainties

Sources of systematic uncertainties are studied when calculating the upper limits, including those in the efficiency estimation and in the yield determination. Systematic uncertainties are summarized in Table 4.23. The total systematic uncertainty is calculated as the quadratic sum of individual uncertainties, assuming all sources to be independent. The systematic uncertainty is dominated by the uncertainty of the L0 trigger efficiency.

**Tracking efficiency uncertainty.** As mentioned in Sec. 4.5.3, the ratio of the tracking efficiencies is corrected for the discrepancy between data and simulated samples. Three sources of systematic uncertainties related to this correction are considered.

The first source is the statistical uncertainty of the tracking correction table. The effect is estimated using 1 000 pseudoexperiments. In each pseudoexperiment, a new

Table 4.23 Summary of the systematic uncertainties in the upper limit setting.

Source	20	2016		2012	
Source	$R_{\Lambda_c^+}$	$R_{\Xi_{cc}^{++}}$	$R_{\varLambda_c^+}$	$R_{\varXi_{cc}^{++}}$	
Tracking	4.4%	3.1%	4.3%	2.6%	
PID	0.9%	0.8%	2.5%	4.6%	
L0 trigger	4.9%	11.2%	11.7%	17.7%	
Fit model	0.6%	0.4%	5.8%	8.9%	
Total	6.7	11.4	14.0	20.5	

correction table is created. The correction factor in each bin is obtained by sampling from the Gaussian distribution with the mean value of the default table and the width equal to its statistical uncertainty. Then the reconstruction and selection efficiency is reevaluated with the new table, using the same procedure as in the estimation of the default efficiency. The Gaussian width of the distribution of the efficiency ratios is assigned as the systematic uncertainty, which, divided by the central value, is estimated to be 0.64% and 1.33% for the  $\Lambda_c^+$  control mode in 2016 and 2012 datasets, respectively, and 0.63% and 0.16% for the  $\Xi_{cc}^{++}$  control mode in 2016 and 2012 datasets, respectively.

The second source is the method used when generating the correction tables. It is found to be 0.8% and 0.4% per track for 2016 and 2012 datasets without the dependence on the kinematics of the track. Assuming the systematic uncertainties for different type of particles in the signal and control mode are fully correlated, the uncertainties due to the same type of particles in both the signal and control mode (e.g., p, K,  $\pi$  from the  $\Lambda_c^+$  decay) cancel out for the  $\Lambda_c^+$  and  $\Xi_{cc}^{++}$  control modes. The uncertainties are found to be 1.6% and 0.8% for 2016 datasets, and 0.8% and 0.4% for 2012 datasets.

The third source is related to the hadronic interaction of the final-state hadrons. To study this effect, the full-simulated sample of  $\Xi_{cc}^{++}$  baryons is used to estimate the fractions of kaons and pions that end up with a hadronic interaction before the last T-station. It is found to be 14.9% and 25.4% for K and  $\pi$ , respectively. Assuming, conservatively, that the overall uncertainty of detector material budget to be 10% as discussed in Section 3.4.1 of [189], the uncertainties for tracking efficiency due to hadronic interaction is thus 1.49% and 2.54% for K and  $\pi$ , respectively. Assuming the systematic uncertainties for different type of particles in the signal and control mode are fully correlated, the uncertainties due to the same type of particles in both the signal and control mode (e.g., p, K,  $\pi$  from the  $\Lambda_c^+$  decay) cancel out. The relative uncertainties for the  $\Lambda_c^+$  and  $\Xi_{cc}^{++}$  control modes are

Table 4.24 Systematic uncertainties on ratios of the tracking efficiency.

Source	2016		2012	
Source	$r(\Lambda_c^+)$	$r(\Xi_{cc}^{++})$	$r(\Lambda_c^+)$	$r(\Xi_{cc}^{++})$
Correction table uncertainty	0.64%	0.63%	1.33%	0.16%
Tracking method	1.6%	0.8%	0.8%	0.4%
Hadronic interaction	4.0%	2.5%	4.0%	2.5%
Total	4.4%	3.1%	4.3%	2.6%

Table 4.25 Systematic uncertainties on the ratios of the PID efficiencies.

PID efficiency Syst. [%]	2016	2012
$r(\Lambda_c^+)$	0.9	2.5
$r(\Xi_{cc}^{++})$	0.8	4.6

found to be 4.0% and 2.5%, respectively.

The systematic uncertainties on tracking efficiency are obtained by combining the above uncertainties as a sum in quadrature, and are summarized in Table 4.24.

**PID efficiency.** The PID efficiency is evaluated with the PIDCalib package. The systematic uncertainties due to the statistical uncertainty of correction tables are evaluated with simulation and are found to be negligible for both  $\Lambda_c^+$  and  $\Xi_{cc}^{++}$  control modes. The systematic uncertainty due to the binning scheme of the kinematic variables is estimated by varying the binning schemes, in this case we double the momentum bins, of the calibration sample. The discrepancy of the efficiency ratios between different binning schemes are taken as a systematic uncertainty. Results are summarised in Table 4.25. Due to the limited statistics, the systematics for 2012 data is larger.

**L0 trigger efficiency.** The default value of the trigger efficiency is estimated with the full-simulated samples. We treat the HLT triggers as well modelled in simulation, with appropriate corrections for tracking efficiency. However, it is known that simulation does not describe the L0 trigger well. To estimate the systematic uncertainty of the L0 trigger efficiencies, two extra control samples of  $\Lambda_b^0 \to \Lambda_c^+ \pi^- \pi^+ \pi^-$  and  $\Lambda_b^0 \to \Lambda_c^+ \pi^-$  are used. These two channels have a similar decay topology compared with that of  $\Xi_{cc}^+$  decays. The

Table 4.26 Summary of the L0 efficiencies of the control channels.

$R^{TOS}$	20	16	2012		
Λ	Data	MC	Data	MC	
$R^{\text{TOS}}(\Lambda_c^+)$	1.17±0.02	1.23±0.12	1.62±0.04	1.45±0.07	
$R^{\rm TOS}(\Xi_{cc}^{++})$	0.99 <u>±</u> 0.02	$0.89 \pm 0.04$	1.13±0.03	$0.96 \pm 0.04$	

Table 4.27 Systematic uncertainties on the L0 efficiency.

L0 efficiency Syst. [%]	2016	2012
$r(\Lambda_c^+)$	4.9	11.7
$r(\Xi_{cc}^{++})$	11.2	17.7

systematic uncertainties of the L0 efficiency are thus calculated with

$$S_{L0}^{TOS}(\Lambda_{c}^{+}) = \frac{|R_{Data}^{TOS}(\Lambda_{c}^{+}) - R_{MC}^{TOS}(\Lambda_{c}^{+})|}{R_{MC}^{TOS}(\Lambda_{c}^{+})}$$

$$S_{L0}^{TOS}(\Xi_{cc}^{++}) = \frac{|R_{Data}^{TOS}(\Xi_{cc}^{++}) - R_{MC}^{TOS}(\Xi_{cc}^{++})|}{R_{MC}^{TOS}(\Xi_{cc}^{++})},$$
(4.16)

where the  $R^{\rm TOS}(\varLambda_c^+)$  and  $R^{\rm TOS}(\Xi_{cc}^{++})$  are defined as

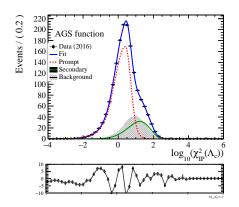
$$R^{\text{TOS}}(\Lambda_c^+) = \frac{\varepsilon^{\text{TOS}}(\Lambda_c^+ \to pK^-\pi^+)}{\varepsilon^{\text{TOS}}(\Lambda_b^0 \to \Lambda_c^+\pi^-\pi^+\pi^-)}$$

$$R^{\text{TOS}}(\Xi_{cc}^{++}) = \frac{\varepsilon^{\text{TOS}}(\Lambda_b^0 \to \Lambda_c^+\pi^-\pi^+\pi^-)}{\varepsilon^{\text{TOS}}(\Lambda_b^0 \to \Lambda_c^+\pi^-)}.$$
(4.17)

The subscripts indicate whether the efficiency is evaluated with real data or simulation. The L0 efficiency  $\varepsilon^{TOS}$  is determined with the TISTOS method by

$$\varepsilon^{\text{TOS}} = \frac{N^{\text{TIS\&TOS}}}{N^{\text{TIS}}} \tag{4.18}$$

where  $N^{\rm TIS\&TOS}$  is the number of events that pass both L0 TIS and Lc\_L0Hadron TOS trigger requirements, and  $N^{\rm TIS}$  is the number of events that pass L0 TIS requirements. To be specific, the L0 TIS events are required to pass either of the following L0 TIS triggers: L0Photon, L0Electron, L0Muon, and L0DiMuon. The discrepancies of the measured L0 TOS efficiencies between simulation and data are assigned as the L0 efficiency systematics. The measured efficiencies and corresponding systematic uncertainties are summarized in Table 4.26 and Table 4.27, respectively.



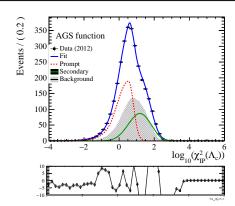


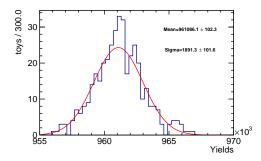
Figure 4.57 Distribution of  $\log \chi_{\rm IP}^2$  in (left) the 2016 data sample and (right) 2012 data sample, along with the fit results.

**Yield determination.** For the  $\Lambda_c^+$  control mode, the yield of the prompt  $\Lambda_c^+$  is extracted by the fit to the  $\log_{10}(\chi_{\rm IP}^2)$  distribution. The systematic effects is mainly due to the signal and background modelling. For the signal modelling, an alternative model with the AR-GUS function is used. The difference of the obtained yields are assigned as the systematic uncertainty.

In the default result, the shape of the combinatorial background is taken from the mass-sideband samples. To evaluate the uncertainty in the background shape, we utilise a toy approach. We take the default histogram and fluctuate the populations in each bin. The combinatorial yield in each bin is the sum of background sWeights. The uncertainty on the yield is the sum of these weights squared. We resample the yield of each bin according to a Gaussian distribution, with the default bin yield as the mean and the uncertainty on that yield as the width. We repeat the fit 1 000 times and perform a Gaussian fit to the distribution of the yield. The width of the distribution is assigned as the systematic uncertainty due to background modelling. The fit result is shown in Fig. 4.58 and the systematic uncertainties are summarized at Table 4.28.

The systematics are also studied using Transverse Impact Parameter (TIP, the minimum distance between the track projection on a plane transverse to the beam and the PV) as the discriminating variable. The corresponding uncertainties are determined to be 4.2% for 2016 sample and 5.5% for 2012 sample.

For the  $\Xi_{cc}^{++}$  control mode, the systematics due to the signal modelling are studied by changing the signal shape to a two-Gaussian function. The resultant changes in the yields are taken as systematics. To estimate the impact of the background model, we alter the background shape to a second order Polynomial function. The relative systematic uncertainties are summarized in Table 4.28.



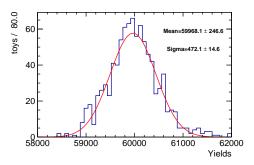


Figure 4.58 Distribution of the extracted prompt yields of toy experiments, for the (left) 2016 data sample and (right) 2012 data sample, along with the fit results.

Source	2016		2012	
Source	$r(\Lambda_c^+)$	$r(\Xi_{cc}^{++})$	$r(\Lambda_c^+)$	$r(\Xi_{cc}^{++})$
signal model	0.6%	0.3%	5.8%	5.7%
background model	0.2%	0.3%	0.4%	6.8%
Total	0.6%	0.4%	5.8%	8.9%

Table 4.28 Systematic uncertainties due to the fit model.

## 4.5.5 Determination of upper limits

With the knowledge of the ratios of luminosity, efficiency, and the yields of the control modes, the upper limit on R, calculated according to Eq. 4.10, can be evaluated with different mass and lifetime hypotheses. The values of single event sensitivity  $\alpha$ , defined in Eq. 4.10, for  $\Lambda_c^+$  and  $\Xi_{cc}^{++}$  control modes are summarised in Table 4.29 and Table 4.30, respectively. Only statistical uncertainties are included in these Tables. One can see that the sensitivity has been improved by more than a factor of ten for 2016 data compared with 2012 data when normalised to  $\Lambda_c^+$ , and by four when normalised to  $\Xi_{cc}^{++}$ , thanks to the improved Run 2 trigger selection. Upper limits will be set in the fiducial region of  $\Xi_{cc}^+$  baryons and will be quoted for two different center of mass energy:  $\sqrt{s}=8\,\text{TeV}$ , corresponding to the 2012 data, and  $\sqrt{s}=13\,\text{TeV}$ , corresponding to 2016-2018 data.

The procedure of setting the upper limits is as follows:

- The mass parameter μ in the signal lineshape is fixed to a given value in the range of [3400, 3800] MeV with a step size of 2.5 MeV, which corresponds to roughly half of the mass resolution.
- An extended unbinned likelihood fit is performed to the  $m(\Lambda_c^+ K^- \pi^+)$  distribution of data sample in the range of [3400, 3800] MeV.

Table 4.29 Single event sensitivity  $\alpha(\Lambda_c^+)$  (×10<sup>-5</sup>) of the  $\Lambda_c^+$  control mode for different datasets and lifetime hypotheses.

	$\tau$ =40 fs	τ=80 fs	$\tau$ =120 fs	$\tau$ =160 fs
2012	$14.218 \pm 4.822$	$4.595 \pm 1.444$	$2.648 \pm 0.770$	$1.913 \pm 0.527$
2016	$0.596 \pm 0.085$	$0.294 \pm 0.025$	$0.198 \pm 0.014$	$0.158 \pm 0.011$
2017	$0.457 \pm 0.042$	$0.226 \pm 0.013$	$0.153 \pm 0.009$	$0.125 \pm 0.008$
2018	$0.518 \pm 0.041$	$0.233 \pm 0.016$	$0.150 \pm 0.012$	$0.115 \pm 0.012$

Table 4.30 Single event sensitivity  $\alpha(\Xi_{cc}^{++})$  (×10<sup>-2</sup>) of the  $\Xi_{cc}^{++}$  control mode for different datasets and lifetime hypotheses.

	$\tau$ =40 fs	τ=80 fs	$\tau$ =120 fs	$\tau$ =160 fs
2012	16.702 ± 7.071	$5.397 \pm 2.179$	$3.111 \pm 1.200$	$2.248 \pm 0.841$
2016	$1.959 \pm 0.425$	$0.964 \pm 0.178$	$0.649 \pm 0.116$	$0.521 \pm 0.092$
2017	$2.514 \pm 0.425$	$1.246 \pm 0.190$	$0.844 \pm 0.129$	$0.685 \pm 0.106$
2018	$2.357 \pm 0.343$	$1.060 \pm 0.149$	$0.682 \pm 0.100$	$0.523 \pm 0.084$

- The negative log likelihood (NLL) as a function of *R* is obtained from the fit and is converted to a likelihood (offset is added to have the minimum of the likelihood at 0).
- The likelihood profile is obtained for 100 values of R in fine steps of equal size.
- The likelihood profile is used to compute the numerical integral and determine the value of *R* corresponding to 95% of the total likelihood integral. This value corresponds to the upper limit of *R* at 95% confidence level.

The resolution parameter  $\sigma$  of the signal lineshape is varied at different mass hypotheses, while other parameters remain the same. The upper limits at different lifetime hypotheses are determined by considering the efficiency variation described in Sec.4.5.3. Due to the different  $\alpha$  values for 2016-2018 data sets, simultaneous fit to the  $m(\Lambda_c^+ K^- \pi^+)$  distribution with shared R is performed to calculate the upper limit at  $\sqrt{s} = 13$  TeV.

The above procedure is tested with a toy experiment and the fits are robust and returns expected results across the mass scan region. As a cross check, the upper limit at  $m(\Lambda_c^+ K^- \pi^+) = 3621.4 \,\text{MeV}/c^2$  is evaluated with the 2011 dataset and is found to be in good agreement of the previous LHCb search using 2011 data [146].

Systematic uncertainties are considered by convolving the normalised likelihood curve with a Gaussian function  $G(\mu, \sigma) = G(0, \sigma_{\text{syst}})$  with  $\sigma_{\text{syst}} = \mu \times \sigma_{\text{rel}}$ , where  $\sigma_{\text{rel}}$ 

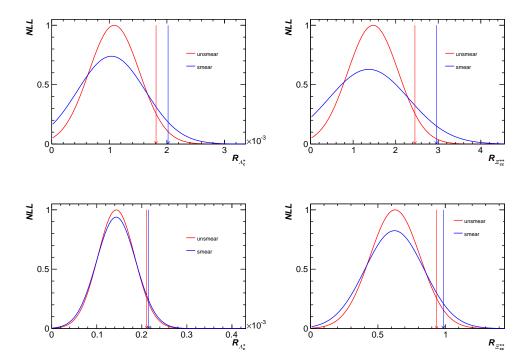


Figure 4.59 Normalized likelihood distribution before (red curve) and after (blue curve) convolution for (left)  $R_{A_c^+}$  and (right)  $R_{\Xi_{cc}^+}$  and for (top) 2012 and (bottom) 2016 data at the best mass point. The arrow shows the 95% upper limit using only statistical uncertainty (red) and using both statistical and systematic uncertainties (blue).

is the relative systematic uncertainty described in Sec. 4.5.4. The convolution can be described in terms of

$$L(N') = \int_0^\infty L(N) \times \frac{1}{\sqrt{2\pi}\sigma_{\text{syst}}} \times \exp\left[\frac{-(N'-N)^2}{2\sigma_{\text{syst}}^2}\right] dN, \tag{4.19}$$

where L(N) is the normalised likelihood distribution obtained from fitting the curve of normalised likelihood value versus the cross-section ratio and parameterised as a Gaussian function. As an illustration, the likelihood distribution before and after the convolution at the mass point with the largest local significance is shown in Fig. 4.59 for 2012 and 2016 data, respectively.

Figures 4.60 and 4.61 show the 95% credibility level upper limits at centre-of-mass energies of  $\sqrt{s} = 8$  TeV and  $\sqrt{s} = 13$  TeV, respectively.

#### 4.6 Result and discussion

A search for the doubly charmed baryon  $\Xi_{cc}^+$  is performed through the  $\Lambda_c^+K^-\pi^+$  final state, with the pp collision data collected by the LHCb experiment at center-of-mass energies of 8 TeV and 13 TeV, corresponding to an integrated luminosity of about 7.7 fb<sup>-1</sup>. No

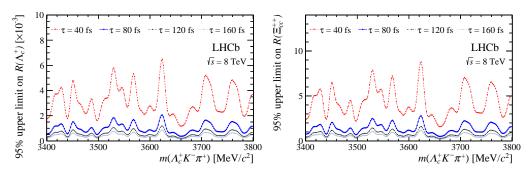


Figure 4.60 Upper limits on (left)  $\mathcal{R}(\Lambda_c^+)$  and (right)  $\mathcal{R}(\Xi_{cc}^{++})$  at 95% credibility level as a function of  $m(\Lambda_c^+K^-\pi^+)$  at  $\sqrt{s}=8$  TeV for four  $\Xi_{cc}^+$  lifetime hypotheses.

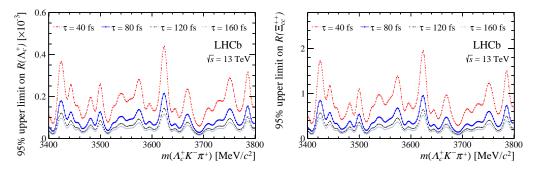


Figure 4.61 Upper limits on (left)  $\mathcal{R}(\Lambda_c^+)$  (right)  $\mathcal{R}(\Xi_{cc}^{++})$  at 95% credibility level as a function of  $m(\Lambda_c^+K^-\pi^+)$  at  $\sqrt{s}=13$  TeV, for four  $\Xi_{cc}^+$  lifetime hypotheses.

significant signal is observed in the mass range 3.4 to 3.8 GeV. A small enhancement is seen near a mass of the  $\Xi_{cc}^{++}$  baryon, with a local significance of 2.7 $\sigma$ . This enhancement is consistent with precise LQCD calculations and isospin symmetry predictions.

Upper limits are set at 95% confidence level on the ratio of the  $\Xi_{cc}^+$  production cross-section times the branching fraction to that of the  $\Lambda_c^+$  and  $\Xi_{cc}^{++}$  baryons. The limits are determined as functions of the  $\Xi_{cc}^+$  mass for different lifetime hypotheses. The limits are set in the fiducial region of the (doubly) charmed baryon where the rapidity is in the range of 2.0 to 4.5 and the transverse momentum ranges from 4 to 15 GeV. The limits are determined as functions of the  $\Xi_{cc}^+$  mass for different lifetime hypotheses, in the rapidity range from 2.0 to 4.5 and the transverse momentum range from 4 to 15 GeV. The upper limit on the production ratio  $R_{\Lambda_c^+}$  ( $R_{\Xi_{cc}^{++}}$ ) depends strongly on the considered mass and lifetime of the  $\Xi_{cc}^+$  baryon, varying from 0.45 × 10<sup>-3</sup> (2.0) for 40 fs to 0.12 × 10<sup>-3</sup> (0.5) for 160 fs, as summarised in Table 4.31. The upper limits on  $R(\Lambda_c^+)$  are improved by more than one order of magnitude compared with the previous LHCb search [146] and are significantly below the value reported by SELEX [137], albeit in a different production environment. Future searches by the LHCb experiment with improved trigger conditions, additional  $\Xi_{cc}^+$  decay modes, and larger data samples should significantly increase the  $\Xi_{cc}^+$ 

Table 4.31 Summary of the largest upper limits on production ratios at 95% credibility level for four lifetime hypotheses and different centre-of-mass energies.

Lifetime	$\sqrt{s} = 8  \text{TeV}$		$\sqrt{s} = 13 \text{ TeV}$	
Lifetime	$\mathcal{R}(\Lambda_c^+) \left[ \times 10^{-3} \right]$	$\mathcal{R}(\Xi_{cc}^{++})$	$\mathcal{R}(\Lambda_c^+) \left[ \times 10^{-3} \right]$	$\mathcal{R}(\Xi_{cc}^{++})$
40 fs	6.5	8.8	0.45	2.0
80 fs	2.1	2.8	0.22	1.0
120 fs	1.2	1.6	0.15	0.6
160 fs	0.9	1.2	0.12	0.5

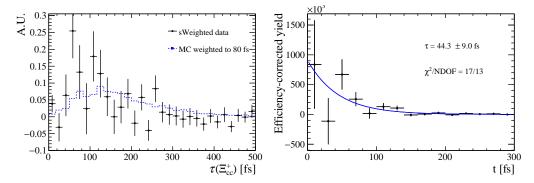


Figure 4.62 The (left) comparison of the simulated and "background-subtracted" decay-time distribution and (right) efficiency-corrected and background-subtracted decay-time distribution, along with the fit result with an exponential function. The selection for setting upper limits is applied. The simulated signals have an input lifetime of 80 fs.

signal sensitivity.

As a guidance to future searches, the lifetime of the  $\Xi_{cc}^+$  baryon is estimated with the sample used to set upper limits, which shows an enhancement at around 3.62 GeV with a local significance above  $3\sigma$ . A comparison of the simulated and the "background-subtracted" decay-time distribution is shown in the left plot in Fig. 4.62. The simulated signals are generated with an input lifetime of 80 fs. The background subtraction is achieved from the mass fit to the invariant-mass distribution. An estimation of the lifetime can be obtained by fitting the efficiency-corrected and background-subtracted data with an exponential function, which is shown in the right plot in Fig. 4.62. The estimation obtains a  $\Xi_{cc}^+$  lifetime of around 40 fs. This value is smaller than most theoretical predictions, while consistent with the predicted lifetime ratio of  $\Xi_{cc}^{++}$  to  $\Xi_{cc}^+$  baryon.

## CHAPTER 5 SUMMARY AND PROSPECTS

Charmed baryons serve as a unique probe of Quantum Chromodynamics in the nonperturbative regime. This thesis reports two measurements of charmed baryons, which provide solid experimental foundations for the refinement of nonperturbative QCD methods and the search for new physics.

Lifetimes of weakly decaying heavy flavour hadrons can be calculated with the framework of Heavy Quark Expansion, in which the total decay width can be expressed as expansions in terms of inverse heavy quark mass. Theoretical prediction of the lifetime hierarchy of charmed baryons is  $\Omega_c^0(css) < \Xi_c^0(csd) < \Lambda_c^+(cud) < \Xi_c^+(csu)$ , which agrees with early measurements within large experimental uncertainties. Recent LHCb measurements report significantly different lifetimes of  $\Omega_c^0$  and  $\Xi_c^0$  baryons, leading to a new lifetime hierarchy of  $\Xi_c^0 < \Lambda_c^+ < \Omega_c^0 < \Xi_c^+$ . This contradicts early measurements as well as theoretical predictions, and calls for independent measurements to clarify the situation. This thesis reports a new measurement of  $\Omega_c^0$  and  $\Xi_c^0$  lifetimes using charmed baryons produced directly from pp collisions. The results are

$$\tau(\Omega_c^0) = 276.5 \pm 13.4 \pm 4.4 \pm 0.7 \text{ fs},$$
  
 $\tau(\Xi_c^0) = 148.0 \pm 2.3 \pm 2.2 \pm 0.2 \text{ fs},$ 

where the uncertainties are statistical, systematic, and due to the limited knowledge of the  $D^0$  lifetime. The results are consistent with previous LHCb measurements using charmed baryons produced in semileptonic beauty hadron decays. Thus the new lifetime hierarchy is confirmed. The precision of  $\Omega_c^0$  lifetime is improved by a factor of two compared with the previous measurement. Higher order corrections and nonperturbative hadronic matrix elements in the HQE have to be reexamined in order to understand the dynamics of weak decays.

Doubly charmed baryons have been predicted by the quark model back in 1970s. They provide an inimitable platform for the development of nonperturbative QCD approaches due to two constituent charm quarks. However only one out of the three doubly charmed baryons, the  $\Xi_{cc}^{++}$  baryon, is established unambiguously by the LHCb experiment recently. This thesis reports a search for the doubly charmed baryon  $\Xi_{cc}^{+}$  in the  $\Lambda_c^+ K^- \pi^+$  decay channel with pp collision data collected by the LHCb experiment, corresponding to an integrated luminosity of 9 fb<sup>-1</sup>. The invariant-mass spectrum of the  $\Lambda_c^+ K^- \pi^+$  final

Table 5.1 Operation conditions for LHCb Upg	grades.
---	---------

Run	Period	$\sqrt{s}$ [TeV]	Instantaneous lumi. [cm <sup>-2</sup> s <sup>-1</sup> ]	Integrated lumi. [fb <sup>-1</sup> ]	Average pile-up
Upgrade I Run 3 Run 4 Upgrade II	2019-2021 2022-2024 2027-2030 2031	14	$2\times10^{33}$	50	5
Run 5	$2032 \rightarrow$	14	$2 \times 10^{34}$	300	50

state exhibits an enhancement in the vicinity of  $m_{\Xi_{cc}^{++}}$ , while no significant signals are observed in the explored region of 3.4-3.8 GeV. Upper limits are set on the production cross-section times branching fraction, relative to that of the  $\Lambda_c^+$  baryon produced directly in pp collision, which is an order of magnitude more strict than the previous LHCb search. Upper limits are also set relative to that of the  $\Xi_{cc}^{++}$  baryon reconstructed in the  $\Lambda_c^+ K^- \pi^+ \pi^+$  decay channel, which put constraints on the lifetime and branching fraction of the  $\Xi_{cc}^+$  baryon and provide information for future experimental expedition.

From the experimental perspective, the lifetimes of some of the weakly decaying heavy flavour hadrons are known with only limited precision. The spectroscopy of doubly charmed baryons is still in its infancy. Prospects of measurements of lifetimes and the spectroscopy of doubly charmed baryons are discussed in Sec. 5.2 and Sec. 5.3, respectively, before which an introduction of current and future experimental programs is presented in Sec. 5.1.

# 5.1 LHCb upgrade and other programs

To fully exploit the opportunities provided by the upgraded LHC, the LHCb detector is currently undergoing a major upgrade [190-191] and will be further upgraded during Long Shutdown 3 [192-193], which is discussed in some detail below. Thereafter, other current and future experimental programs will be discussed briefly in this section.

**LHCb upgrade.** Two phases of upgrade are scheduled for the LHCb detector. The data taking plan and operation conditions are summarised in Table 5.1.

The key feature of Upgrade I is the trigger-less readout and fully flexible software trigger. The maximum readout rate of the LHCb detector in Run 2 is determined by frontend (FE) electronics to be 1 MHz. A hardware trigger is used to reduce the LHC clock

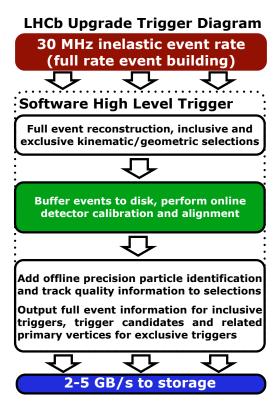


Figure 5.1 LHCb upgrade trigger diagram.

rate of 40 MHz, based on the deposit of several GeV of transverse energy in the Calorimeter and Muon systems by charged hadrons, muons, electrons or photons, as discussed in Sec. 2.2.1. The trigger yield therefore saturates for hadronic channels with increasing luminosity. The detector in Upgrade I will employ a trigger-less readout by upgrading all the front-end electronics using modern technologies adapted for high energy physics. This will allow to perform data acquisition and event building at the full rate of 40 MHz. The upgrade trigger diagram is shown in Fig. 5.1 [194]. The software HLT shares the basic feature with Run 2 trigger, with an significantly increased output bandwidth due to the increase of computational resources. The discriminating power of the trigger is enhanced with the full event information, including whether tracks originate from the displaced vertex that is characteristic of heavy flavour decays. An evolved reduced event model is extensively used, in which additional reconstructed objects in the event are selected and persisted. This is implemented with sufficient flexibility, thus allowing for fin-grained tuning between trigger output bandwidth and event utility offline.

In addition, subdetectors have to be replaced to cope with high occupancy conditions of the upgrade with  $2 \times 10^{33} \, \mathrm{cm}^{-2} \, \mathrm{s}^{-1}$  luminosity. In particular, a pixel Vertex Locator (VELO), a silicon tracking station before the magnet (UT), and a large-scale downstream

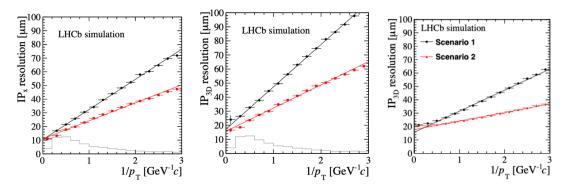


Figure 5.2 Impact parameter resolution (left) in the x projection for Upgrade I, (middle) 3D resolution for Upgrade I, and (right) 3D resolution for Upgrade II. In the left and middle plots, the VELO in Run 2 is shown with black circles and the Upgrade I VELO with red squares. In the right plot, different circles correspond to different design scenarios.

Scintillating Fibre (SciFi) tracker system will be installed. The impact parameter resolution of the upgrade detector is studied using simulation in the upgrade condition, as shown in Fig. 5.2 [195]. The impact parameter resolution is improved relative to the Run 2 detector, leading to an improvement of 5 fs in decay-time resolution for the  $B_s^0 \rightarrow J h \psi \phi$  mode.

Further data taking with the Upgrade I detector will not be attractive beyond Run 4 due to the excessive "data-doubling" time and that many of its components will have reached the end of their natural life span due to radiation exposure. During Upgrade II, the detector will collect data with ten times larger luminosity of  $2 \times 10^{34}$  cm<sup>-2</sup> s<sup>-1</sup>. The increased particle multiplicity and rates will present even more significant problems for all subdetectors. The key features of the Upgrade II detector include:

- Precise timing in the VELO detector and also downstream of the magnet for both charged tracks and neutrals. This information will allow charged tracks and photons to be associated to the correct interaction vertex and therefore to suppress combinatoric background.
- A high granularity tungsten sampling electromagnetic calorimeter will extend the experiment's capabilities in final states involving photons,  $\pi^0$  mesons and electrons.
- The tracking acceptance will be significantly increased for soft tracks by instrumenting the side walls of the dipole, improving the experiment's efficiency for high multiplicity decays.

A similar performance of vertex resolution to Upgrade I is achieved in much hash conditions, as illustrated in Fig. 5.2.

Table 5.2 Current and future experimental programs that are candidate players of doubly charmed baryon studies.

Programs	Туре	Energy	Luminosity [cm <sup>-2</sup> s <sup>-1</sup> ]	Comment
Belle II	$e^+e^-$	$\sqrt{s} = 10.58 \text{GeV}$	$8 \times 10^{35}$	$\Upsilon(4S)$
CEPC	$e^+e^-$	$\sqrt{s} = 91 \text{GeV}$	$32 \times 10^{34}$	Z-mode
FCC	$e^+e^-$	$\sqrt{s} = 91 \text{GeV}$	$2 \times 10^{36}$	FCC-ee-Z
ILC	$e^+e^-$	$\sqrt{s} = 250 \text{GeV}$	$7.5 \times 10^{33}$	1st stage
CLIC	$e^+e^-$	$\sqrt{s} = 500 \text{GeV}$	$2.3 \times 10^{34}$	
LHeC	ep	$E_e = 60 \text{GeV}, E_p = 7 \text{TeV}$	$1 \times 10^{33}$	LHC Run 5
LHCb Upgrade I	pp	$\sqrt{s} = 14  \text{TeV}$	$2 \times 10^{33}$	LHC Run 3-4
LHCb Upgrade II	pp	$\sqrt{s} = 14  \text{TeV}$	$2 \times 10^{34}$	HL-LHC
ALICE Upgrade	PbPb	$\sqrt{s_{NN}} = 5.5 \mathrm{TeV}$	$6 \times 10^{27}$	

Other programs. As discussed in Sec. 1.3.1, there are potentially a large number of doubly charmed baryons produced in different environments other than pp collision, including the super B factory experiment Belle II at SuperKEKB [196], the Circular Electron Positron Collider (CEPC) as a Super Z factory [197], the Future Circular Collider (FCC), as a super Z factory [198], the International Linear Collider (ILC) at 1st stage [199], the Compact Linear Collider (CLIC) [200], the Large Hadron-Electron Collider (LHeC) at the HL-LHC [201], and A Large Ion Collider Experiment (ALICE) [202]. The operation conditions are summarised in Table 5.2.

# 5.2 Prospects for lifetime measurements

The current precisions of lifetimes of weakly decaying heavy flavour baryons are summarised in Table 5.3.

In the charm sector, the lifetime of  $\Omega_c^0$  baryon is still the worst known among singly charmed baryons, despite a significant improvement achieved in the measurement performed in this thesis. The LHCb measurement using signals from semileptonic beauty hadron decays was performed with data collected during 2011-2012 in pp collisions at center-of-mass energy of 7, 8 TeV, corresponding to an integrated luminosity of 3 fb<sup>-1</sup> [45]. This measurement can be updated with data during 2015-2018, with both the center-of-mass energy and integrated luminosity increased by a factor of about two. At least a four times increase of the number of signals (assuming the same selection efficiency) can be achieved, which will reduce the statistical uncertainty by a factor of two,

Table 5.3 Precisions of lifetimes of weakly decaying heavy flavour baryons [2]. The combination values in this thesis are used for lifetimes of  $\Omega_c^0$  and  $\Xi_c^0$  baryon.

Particles	Lifetime [fs]	Uncertainty [fs]	Relative uncertainty [%]
$\Xi_c^0$	152	2	1
$\Lambda_c^+$	202	3	1
$arOmega_c^0$	275	12	4
$\Xi_c^+$	456	5	1
$\Xi_{cc}^{++}$	256	27	11
$A_b^0$	1464	11	1
$\varXi_b^0$	1480	30	2
$\varXi_b^-$	1572	40	3
$\Omega_b^-$	1640	175	11

down to 10 fs or so. The lifetime of  $\Omega_c^0$  baryon can also be measured with full LHCb data using signals from nonleptonic beauty hadron decays. This will provide additional validation with different techniques and data sets, although no significant improvement on the precision is expected due to limited sample size of nonleptonic decays. The lifetimes of doubly charmed baryons  $\Xi_{cc}^+$  and  $\Omega_{cc}^+$  can only be measured when they are observed with high significance in the future.

In the beauty sector, the lifetime of the  $\Omega_b^-$  baryon is the worst known. The current precision is dominated by LHCb measurements using nonleptonic  $\Omega_b^- \to J h \psi \Omega^-$  [203] and  $\Omega_b^- \to \Omega_c^0 \pi^-$  [204] decays. These measurements can also be updated with LHCb Run 2 data and the precision is expected to be improved by at least a factor of two.

# 5.3 Prospects for doubly heavy baryons

The focus of the experimental study in the doubly charmed sector is different in the near future for each doubly charmed baryon. Therefore, we will discuss their prospects separately below.

LHCb will be the primary experiment for studies of the physics of doubly charmed baryons for the foreseeable future, with benefits from increased luminosity, improved selection efficiency, and reduced combinatorial background level. With the data collected in Run 3, LHCb is expected to observe the remaining two weakly decaying doubly charmed baryons and characterise their physical properties. Run 4 and 5 will supply pre-

Table 5.4 The expected yield of doubly heavy baryons for LHCb Upgrade.

Channels	$23 \text{ fb}^{-1}$	$50  \mathrm{fb^{-1}}$	$300  \mathrm{fb^{-1}}$
$\Xi_{cc}^{++} \to \Lambda_c^+ K^- \pi^+ \pi^+$	7 000	15 000	90 000
$\Xi_{cc}^+\to \Lambda_c^+ K^- \pi^+$	3 500	7 500	45 000
$\varOmega_{cc}^+\to \varXi_c^+ K^- \pi^+$	1 000	2 200	13 000
$\varXi_{bc}^{+} o J/\!\psi\varXi_{c}^{+}$	50	100	600

cision measurements of doubly differential cross-sections that will provide insight into production mechanisms of doubly heavy baryons. In addition, the spectroscopy of exinlinecited states will be probed. A projection of the expected yield for LHCb Upgrade is shown in Table 5.4. The projection is based on the observed yield of around 300 for  $\Xi_{cc}^{++} \to \Lambda_c^+ K^- \pi^+ \pi^+$  decay in 2016. The reconstruction and selection efficiency is assumed to be improved by a factor of two due to the trigger-less readout and fully software trigger. The decay branching fraction for dominant channels and the reconstruction efficiency is assumed to be comparable between doubly charmed baryons. A factor of 0.5 is assigned to  $\Xi_{cc}^+$  and  $\Omega_{cc}^+$  baryon to account for the inefficiency due to lower lifetimes of  $\Xi_{cc}^+$  and  $\Omega_{cc}^+$  baryon. An additional factor of 0.3 is assigned to  $\Omega_{cc}^+$  baryon to take into account the lower production cross-section compared with  $\Xi_{cc}$  baryon. For completeness, the expected yield for  $\Xi_{bc}$  is also shown as given in Ref. [193].

Study of doubly charmed baryons in other production environment can provide complementary information to pp collisions due to different production mechanism. For example, the absolute branching fraction of  $\Xi_{cc}$  decays can be measured at the  $e^+e^-$  colliders. Doubly charmed baryons in heavy ion collisions provide unique probe of properties of the quark-gluon plasma (QGP). A projection of the annual number of doubly charmed baryons produced at future colliders is shown in Table 5.5. The projection is based on the production cross-section discussed in Sec. 1.3.1 and the instantaneous luminosity discussed in Sec. 5.1. A conventional detector year of  $10^7$  s is used to calculate the annual integrated luminosity. It should be noted that decay branching fractions and detection efficiency are *not* considered in the projection. Therefore, care should be taken when comparing these numbers with those in Table 5.5. In addition, the background level varies significantly from low in the  $e^+e^-$  machine to high in the PbPb collisions.

**Searches for**  $\Xi_{cc}^+$  **baryon.** At present (2022), the highest priority of the  $\Xi_{cc}^+$  baryon study is still to establish its existence with high significance. To achieve this purpose,

Table 5.5	Projection of the number	of doubly charmed	l baryons produced at f	future colliders.
-----------	--------------------------	-------------------	-------------------------	-------------------

Programs	Production per year
Belle II	$2 \times 10^6$
CEPC	$1 \times 10^{6}$
FCC	$8 \times 10^{6}$
ILC	$3 \times 10^4$
CLIC	$5 \times 10^4$
LHeC	$5 \times 10^5$
ALICE Upgrade	$1 \times 10^9$

we need to identify the decay channels with easiest experimental access, reconstruct and select signal decays with high efficiency and purity. An easy experimental access means a large number of reconstructed signal decays with good signal purity. This requires an optimal combination of a) a large branching fraction of doubly charmed baryon decays; b) a large decay branching fraction of decay products of doubly charmed baryons; c) no or few neutral final-state particles which can not be detected efficiently. Theoretical predictions of branching fractions of nonleptonic  $\Xi_{cc}^+$  decays are shown in Table 1.8. Relevant branching fractions of subsequent decays of doubly charmed baryon products are shown in Table 5.6. Semileptonic  $\Xi_{cc}^+$  decays as well as decays with more than two neutral particles are not considered at the present stage. We then conclude that the following final states are favoured for future searches with current and upgraded LHCb data sets:

- $\Lambda_c^+ K^- \pi^+$ : access to fully reconstructed  $\varXi_{cc}^+ \to \Lambda_c^+ \bar{K}^{*0}$  decay.
- $\Xi_c^0 \pi^+$ : access to fully reconstructed  $\Xi_{cc}^+ \to \Xi_c^0 \pi^+$  decay and partially reconstructed  $\Xi_{cc}^+ \to \Xi_c^0 \rho^+$ ,  $\Xi_{cc}^+ \to \Xi_c^{\prime 0} \pi^+$ ,  $\Xi_{cc}^+ \to \Xi_c^{\prime 0} \rho^+$  decays. The  $\Xi_c^0$  baryon can be reconstructed in both  $pK^-K^-\pi^+$  and  $\Lambda K^-\pi^+$  decays.
- $\Xi_c^+\pi^+\pi^-$ : access to fully reconstructed  $\Xi_{cc}^+ \to \Xi_c^+\rho^0$   $\Xi_{cc}^+ \to \Xi_c^+\eta$ , and  $\Xi_{cc}^+ \to \Xi_c^{*0}\pi^+$  decays, and partially reconstructed  $\Xi_{cc}^+ \to \Xi_c^{'+}\eta$  and  $\Xi_{cc}^+ \to \Xi_c^{*0}\rho^+$  decays. This final state is studied very recently with LHCb Run 1 and 2 data sets [205]. No significant signal is observed in the expected mass region. The  $\Xi_c^+$  baryon is reconstructed in  $pK^-\pi^+$  decay.
- $\Lambda D^0 \pi^+$ : access to fully reconstructed  $\Xi_{cc}^+ \to \Lambda D^{*+}$  decay. The  $D^0$  meson is reconstructed in  $K^- \pi^+$  decay.

On the other hand, it is possible to implement MVA selection with cut-based quality in the upgrade software trigger. This, along with the full software trigger in the upgrade,

Table 5.6 Relevant branching fractions of decay products of doubly charmed baryons.

Channels	Branching fraction
$\Xi_c^{\prime0} o\Xi_c^0\gamma$	1
$\Xi_c^{*0} \to \Xi_c^+ \pi^- (\Xi_c^0 \pi^0)$	2/3(1/3)
$\Xi_c^{\prime+}  o \Xi_c^+ \gamma$	1
$\Xi_c^{*+}\to\Xi_c^0\pi^+(\Xi_c^+\pi^0)$	2/3(1/3)
$\Sigma_c^{++} \to \Lambda_c^+ \pi^+$	1
$\Sigma_c^+ \to \Lambda_c^+ \pi^0$	1
$D^{*+} \to D^0 \pi^+ (D^+ \pi^0)$	2/3(1/3)
$\bar{K}^{*0} \to K^- \pi^+ (\bar{K}^0 \pi^0)$	2/3(1/3)
$\rho^0 \to \pi^+\pi^-$	1
$\rho^+ \to \pi^+ \pi^0$	1
$\Omega_c^0 \to pK^-K^-\pi^+(\Omega^-\pi^+)$	N/A
$\Xi_c^+ \to p K^- \pi^+$	$4.5 \times 10^{-3} \text{ (w.r.t }\Xi^{-}2\pi^{+}\text{)}$
$\Xi_c^0 \to p K^- K^- \pi^+ (\Lambda K^- \pi^+)$	$4.8 \times 10^{-3} (1.5 \times 10^{-2})$
$\Lambda_c^+ \to p K^- \pi^+$	$6.3 \times 10^{-2}$
$\Omega^- \to \varLambda K^-$	2/3
$\Xi^- \to \Lambda \pi^-$	1
$\Lambda \to pK^-$	2/3

will improve the signal efficiency and purity significantly.

These decay channels, along with Cabbibo-suppressed channels and nonphysical channels serving as control channels, are being implemented in the LHCb upgrade software trigger to enable the programs in the upcoming Run 3 data-taking. With the preparations and improvements discussed above, there stands a good chance to observe  $\Xi_{cc}^+$  baryon at the LHCb experiment with data collected during the Run 3 of LHC.

What is more, as discussed in Sec. 1.3.1, the production cross-section of exinlinecited  $\Xi_{cc}$  baryons is supposed to be sizeable compared to the ground state. With the benefit of the long lifetime of  $\Xi_{cc}^{++}$  baryon and improved signal purity in the  $\Xi_{cc}^{++}$  baryon data sample, it is possible to search for exinlinecited  $\Xi_{cc}^{+}$  states via the  $\Xi_{cc}^{+}(nS) \to \Xi_{cc}^{++}\pi^{-}$  transition.

**Measurement of**  $\Xi_{cc}^{++}$  **baryon.** As discussed in Sec. 1.3.2, the mass, lifetime, production cross-section of  $\Xi_{cc}^{++}$  baryon have been measured. Limited information on the branch-

ing fractions is also available by studying the  $\Lambda_c^+ K^- \pi^+ \pi^+$ ,  $\Xi_c^+ \pi^+$ , and  $D^+ p K^- \pi^+$  decay channels. More decay channels are important to understand the dynamics of the  $\Xi_{cc}^{++}$  baryon. With the same consideration as in the  $\Xi_{cc}^+$  baryon case, we identify favoured decay channels for future programs:

- $\Lambda_c^+ K^- \pi^+ \pi^+$ : access to fully reconstructed  $\Xi_{cc}^{++} \to \Sigma_c^{++} \bar{K}^{*0}$  decay.
- $\Xi_c^+\pi^+$ : access to fully reconstructed  $\Xi_{cc}^{++} \to \Xi_c^+\pi^+$  decay, and partially reconstructed  $\Xi_{cc}^{++} \to \Xi_c^+\rho^+$ ,  $\Xi_{cc}^{++} \to \Xi_c^{\prime+}\pi^+$  decays. The latter has already been observed in the partial reconstruction very recently [206].
- $\Xi_c^0 \pi^+ \pi^+$ : access to fully reconstructed  $\Xi_{cc}^{++} \to \Xi_c^{*+} \pi^+$  decay and partially reconstructed  $\Xi_{cc}^{++} \to \Xi_c^{*+} \rho^+$  decay.

These decay channels, along with Cabbibo-suppressed channels and nonphysical channels serving as control channels, are being implemented in the LHCb upgrade software trigger to enable the programs in the upcoming Run 3 data-taking.

Searches for other doubly heavy baryons. As discussed in Sec. 1.3.1, the production cross-section of  $\Omega_{cc}^+$  is about 30% of that of the  $\Xi_{cc}^{++}$  baryon. With a lifetime in between the  $\Xi_{cc}^+$  and  $\Xi_{cc}^{++}$  baryon, the  $\Omega_{cc}^+$  baryon is expected to be within the reach of the upgraded LHCb experiment, if appropriate decay channels are identified.

The production cross-section of doubly heavy baryon  $\Xi_{bc}$  is expected to be comparable, though smaller by a factor of about two, with that of  $\Xi_{cc}$  baryons [207]. It is possible to search for  $\Xi_{bc}$  baryons with promising exclusive decay channels in the LHCb upgrade era. It is also proposed to perform an inclusive search by searching for displaced  $\Xi_{cc}^{++}$  baryons given the large  $\Xi_{bc} \to \Xi_{cc} X$  branching fraction and nonnegligible  $\Xi_{bc}$  lifetime [208].

# APPENDIX A BOOKKEEPING OF DATA AND SIMULATION SAMPLES

In Run 1, the charmed baryon decays are triggered and reconstructed offline, using dedicated Stripping lines. In Run 2, the charmed baryon decays are reconstructed online and the trigger outputs are used directly for further analysis, as discussed in Sec. 2.2.1. The luminosity for each data-taking year is shown in Table 2.3.

For  $\Omega_c^0$  and  $\Xi_c^0$  baryon, data sets collected during 2016-2018 are used for the measurement. The same data-taking period is used for the  $D^0 \to K^+K^-\pi^+\pi^-$  control mode. Earlier data-taking periods are not used due to the lack of dedicated trigger lines. For  $\Xi_{cc}^+$  baryon, data sets collected during 2011-2012 and 2015-2018 are used for the search. The same data-taking period is used for the  $\Lambda_c^+ \to pK^-\pi^+$  and  $\Xi_{cc}^{++} \to \Lambda_c^+K^-\pi^+\pi^+$  control modes. Besides signal and control modes, the wrong-sign (WS) combinations of  $\Lambda_c^+K^+\pi^-$  and  $\Lambda_c^+K^-\pi^-\pi^+$  are recorded to mimic the distribution of combinatorial background in  $\Xi_{cc}^+$  and  $\Xi_{cc}^{++}$  decay samples in the study of event selection.

To determine event selection requirements, model the detector acceptance effect, and estimate selection efficiency, simulated signals are generated for each data-taking year. The  $\Omega_c^0$  and  $\Xi_c^0$  baryons are generated using Pythia with a lifetime hypothesis of 250 fs. The  $\Lambda_c^+$  baryon and  $D^0$  meson are are generated with their known lifetimes [2]. The  $\Xi_{cc}^+$  and  $\Xi_{cc}^{++}$  baryon are generated using GENXICC, with an input lifetime of 80 fs and 256 fs, respectively. All hadrons decay according to the phase-space model implemented in EvtGen, except for  $\Lambda_c^+$  baryon. The  $\Lambda_c^+$  baryon decays according to the pseudo-resonant model, in which the  $K^{*0}$ ,  $\Delta^{++}$ , and  $\Lambda(1520)^0$  resonances are considered. Differences of kinematic distributions between data and simulation are taken into account with a weighting procedure when we estimate the selection efficiency using simulated samples.

The simulated samples contain combinatorial backgrounds due to the random combination of tracks in the event reconstruction and selection. To avoid the bias in efficiency estimation, these background candidates are rejected by matching the reconstructed signal to the generated one. The matching procedure requires both a correctly reconstructed track and the correct correspondence between final-state tracks and their ancestor resonances.

There exists evolution in the reconstruction software, which has an impact on the lifetime measurement. This effect and corresponding correction is described below.

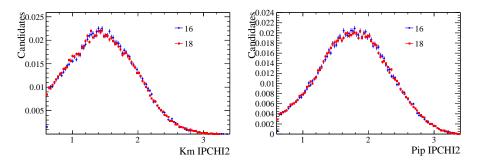


Figure A.1 The comparison of the log-sized  $\chi_{\rm IP}^2$  distributions of the final-state (left) Kaons and (right) Pions in 2016 and 2018 data for  $D^0$  control mode. The  $\chi_{\rm IP}^2$  distributions in 2016 data are scaled by a factor of 1.05.

## A.1 Change of VELO hit error parametrization in 2017–2018 data

It is known that the change of VELO hit error parametrization in 2017-2018 data makes the data-simulation agreement of some decay-time related variables worse than that in 2016 data, including the decay-time resolution and the  $\chi_{\rm IP}^2$  distributions of the final-state tracks. It is due to the fact that the change of VELO error parametrization is not implemented in 2017-2018 simulation as is done for data. The effect of the discrepancy of decay-time resolution is discussed in Sec. 3.6.5. The discrepancy of the  $\chi_{\rm IP}^2$  distributions may lead to an inaccurate description of the decay-time acceptance and need to be taken into account.

To correct for the discrepancy of the  $\chi_{\rm IP}^2$  distributions due to different VELO error parametrization between data and simulation in 2017-2018, we scale the  $\chi_{\rm IP}^2$  distributions of the final-state tracks in 2017-2018 simulation by multiplying a constant scaling factor before any  $\chi_{\rm IP}^2$ -related selections are applied. The scaling factor is determined by comparing the background-subtracted  $\chi_{\rm IP}^2$  distributions of the final-state tracks in 2016 and 2017–2018 data. The idea is that the difference due to the change of VELO parametrization should be the same in data and in simulation. For  $D^0$  control mode, it can be observed that a scaling factor of 1.05 makes a good agreement between 2016 and 2017–2018 data. As an illustration, Fig. A.1 shows a comparison of 2016 and 2018 data, and Fig. A.2 shows a comparison of data and MC for 2016 and 2018. Therefore, the  $\chi_{\rm IP}^2$  distributions of all (four in total) final-state tracks in 2017–2018 simulation for both signal and control modes are multiplied by 1.05 before the original  $\chi_{\rm IP}^2$  selection criteria are applied.

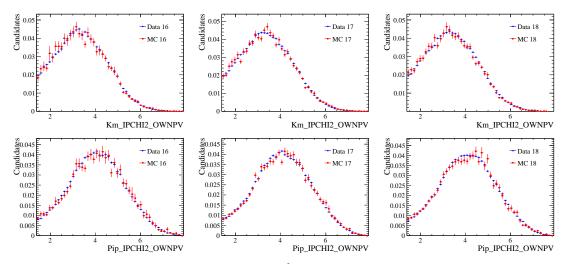


Figure A.2 The comparison of the log-sized  $\chi_{\rm IP}^2$  distributions of the final-state (top) Kaons and (bottom) Pions in (left) 2016 data and simulation and (right) 2018 data and simulation for  $D^0$  control mode. The  $\chi_{\rm IP}^2$  distributions in 2018 simulation are scaled by a factor of 1.05.

### A.2 Offline PV refit

To obtain an unbiased measure of the displacement of a particle w.r.t. a PV, PVs are supposed to be refitted excluding the signal tracks under consideration. However, the ReFitPVs option is not enabled in the Xic@ToPpKmKmPip turbo line. If one or more tracks from your signal candidate are included in the PV fit, this will pull the position of the PV towards those tracks and so will bias any displacement variables calculated wrt the PV.

As the Turbo line Xic@ToPpKmKmPipTurbo used to collect the signal decays enables the PersistReco option, we are able to re-fit the PVs with the persisted HLT1 VELO tracks offline in DaVinci jobs. This is done for 2016–2018 data of the signal mode, where data are processed with the original P2PV relations killed and ReFitPVs=True for DecayTreeTuple in the DaVinci option file, which triggers the offline PV re-fitting and the re-fitted PVs are used by various TupleTools to calculate physics quantities.

For the Turbo line Hlt2CharmHadDstp2D0Pip\_D02KmKpPimPipTurbo used to collect the decays of the control mode, the PersistReco option is not enabled. However, with the available VELO clusters the PV-refit can be recovered by recalculating the weight used for tracks in the PV fit. This is done for 2017-2018 data of the control mode. As no VELO clusters are available for 2016 data, the calculated decay time is smeared by the bias observed in 2018 data with and without the offline PV refit.

Pseudo-experiments are performed to study the impact of offline PVFit on the measured lifetime. A similar approach to the study of decay time resolution is used. First,

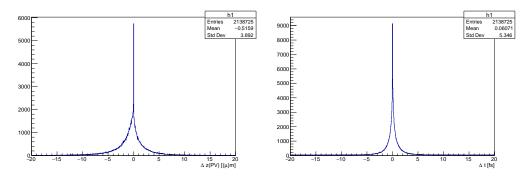


Figure A.3 An event-by-event comparison of (left) the z coordinates of the best PV and (right) of the decay time with and without the PV refitted offline for 2018 data sample.

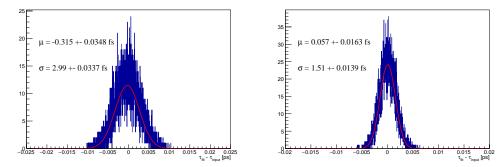


Figure A.4 The distribution of the difference between the input and fitted lifetime for (left)  $\Omega_c^0$  and (right)  $\Xi_c^0$  mode.

pseudo-data and pseudo-mc samples are generated according to

$$(\exp(-t/\tau) \times Acc(t)) * Gaus(t; 0, \sigma_t) * Smear(t), \tag{A.1}$$

for each signal and control modes, where Acc(t) is obtained from corresponding simulation samples as shown in Sec. 3.4.6,  $\sigma_t$  is the decay time resolution obtained from corresponding simulation samples as discussed in Sec. 3.6.5. The decay time is smeared by an additional value sampled from the  $\Delta t$  distribution shown in Fig. A.3 to account for the effect due to offline PV-refit. Second, the decay time fit discussed in Sec. 3.5 is performed with the pseudo samples. Finally, run the above pseudo-experiment about 10K times and examine the distribution of the difference between the input and fitted lifetime, as shown in Fig. A.4. The distribution is fitted with a Gaussian function, whose mean value indicates the bias due to the lack of PV refit. The result is 0.31 fs and 0.06 fs for  $\Omega_c^0$  and  $\Xi_c^0$  mode, respectively. The width of the Gaussian function shows the statistical uncertainty of the decay time fit.

### APPENDIX B STATISTICAL MODELS

There are various analytical functions used in the maximum likelihood fit to describe the probability distribution function (different from the parton distribution function in a hadron), as discussed below.

**Gaussian distribution.** Gaussian distribution function is the most important one, defined as

$$\mathcal{P}(x; \mu, \sigma) = \exp\left(-\frac{1}{2}\left(\frac{x-\mu}{\sigma}\right)^2\right). \tag{B.1}$$

It can be used to describe the resolution effect of a measured quantity. It can also be used to build more involved functions.

**Double-sided crystal ball function.** The double-sided crystal ball function has a Gaussian core and power-lay tails on each side, defined as

$$\mathcal{P}(x;\mu,\sigma,a_L,n_L,a_R,n_R) = \begin{cases} A_L \times \left(B_L - \frac{x-\mu}{\sigma}\right)^{-n_L} & \text{for } \frac{x-\mu}{\sigma} \leqslant -|a_L|, \\ \exp\left(-\frac{1}{2}\left(\frac{x-\mu}{\sigma}\right)^2\right) & \text{for } -|a_L| < \frac{x-\mu}{\sigma} \leqslant |a_R|, \\ A_R \times \left(B_R + \frac{x-\mu}{\sigma}\right)^{-n_R} & \text{for } \frac{x-\mu}{\sigma} > |a_R|, \end{cases}$$
(B.2)

where  $A_L = \left(\frac{n_L}{|a_L|}\right)^{n_L} \times \exp\left(-\frac{a_L^2}{2}\right)$ ,  $B_L = \frac{n_L}{|a_L|} - |a_L|$ ,  $A_R = \left(\frac{n_R}{|a_R|}\right)^{n_R} \times \exp\left(-\frac{a_R^2}{2}\right)$ , and  $B_R = \frac{n_R}{|a_R|} - |a_R|$ . It can be used to describe the effect due to final-state radiation and the kinematic refit of the decay tree.

**Bukin function.** Bukin function has a Gaussian-like core with exponential tails on both sides, defined as

$$\mathcal{P}(x; \mu, \sigma, \xi, \rho_{1}, \rho_{2}) = \begin{cases} \exp\left\{\frac{(x-x_{1})\xi\sqrt{\xi^{2}+1}\sqrt{2\ln 2}}{\sigma\left(\sqrt{\xi^{2}+1}-\xi\right)^{2}\ln\left(\sqrt{\xi^{2}+1}+\xi\right)} + \rho_{1}\left(\frac{x-x_{1}}{\mu-x_{1}}\right)^{2} - \ln 2\right\} & x \leq x_{1}, \\ \exp\left\{-\left[\frac{\ln\left(1+2\xi\sqrt{\xi^{2}+1}\frac{x-\mu}{\sigma\sqrt{2\ln 2}}\right)}{\ln\left(1+2\xi^{2}-2\xi\sqrt{\xi^{2}+1}\right)}\right]^{2} \times \ln 2\right\} & x_{1} < x < x_{2}, \\ \exp\left\{\frac{(x-x_{2})\xi\sqrt{\xi^{2}+1}\sqrt{2\ln 2}}{\sigma\left(\sqrt{\xi^{2}+1}-\xi\right)^{2}\ln\left(\sqrt{\xi^{2}+1}+\xi\right)} + \rho_{2}\left(\frac{x-x_{2}}{\mu-x_{2}}\right)^{2} - \ln 2\right\} & x \geq x_{2}, \end{cases}$$
(B.3)

where  $x_1 = \mu + \sigma \sqrt{2 \ln 2} \left( \frac{\xi}{\sqrt{\xi^2 + 1}} - 1 \right)$ , and  $x_2 = \mu + \sigma \sqrt{2 \ln 2} \left( \frac{\xi}{\sqrt{\xi^2 + 1}} + 1 \right)$ . Its tail parameters are flexible enough to describe asymmetric distributions such as a monotonic distribution after a logarithmic transformation. As an illustration, a family of Bukin functions with different parameters are shown in Fig. B.1. The parameter  $\mu$  is the peak position,  $\sigma$  describes the width of the distribution,  $\xi$  indicates the degree of deviation from the Gaussian, and  $\rho_1$  and  $\rho_2$  control the shape of the left and right tail, respectively.

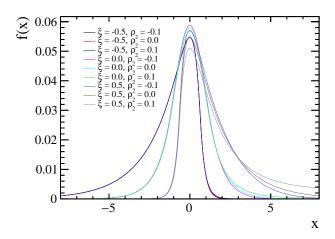


Figure B.1 A family of Bukin functions with different parameters and  $\mu = 0$ ,  $\sigma = 1$ ,  $\rho_1 = 0$ .

**ARGUS function.** The ARGUS distribution, named after the high-energy physics experiment ARGUS, is defined as

$$\mathcal{P}(x; \chi, c) = \frac{\chi^3}{\sqrt{2\pi}\Psi(\chi)} \times \frac{x}{c^2} \sqrt{1 - \frac{x^2}{c^2}} \exp\left\{-\frac{1}{2}\chi^2 \left(1 - \frac{x^2}{c^2}\right)\right\}$$
 (B.4)

for 0 < x < c, where  $\Psi(\chi) = \Phi(\chi) - \chi \phi(\chi) - \frac{1}{2}$ . It is usually used to describe the invariant-mass distribution of the partially reconstructed decay. A family of ARGUS function with different parameters is shown in Fig. B.2.

**Chebychev polynomial.** The Chebyshev polynomials of the first kind are obtained from the recurrence relation

$$T_0(x) = 1,$$
  
 $T_1(x) = x,$  (B.5)  
 $T_{n+1}(x) = 2xT_n(x) + T_{n-1}(x).$ 

The first five Chebychev polynomials are shown in Fig. B.3. They are widely used to describe smooth background distributions. They are favored over a geometric series thanks

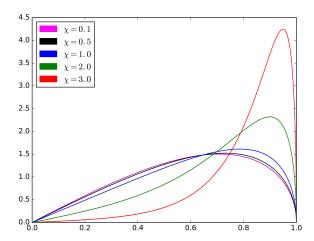


Figure B.2 A family of ARGUS function with different parameters.

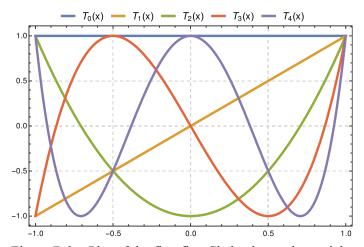


Figure B.3 Plot of the first five Chebychev polynomials.

to the numerical stability of the coefficients in the minimisation process.

# APPENDIX C FIT RESULTS FOR PROMPT YIELD DETERMINATION

Extended unbinned maximum likelihood fits to the invariant mass and  $\log_{10}(\chi_{\text{IP}}^2)$  distributions are performed to estimate the prompt yields simultaneously in decay-time bins and different data-taking periods.

The fit projections to  $\log_{10}(\chi_{\rm IP}^2)$  distributions with the mass in  $\pm 2\sigma$  range of the signal mass peak of 2017 data for signal and control modes are shown in  $(\Omega_c^0)$  Fig. C.2,  $(\Xi_c^0)$  C.4, and  $(D^0)$  C.6.

The fit projections to  $\log_{10}(\chi_{\rm IP}^2)$  distributions with the mass in  $\pm 2\sigma$  range of the signal mass peak of 2018 data for signal and control modes are shown in  $(\Omega_c^0)$  Fig. C.8,  $(\Xi_c^0)$  C.10, and  $(D^0)$  C.12.

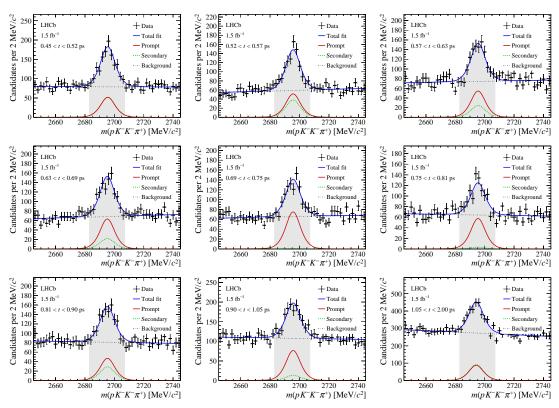


Figure C.1 The fit projections to the invariant mass distribution of 2017 data for the  $\Omega_c^0$  mode.

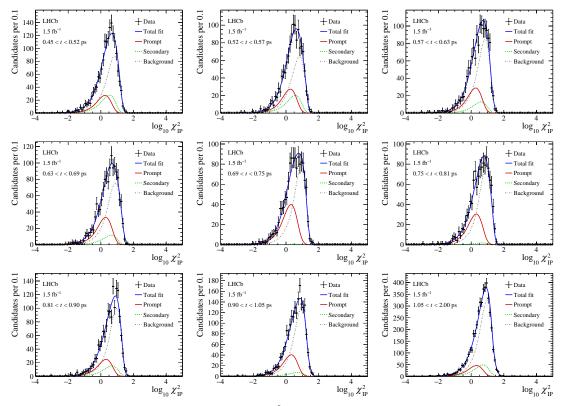


Figure C.2 The fit projections to the  $\log_{10}(\chi_{\rm IP}^2)$  distribution with the mass in  $\pm 2\sigma$  range of the signal mass peak of 2017 data for the  $\Omega_c^0$  mode.

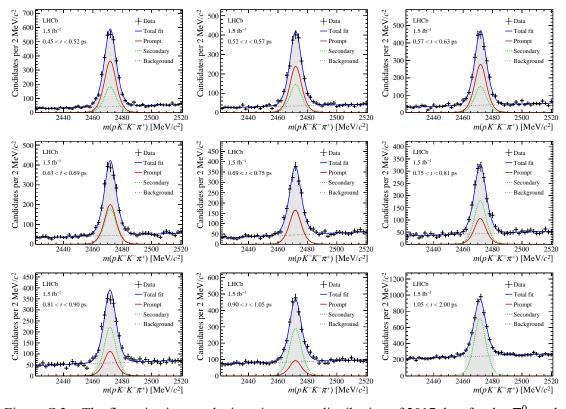


Figure C.3 The fit projections to the invariant mass distribution of 2017 data for the  $\Xi_c^0$  mode.

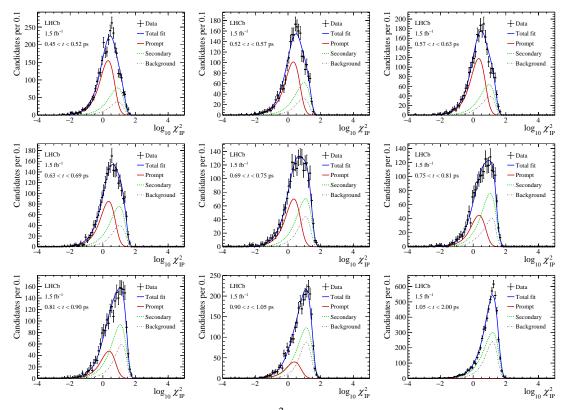


Figure C.4 The fit projections to the  $\log_{10}(\chi_{\text{IP}}^2)$  distribution with the mass in  $\pm 2\sigma$  range of the signal mass peak of 2017 data for the  $\Xi_c^0$  mode.

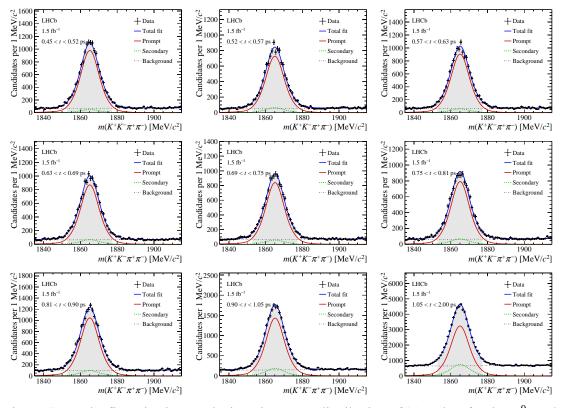


Figure C.5 The fit projections to the invariant mass distribution of 2017 data for the  $D^0$  mode.

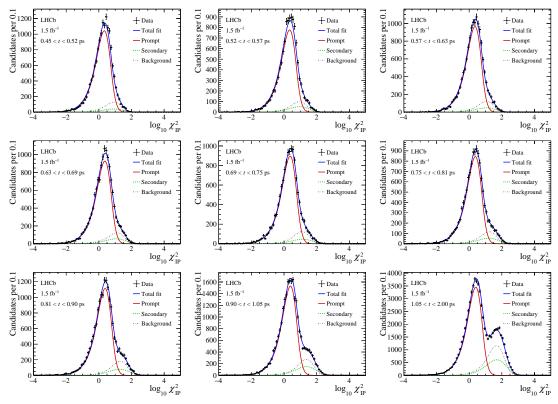


Figure C.6 The fit projections to the  $\log_{10}(\chi_{\text{IP}}^2)$  distribution with the mass in  $\pm 2\sigma$  range of the signal mass peak of 2017 data for the  $D^0$  mode.

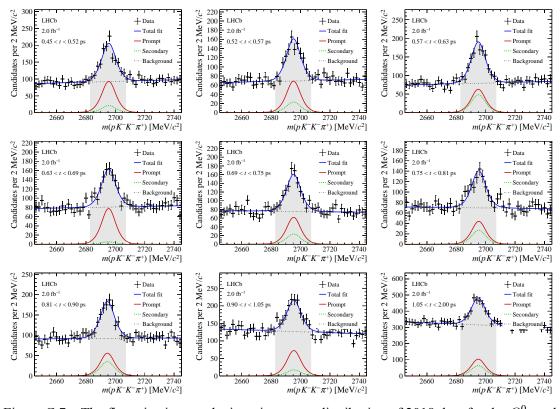


Figure C.7 The fit projections to the invariant mass distribution of 2018 data for the  $\Omega_c^0$  mode.

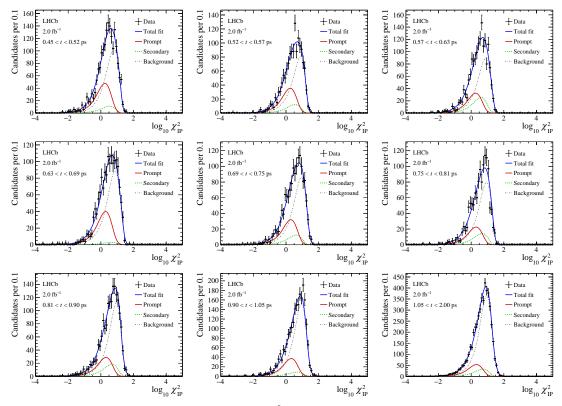


Figure C.8 The fit projections to the  $\log_{10}(\chi_{\text{IP}}^2)$  distribution with the mass in  $\pm 2\sigma$  range of the signal mass peak of 2018 data for the  $\Omega_c^0$  mode.

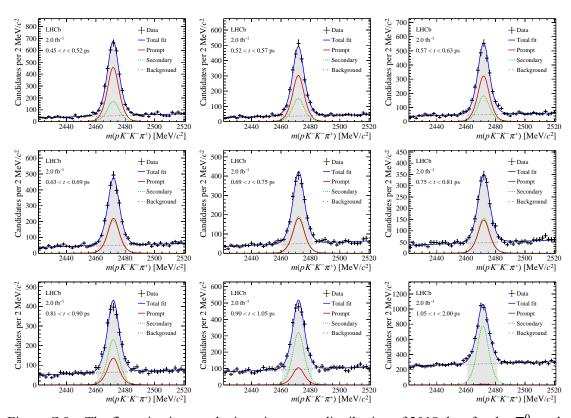


Figure C.9 The fit projections to the invariant mass distribution of 2018 data for the  $\Xi_c^0$  mode.

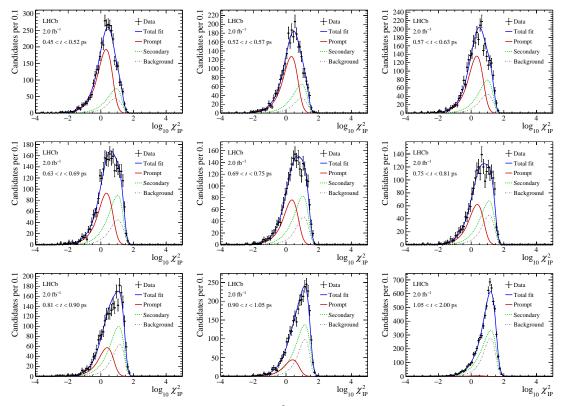


Figure C.10 The fit projections to the  $\log_{10}(\chi_{\rm IP}^2)$  distribution with the mass in  $\pm 2\sigma$  range of the signal mass peak of 2018 data for the  $\Xi_c^0$  mode.

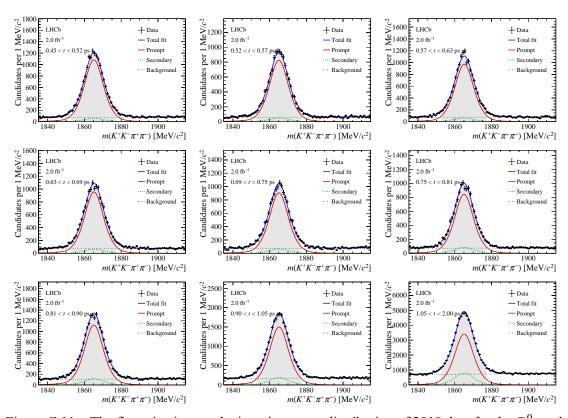


Figure C.11 The fit projections to the invariant mass distribution of 2018 data for the  $D^0$  mode.

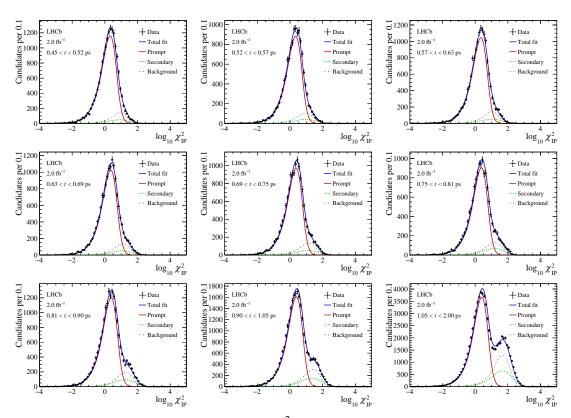


Figure C.12 The fit projections to the  $\log_{10}(\chi_{\text{IP}}^2)$  distribution with the mass in  $\pm 2\sigma$  range of the signal mass peak of 2018 data for the  $D^0$  mode.

# APPENDIX D EVENT SELECTION FOR $\varLambda_c^+$ AND $\varXi_{cc}^{++}$ CONTROL MODES

To calculate upper limits in the search for  $\Xi_{cc}^+$  baryon, exclusive decays of  $\Lambda_c^+$  and  $\Xi_{cc}^{++}$  candidates are reconstructed and selected. Selection requirements are shown in this section.

## D.1 Fiducial region

For  $\Lambda_c^+$  and  $\Xi_{cc}^{++}$  control modes, the  $\Lambda_c^+$  and  $\Xi_{cc}^{++}$  candidates are required to lie in the same fiducial region as the  $\Xi_{cc}^+$  signal candidates.

# **D.2** Trigger selection for $\Lambda_c^+$ control mode.

Trigger requirements are the same as the signal mode. In terms of HLT2 trigger, for 2011-2012 data selection requirements are summarised in Table D.1. Additional requirement of Hlt2CharmHadLambdaC2KPPi TOS on  $\Lambda_c^+$  candidates is applied. For 2015-2018 data, the trigger selection for the  $\Lambda_c^+$  control mode is very similar to the requirements on the intermediate  $\Lambda_c^+$  candidates the 2016 HLT2 selection of the signal mode, with only one difference of vertex distance  $\chi^2$  for 2015 data, as shown in Table D.2. Additional requirement of Hlt2CharmHadLcpToPpKmPip TOS or Hlt2Global TIS on  $\Lambda_c^+$  candidate is applied for 2015 data. In addition, the selection of the signal mode and the  $\Xi_{cc}^{++}$  control mode is tightened by the requirements marked with a dagger (†) in Table D.1.

## D.3 Trigger selection for $\Xi_{cc}^{++}$ control mode.

For 2011-2012 and 2015 data, the trigger selection is similar to the signal mode with the exception of the  $\chi^2_{\rm vtx}$  requirement, due to a larger number of final-state tracks in the  $\Xi_{cc}^{++}$  decay. The selections for  $\Xi_{cc}^{++}$  control mode are summarized in Table D.3. For 2016-2018 data, the trigger selection for  $\Xi_{cc}^{++}$  control mode is similar to the signal mode with the exception of the  $\chi^2_{\rm vtx}$ /ndf requirement and the requirements on the  $\pi^+$  from  $\Xi_{cc}^{++}$  decay.

Table D.1 Selection requirements of Lambdac2PHHLambdac2PKPiLine. The selection of the signal mode is tightened by the cuts marked with the dagger  $\dagger$ .

Particle	Variable	Cut
	Momentum †	(3, 100) GeV
	Transverse momentum	> 0.4 GeV
	Pseudorapidity †	(2, 5)
Daughters of $\Lambda_c^+$	$\chi_{\mathrm{IP}}^2$ to PV	> 4
	HASRICH	1
	Proton ID $\mathrm{DLL}_{p\pi}$	> 5
	Kaon ID DLL $_{K\pi}$	> 5
	Pion ID $\mathrm{DLL}_{K\pi}$	< 0
	Maximum of daughters' $p_T$	> 1.2 GeV
	Distance of closest approach †	< 0.1
	Vertex $\chi^2_{\rm vtx}$ /ndf	< 20
$arLambda_c^+$	Cosine of decay angle (DIRA) †	$> \cos(0.0141)$
	Maximum of daughters' $\chi_{IP}^2$ to PV	> 8.0
	Vertex distance $\chi^2$	> 16.0
	Invariant mass	$ m(\Lambda_c^+) - m  < 90\text{MeV}$

#### **D.4** Preselection

The preselection is the same as in the signal mode.

# D.5 Multivariate analysis for $\Lambda_c^+$ control mode

The first-step MVA classifier developed for the signal mode in Sec. 4.5.1 with the working point of  $t_1 > 0.0$  is also applied to the  $\Lambda_c^+$  control sample.

# D.6 Multivariate analysis for $arpi_{cc}^{++}$ control mode

A similar two-step MVA selection is developed for the  $\Xi_{cc}^{++}$  control mode. For the first MVA, the simulated  $\Xi_{cc}^{++} \to \Lambda_c^+ K^- \pi^+ \pi^+$  events (with  $\tau_{\Xi_{cc}^{++}} = 260$  fs as input) with preselection applied are used as signals, while the WS sample in the  $\Lambda_c^+$  mass sidebands and  $\Xi_{cc}^{++}$  mass signal region are used as the background sample. For the second MVA, the simulation sample survived the MVA1 selection are used as signals, the WS sample in the  $\Lambda_c^+$  and  $\Xi_{cc}^{++}$  mass signal region after the preselection and the MVA1 selection are used as the background sample. The correlation matrices of training variables are shown in Fig. D.1 and Fig. D.2 for the first and second MVA, respectively.

The ROC curves for the first and second MVA are shown in Fig. D.3, while the responses are illustrated in Fig. D.4.

Table D.2 Run 2 CharmHadLcpToPpKmPipTurbo selections for  $\Lambda_c^+$  control mode. The "-" indicates that no selection is applied for that variable.

Particle	Variable	Requir	uirements	
ratucie	variable	2015	2016–2018	
	Track χ²/ndf	< 3	< 3	
	Kaon and Pion Momentum	> 1 GeV	> 1 GeV	
	Proton momentum	> 10 GeV	> 10 GeV	
	Transverse momentum	> 0.2 GeV	> 0.2 GeV	
	Arithmetic sum of daughter $p_T$	> 3 GeV	> 3 GeV	
	Maximum of daughter $p_T$	> 1 GeV	> 1 GeV	
	Second maximum of daughter $p_{\rm T}$	> 0.4 GeV	> 0.4 GeV	
$\Lambda_c^+$ daughters	$\chi_{\rm IP}^2$ to PV	> 6	> 6	
	Maximum of daughter $\chi_{IP}^2$	> 16	> 16	
	Second maximum of daughter $\chi_{\rm IP}^2$	> 9	> 9	
	Proton particle ID $\mathrm{DLL}_{p\pi}$	> 5	> 5	
	Proton particle ID $DLL_{pK}$	> 5	> 5	
	Kaon particle ID $DLL_{K\pi}$	> 5	> 5	
	Pion particle ID $\mathrm{DLL}_{K\pi}$	< 5	< 5	
	Vertex $\chi^2_{\rm vtx}$ /ndf	< 10	< 10	
	Vertex distance $\chi^2$	> 25.0	_	
$arLambda_c^+$	Cosine of decay angle (DIRA)	> 0.99995	> 0.99995	
	Decay time	> 0.15 ps	> 0.15 ps	
	Invariant mass [ MeV ]	(2211, 2362)	(2211, 2362)	

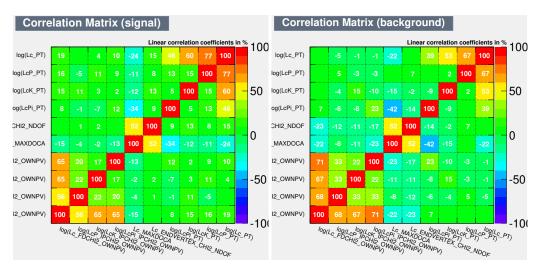


Figure D.1 Correlation matrices of training variables for (left) signal and (right) background samples for the first MVA classifier for  $\Xi_{cc}^{++}$  selection.

Punzi FoM is computed at different threshold values of MVA1 and MVA2, as is shown in Fig D.5. The maximal FoM value is  $7.69\times10^{-6}$ , corresponding to a working point of BDTG1 > -0.4 and BDTG2 > 0.74.

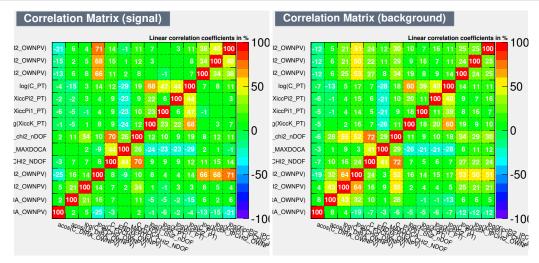


Figure D.2 Correlation matrices of training variables for (left) signal and (right) background samples for the second MVA classifier for  $\Xi_{cc}^{++}$  selection.

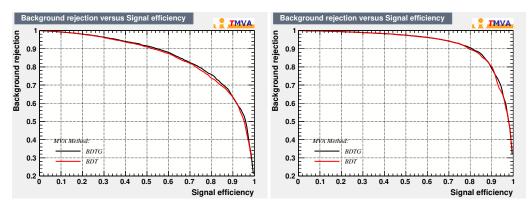


Figure D.3 ROC curves for the (left) first and (right) second MVA classifier for  $\Xi_{cc}^{++}$  selection.

## D.7 Removal of track-clone and duplicate candidates

The track-clone and duplicate candidates are defined in Sec. 4.2.4 and Sec. 4.2.5. The same strategy as described in Sec. 4.2.4 is adopted to remove track-clone candidates. A requirement of  $\delta\theta_{i,j} > 0.5$  mrad is included in the selection sequence for the control modes. The efficiency of this requirement is larger than 99.9% for both control modes. Therefore, the inefficiency due to this requirement is not considered when setting the upper limits.

The duplicate candidates are handled with the same procedure discussed in Sec. 4.2.5. Since one of the duplicate candidates in an event are preserved and the probability of producing two doubly charmed baryons in a single event is negligible, this procedure dose not reduce the number of signals and is completely efficient.

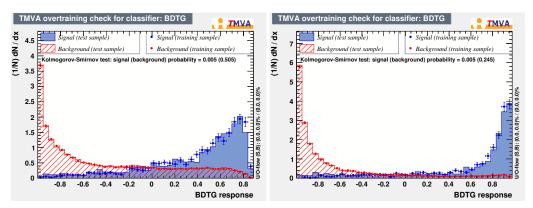


Figure D.4 Response curves for the (left) first and (right) second MVA classifier under the default lifetime hypothesis. For the second step, the requirement of  $t_1 > -0.4$  for MVA1 response is applied.

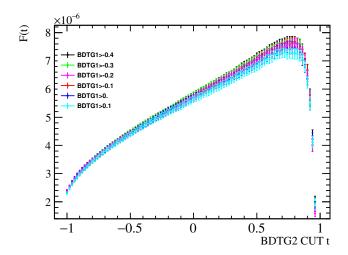


Figure D.5 Punzi figure of merit  $F(t_1, t_2)$ , for BDTG selectors.

Table D.3 Trigger and stripping selections for the  $\Xi_{cc}^{++}$  control mode. The "–" indicates that no selection is applied for that variable.

Particle	Variable	2012 and 2015	Requirements 2016	2017–2018
	Track χ²/ndf	< 5	< 3	< 3
	Kaon and Pion Momentum	> 2 GeV	> 1 GeV	> 1 GeV
	Proton momentum	> 2 GeV	> 10 GeV	> 10 GeV
	Transverse momentum	> 0.25 GeV	> 0.2 GeV	> 0.2 GeV
	Arithmetic sum of daughter $p_T$	_	> 3 GeV	> 3 GeV
	Maximum of daughter $p_T$	_	> 1 GeV	> 1 GeV
	Second maximum of daughter $p_T$	_	> 0.4 GeV	> 0.4 GeV
$\Lambda_c^+$ daughters	$\chi_{\mathrm{IP}}^2$ to PV	> 4	> 6	> 6
	Maximum of daughter $\chi_{\rm IP}^2$	> 4	> 16	> 16
	Second maximum of daughter $\chi_{IP}^2$	_	> 9	> 9
	HASRICH	1	_	_
	Proton particle ID DLL <sub>pg</sub>	> 5	> 5	> 5
	•	> 0	> 5	> 5
			> 5	> 5
Proton particle ID DLL <sub><math>p\pi</math></sub> > 5	< 5	< 5		
	Transverse momentum	> 1 GeV	_	_
	Vertex $\chi^2_{\rm vt}$ /ndf	< 10	< 10	< 10
		< 0.5 mm	_	_
$\Lambda_c^+$	Cosine of decay angle (DIRA)	> 0.99	> 0.99995	> 0
·		> 16.0	_	_
		_	> 0.15 ps	> 0.15 ps
	Invariant mass [ MeV/c <sup>2</sup> ]	(2211, 2362)	(2211, 2362)	(2211, 2362)
	Track $\chi^2$ /ndf	< 5	< 3	< 3
	Kaon Transverse momentum	> 0.25 GeV	> 0.5 GeV	> 0.5 GeV
	Pion Transverse momentum	> 0.25 GeV	> 0.5 GeV	> 0.2 GeV
$\Xi_{cc}^{++}$ daughters	Momentum	> 2 GeV	> 1 GeV	> 1 GeV
	Pion $\chi_{\rm IP}^2$ to PV	_	_	> 1
	HASRICH	1	_	_
	Kaon particle ID $\mathrm{DLL}_{K\pi}$	> 5	> 10	> 10
	Pion particle ID DLL <sub><math>K\pi</math></sub>	< 0	< 0	< 0
	Vector sum of daughter $p_{T}$	> 2 GeV	> 2 GeV	> 2 GeV
	Vertex $\chi^2_{\text{vtx}}/\text{ndf}$	< 12	< 60	< 60
	Maximum DOCA	_	< 0.5 mm	< 0.5 mm
	DOCA between $(\Lambda_c^+, \pi^+), (K^-, \pi^+)$	_	< 10 mm	< 10 mm
$\varXi_{cc}^{++}$	$\Lambda_c^+$ vertex z displacement w.r.t. $\Xi_{cc}^{++}$	> 0.01 mm	> 0.01 mm	> 0.01 mm
— cc	DIRA	> 0.01 mm	> 0.01 mm	> 0.01 mm
			- 0	~ 0
	Vertex distance $\chi^2$	> -1	_	_

# APPENDIX E SELECTION EFFICIENCY FOR RUN 2 DATA

Following the procedure described in Sec. 4.5.3, we evaluate the efficiencies of the signal and control modes for 2015, 2017 and 2018 data. The efficiency of acceptance is assumed to be same throughout the years. PID efficiency corrections are applied with PIDCalib samples for different years. The correction of  $p_T$ , nSPDHits and Dalitz distributions are also implemented. The results are summarised in Table E.1, E.2, and E.3 for the signal,  $\Lambda_c^+$ , and  $\Xi_{cc}^{++}$  control modes, respectively.

The ratios of control to signal mode are shown in Table E.4 for the  $\Lambda_c^+$  control mode, and Table E.5 for the  $\Xi_{cc}^{++}$  control mode. Due to the evolvement of the HLT2 selection in 2017 and 2018, the ratios of efficiency for 2016-2018 data are not the same. For 2017 and 2018 data, the  $p_{\rm T}$  requirement for the pion from  $\Xi_{cc}^{++}$  and the DIRA requirement on  $\Lambda_c^+$  is loosened compared with that in 2016 data as shown in Table 4.1. Efforts are made to keep the HLT2 selections consistent throughout the years. However, it is found that despite the same HLT2 selections, the ratios of efficiency are still different due to different L0 threshold settings. The L0 threshold for 2017 data is relatively loose. As a result, instead of aligning the HLT2 selections, we use the simultaneous fit to calculate upper limits with combined 2016-2018 data.

The signal efficiency varies with the lifetime hypothesis of the  $\Xi_{cc}^+$  baryon. Following the procedure discussed in Sec. 4.5.3, variations are shown in Table E.6 for 2017 data and Table E.7 for 2018 data.

Table E.1 Efficiencies of  $\Xi_{cc}^+$  signal for 2015-2018 data, assuming the  $\Xi_{cc}^+$  lifetime of 80 fs. The total efficiency is corrected by MC-Match efficiency.

	2015	2016	2017	2018
Acc [10 <sup>-2</sup> ]	$(92.922 \pm 0.210)$	$(92.922 \pm 0.210)$	$(92.922 \pm 0.210)$	$(92.922 \pm 0.210)$
Sel $[10^{-2}]$	$(0.013 \pm 0.001)$	$(0.290 \pm 0.004)$	$(0.329 \pm 0.003)$	$(0.326 \pm 0.003)$
$PID [10^{-2}]$	$(69.692 \pm 2.294)$	$(65.595 \pm 0.746)$	$(66.551 \pm 0.524)$	$(65.975 \pm 0.494)$
$MVA1 [10^{-2}]$	$(80.183 \pm 2.034)$	$(73.202 \pm 0.638)$	$(71.363 \pm 0.499)$	$(71.338 \pm 0.465)$
$MVA2 [10^{-2}]$	$(50.739 \pm 2.555)$	$(29.742 \pm 0.725)$	$(30.581 \pm 0.564)$	$(30.236 \pm 0.549)$
Trigger [10 <sup>-2</sup> ]	$(16.712 \pm 2.473)$	$(21.606 \pm 1.184)$	$(25.085 \pm 0.965)$	$(18.717 \pm 0.830)$
Total [10 <sup>-5</sup> ]	$(0.634 \pm 0.103)$	$(9.053 \pm 0.576)$	$(12.097 \pm 0.541)$	$(8.775 \pm 0.428)$

Table E.2 Efficiencies of  $\Lambda_c^+$  signal for 2015-2018 data. The total efficiency is corrected by MC-Match efficiency.

	2015	2016	2017	2018
Acc [10 <sup>-2</sup> ]	$(98.587 \pm 0.076)$	$(98.587 \pm 0.076)$	$(98.587 \pm 0.076)$	$(98.587 \pm 0.076)$
Sel $[10^{-2}]$	$(0.873 \pm 0.017)$	$(1.545 \pm 0.037)$	$(1.587 \pm 0.028)$	$(1.586 \pm 0.034)$
$PID [10^{-2}]$	$(79.507 \pm 0.941)$	$(79.304 \pm 1.179)$	$(81.612 \pm 0.853)$	$(80.024 \pm 1.048)$
$MVA1 [10^{-2}]$	$(83.069 \pm 0.714)$	$(82.152 \pm 0.969)$	$(81.184 \pm 0.761)$	$(80.689 \pm 0.919)$
$MVA2 [10^{-2}]$	$(100.000 \pm 0.000)$	$(100.000 \pm 0.000)$	$(100.000 \pm 0.000)$	$(100.000 \pm 0.000)$
Trigger [10 <sup>-2</sup> ]	$(22.340 \pm 0.847)$	$(19.968 \pm 1.002)$	$(26.042 \pm 0.845)$	$(22.569 \pm 0.989)$
Total [10 <sup>-3</sup> ]	$(1.274 \pm 0.053)$	$(1.987 \pm 0.109)$	$(2.707 \pm 0.099)$	$(2.286 \pm 0.112)$

Table E.3 Efficiencies of  $\Xi_{cc}^{++}$  signal for 2015-2018 data. The total efficiency is corrected by MC-Match efficiency. The efficiencies of the 2017 and 2018 data are relatively higher due to the difference in HLT2 selections.

	2015	2016	2017	2018
Acc [10 <sup>-2</sup> ]	$(96.600 \pm 0.030)$	$(96.600 \pm 0.030)$	$(96.600 \pm 0.030)$	$(96.600 \pm 0.030)$
Sel $[10^{-2}]$	$(0.059 \pm 0.001)$	$(0.235 \pm 0.005)$	$(0.422 \pm 0.003)$	$(0.418 \pm 0.003)$
$PID [10^{-2}]$	$(63.977 \pm 1.184)$	$(63.635 \pm 1.039)$	$(61.790 \pm 0.398)$	$(60.316 \pm 0.391)$
$MVA1 [10^{-2}]$	$(76.932 \pm 1.068)$	$(81.421 \pm 0.788)$	$(77.786 \pm 0.336)$	$(77.853 \pm 0.343)$
$MVA2 [10^{-2}]$	$(74.395 \pm 1.095)$	$(50.722 \pm 1.180)$	$(56.696 \pm 0.436)$	$(57.207 \pm 0.434)$
Trigger $[10^{-2}]$	$(15.254 \pm 1.353)$	$(15.861 \pm 1.064)$	$(18.580 \pm 0.443)$	$(14.438 \pm 0.442)$
Total [10 <sup>-5</sup> ]	$(3.562 \pm 0.351)$	$(10.562 \pm 0.764)$	$(23.059 \pm 0.597)$	$(17.478 \pm 0.581)$

Table E.4 Efficiency ratios of the  $\Lambda_c^+$  control mode to the signal mode.

	2016	2017	2018
Acc	$1.061 \pm 0.003$	$1.061 \pm 0.003$	$1.061 \pm 0.003$
Sel	$5.319 \pm 0.147$	$4.829 \pm 0.099$	$4.865 \pm 0.114$
PID	$1.209 \pm 0.023$	$1.226 \pm 0.016$	$1.213 \pm 0.018$
MVA1	$1.122 \pm 0.016$	$1.138 \pm 0.013$	$1.131 \pm 0.015$
MVA2	$3.362 \pm 0.082$	$3.270 \pm 0.060$	$3.307 \pm 0.060$
Trigger	$0.924 \pm 0.069$	$1.038 \pm 0.052$	$1.206 \pm 0.075$
MC-match	$0.922 \pm 0.007$	$0.922 \pm 0.007$	$0.922 \pm 0.007$
Total	$21.947 \pm 1.850$	$22.379 \pm 1.308$	$26.048 \pm 1.814$

Table E.5 Efficiency ratios of the  $\Xi_{cc}^{++}$  control mode to the signal mode.

	2016	2017	2018
Acc	$1.040 \pm 0.002$	$1.040 \pm 0.002$	$1.040 \pm 0.002$
Sel	$0.809 \pm 0.020$	$1.285 \pm 0.016$	$1.282 \pm 0.015$
PID	$0.970 \pm 0.019$	$0.928 \pm 0.009$	$0.914 \pm 0.009$
MVA1	$1.112 \pm 0.014$	$1.090 \pm 0.009$	$1.091 \pm 0.009$
MVA2	$1.705 \pm 0.057$	$1.854 \pm 0.037$	$1.892 \pm 0.037$
Trigger	$0.734 \pm 0.064$	$0.741 \pm 0.034$	$0.771 \pm 0.042$
MC-match	$1.027 \pm 0.019$	$1.027 \pm 0.019$	$1.027 \pm 0.019$
Total	$1.167 \pm 0.114$	$1.906 \pm 0.105$	$1.992 \pm 0.123$

Table E.6 Efficiencies at different lifetime hypotheses for 2017 data.

ε [×10 <sup>-2</sup> ]	$\tau = 40 \text{ fs}$	$\tau = 80 \text{ fs}$	$\tau = 120 \text{ fs}$	$\tau = 160 \text{ fs}$
Acc	$92.922 \pm 0.210$	$92.922 \pm 0.210$	$92.922 \pm 0.210$	$92.922 \pm 0.210$
Sel	$0.215 \pm 0.003$	$0.329 \pm 0.003$	$0.459 \pm 0.006$	$0.589 \pm 0.010$
PID	$66.956 \pm 0.682$	$66.551 \pm 0.524$	$65.966 \pm 0.649$	$65.366 \pm 0.955$
MVA1	$72.003 \pm 0.711$	$71.363 \pm 0.499$	$69.495 \pm 0.618$	$67.213 \pm 0.916$
MVA2	$20.024 \pm 0.623$	$30.581 \pm 0.564$	$35.327 \pm 0.686$	$36.531 \pm 0.883$
Trigger	$28.603 \pm 1.869$	$25.085 \pm 0.965$	$23.779 \pm 0.960$	$23.034 \pm 1.089$
Total [×10 <sup>-5</sup> ]	$5.996 \pm 0.509$	$12.097 \pm 0.541$	$17.866 \pm 0.798$	22.001 ± 1.130

Table E.7 Efficiencies at different lifetime hypotheses for 2018 data.

$\varepsilon \left[ \times 10^{-2} \right]$	$\tau = 40 \text{ fs}$	$\tau = 80 \text{ fs}$	$\tau = 120 \text{ fs}$	$\tau = 160 \text{ fs}$
Acc	$92.922 \pm 0.210$	$92.922 \pm 0.210$	$92.922 \pm 0.210$	$92.922 \pm 0.210$
Sel	$0.213 \pm 0.003$	$0.326 \pm 0.003$	$0.457 \pm 0.005$	$0.591 \pm 0.012$
PID	$66.410 \pm 0.640$	$65.975 \pm 0.494$	$65.331 \pm 0.632$	$64.656 \pm 1.126$
MVA1	$71.838 \pm 0.571$	$71.338 \pm 0.465$	$70.191 \pm 0.563$	$69.001 \pm 0.842$
MVA2	$18.878 \pm 0.511$	$30.236 \pm 0.549$	$35.446 \pm 0.716$	$36.878 \pm 1.035$
Trigger	$20.329 \pm 1.131$	$18.717 \pm 0.830$	$18.158 \pm 1.039$	$18.078 \pm 1.436$
Total [×10 <sup>-5</sup> ]	$3.945 \pm 0.245$	$8.775 \pm 0.428$	$13.639 \pm 0.873$	17.772 ± 1.599

- [1] Pais A, Treiman S B. How Many Charm Quantum Numbers Are There?[J/OL]. Phys. Rev. Lett., 1975, 35: 1556. DOI: 10.1103/PhysRevLett.35.1556.
- [2] Zyla P A, et al. Review of Particle Physics[J/OL]. PTEP, 2020, 2020(8): 083C01. DOI: 10.1093/ptep/ptaa104.
- [3] MissMJ C. File:standard model of elementary particles.svg[EB/OL]. 2019[2022-05-18]. https://commons.wikimedia.org/wiki/File:Standard Model of Elementary Particles.svg.
- [4] Abi B, et al. Measurement of the Positive Muon Anomalous Magnetic Moment to 0.46 ppm [J/OL]. Phys. Rev. Lett., 2021, 126(14): 141801. DOI: 10.1103/PhysRevLett.126.141801.
- [5] Aaij R, et al. Test of lepton universality in beauty-quark decays[J]. 2021.
- [6] Gell-Mann M. A Schematic Model of Baryons and Mesons[J/OL]. Phys. Lett., 1964, 8: 214-215. DOI: 10.1016/S0031-9163(64)92001-3.
- [7] Zweig G. An SU<sub>3</sub> model for strong interaction symmetry and its breaking; Version 1: CERN-TH-401[R]. Geneva: CERN, 1964.
- [8] Zweig G. An SU<sub>3</sub> model for strong interaction symmetry and its breaking; Version 2[J/OL]. Developments in the Quark Theory of Hadrons, Volume 1. Edited by D. Lichtenberg and S. Rosen. pp. 22-101, 1964(CERN-TH-412): 22-101. http://cds.cern.ch/record/570209.
- [9] Aubert J J, et al. Experimental Observation of a Heavy Particle *J*[J/OL]. Phys. Rev. Lett., 1974, 33: 1404-1406. DOI: 10.1103/PhysRevLett.33.1404.
- [10] Augustin J E, et al. Discovery of a Narrow Resonance in  $e^+e^-$  Annihilation[J/OL]. Phys. Rev. Lett., 1974, 33: 1406-1408. DOI: 10.1103/PhysRevLett.33.1406.
- [11] De Rujula A, Georgi H, Glashow S L. Hadron Masses in a Gauge Theory[J/OL]. Phys. Rev. D, 1975, 12: 147-162. DOI: 10.1103/PhysRevD.12.147.
- [12] Roncaglia R, Lichtenberg D B, Predazzi E. Predicting the masses of baryons containing one or two heavy quarks[J/OL]. Phys. Rev. D, 1995, 52: 1722-1725. DOI: 10.1103/PhysRevD.52.17 22.
- [13] Itoh C, Minamikawa T, Miura K, et al. Doubly charmed baryon masses and quark wave functions in baryons[J/OL]. Phys. Rev. D, 2000, 61: 057502. DOI: 10.1103/PhysRevD.61.057502.
- [14] Fleck S, Richard J M. Baryons with double charm[J/OL]. Prog. Theor. Phys., 1989, 82: 760-774. DOI: 10.1143/PTP.82.760.
- [15] Fleck S, Silvestre-Brac B, Richard J M. Search for Diquark Clustering in Baryons[J/OL]. Phys. Rev. D, 1988, 38: 1519-1529. DOI: 10.1103/PhysRevD.38.1519.
- [16] Kerbikov B O, Polikarpov M I, Shevchenko L V. Multiquark masses and wave functions through a modified Green function Monte Carlo method[J/OL]. Nucl. Phys., 1990, B331: 19. DOI: 10.1016/0550-3213(90)90016-7.
- [17] Silvestre-Brac B. Spectrum and static properties of heavy baryons[J/OL]. Few Body Syst., 1996, 20: 1-25. DOI: 10.1007/s006010050028.

- [18] Ebert D, Faustov R, Galkin V, et al. Mass spectra of doubly heavy baryons in the relativistic quark model[J/OL]. Phys.Rev., 2002, D66: 014008. DOI: 10.1103/PhysRevD.66.014008.
- [19] Eichmann G, Sanchis-Alepuz H, Williams R, et al. Baryons as relativistic three-quark bound states[J/OL]. Prog. Part. Nucl. Phys., 2016, 91: 1-100. DOI: 10.1016/j.ppnp.2016.07.001.
- [20] Brown Z S, Detmold W, Meinel S, et al. Charmed bottom baryon spectroscopy from lattice QCD[J/OL]. Phys. Rev. D, 2014, 90(9): 094507. DOI: 10.1103/PhysRevD.90.094507.
- [21] Shifman M A, Voloshin M B. Hierarchy of Lifetimes of Charmed and Beautiful Hadrons[J]. Sov. Phys. JETP, 1986, 64: 698.
- [22] Colangelo P, Khodjamirian A. QCD sum rules, a modern perspective[J/OL]. 2000: 1495-1576.
  DOI: 10.1142/9789812810458 0033.
- [23] Korner J G, Kramer M, Pirjol D. Heavy baryons[J/OL]. Prog. Part. Nucl. Phys., 1994, 33: 787-868. DOI: 10.1016/0146-6410(94)90053-1.
- [24] Caswell W E, Lepage G P. Effective Lagrangians for Bound State Problems in QED, QCD, and Other Field Theories[J/OL]. Phys. Lett. B, 1986, 167: 437-442. DOI: 10.1016/0370-269 3(86)91297-9.
- [25] Bodwin G T, Braaten E, Lepage G P. Rigorous QCD analysis of inclusive annihilation and production of heavy quarkonium[J/OL]. Phys. Rev. D, 1995, 51: 1125-1171. DOI: 10.1103/PhysRevD.55.5853.
- [26] Ecker G. Chiral perturbation theory[J/OL]. Prog. Part. Nucl. Phys., 1995, 35: 1-80. DOI: 10.1016/0146-6410(95)00041-G.
- [27] Bellini G, Bigi I I Y, Dornan P J. Lifetimes of charm and beauty hadrons[J/OL]. Phys. Rept., 1997, 289: 1-155. DOI: 10.1016/S0370-1573(97)00005-7.
- [28] Bigi I I Y, Uraltsev N G, Vainshtein A I. Nonperturbative corrections to inclusive beauty and charm decays: QCD versus phenomenological models[J/OL]. Phys. Lett. B, 1992, 293: 430-436. DOI: 10.1016/0370-2693(92)90908-M.
- [29] Blok B, Shifman M A. The Rule of discarding 1/N(c) in inclusive weak decays. 1.[J/OL]. Nucl. Phys. B, 1993, 399: 441-458. DOI: 10.1016/0550-3213(93)90504-I.
- [30] Blok B, Shifman M A. The Rule of discarding 1/N(c) in inclusive weak decays. 2.[J/OL]. Nucl. Phys. B, 1993, 399: 459-476. DOI: 10.1016/0550-3213(93)90505-J.
- [31] Blok B, Shifman M A. Lifetimes of charmed hadrons revisited. Facts and fancy[C]//3rd Workshop on the Tau-Charm Factory. 1991.
- [32] Lenz A. Lifetimes and heavy quark expansion[J/OL]. Int. J. Mod. Phys. A, 2015, 30(10): 1543005. DOI: 10.1142/S0217751X15430058.
- [33] Bianco S, Fabbri F L, Benson D, et al. A Cicerone for the physics of charm[J/OL]. Riv. Nuovo Cim., 2003, 26(7-8): 1-200. DOI: 10.1393/ncr/i2003-10003-1.
- [34] Cheng H Y. Phenomenological Study of Heavy Hadron Lifetimes[J/OL]. JHEP, 2018, 11: 014. DOI: 10.1007/JHEP11(2018)014.
- [35] Tanabashi M, et al. Review of particle physics[J/OL]. Phys. Rev., 2018, D98: 030001. DOI: 10.1103/PhysRevD.98.030001.

- [36] Kiselev V, Likhoded A, Onishchenko A. Lifetimes of doubly charmed baryons:  $\Xi_{cc}^+$  and  $\Xi_{cc}^{++}$  [J/OL]. Phys.Rev., 1999, D60: 014007. DOI: 10.1103/PhysRevD.60.014007.
- [37] Kiselev V, Likhoded A. Baryons with two heavy quarks[J/OL]. Phys.Usp., 2002, 45: 455-506. DOI: 10.1070/PU2002v045n05ABEH000958.
- [38] Guberina B, Melic B, Stefancic H. Inclusive decays and lifetimes of doubly charmed baryons [J/OL]. Eur. Phys. J. C, 1999, 9: 213-219. DOI: 10.1007/s100529900039.
- [39] Onishchenko A I. Inclusive and exclusive decays of doubly heavy baryons[C]//5th International Workshop on Heavy Quark Physics. 2000.
- [40] Chang C H, Li T, Li X Q, et al. Lifetime of doubly charmed baryons[J/OL]. Commun. Theor. Phys., 2008, 49: 993-1000. DOI: 10.1088/0253-6102/49/4/38.
- [41] Karliner M, Rosner J L. Baryons with two heavy quarks: Masses, production, decays, and detection[J/OL]. Phys. Rev. D, 2014, 90(9): 094007. DOI: 10.1103/PhysRevD.90.094007.
- [42] Cheng H Y, Shi Y L. Lifetimes of Doubly Charmed Baryons[J/OL]. Phys. Rev. D, 2018, 98 (11): 113005. DOI: 10.1103/PhysRevD.98.113005.
- [43] Likhoded A K, Luchinsky A V. Lifetimes of Doubly Heavy Baryons[J/OL]. Phys. Atom. Nucl., 2018, 81(6): 737-747. DOI: 10.1134/S1063778818050125.
- [44] Cheng H Y. Charmed baryons circa 2015[J/OL]. Front. Phys. (Beijing), 2015, 10(6): 101406.
  DOI: 10.1007/s11467-015-0483-z.
- [45] Aaij R, et al. Measurement of the  $\Omega_c^0$  lifetime[J/OL]. Phys. Rev. Lett., 2018, 121: 092003. DOI: 10.1103/PhysRevLett.121.092003.
- [46] Aaij R, et al. Precision measurement of the  $\Lambda_c^+$ ,  $\Xi_c^+$ , and  $\Xi_c^0$  baryon lifetimes[J/OL]. Phys. Rev., 2019, D100: 032001. DOI: 10.1103/PhysRevD.100.032001.
- [47] Li H S, Meng L, Liu Z W, et al. Magnetic moments of the doubly charmed and bottom baryons [J/OL]. Phys. Rev. D, 2017, 96(7): 076011. DOI: 10.1103/PhysRevD.96.076011.
- [48] Hiller Blin A N, Sun Z F, Vicente Vacas M J. Electromagnetic form factors of spin 1/2 doubly charmed baryons[J/OL]. Phys. Rev. D, 2018, 98(5): 054025. DOI: 10.1103/PhysRevD.98.05 4025.
- [49] Özdem U. Magnetic moments of doubly heavy baryons in light-cone QCD[J/OL]. J. Phys. G, 2019, 46(3): 035003. DOI: 10.1088/1361-6471/aafffc.
- [50] Özdem U. Magnetic dipole moments of the spin- $\frac{3}{2}$  doubly heavy baryons[J/OL]. Eur. Phys. J. A, 2020, 56(2): 34. DOI: 10.1140/epja/s10050-020-00049-4.
- [51] Shi R X, Geng L S. Magnetic moments of the spin- $\frac{3}{2}$  doubly charmed baryons in covariant baryon chiral perturbation theory[J/OL]. Phys. Rev. D, 2021, 103(11): 114004. DOI: 10.1103/PhysRevD.103.114004.
- [52] Zhang W X, Xu H, Jia D. Masses and magnetic moments of hadrons with one and two open heavy quarks: Heavy baryons and tetraquarks[J/OL]. Phys. Rev. D, 2021, 104(11): 114011. DOI: 10.1103/PhysRevD.104.114011.
- [53] Ma J P, Si Z G. Factorization approach for inclusive production of doubly heavy baryon[J/OL]. Phys. Lett. B, 2003, 568: 135-145. DOI: 10.1016/j.physletb.2003.06.064.

- [54] Berezhnoy A V, Kiselev V V, Likhoded A K, et al. Doubly charmed baryon production in hadronic experiments[J/OL]. Phys. Rev. D, 1998, 57: 4385-4392. DOI: 10.1103/PhysRevD.5 7.4385.
- [55] Chang C H, Qiao C F, Wang J X, et al. Estimate of the hadronic production of the doubly charmed baryon Xi(cc) under GM-VFN scheme[J/OL]. Phys. Rev. D, 2006, 73: 094022. DOI: 10.1103/PhysRevD.73.094022.
- [56] Chang C H, Ma J P, Qiao C F, et al. Hadronic production of the doubly charmed baryon Xi(cc) with intrinsic charm[J/OL]. J. Phys. G, 2007, 34: 845. DOI: 10.1088/0954-3899/34/5/006.
- [57] Chen G, Wu X G, Sun Z, et al. Photoproduction of doubly heavy baryon at the ILC[J/OL]. JHEP, 2014, 12: 018. DOI: 10.1007/JHEP12(2014)018.
- [58] Sun Z, Wu X G. The production of the doubly charmed baryon in deeply inelastic *ep* scattering at the Large Hadron Electron Collider[J/OL]. JHEP, 2020, 07: 034. DOI: 10.1007/JHEP07(20 20)034.
- [59] Zheng X C, Chang C H, Feng T F. A proposal on complementary determination of the effective electro-weak mixing angles via doubly heavy-flavored hadron production at a super Z-factory [J/OL]. Sci. China Phys. Mech. Astron., 2020, 63(8): 281011. DOI: 10.1007/s11433-019-149 7-9.
- [60] Ginzburg I F, Kotkin G L, Serbo V G, et al. Colliding gamma e and gamma gamma Beams Based on the Single Pass Accelerators (of Vlepp Type)[J/OL]. Nucl. Instrum. Meth., 1983, 205: 47-68. DOI: 10.1016/0167-5087(83)90173-4.
- [61] Chang C H, Wang J X, Wu X G. GENXICC: A Generator for hadronic production of the double heavy baryons Xi(cc), Xi(bc) and Xi(bb)[J/OL]. Comput. Phys. Commun., 2007, 177: 467-478. DOI: 10.1016/j.cpc.2007.05.012.
- [62] Chang C H, Wang J X, Wu X G. GENXICC2.0: An Upgraded Version of the Generator for Hadronic Production of Double Heavy Baryons Xi(cc), Xi(bc) and Xi(bb)[J/OL]. Comput. Phys. Commun., 2010, 181: 1144-1149. DOI: 10.1016/j.cpc.2010.02.008.
- [63] Wang X Y, Wu X G. GENXICC2.1: An Improved Version of GENXICC for Hadronic Production of Doubly Heavy Baryons[J/OL]. Comput. Phys. Commun., 2013, 184: 1070-1074. DOI: 10.1016/j.cpc.2012.10.022.
- [64] Sjöstrand T, Mrenna S, Skands P. PYTHIA 6.4 physics and manual[J/OL]. JHEP, 2006, 05: 026. DOI: 10.1088/1126-6708/2006/05/026.
- [65] Yao X, Müller B. Doubly charmed baryon production in heavy ion collisions[J/OL]. Phys. Rev. D, 2018, 97(7): 074003. DOI: 10.1103/PhysRevD.97.074003.
- [66] Chen G, Chang C H, Wu X G. Hadronic production of the doubly charmed baryon via the proton–nucleus and the nucleus–nucleus collisions at the RHIC and LHC[J/OL]. Eur. Phys. J. C, 2018, 78(10): 801. DOI: 10.1140/epjc/s10052-018-6283-1.
- [67] Berezhnoy A V, Belov I N, Likhoded A K. Production of doubly charmed baryons with the excited heavy diquark at LHC[J/OL]. Int. J. Mod. Phys. A, 2019, 34(06n07): 1950038. DOI: 10.1142/S0217751X19500386.

- [68] Bjorken J D. Is the ccc a new deal for baryon spectroscopy?[J/OL]. AIP Conf. Proc., 1985, 132: 390-403. DOI: 10.1063/1.35379.
- [69] Karliner M, Rosner J L. Strange baryons with two heavy quarks[J/OL]. Phys. Rev. D, 2018, 97(9): 094006. DOI: 10.1103/PhysRevD.97.094006.
- [70] Weng X Z, Chen X L, Deng W Z. Masses of doubly heavy-quark baryons in an extended chromomagnetic model[J/OL]. Phys. Rev. D, 2018, 97(5): 054008. DOI: 10.1103/PhysRevD.97.054008.
- [71] Bagan E, Dosch H G, Gosdzinsky P, et al. Hadrons with charm and beauty[J/OL]. Z. Phys. C, 1994, 64: 57-72. DOI: 10.1007/BF01557235.
- [72] Kiselev V V, Likhoded A K, Pakhomova O N, et al. Mass spectra of doubly heavy  $\Omega_{QQ'}$  baryons [J/OL]. Phys. Rev. D, 2002, 66: 034030. https://link.aps.org/doi/10.1103/PhysRevD.66.03403 0.
- [73] Albertus C, Hernandez E, Nieves J, et al. Static properties and semileptonic decays of doubly heavy baryons in a nonrelativistic quark model[J/OL]. Eur. Phys. J. A, 2007, 32: 183-199. DOI: 10.1140/epja/i2007-10364-y.
- [74] Roberts W, Pervin M. Heavy baryons in a quark model[J/OL]. Int. J. Mod. Phys. A, 2008, 23: 2817-2860. DOI: 10.1142/S0217751X08041219.
- [75] Vijande J, Garcilazo H, Valcarce A, et al. Spectroscopy of doubly charmed baryons[J/OL]. Phys.Rev., 2004, D70: 054022. DOI: 10.1103/PhysRevD.70.054022.
- [76] Garcilazo H, Vijande J, Valcarce A. Faddeev study of heavy baryon spectroscopy[J/OL]. J. Phys. G, 2007, 34: 961-976. DOI: 10.1088/0954-3899/34/5/014.
- [77] Lee T D. Particle Physics and Introduction to Field Theory: volume 1[M]. 1981.
- [78] DeGrand T A, Jaffe R L, Johnson K, et al. Masses and Other Parameters of the Light Hadrons [J/OL]. Phys. Rev. D, 1975, 12: 2060. DOI: 10.1103/PhysRevD.12.2060.
- [79] Hasenfratz P, Kuti J. The Quark Bag Model[J/OL]. Phys. Rept., 1978, 40: 75-179. DOI: 10.1016/0370-1573(78)90076-5.
- [80] Izatt D, Detar C E, Stephenson M. Spectroscopy of Hadrons Containing One Heavy Quark [J/OL]. Nucl. Phys. B, 1982, 199: 269-289. DOI: 10.1016/0550-3213(82)90347-9.
- [81] Jaffe R L, Kiskis J E. Spectra of New Hadrons[J/OL]. Phys. Rev. D, 1976, 13: 1355. DOI: 10.1103/PhysRevD.13.1355.
- [82] He D H, Qian K, Ding Y B, et al. Evaluation of spectra of baryons containing two heavy quarks in bag model[J/OL]. Phys. Rev. D, 2004, 70: 094004. DOI: 10.1103/PhysRevD.70.094004.
- [83] Bernotas A, Simonis V. Heavy hadron spectroscopy and the bag model[J/OL]. Lith. J. Phys., 2009, 49: 19-28. DOI: 10.3952/lithjphys.49110.
- [84] Martynenko A. Ground-state triply and doubly heavy baryons in a relativistic three-quark model [J/OL]. Phys.Lett., 2008, B663: 317-321. DOI: 10.1016/j.physletb.2008.04.030.
- [85] Giannuzzi F. Doubly heavy baryons in a Salpeter model with AdS/QCD inspired potential [J/OL]. Phys. Rev. D, 2009, 79: 094002. DOI: 10.1103/PhysRevD.79.094002.

- [86] Lü Q F, Wang K L, Xiao L Y, et al. Mass spectra and radiative transitions of doubly heavy baryons in a relativized quark model[J/OL]. Phys. Rev. D, 2017, 96(11): 114006. DOI: 10.110 3/PhysRevD.96.114006.
- [87] Migura S, Merten D, Metsch B, et al. Charmed baryons in a relativistic quark model[J/OL]. Eur. Phys. J. A, 2006, 28: 41. DOI: 10.1140/epja/i2006-10017-9.
- [88] Kiselev V V, Onishchenko A I. Doubly heavy baryons in sum rules of NRQCD[J/OL]. Nucl. Phys. B, 2000, 581: 432-448. DOI: 10.1016/S0550-3213(00)00128-0.
- [89] Kiselev V V, Kovalsky A E. Doubly heavy baryons Omega(QQ') versus Xi(QQ') in sum rules of NRQCD[J/OL]. Phys. Rev. D, 2001, 64: 014002. DOI: 10.1103/PhysRevD.64.014002.
- [90] Zhang J R, Huang M Q. Doubly heavy baryons in QCD sum rules[J/OL]. Phys. Rev. D, 2008, 78: 094007. DOI: 10.1103/PhysRevD.78.094007.
- [91] Wang Z G. Analysis of the  $\frac{1}{2}$  doubly heavy baryon states with QCD sum rules[J/OL]. Eur. Phys. J. A, 2010, 45: 267-274. DOI: 10.1140/epja/i2010-11004-3.
- [92] Aliev T M, Azizi K, Savci M. Doubly Heavy Spin–1/2 Baryon Spectrum in QCD[J/OL]. Nucl. Phys. A, 2012, 895: 59-70. DOI: 10.1016/j.nuclphysa.2012.09.009.
- [93] Chen H X, Mao Q, Chen W, et al. Establishing low-lying doubly charmed baryons[J/OL]. Phys. Rev. D, 2017, 96(3): 031501. DOI: 10.1103/PhysRevD.96.031501.
- [94] Wang Z G. Analysis of the doubly heavy baryon states and pentaquark states with QCD sum rules[J/OL]. Eur. Phys. J. C, 2018, 78(10): 826. DOI: 10.1140/epjc/s10052-018-6300-4.
- [95] Wang C Y, Meng C, Ma Y Q, et al. NLO effects for doubly heavy baryons in QCD sum rules [J/OL]. Phys. Rev. D, 2019, 99(1): 014018. DOI: 10.1103/PhysRevD.99.014018.
- [96] Brambilla N, Vairo A, Rosch T. Effective field theory Lagrangians for baryons with two and three heavy quarks[J/OL]. Phys. Rev. D, 2005, 72: 034021. DOI: 10.1103/PhysRevD.72.034021.
- [97] Hwang C W, Chung C H. Isospin mass splittings of heavy baryons in HQS[J/OL]. Phys. Rev. D, 2008, 78: 073013. DOI: 10.1103/PhysRevD.78.073013.
- [98] Brodsky S J, Guo F K, Hanhart C, et al. Isospin splittings of doubly heavy baryons[J/OL]. Phys. Lett. B, 2011, 698: 251-255. DOI: 10.1016/j.physletb.2011.03.014.
- [99] Sun Z F, Liu Z W, Liu X, et al. Masses and axial currents of the doubly charmed baryons[J/OL]. Phys. Rev., 2015, D91: 094030. DOI: 10.1103/PhysRevD.91.094030.
- [100] Sun Z F, Vicente Vacas M J. Masses of doubly charmed baryons in the extended on-mass-shell renormalization scheme[J/OL]. Phys. Rev., 2016, D93: 094002. DOI: 10.1103/PhysRevD.93. 094002.
- [101] Liu L, Lin H W, Orginos K, et al. Singly and Doubly Charmed J=1/2 Baryon Spectrum from Lattice QCD[J/OL]. Phys. Rev. D, 2010, 81: 094505. DOI: 10.1103/PhysRevD.81.094505.
- [102] Durr S, Koutsou G, Lippert T. Meson and Baryon dispersion relations with Brillouin fermions [J/OL]. Phys. Rev. D, 2012, 86: 114514. DOI: 10.1103/PhysRevD.86.114514.
- [103] Briceno R A, Lin H W, Bolton D R. Charmed-Baryon Spectroscopy from Lattice QCD with  $N_f$  = 2+1+1 Flavors[J/OL]. Phys. Rev. D, 2012, 86: 094504. DOI: 10.1103/PhysRevD.86.094504.

- [104] Namekawa Y, et al. Charmed baryons at the physical point in 2+1 flavor lattice QCD[J/OL]. Phys. Rev., 2013, D87: 094512. DOI: 10.1103/PhysRevD.87.094512.
- [105] Alexandrou C, Drach V, Jansen K, et al. Baryon spectrum with  $N_f = 2 + 1 + 1$  twisted mass fermions [J/OL]. Phys. Rev. D, 2014, 90(7): 074501. DOI: 10.1103/PhysRevD.90.074501.
- [106] Pérez-Rubio P, Collins S, Bali G S. Charmed baryon spectroscopy and light flavor symmetry from lattice QCD[J/OL]. Phys. Rev. D, 2015, 92(3): 034504. DOI: 10.1103/PhysRevD.92.03 4504.
- [107] Padmanath M, Edwards R G, Mathur N, et al. Spectroscopy of doubly charmed baryons from lattice QCD[J/OL]. Phys. Rev., 2015, D91: 094502. DOI: 10.1103/PhysRevD.91.094502.
- [108] Alexandrou C, Kallidonis C. Low-lying baryon masses using  $N_f=2$  twisted mass clover-improved fermions directly at the physical pion mass[J/OL]. Phys. Rev. D, 2017, 96(3): 034511. DOI: 10.1103/PhysRevD.96.034511.
- [109] Chen Y C, Chiu T W. Lattice QCD with  $N_f = 2 + 1 + 1$  domain-wall quarks[J/OL]. Phys. Lett. B, 2017, 767: 193-198. DOI: 10.1016/j.physletb.2017.01.068.
- [110] Mathur N, Padmanath M. Lattice QCD study of doubly-charmed strange baryons[J/OL]. Phys. Rev. D, 2019, 99(3): 031501. DOI: 10.1103/PhysRevD.99.031501.
- [111] Bahtiyar H, Can K U, Erkol G, et al. Charmed baryon spectrum from lattice QCD near the physical point[J/OL]. Phys. Rev. D, 2020, 102(5): 054513. DOI: 10.1103/PhysRevD.102.054513.
- [112] Savage M J, Wise M B. Spectrum of baryons with two heavy quarks[J/OL]. Phys. Lett. B, 1990, 248: 177-180. DOI: 10.1016/0370-2693(90)90035-5.
- [113] Lichtenberg D B. Baryon Electromagnetic Mass Differences in the Charmed Quark Model [J/OL]. Phys. Rev. D, 1977, 16: 231. DOI: 10.1103/PhysRevD.16.231.
- [114] Tiwari K P, Singh C P, Khanna M P. ELECTROMAGNETIC MASS SPLITTINGS OF HEAV-IER HADRONS IN THE MIT BAG MODEL[J/OL]. Phys. Rev. D, 1985, 31: 642-644. DOI: 10.1103/PhysRevD.31.642.
- [115] Karliner M, Rosner J L. Isospin splittings in baryons with two heavy quarks[J/OL]. Phys. Rev. D, 2017, 96(3): 033004. DOI: 10.1103/PhysRevD.96.033004.
- [116] Borsanyi S, et al. Ab initio calculation of the neutron-proton mass difference[J/OL]. Science, 2015, 347: 1452-1455. DOI: 10.1126/science.1257050.
- [117] Xing Z P, Zhao Z X. Weak decays of doubly heavy baryons: the FCNC processes[J/OL]. Phys. Rev. D, 2018, 98(5): 056002. DOI: 10.1103/PhysRevD.98.056002.
- [118] Bjorken J D. Estimates of Decay Branching Ratios for Hadrons Containing Charm and Bottom Quarks.[J]. 1986.
- [119] Hu X H, Shi Y J. Light-cone sum rules analysis of  $\Xi_{QQ'} \to \Sigma_{Q'}$  weak decays[J/OL]. Eur. Phys. J. C, 2020, 80(1): 56. DOI: 10.1140/epjc/s10052-020-7635-1.
- [120] Shi Y J, Wang W, Zhao Z X. QCD Sum Rules Analysis of Weak Decays of Doubly-Heavy Baryons[J/OL]. Eur. Phys. J. C, 2020, 80(6): 568. DOI: 10.1140/epjc/s10052-020-8096-2.

- [121] Shi Y J, Wang W, Zhao Z X, et al. Towards a Heavy Diquark Effective Theory for Weak Decays of Doubly Heavy Baryons[J/OL]. Eur. Phys. J. C, 2020, 80(5): 398. DOI: 10.1140/epjc/s1005 2-020-7949-z.
- [122] Wang W, Yu F S, Zhao Z X. Weak decays of doubly heavy baryons: the  $1/2 \rightarrow 1/2$  case[J/OL]. Eur. Phys. J. C, 2017, 77(11): 781. DOI: 10.1140/epjc/s10052-017-5360-1.
- [123] Gutsche T, Ivanov M A, Körner J G, et al. Analysis of the semileptonic and nonleptonic two-body decays of the double heavy charm baryon states  $\Xi_{cc}^{++}$ ,  $\Xi_{cc}^{+}$  and  $\Omega_{cc}^{+}$ [J/OL]. Phys. Rev. D, 2019, 100(11): 114037. DOI: 10.1103/PhysRevD.100.114037.
- [124] Hu X H, Li R H, Xing Z P. A comprehensive analysis of weak transition form factors for doubly heavy baryons in the light front approach[J/OL]. Eur. Phys. J. C, 2020, 80(4): 320. DOI: 10.1140/epjc/s10052-020-7851-8.
- [125] Shi Y J, Wang W, Xing Y, et al. Weak Decays of Doubly Heavy Baryons: Multi-body Decay Channels[J/OL]. Eur. Phys. J. C, 2018, 78(1): 56. DOI: 10.1140/epjc/s10052-018-5532-7.
- [126] Li D M, Zhang X R, Xing Y, et al. Weak decays of doubly heavy baryons: four-body nonleptonic decay channels[J/OL]. Eur. Phys. J. Plus, 2021, 136(7): 772. DOI: 10.1140/epjp/s1336 0-021-01757-6.
- [127] Ivanov M A, Körner J G, Lyubovitskij V E. Nonleptonic Decays of Doubly Charmed Baryons [J/OL]. Phys. Part. Nucl., 2020, 51(4): 678-685. DOI: 10.1134/S1063779620040358.
- [128] Jiang L J, He B, Li R H. Weak decays of doubly heavy baryons:  $\mathcal{B}_{cc} \to \mathcal{B}_c V$  [J/OL]. Eur. Phys. J. C, 2018, 78(11): 961. DOI: 10.1140/epjc/s10052-018-6445-1.
- [129] Han J J, Jiang H Y, Liu W, et al. Rescattering mechanism of weak decays of double-charm baryons[J/OL]. Chin. Phys. C, 2021, 45(5): 053105. DOI: 10.1088/1674-1137/abec68.
- [130] Li R H, Hou J J, He B, et al. Weak Decays of Doubly Heavy Baryons:  $B_{cc} \rightarrow BD^{(*)}$ [J/OL]. 2020. DOI: 10.1088/1674-1137/abe0bc.
- [131] Cheng H Y, Meng G, Xu F, et al. Two-body weak decays of doubly charmed baryons[J/OL]. Phys. Rev. D, 2020, 101(3): 034034. DOI: 10.1103/PhysRevD.101.034034.
- [132] Aaij R, et al. Observation of the doubly charmed baryon  $\Xi_{cc}^{++}$  [J/OL]. Phys. Rev. Lett., 2017, 119: 112001. DOI: 10.1103/PhysRevLett.119.112001.
- [133] Yu F S, Jiang H Y, Li R H, et al. Discovery Potentials of Doubly Charmed Baryons[J/OL]. Chin. Phys. C, 2018, 42(5): 051001. DOI: 10.1088/1674-1137/42/5/051001.
- [134] Gutsche T, Ivanov M A, Körner J G, et al. Decay chain information on the newly discovered double charm baryon state  $\Xi_{cc}^{++}$  [J/OL]. Phys. Rev. D, 2017, 96(5): 054013. DOI: 10.1103/Ph ysRevD.96.054013.
- [135] Aaij R, et al. First observation of the doubly charmed baryon decay  $\Xi_{cc}^{++} \to \Xi_c^+ \pi^+$  [J/OL]. Phys. Rev. Lett., 2018, 121: 162002. DOI: 10.1103/PhysRevLett.121.162002.
- [136] Aaij R, et al. Precision measurement of the  $\Xi_{cc}^{++}$  mass[J/OL]. JHEP, 2020, 02: 049. DOI: 10.1007/JHEP02(2020)049.
- [137] Mattson M, et al. First observation of the doubly charmed baryon  $\Xi_{cc}^+$ [J/OL]. Phys.Rev.Lett., 2002, 89: 112001. DOI: 10.1103/PhysRevLett.89.112001.

- [138] Ocherashvili A, et al. Confirmation of the double charm baryon Xi+(cc)(3520) via its decay to p D+ K-[J/OL]. Phys. Lett. B, 2005, 628: 18-24. DOI: 10.1016/j.physletb.2005.09.043.
- [139] Russ J S. First Observation of a Family of Double Charm Baryons[J]. Frascati Phys. Ser., 2003, 31: 25-28.
- [140] Moinester M A, et al. First Observation of Doubly Charmed Baryons[J]. Czech. J. Phys., 2003, 53: B201-B213.
- [141] Kiselev V V, Likhoded A K. Comment on 'First observation of doubly charmed baryon Xi(cc)+' [J]. 2002.
- [142] Gross E, Vitells O. Trial factors for the look elsewhere effect in high energy physics[J/OL]. Eur. Phys. J., 2010, C70: 525-530. DOI: 10.1140/epjc/s10052-010-1470-8.
- [143] Ratti S P. New results on c-baryons and a search for cc-baryons in FOCUS[J/OL]. Nucl. Phys. B Proc. Suppl., 2003, 115: 33-36. DOI: 10.1016/S0920-5632(02)01948-5.
- [144] Aubert B, et al. Search for doubly charmed baryons  $\Xi_{cc}^+$  and  $\Xi_{cc}^{++}$  in BaBar[J/OL]. Phys.Rev., 2006, D74: 011103. DOI: 10.1103/PhysRevD.74.011103.
- [145] Chistov R, et al. Observation of new states decaying into  $\Lambda_c^+ K^- \pi^+$  and  $\Lambda_c^+ K_S^0 \pi^-$  [J/OL]. Phys.Rev.Lett., 2006, 97: 162001. DOI: 10.1103/PhysRevLett.97.162001.
- [146] Aaij R, et al. Search for the doubly charmed baryon  $\Xi_{cc}^+$ [J/OL]. JHEP, 2013, 12: 090. DOI: 10.1007/JHEP12(2013)090.
- [147] Aaij R, et al. A search for  $\Xi_{cc}^{++} \to D^+ p K^- \pi^+$  decays[J/OL]. JHEP, 2019, 10: 124. DOI: 10.1007/JHEP10(2019)124.
- [148] Aaij R, et al. Measurement of the lifetime of the doubly charmed baryon  $\Xi_{cc}^{++}$ [J/OL]. Phys. Rev. Lett., 2018, 121: 052002. DOI: 10.1103/PhysRevLett.121.052002.
- [149] Aaij R, et al. Measurement of the lifetimes of promptly produced  $\Omega$ c0 and  $\Xi$ c0 baryons[J/OL]. Sci. Bull., 2022, 67(5): 479-487. DOI: 10.1016/j.scib.2021.11.022.
- [150] Aaij R, et al. Search for the doubly charmed baryon  $\Xi_{cc}^+$  [J/OL]. Sci. China Phys. Mech. Astron., 2020, 63: 221062. DOI: 10.1007/s11433-019-1471-8.
- [151] Aad G, et al. The ATLAS Experiment at the CERN Large Hadron Collider[J/OL]. JINST, 2008, 3: S08003. DOI: 10.1088/1748-0221/3/08/S08003.
- [152] Chatrchyan S, et al. The CMS Experiment at the CERN LHC[J/OL]. JINST, 2008, 3: S08004. DOI: 10.1088/1748-0221/3/08/S08004.
- [153] Aamodt K, et al. The ALICE experiment at the CERN LHC[J/OL]. JINST, 2008, 3: S08002. DOI: 10.1088/1748-0221/3/08/S08002.
- [154] LHC Design Report Vol.1: The LHC Main Ring[J/OL]. 2004. DOI: 10.5170/CERN-2004-0 03-V-1.
- [155] LHC Design Report. 2. The LHC infrastructure and general services[J/OL]. 2004. DOI: 10.5 170/CERN-2004-003-V-2.
- [156] LHC Design Report. 3. The LHC injector chain[J/OL]. 2004. DOI: 10.5170/CERN-2004-003-V-3.
- [157] LHC Machine[J/OL]. JINST, 2008, 3: S08001. DOI: 10.1088/1748-0221/3/08/S08001.

- [158] Zurbano Fernandez I, et al. High-Luminosity Large Hadron Collider (HL-LHC): Technical design report[J/OL]. 2020, 10/2020. DOI: 10.23731/CYRM-2020-0010.
- [159] Alves Jr. A A, et al. The LHCb detector at the LHC[J/OL]. JINST, 2008, 3(LHCb-DP-2008-001): S08005. DOI: 10.1088/1748-0221/3/08/S08005.
- [160] Aaij R, et al. LHCb detector performance[J/OL]. Int. J. Mod. Phys., 2015, A30: 1530022. DOI: 10.1142/S0217751X15300227.
- [161] R. Aaij *et al.*, and A. Bharucha, et al. Implications of LHCb measurements and future prospects [J/OL]. Eur. Phys. J., 2013, C73: 2373. DOI: 10.1140/epjc/s10052-013-2373-2.
- [162] Christian Elsasser.  $\bar{b}b$  production angle plots[EB/OL]. [2022-03-24]. https://lhcb.web.cern.ch/lhcb/speakersbureau/html/bb ProductionAngles.html.
- [163] Aaij R, et al. A comprehensive real-time analysis model at the LHCb experiment[J/OL]. JINST, 2019, 14: P04006. DOI: 10.1088/1748-0221/14/04/P04006.
- [164] Aaij R, et al. Precision luminosity measurements at LHCb[J/OL]. JINST, 2014, 9: P12005. DOI: 10.1088/1748-0221/9/12/P12005.
- [165] Sjöstrand T, Mrenna S, Skands P. A brief introduction to PYTHIA 8.1[J/OL]. Comput. Phys. Commun., 2008, 178: 852-867. DOI: 10.1016/j.cpc.2008.01.036.
- [166] Belyaev I, et al. Handling of the generation of primary events in Gauss, the LHCb simulation framework[J/OL]. J. Phys. Conf. Ser., 2011, 331: 032047. DOI: 10.1088/1742-6596/331/3/03 2047.
- [167] Lange D J. The EvtGen particle decay simulation package[J/OL]. Nucl. Instrum. Meth., 2001, A462: 152-155. DOI: 10.1016/S0168-9002(01)00089-4.
- [168] Golonka P, Was Z. PHOTOS Monte Carlo: A precision tool for QED corrections in Z and W decays[J/OL]. Eur. Phys. J., 2006, C45: 97-107. DOI: 10.1140/epjc/s2005-02396-4.
- [169] Agostinelli S, et al. Geant4: A simulation toolkit[J/OL]. Nucl. Instrum. Meth., 2003, A506: 250. DOI: 10.1016/S0168-9002(03)01368-8.
- [170] Allison J, Amako K, Apostolakis J, et al. Geant4 developments and applications[J/OL]. IEEE Trans.Nucl.Sci., 2006, 53: 270. DOI: 10.1109/TNS.2006.869826.
- [171] Clemencic M, et al. The LHCb simulation application, Gauss: Design, evolution and experience [J/OL]. J. Phys. Conf. Ser., 2011, 331: 032023. DOI: 10.1088/1742-6596/331/3/032023.
- [172] Müller D, Clemencic M, Corti G, et al. ReDecay: A novel approach to speed up the simulation at LHCb[J/OL]. Eur. Phys. J., 2018, C78: 1009. DOI: 10.1140/epjc/s10052-018-6469-6.
- [173] Barrand G, et al. GAUDI A software architecture and framework for building HEP data processing applications[J/OL]. Comput. Phys. Commun., 2001, 140: 45-55. DOI: 10.1016/S0 010-4655(01)00254-5.
- [174] Aaij R, et al. Performance of the LHCb trigger and full real-time reconstruction in Run 2 of the LHC[J/OL]. JINST, 2019, 14(LHCb-DP-2019-001): P04013. DOI: 10.1088/1748-0221/14/0 4/P04013.
- [175] Aaij R, et al. Measurement of the track reconstruction efficiency at LHCb[J/OL]. JINST, 2015, 10: P02007. DOI: 10.1088/1748-0221/10/02/P02007.

- [176] Anderlini L, Contu A, Jones C R, et al. The PIDCalib package: LHCb-PUB-2016-021[EB/OL]. 2016. http://cds.cern.ch/record/2202412.
- [177] Voss H, Hoecker A, Stelzer J, et al. TMVA Toolkit for Multivariate Data Analysis with ROOT [J/OL]. PoS, 2007, ACAT: 040. DOI: 10.22323/1.050.0040.
- [178] Hoecker A, et al. TMVA 4 Toolkit for Multivariate Data Analysis with ROOT. Users Guide. [J]. 2009.
- [179] Martin Sanchez A, Robbe P, Schune M H. Performances of the LHCb L0 Calorimeter Trigger: LHCb-PUB-2011-026; CERN-LHCb-PUB-2011-026[R/OL]. Geneva: CERN, 2012. https://cds.cern.ch/record/1407893.
- [180] Rogozhnikov A. Reweighting with Boosted Decision Trees[J/OL]. J. Phys. Conf. Ser., 2016, 762(1). https://github.com/arogozhnikov/hep\_ml. DOI: 10.1088/1742-6596/762/1/012036.
- [181] d'Argent P, Skidmore N, Benton J, et al. Amplitude Analyses of  $D^0 \to \pi^+\pi^-\pi^+\pi^-$  and  $D^0 \to K^+K^-\pi^+\pi^-$  Decays[J/OL]. JHEP, 2017, 05: 143. DOI: 10.1007/JHEP05(2017)143.
- [182] Cheng H Y. Charmed Baryon Physics Circa 2021[J]. 2021.
- [183] Cheng H Y. The strangest lifetime: A bizarre story of  $\tau(\Omega_c^0)$ [J/OL]. 2021. DOI: 10.1016/j.scib .2021.11.025.
- [184] Punzi G. Sensitivity of searches for new signals and its optimization[J]. eConf, 2003, C030908: MODT002.
- [185] Needham M. Momentum scale calibration of the LHCb spectrometer: CERN-LHCb-INT-2017-008[Z]. 2017.
- [186] Aaij R, et al. Measurement of *b*-hadron masses[J/OL]. Phys. Lett., 2012, B708: 241. DOI: 10.1016/j.physletb.2012.01.058.
- [187] Aaij R, et al. Precision measurement of *D* meson mass differences[J/OL]. JHEP, 2013, 06: 065. DOI: 10.1007/JHEP06(2013)065.
- [188] Rogozhnikov A. Reweighting with boosted decision trees[C/OL]//Journal of Physics: Conference Series. 2016. https://arxiv.org/pdf/1608.05806.pdf.
- [189] et.al A J. Measurement of the track finding efficiency[J]. 2011(LHCb-PUB-2011-025).
- [190] Letter of Intent for the LHCb Upgrade[J]. 2011.
- [191] Bediaga I, et al. Framework TDR for the LHCb Upgrade: Technical Design Report[J]. 2012.
- [192] Aaij R, et al. Expression of Interest for a Phase-II LHCb Upgrade: Opportunities in flavour physics, and beyond, in the HL-LHC era[R/OL]. Geneva: CERN, 2017. https://cds.cern.ch/record/2244311.
- [193] Aaij R, et al. Physics case for an LHCb Upgrade II Opportunities in flavour physics, and beyond, in the HL-LHC era[J]. 2018.
- [194] LHCb Trigger and Online Technical Design Report: CERN-LHCC-2014-016[Z]. Geneva: CERN, 2014.
- [195] LHCb VELO Upgrade Technical Design Report: CERN-LHCC-2013-021[Z]. Geneva: CERN, 2013.

- [196] Altmannshofer W, et al. The Belle II Physics Book[J/OL]. PTEP, 2019, 2019(12): 123C01. DOI: 10.1093/ptep/ptz106.
- [197] CEPC Conceptual Design Report: Volume 1 Accelerator[J]. 2018.
- [198] Abada A, et al. FCC Physics Opportunities: Future Circular Collider Conceptual Design Report Volume 1[J/OL]. Eur. Phys. J. C, 2019, 79(6): 474. DOI: 10.1140/epjc/s10052-019-6904-3.
- [199] The International Linear Collider Technical Design Report Volume 1: Executive Summary [J]. 2013.
- [200] A Multi-TeV Linear Collider Based on CLIC Technology: CLIC Conceptual Design Report [J/OL]. 2012. DOI: 10.5170/CERN-2012-007.
- [201] Agostini P, et al. The Large Hadron-Electron Collider at the HL-LHC[J/OL]. J. Phys. G, 2021, 48(11): 110501. DOI: 10.1088/1361-6471/abf3ba.
- [202] Abelev B, et al. Upgrade of the ALICE Experiment: Letter Of Intent[J/OL]. J. Phys. G, 2014, 41: 087001. DOI: 10.1088/0954-3899/41/8/087001.
- [203] Aaij R, et al. Measurement of the  $\Xi_b^-$  and  $\Omega_b^-$  baryon lifetimes[J/OL]. Phys. Lett., 2014, B736: 154. DOI: 10.1016/j.physletb.2014.06.064.
- [204] Aaij R, et al. Measurements of the mass and lifetime of the  $\Omega_b^-$  baryon[J/OL]. Phys. Rev., 2016, D93: 092007. DOI: 10.1103/PhysRevD.93.092007.
- [205] Aaij R, et al. Search for the doubly charmed baryon  $\Xi_{cc}^+$  in the  $\Xi_c^+\pi^-\pi^+$  final state[J/OL]. JHEP, 2021, 12: 107. DOI: 10.1007/JHEP12(2021)107.
- [206] Aaij R, et al. Observation of the doubly charmed baryon decay  $\Xi_{cc}^{++} \to \Xi_{c}^{'+} \pi^{+}[J]$ . 2022.
- [207] Zhang J W, Wu X G, Zhong T, et al. Hadronic Production of the Doubly Heavy Baryon  $\Xi_{bc}$  at LHC[J/OL]. Phys. Rev. D, 2011, 83: 034026. DOI: 10.1103/PhysRevD.83.034026.
- [208] Qin Q, Shi Y J, Wang W, et al. Inclusive approach to hunt for the beauty-charmed baryons  $\Xi_{bc}$  [J/OL]. Phys. Rev. D, 2022, 105(3): L031902. DOI: 10.1103/PhysRevD.105.L031902.

## 致谢

感谢我的导师高原宁老师,从我本科入学以来,您高屋建瓴的指导和无微不至的关心,激发了我对高能物理学科的好奇心,熏陶了我的学术修养和品味,开拓了我的学术视野,奠定了我的学术基础。

感谢我的指导老师杨振伟老师,从我本科入学以来,您事无巨细的指导和帮助,培养了我的学术技能,塑造了我的学术规范,提高了我的学术交流能力。

感谢张艳席老师、何吉波老师、钱文斌老师对我的研究课题耐心细致的指导和帮助。

感谢张黎明老师、朱相雷老师、陈少敏老师、王喆老师的讨论指导和潜移默化的熏陶。

感谢实验组安刘攀、王梦臻、许泽华、赵明锐、陈晨、任赞、罗毅恒、张舒楠、 许立、王剑桥、徐蔚然、沈志宏、王子涵等同学,与你们的讨论交流使我受益匪浅, 受到激励和鼓舞。